
THE UNIVERSITY OF QUEENSLAND

AUSTRALIA

# Growth of Metal Chalcogenide Nanomaterials and Their Characterizations

Yichao Zou

Bachelor of Engineering

*A thesis submitted for the degree of Doctor of Philosophy at*

*The University of Queensland in 2016*

School of Mechanical and Mining Engineering

**Abstract**

Metal chalcogenides, such as IV-VI and V-VI compounds (SnTe, $Bi_2Te_3$, $Bi_2Se_3$), are ideal candidates for applications in thermoelectricity and topological (crystalline) insulators. This PhD thesis focuses on the controllable synthesis of metal chalcogenide nanostructures via chemical vapour deposition method (CVD), and on the understanding of the crystal structure, growth mechanism, and structure-property correlation in the as-grown nanomaterials. IV-VI and V-VI compounds have attracted extensive research interest because of their excellent thermoelectric properties and exotic physical properties. Nevertheless, there still exist unresolved issues that prevent the further applications of IV-VI and V-VI nanomaterials by rational design, including (1) it is still difficult to grow these nanomaterials with controllable morphology and (2) crystal structure; (3) limited investigations of their growth mechanisms; (4) limited study on structure-property relationships in the nanostructures. Therefore, in this thesis, the controllable growth technique, growth mechanism and structure-property relation in IV-VI and V-VI based nanostructures are explored. The objective is achieved in the following steps:

- Realizing the morphological control of the nanostructures. (i) By catalyst engineering in Au-catalysed CVD. For SnTe nanostructures, catalyst composition was found to be a key factor controlling the morphology. AuSn catalysts induce growth of triangular SnTe nanoplates, whereas $Au_5Sn$ catalysts result in <010> SnTe NWs. For $Bi_2Se_3$ nanostructures, catalyst-nanostructure interface was found to have an impact on their growth directions. A {0001} interface between the catalyst/nanostructure induces the growth of {0001} NWs, while when the interface is not defined, $< 11\bar{2}0 >$ nanoribbons are grown. (ii) By doping in catalyst-free CVD. It has been found that Bi doping induces a switch of dominant surface facet in SnTe nanostructures, from {100} to {111}. This transition is driven by surface-energy minimization according to our energetic calculation results, which suggests that incorporation of Bi dopant reduces the surface energy of $\{111\}_{Te}$ facet in SnTe.
- Realizing the crystal-structure control of the nanostructures. Bi dopant was found to be an essential parameter that can control the crystal structure of SnTe based nanostructures. Bi dopants promote the formation of Sn planar vacancies in $Sn_{1-}$

$_xBi_xTe$ nanoribbons. The density of the planar vacancies can be engineered by varying the Bi concentration. Through combination of sub-ångström-resolution imaging and calculation within density functional theory, these planar vacancies are found to be associated with Bi segregation, which significantly lowers the formation energies of the vacancies. The planar vacancies exhibit polymorphic structures with local variations in lattice relaxation level, determined by their proximity to nanoribbon surface.

- Understanding the growth mechanism. For the growth of $Bi_2Se_3$, Au catalyst was found to initiate the nucleation of nanostructures by absorbing V vapour species (Bi) via a vapour-solid-solid mechanism. For growth of SnTe, the catalyst was found to preferentially absorb IV resources (Sn) to form Au-Sn alloy particles to initiate the nanostructure growth, where both vapour-solid-solid and vapour-liquid-solid mechanisms may dominate.
- Understanding the structure-property correlation. (i) By experimental measurement of individual nanostructures. $Bi_2Te_3$ and $Bi_2Se_3$ have a layered rhombohedral crystal structure. Within each quintuple layer, atoms are joined by strong covalent bonding. While between neighboring quintuple layers, the interaction is only weak van der Waals. This anisotropic bonding is expected to result in a strong anisotropy in electronic properties. We demonstrate that such electronic anisotropy may be enhanced in nanoscale samples, by comparing the conductivities of <0001> and $<11\bar{2}0>$ grown $Bi_2Se_3$ nanostructures using an *in-situ* TEM-STM facility. The conductivity anisotropic ratio at nanoscale is found to be ~50 times larger than their bulk counterparts. (ii) By electronic-structure calculation within density functional theory in combination of atomic-scale imaging. In planar-vacancy engineered $Sn_{1-x}Bi_xTe$ nanoribbons, calculations show that the Bi segregated planar vacancies introduce newly localized distorted density of states into the system. In $Bi_2SnTe_4$ nanostructures, cation-atom disordering was observed by aberration-corrected STEM. Calculations show that such cation disordering may narrow the bandgap of this semiconductor system.

**Declaration by author**

This thesis *is composed of my original work, and contains* no material previously published or written by another person except where due reference has been made in the text. I have clearly stated the contribution by others to jointly-authored works that I have included in my thesis.

I have clearly stated the contribution of others to my thesis as a whole, including statistical assistance, survey design, data analysis, significant technical procedures, professional editorial advice, and any other original research work used or reported in my thesis. The content of my thesis is the result of work I have carried out since the commencement of my research higher degree candidature and does not include a substantial part of work that has been submitted *to qualify for the award of any* other degree or diploma in any university or other tertiary institution. I have clearly stated which parts of my thesis, if any, have been submitted to qualify for another award.

I acknowledge that an electronic copy of my thesis must be lodged with the University Library and, subject to the policy and procedures of The University of Queensland, the thesis be made available for research and study in accordance with the Copyright Act 1968 unless a period of embargo has been approved by the Dean of the Graduate School.

I acknowledge that copyright of all material contained in my thesis resides with the copyright holder(s) of that material. Where appropriate I have obtained copyright permission from the copyright holder to reproduce material in this thesis.

**Publications during candidature**

Published papers included in this Thesis:

1. **Zou, Y.;** Chen, Z.-G.; Lin, J.; Zhou, X.; Lu, W.; Drennan, J.; Zou, J., Morphological Control of SnTe Nanostructures by Tuning Catalyst Composition. *Nano Res.* **2015**, 8, 3011-3019.
2. **Zou, Y.**; Chen, Z.-G.; Huang, Y.; Yang, L.; Drennan, J.; Zou, J., Anisotropic Electrical Properties from Vapor–Solid–Solid Grown $Bi_2Se_3$ Nanoribbons and Nanowires. *J. Phys. Chem. C* **2014**, 118, 20620-20626.
3. **Zou, Y.**; Chen, Z.-G.; Kong, F.; Lin, J.; Drennan, J.; Cho, K. J.; Wang, Z.; Zou, J., Planar Vacancies in $Bi_{1-x}Sn_xTe$ Nanoribbons. *ACS Nano* **2016**, 10, 5507-5515.

Published co-authored papers:

1. Chen, Z.-G.; Zhang, C.; **Zou, Y.**; Zhang, E.; Yang, L.; Hong, M.;. Xiu, F.-X; Zou, J., Scalable Growth of High Mobility Dirac Semimetal $Cd_3As_2$ Microbelts. *Nano Lett.* **2015**, 15, 5830−5834
2. Yang, L.; Chen, Z.-G.; Han, G.; Hong, M.; **Zou, Y.**; Zou, J., High-Performance Thermoelectric $Cu_2Se$ Nanoplates Through Nanostructure Engineering. *Nano Energy* **2015**, 16, 367-374.
3. Yuan, X.; Tang, L.; Liu, S.; Wang, P.; Chen, Z.; Zhang, C.; Liu, Y.; Wang, W.; **Zou, Y.**; Liu, C.; Guo, N.; Zou, J.; Zhou, P.; Hu, W.-D.; Xiu, F.-X., Arrayed van der Waals Vertical Heterostructures Based on 2D GaSe Grown by Molecular Beam Epitaxy. *Nano Lett.* **2015**, 15, 3571-3577.
4. Yuan, X.; Tang, L.; Wang, P.; Chen, Z.; **Zou, Y.**; Su, X.; Zhang, C.; Liu, Y.; Wang, W.; Liu, C.; Chen, F.-S.; Zou, J.; Zhou, P.; Hu, W.-D.; Xiu, F.-X., Wafer-Scale Arrayed p-n Junctions Based on Few-Layer Epitaxial GaTe. *Nano Res.* **2015**, DOI: 10.1007/s12274-015-0833-8.
5. Han, G.; Chen, Z.-G.; Ye, D.; Wang, B.; Yang, L.; **Zou, Y.**; Wang, L.; Drennan, J.; Zou, J., $In_3Se_4$ and S-Doped $In_3Se_4$ Nano/Micro-Structures as New Anode Materials for Li-Ion Batteries. *J. Mater. Chem. A* **2015**, 3, 7560-7567.
6. Han, G.; Chen, Z.-G.; **Zou, Y.**; Drennan, J.; Zou, J., Long Wavelength Emissions of $Se^{4+}$-Doped $In_2O_3$ Hierarchical Nanostructures. *J. Mater. Chem. C* **2014**, 2, 6529-6535.

Conference abstract

1. **Zou, Y. C.**; Chen, Z. G.; and Drennan, J.; Zou, J.; Morphology Control of SnTe Nanostructures by Catalyst Engineering. ***ACMM 2016.*** (Canberra, Oral presentation)
2. Zou, J.; **Zou, Y. C.**; Chen, Z. G.; and Drennan, J.; Catalyst Impact on Morphologies of SnTe Nanostructures. ***ICONN 2016***. (Canberra, Poster presentation)
3. **Zou, Y. C.**; Chen, Z. G.; and Drennan, J.; Zou, J.; Gold Catalyzed and Catalyst-Free Growth of One-Dimensional $Bi_2Se_3$ Nanostructures. ***COMMAD 2014.*** (Perth, Oral presentation)
4. **Zou, Y. C.**; Chen, Z. G.; and Drennan, J.; Zou, J.; Vapor-Solid-Solid Grown $Bi_2Se_3$ Nanoribbons and Nanowires with Anisotropic Electronic Properties. ***ICAMP8 2014.*** (Gold Coast, Oral presentation)

**Publications included in this thesis**

**Zou, Y.**; Chen, Z.-G.; Kong, F.; Lin, J.; Drennan, J.; Cho, K. J.; Wang, Z.; Zou, J., Planar Vacancies in $Bi_{1-x}Sn_xTe$ Nanoribbons. *ACS Nano* **2016**, 10, 5507-5515.

| Contributions | Statement of contribution |
|---|---|
| Yichao Zou (Candidate) | Designed experiments (60%)<br>Carried out materials synthesis (100%)<br>Carried out characterization (60%)<br>Carried out data analysis (60%)<br>Wrote the paper (60%) |
| Zhigang Chen | Designed experiments (15%)<br>Carried out characterization (10%)<br>Carried out data analysis (5%)<br>Wrote the paper (15%)<br>Supervision (20%) |
| Fantai Kong | Carried out modelling and calculations (50%)<br>Carried out data analysis (25%)<br>Wrote the paper (5%) |
| Jing Lin | Wrote the paper (5%) |
| John Drennan | Supervision (20%) |
| Kyeongjae Cho | Carried out modelling and calculations (10%) |
| Zhongchang Wang | Designed experiments (10%)<br>Carried out characterization (30%)<br>Carried out modelling and calculations (40%) |
| Jin Zou | Designed experiments (15%)<br>Carried out data analysis (10%)<br>Wrote the paper (15%)<br>Supervision (60%) |

**Zou, Y.**; Chen, Z.-G.; Lin, J.; Zhou, X.; Lu, W.; Drennan, J.; Zou, J., Morphological Control of SnTe Nanostructures by Tuning Catalyst Composition. *Nano Res.* **2015**, 8, 3011-3019.

| Contributor | Statement of contribution |
|---|---|
| Yichao Zou (Candidate) | Designed experiments (70%)<br>Carried out materials synthesis (100%)<br>Carried out characterization (90%)<br>Carried out data analysis (70%)<br>Wrote the paper (60%) |
| Zhigang Chen | Designed experiments (10%)<br>Carried out characterization (10%)<br>Carried out data analysis (10%)<br>Wrote the paper (15%)<br>Supervision (20%) |
| Jing Lin | Wrote the paper (5%) |
| Xiaohao Zhou | Carry out modelling (80%) |
| Wei Lu | Carry out modelling (20%) |
| John Drennan | Wrote the paper (5%)<br>Supervision (20%) |
| Jin Zou | Designed experiments (20%)<br>Carried out data analysis (20%)<br>Wrote the paper (15%)<br>Supervision (60%) |

**Zou, Y.**; Chen, Z.-G.; Huang, Y.; Yang, L.; Drennan, J.; Zou, J., Anisotropic Electrical Properties from Vapor–Solid–Solid Grown $Bi_2Se_3$ Nanoribbons and NWs. *J. Phys. Chem. C* **2014**, 118, 20620-20626.

| Contributor | Statement of contribution |
|---|---|
| Yichao Zou (Candidate) | Designed experiments (60%)<br>Carried out materials synthesis (100%)<br>Carried out characterization (60%)<br>Carried out data analysis (70%)<br>Wrote the paper (60%) |
| Zhigang Chen | Designed experiments (20%)<br>Carried out characterization (10%)<br>Carried out data analysis (10%)<br>Wrote the paper (15%)<br>Supervision (20%) |
| Yang Huang | Carried out characterization (30%) |
| Lei Yang | Wrote the paper (5%) |
| John Drennan | Supervision (20%) |
| Jin Zou | Designed experiments (20%)<br>Carried out data analysis (10%)<br>Wrote the paper (15%)<br>Supervision (60%) |

**Contributions by others to the thesis**

“No contributions by others”

**Statement of parts of the thesis submitted to qualify for the award of another degree**

“No”

**Acknowledgements**

At first, I would like to express my sincere gratitude to my research supervisors, Prof. Jin Zou, Dr. Zhigang Chen and Prof. John Drennan for their encouragement, guidance and patience in every respect of my PhD research.

Also, I would like to thank my co-workers in the group, Dr. Kun Zheng, Dr. Lihua Wang, Dr. Yang Huang, Dr. Jing Lin, Dr. Yanan Guo, Dr. Lina Chen, Dr Justin (Hongyi) Xu, Dr. Guang Han, Dr. Wen Sun, Dr. Zhi Zhang, Dr. Lei Yang, Dr. Min Hong, Mr. Zhiming Liao, Miss Chen Zhou, Miss Abby Soo and Mr. Liqing Huang. Thank you very much for your great help and support in my research and life in Brisbane.

Meanwhile, I gratefully thank Dr. Xiaohao Zhou from SITP and Mr. Fantai Kong from University of Texas at Dallas, for their knowledge in first-principles calculation and their generous help for my data analysis. I'd like to show special thanks to staff of Centre for Microscopy and Microanalysis (CMM) at UQ, who trained me with practical TEM and SEM skills, including Dr. Graeme Auchtermonie, Mr Gary Morgan, Dr. Ron Rasch, Dr. Kim Sewell, Mrs Eunice Grinan, and Mrs Ying Yu. I'd like to extend my thanks to staff of Mechanical Workshop and Glassware Workshop at UQ, who helped my experiment setups in many ways.

Financial support from China Scholarship Council (CSC) is greatly acknowledged. I sincerely thank UQ graduate school for providing me tuition-waive scholarship, top-tup scholarship, and GSITA travel grant for my research travel to Japan.

Finally, I want to give my great thanks to my family members and my friends in China for their endless love and support that keep me move forward in my life.

**Keywords**

metal chalcogenides, bismuth selenide, tin telluride, nanostructure engineering, chemical vapour deposition, topological insulator, thermoelectric, scanning transmission electron microscopy, density functional theory

**Australian and New Zealand Standard Research Classifications (ANZSRC)**

ANZSRC code: 100712, Nanoscale Characterization, 40%

ANZSRC code: 100716, Nanofabrication, Growth and Self-Assembly 40%

ANZSRC code: 091203, Compound Semiconductors, 20%

**Fields of Research (FoR) Classification**

FoR code: 0912, Materials Engineering, 50%

FoR code: 1007, Nanotechnology, 50%

**Table of Contents**

## List of Figures

displacements happened near the dash line for the transition to (b). (b) Atomic model of the hexagonal structured $GeSb_2Te_4$, with an ordered arrangement of the vacancies at the dash line. Cation vacancies, Te atoms and cation atoms, are respectively denoted by hollow circles, green filled circles and orange circles.

**Figure 2.13** Total energy per atom, $E_{diff}$, of the models of cubic $GeSb_2Te_4$, hexagonal $GeSb_2Te_4$ and intermediate structures studied. In the plot the zero of the energy coincides with the energy of the most favourable structure, hexagonal 100%-*d*. Insets show the starting random cubic phase, the final hexagonal phase 100%-*d* and two intermediate phases (cubic-$l_{Vac}$=50% and hexagonal-$l_{Vac}$=75%). The last four points (100%-*a*~*d*) correspond to hexagonal structures containing completely formed vacancy layers, which differ in the distribution of Ge and Sb atoms in the Ge/Sb layers.

**Figure 2.14** (a) The rock-salt crystal structure of SnTe. (b) Corresponding face-centered-cubic (FCC) Brillouin zone, showing the plane $\Gamma L_1 L_2$, which is invariant under reflection about the (110) axis and projects onto the $\overline{\Gamma X_1}$ line in the [001] surface. (c) Calculated band structures of bulk SnTe. The size of the red dots represents the fraction of electronic charge residing on Te atoms. The exchange of the band character at *L* point as highlighted in the grey area indicates the intrinsic band inversion of SnTe. (d) Band dispersion of (001) surface.

**Figure 2.15** (a) Primitive unit cell (left) and Brillouin zone (right) for $Bi_2Se_3$ with space group $R\bar{3}m$. The blue hexagon shows the 2D Brillouin zone of the projected (111) surface. (b, c) Calculated and structure for $Bi_2Se_3$ without considering SOC (b) and with SOC (c). (d) Energy and momentum dependence of the LDOS for $Bi_2Se_3$ on the (111) surface. The red regions indicate bulk energy bands and the blue regions indicate bulk energy gaps.

**Figure 2.16** Thermoelectric modules: (a) power generator by the Seebeck Effect, (b) cooling refrigerator by the Peltier Effect.

**Figure 2.17** (a) Idealized band structure of TI with metallic edge states (green lines) in the bulk bandgap, in which up and down spins propagate in opposite directions. (b) Metallic edge of a 2D TI (left), and the corresponding spin-resolved surface band structure (right). (c) Metallic surface of 3D TI (left) and the corresponding spin-resolved surface band structure (right). (d) Band diagram of a TI before surface

modification (left) and after surface modification (right), in which the grey area denotes the bulk states. (e) Band structures of an ordinary semiconductor before surface modification (left) and after surface modification (right).

**Figure 2.18** (a, b) High-resolution ARPES measurements of the surface electronic band dispersion of $Bi_2Se_3$(111) near the $\bar{\Gamma}$ point along the $\bar{\Gamma}-\bar{M}$ (a) and $\bar{\Gamma}-\bar{K}$ (b) momentum-space cuts. (c, d) ARPES map of the surface band dispersion of $Bi_{2-x}Ca_xSe_3$ (111) after a 2 L dosage of $NO_2$, taken at 300K (c) and 10K (d).

**Figure 2.19** (a) Schematic 2D band dispersions near Fermi level $E_F$ depicting the evolution of the surface Dirac cones. (b) Near-$E_F$ energy distribution curves around the $\bar{\Lambda}$ point for SnTe.

**Figure 2.20** (a) SEM image showing a Hall bar device fabricated for SnTe NW transport measurement. (b) Normalized magnetoresistance under magnetic field. (c) Fast Fourier transform of the derivate dR/dB, showing a prominent AB oscillation frequency of *h/e* at high magnetic field.

**Figure 2.21** SEM images of electrodeposition grown $Bi_2Te_3$ NWs. (a) Cross-section back-scattered SEM images of the NWs embedded in AAO templates. (b) NWs after the removal of the template.

**Figure 2.22** TEM images of solvothermal method synthesised products. (a) $Bi_2Te_3$ ultrathin NWs (~8nm). (b) $Bi_2Te_3$ nanoplates.

**Figure 2.23** TEM images of solution-based synthesised monodisperse cubic SnTe nanocubic (a-b), and NRs (c-d).

**Figure 2.24** (a) HAADF STEM image of the atomically abrupt $Bi_2Te_3$/GaAs interface viewed along $\langle 110\rangle_{GaAs}$ axis. (b) HAADF STEM image of the interface between $Bi_2Te_3$ and $SiO_2$/Si substrate. (c) HAADF STEM image of the interface between $Bi_2Te_3$ and mica substrate.

**Figure 2.25** (a) Scheme of a typical CVD reactor and the CVD growth parameters used for controlling the products. (b) Schematic diagram showing the vapour-solid growth process using bismuth chalcogenide nanoplate as an example.

**Figure 2.26** Morphology and structure of CVD-grown $Bi_2Te_3$ and $Bi_2Se_3$ NPs. (a) SEM image of the CVD-grown $Bi_2Se_3$ NPs; (b) TEM image of a $Bi_2Se_3$ NP and (c)

## List of Tables

## List of Abbreviations

| | |
|---|---|
| **ARPES** | angle resolved photoemission spectroscopy |
| **At%** | atomic ratio |
| **BF** | bright-field |
| **BSE** | back-scattered electron image |
| **CVD** | chemical vapour deposition |
| **DFT** | density functional theory |
| **DOS** | density of states |
| **EDS** | energy dispersive X-ray spectroscopy |
| **FFT** | fast Fourier transform |
| **HAADF** | high angle angular dark field |
| **HRTEM** | high resolution transmission electron microscopy |
| **MBE** | molecular beam epitaxy |
| **NW** | nanowire |
| **NB** | nanobelt |
| **NR** | nanoribbon |
| **NP** | nanoplate |
| **SAED** | selective-area electron diffraction pattern |
| **SE** | secondary electron |
| **SEM** | scanning electron microscopy |
| **S.G.** | space group |
| **SOC** | spin orbit coupling |
| **STEM** | scanning transmission electron microscopy |
| **T** | temperature |
| **TCI** | topological crystalline insulator |
| **TEM** | transmission electron microscopy |
| **TE** | thermoelectric |
| **TI** | topological insulator |
| **VLS** | vapour-liquid-solid growth |
| **VSS** | vapour-solid-solid growth |
| **VDW** | van der Waals force |
| **XPS** | X-ray photoelectron spectroscopy |

| | |
|---|---|
| **XRD** | X-ray diffraction |
| **Z** | atomic number |
| **ZT** | figure of merit |
| **1D** | one-dimensional |
| **2D** | two-dimensional |
| **3D** | three-dimensional |

# 1
# Introduction

## 1.1 Background

Metal chalcogenide materials, such as $Bi_2Se_3$, $Bi_2Te_3$ and SnTe, have attracted numerous research interests recently in modern physics and energy materials.[1-2] For the past half century, chalcogenides have been studied as classical thermoelectric (TE) materials. TE technology can convert temperature differences into electricity, and thus plays a very important role in novel power-generation devices for solving the energy-crisis issues nowadays. Compared to the conventional electricity generation methods, TE technology has key advantages such as high reliability, small sizes and no noise.[1-3] Among the current TE materials, chalcogenide compounds, such as PbTe and $Bi_2Te_3$, are recognized as high-efficiency TE materials, and have already been used in commercial thermoelectric refrigeration and generators.[3]

Very recently, chalcogenides, such as $Bi_2Te_3$, $Bi_2Se_3$ and SnTe, have been demonstrated to be topological insulators (TIs) or topological crystalline insulator (TCI). TI or TCI is a gapped insulator in the bulk but the surface states are metallic, which endows them with novel physical properties, such as anomalous quantum Hall effect,[4] time-reversal invariant topological superconductivity,[5-7] and massless electrical transport.[8]

One of the main approaches to enhance the TE and TI (TCI) properties of chalcogenides is scaling down the sample size into nanoscale.[9-15] For applications in TE, a high-efficiency TE material requires a high power factor and low thermal conductivity. This can be achieved by introducing low-dimensional nanoscale constituents into the system, which may bring a simultaneous increase in the power factor and decrease in the thermal conductivity because of enhanced quantum-confinement effects and phonon scattering.[9] For the probing of TI (TCI) surface state, the low-dimensional materials with large surface-to-bulk ratio is an interesting system to study, in which the contribution from surface carriers is largely increased

and the surface states are manifested.[10-13] Thus, it is highly important to develop low-dimensional metal chalcogenide nanostructures, of which an essential prerequisite is the realization of their controllable growth.

Various methods, including CVD,[10-14] molecular beam epitaxy (MBE)[16,17] and solution-based methods,[18,19] have been used for the synthesis of low-dimensional chalcogenide nanostructures. For solution-based methods, products generally exhibit disadvantages of low-crystallinity and surface contamination.[19] Alternatively, CVD and MBE can fabricate chalcogenide nanostructures with high crystallinity and purity. As MBE is very expensive and not as accessible as CVD, CVD is widely used for growth of high-quality low-dimensional metal chalcogenide nanostructures.[10-13] In these CVD grown nanostructures, exotic physical phenomenon have been observed, such as superconductivity, magnetoresistance, and quantum oscillations.[13] Although the property of CVD grown low-dimensional chalcogenides has been intensively investigated, the growth mechanisms and detail structural characteristics of grown samples are far from thorough understanding. The objective of this PhD thesis is to realize the controllable growth of binary and ternary chalcogenide nanomaterials, and to understand their crystal structures by detailed electron microscopy analysis.

## 1.2 Objectives

The aim of this thesis is to grow low-dimensional IV-VI and V-VI compound nanomaterials using CVD method and to understand their structural characteristics and their physical properties. The specific objectives are as follows:

- Growth of high-quality low-dimensional metal chalcogenide nanostructures using a CVD approach, and understanding their morphological, structural and compositional characteristics;
- Understanding the growth mechanism by closely correlating the nanostructure growth and the as-determined morphological, structural and chemical characteristics;
- Examination and modification of the physical properties of the as-grown nanostructures and understanding the structure-property relation in the nanostructure.

## 1.3 Thesis Outline

In this thesis, SnTe, $Bi_2Se_3$, $Bi_2Te_3$ and Sn-Bi-Te nanostructures were grown by CVD method. The structural characteristics and growth mechanism of the as-grown nanostructures are investigated by advanced electron microscopy.

Chapter 1 gives an introduction of this thesis.

Chapter 2 provides a literature review of the current research progress on the crystal structure, physical properties, and the growth techniques for low-dimensional IV-VI and V-VI nanostructures.

Chapter 3 introduces the experimental and characterization methods involved in this thesis. The details of the CVD method used to grow nanostructures are summarised. The characterization methods, including scanning electron microscopy (SEM), transmission electron microscopy (TEM), X-ray diffraction (XRD), and scanning transmission electron microscopy (STEM) are explained in this chapter.

Chapter 4-7 shows our findings in binary IV-VI and V-VI nanostructures grown by CVD. Chapter 4 discusses the effect of growth direction on the electrical property of $Bi_2Se_3$ nanostructures, and their growth mechanism in Au-catalyzed CVD. This chapter is included as the Journal of Physical Chemistry C, 2014, 118, 20620-20626. Chapter 5 demonstrates a morphological control method of SnTe nanostructures by catalyst engineering in CVD. This chapter is included as the Nano Research, 2015, 8, 3011-3019. Chapter 6 demonstrates the planar-vacancy engineering in SnTe nanostructures by Bi doping, and the detail atomic structure will be discussed. This chapter has been published in ACS Nano, 2016, 10, 5507-5515. Chapter 7 demonstrates a surface-facet control method of doped SnTe nanostructures by Bi doping.

Chapter 8 shows our findings in ternary IV-V-VI nanostructures grown by CVD. We investigated into the metal-atom disordering in $Bi_2SnTe_4$ nanostructures using STEM in combination with density functional theory calculation.

Chapter 9 summarizes the conclusions of this PhD research work and the recommendations for future work.

# 2

# Literature Review

## 2.1 Crystal Structure

### 2.1.1 IV-VI Compound

The binary IV-VI compounds are composed of group IV (Ge, Sn, Pb) and VI elements (Se, Te). Many of these compounds have a rock-salt crystal structure, with a space group of $\mathrm{Fm\bar{3}m}$, including PbSe (*a*=6.12 Å), PbTe (*a*=6.46 Å), GeTe ($\alpha$-GeTe, *a*=6.02 Å) and SnTe (*a*=6.31 Å). In the lattice of a rock-salt structured IV-VI compound, each metal cation is coordinated to the octahedral interstice of six chalcogenide anions, and vice versa (Fig. 2.1).

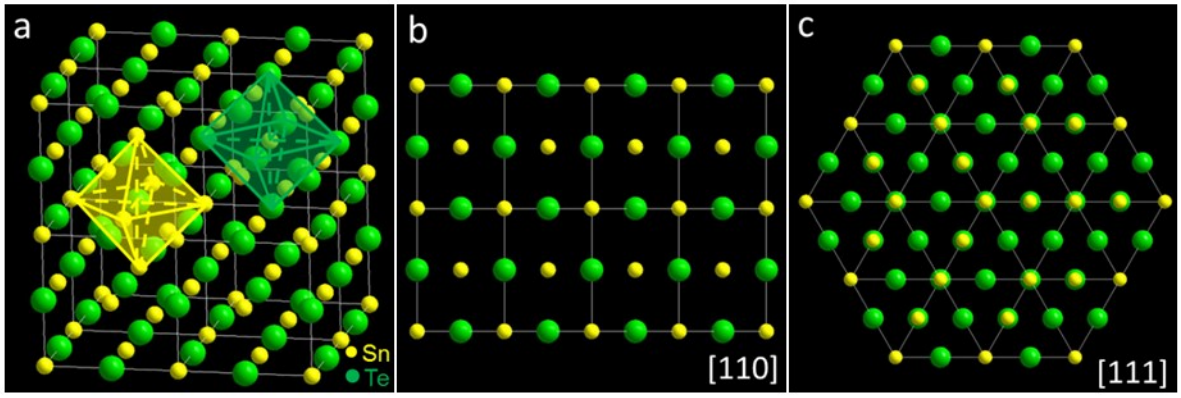


**Figure 2.1** (a) Atomic model showing rock-salt structured SnTe, and (b, c) its projections along axis of [110] (b) and [111] (c).

In these IV-VI compounds, SnTe and GeTe are non-stoichiometric compounds. Their natively grown samples are characterized by a considerable deviation from stoichiometry, due to the intrinsic cation vacancies in the crystal. Figure 2.2 shows a Sn-Te phase diagram, in which a narrow range of homogeneity near 50 at.% Te can be seen, indicating that a small deviation from perfect stoichiometry is likely to happen during the formation of SnTe samples. This was confirmed by experimental results that un-doped SnTe sample shows a *p*-type semiconducting behavior, characterized by large hole concentration induced by Sn vacancies.[20-21]

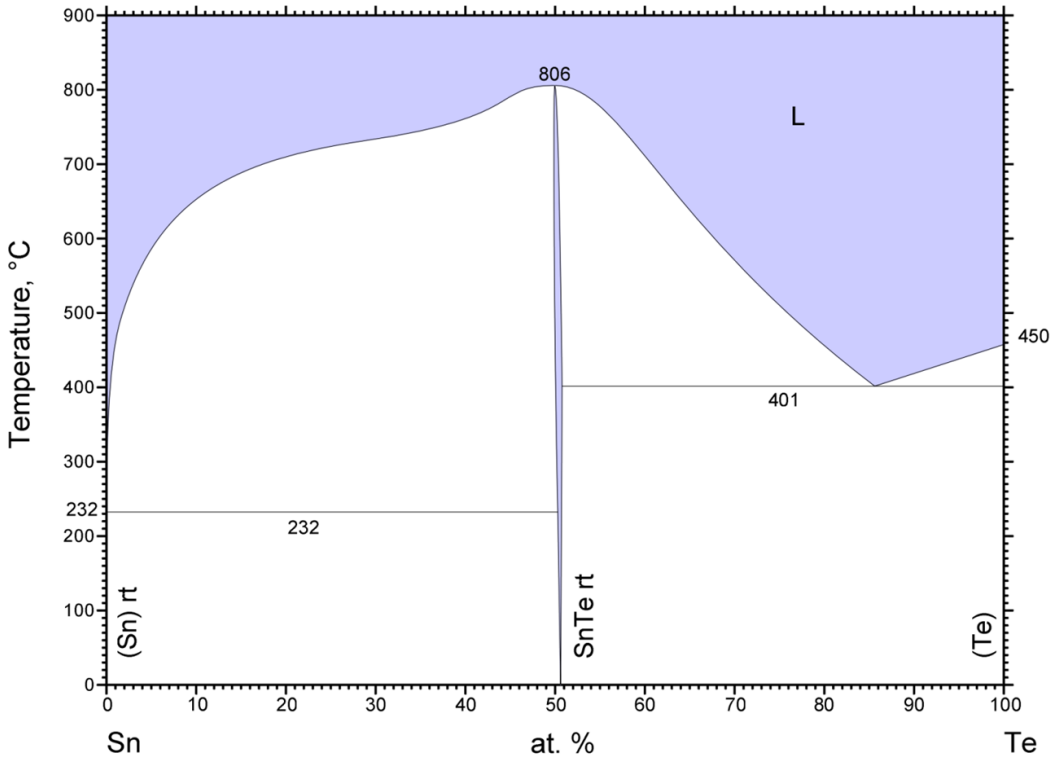


**Figure 2.2** Sn-Te binary phase diagram.[22]

### 2.1.2 V-VI Compound

The binary V-VI compounds (V=Bi, Sb, VI=Se, Te) have tetradymite layered crystal structures.[23-24] Here, we denote the V-VI phases as M-X, where M=Bi, Sb; X= Se, Te. The layer structure of these phases can be considered as stacking variants within part of a single homologous series. Their structures can be expressed as the combination of charge-balanced $M_2X_3$ (5, five-atom layer unit) and $M_2$ (2, two-atom layer unit), or $M_3X_4$ (7, seven-atom layer unit) slabs stacking along *c* axis. Table 1 lists the crystal structure parameters of layered structured V-VI phases, which all have a feature of large *c*. In these phases, $M_2X_3$, including $Bi_2Se_3$, $Bi_2Te_3$ and $Sb_2Te_3$, has the regular "555" structure, with each unit cell consisting of three $M_2X_3$ units and 15 atomic layers (*N*=15). $M_3X_4$ ($Bi_3Se_4$ and $Bi_3Te_4$) has a "777" structure, with each unit cell consisting of consisting of three $M_3X_4$ units and 21 atomic layers (*N*=15). In the case of MX (BiSe and BiTe), a $M_2$ unit is inserted between every second $M_2X_3$ unit and forms a "552" structure. $M_4X_3$ has the "525252" structure, with each $M_2X_3$ unit separated by a $M_2$ unit, and has 21 atomic layers in the unit cell.

**Table 2.1** Number of atomic layers each unit cell (*N*), space group (S. G.), and lattice parameter of layer structured V-VI compounds.

| Compound | *N* | S. G. | *a*(Å) | *c*(Å) | Ref. |
|---|---|---|---|---|---|
| $Bi_2Se_3$ | 15 | $R\bar{3}m$ | 4.16 | 28.63 | [25] |
| $Bi_2Te_3$ | 15 | $R\bar{3}m$ | 4.36 | 30.47 | [25] |
| $Sb_2Te_3$ | 15 | $R\bar{3}m$ | 4.25 | 30.00 | [26] |
| $Bi_3Se_4$ | 21 | $R\bar{3}m$ | 4.23 | 40.40 | [27] |
| $Bi_3Te_4$ | 21 | $R\bar{3}m$ | 4.42 | 41.49 | [29] |
| BiSe | 12 | $P\bar{3}m1$ | 4.18 | 22.80 | [30] |
| BiTe | 12 | $P\bar{3}m1$ | 4.42 | 24.05 | [28] |
| $Bi_4Se_3$ | 21 | $R\bar{3}m$ | 4.27 | 39.90 | [29] |
| $Bi_4Te_3$ | 21 | $R\bar{3}m$ | 4.54 | 41.89 | [28] |
| $Bi_7Se_3$ | 60 | $R\bar{3}m$ | 4.43 | 116.40 | [31] |
| $Bi_7Te_3$ | 60 | $R\bar{3}m$ | 4.49 | 120.04 | [29] |

Among these V-VI compound phases, $M_2X_3$ ($Bi_2Te_3$, $Bi_2Se_3$ and $Sb_2Te_3$) are recognized as the most stable phases, and all have a “555” rhombohedral crystal structure.[24-27] Figure 2.3 shows the atomic model of a $M_2X_3$ crystal. Each metal atom occupies the distorted octahedral interstice of six chalcogenide atoms. Along the *c* axis of $M_2X_3$, the atomic arrangement can be considered as a quintuple-layer (QL) structure with each QL consisting of XI-M-XII-M-XI, where XI denotes the chalcogenide atoms at the border of QL, and XII denotes these in the middle of QL. Within each QL, there exist both covalent and ionic bonds. Between the adjacent QL layers, only van der Waals (VDW) interaction exists, corresponding to the weakest bond and the largest atom-plane spacing in this structure. The presence of VDW gaps enables the easy disassembly of bulk $M_2X_3$ to its QL building blocks (possibly just by Scotch tapes), and makes them prone to accommodate foreign atoms or foreign layered phases.[7,32] This may further introduce novel physical properties into the system, such as superconductivity[7] and a locally conductivity variation.[32] For examples, by the intercalation of Cu in the VDW gaps of $Bi_2Se_3$, researchers found

$Cu_xBi_2Se_3$ becomes a superconductor (Fig. 2.4a).[7] Figure 2.4b-c show the STEM images taken from $Bi_2Te_3$ films, in which a defect region of a seven-layer $Bi_3Te_4$ nanolamella can be found (Te-Bi-Te-Bi-Te-Bi-Te), suggesting that such layered structured defect may be an universal feature in $Bi_2Te_3$ crystals.[32]

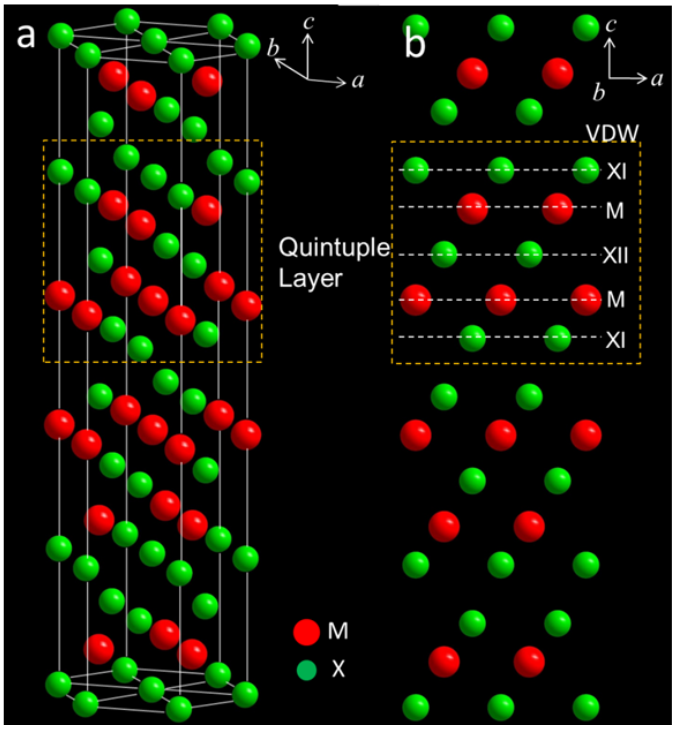


**Figure 2.3** Crystal structure of $M_2X_3$ (X=Te, Se).

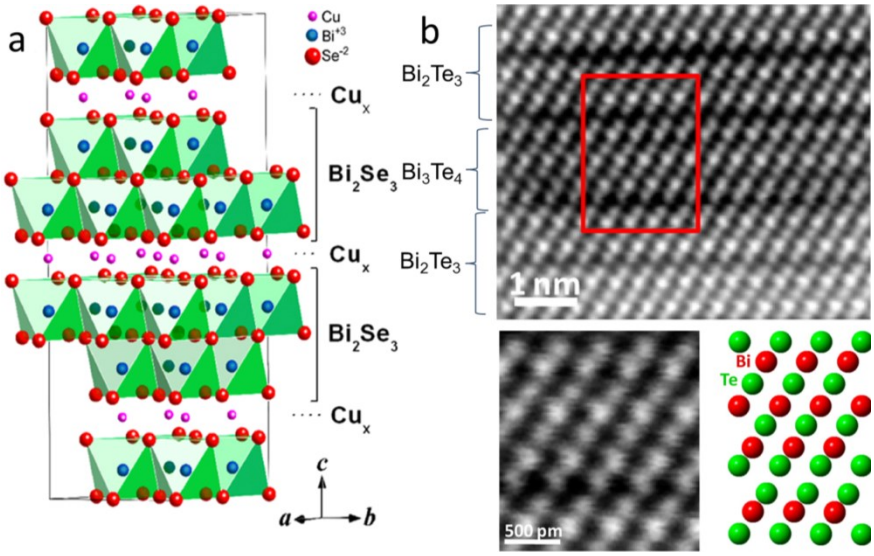


**Figure 2.4** (a) The crystal structure of $Cu_xBi_2Se_3$.[7] (b) HAADF-STEM image of $Bi_2Te_3$, projected along ⟨100⟩, showing its five-layer host structure interacted by a defect region of seven-layer $Bi_3Te_4$ defect lamella.[32]

### 2.1.3 Ternary IV-V-VI Compound

Search for new materials with $Bi_2Te_3$-type layer structures has led many researchers to focus on $nA^{IV}Te{\cdot}mB^{V}{}_2Te_3$ systems ($A^{IV}$ denoting the metal elements in Group IV: Ge, Sn, Pb, $B^{V}$ denoting Group V elements of Sb, Bi). Through variation in m and n integers, one is able to obtain a series of tetradymite-like layer structured compounds, *i.e.* $GeBi_2Te_4$, $SnBi_2Te_4$ and $PbBi_2Te_4$ (m=n=1). Experimental studies have shown that these compounds have low thermal conductivities compared to their constituent tellurides, making them attractive for thermoelectric applications.[33] Meanwhile, most of these compounds, including $GeBi_2Te_4$, $SnBi_2Te_4$ and $PbBi_2Te_4$, have been theoretically proved to be 3D TIs with complicated surface electronic structures.[34]

*2.1.3.1 Phase Relation*

Understanding the phase relation between rock-salt and rhombohedral structured chalcogenides is very important for the understanding of the crystal structure of ternary IV-V-VI compound. As mentioned in previous sections, IV-VI compounds (eg. GeTe, SnTe, PbTe, denoted as MX) mostly have a rock-salt structure, while V-VI compounds (eg. $Bi_2Te_3$, $Sb_2Te_3$, denoted as $M_2X_3$) mostly have a rhombohedral crystal structure. Figure 2.5 presents the stacking sequences of MX and $M_2X_3$ crystals, which can be represented respectively by the stacking symbols as below,

$$\underline{A\alpha B}\ \underline{A\alpha B\beta C}\ \underline{B\beta C\gamma A}\ \underline{C\gamma A\alpha B}\ \underline{A\alpha} \qquad (M_2X_3)$$

$$\underline{A\alpha B\beta C\gamma A\alpha B\beta C\gamma A}\alpha B\beta\underline{C\gamma A\alpha B\beta C} \qquad (MX)$$

where the stacking sequences of metal (M) and chalcogenide (X) atomic planes are respectively denoted by Greek and Capital letters.[33] The same sequences shown in $M_2X_3$ and MX are highlighted with underlines.

Figure 2.5a shows that $M_2X_3$ is composed of slabs ordered along c axis, and within each slab, the stacking sequence is of close-packed periodicity, which is the same with that of MX. The essential difference between the two structures is that in the MX structure, the layers alternate between metal and chalcogenide layers throughout the whole structure, whereas, in the $M_2X_3$ structure, one metal vacancy layer (two adjacent chalcogenide layers, indicated by white dashed line in Fig. 2.5b) arises every five planes. This suggests that $M_2X_3$ structure can be generated from MX by

removing every sixth metal plane, closing the resulting gap, and shearing each remaining five-layer block laterally to form a hexagonal stacking sequence (i.e. A$\alpha$B A$\alpha$B) at the two chalcogenide layers adjacent to the metal vacancy layer.[33]

The similarity between the rock-salt and rhombohedral structures can also be reflected in their unit cells. Figure 2.6a and 2.6b respectively shows the unit cells of rock-salt and rhombohedral structures.[35] By comparing of their cubic unit cells (denoted as c), one can see the only difference is the inter-axial angle, which is respectively $90^o$ and $88^o$. This means that the phase transformation between these two structures only needs an elongation of the unit cell along <111> direction and a relative shift of sublattices. The crystallographic orientation relations between the cubic (C) and rhombohedral (R) unit cells can be theoretically proposed as $[1\bar{1}0]_C//[2\bar{1}\bar{1}0]_R(=[100]_C)$, $[112]_C//[\bar{1}100]_R(=[1\bar{1}0]_C)$, $[11\bar{1}]_C//[0001]_R(=[001]_C)$. This relationship has been proved by many microscopic experiments regarding the interfaces relationship between $A^{IV}Te$ and $B^{V}{}_2Te_3$ compounds. For example, Ikeda *et al.* have extensively investigated the $PbTe/Sb_2Te_3$ system.[36] Figure 2.7a presents a back-scattered electron (BSE) image showing $Sb_2Te_3$ precipitates (dark contrast) in PbTe matrix. Electron back-scatter diffraction (EBSD) analysis shows that the habit planes of $Sb_2Te_3$ precipitates are {111} planes of PbTe, and the crystallographic relationship is $(0001)_{Sb2Te3}//\{111\}_{PbTe}$ and $<11\bar{2}0>_{Sb2Te3}//<110>_{PbTe}$.

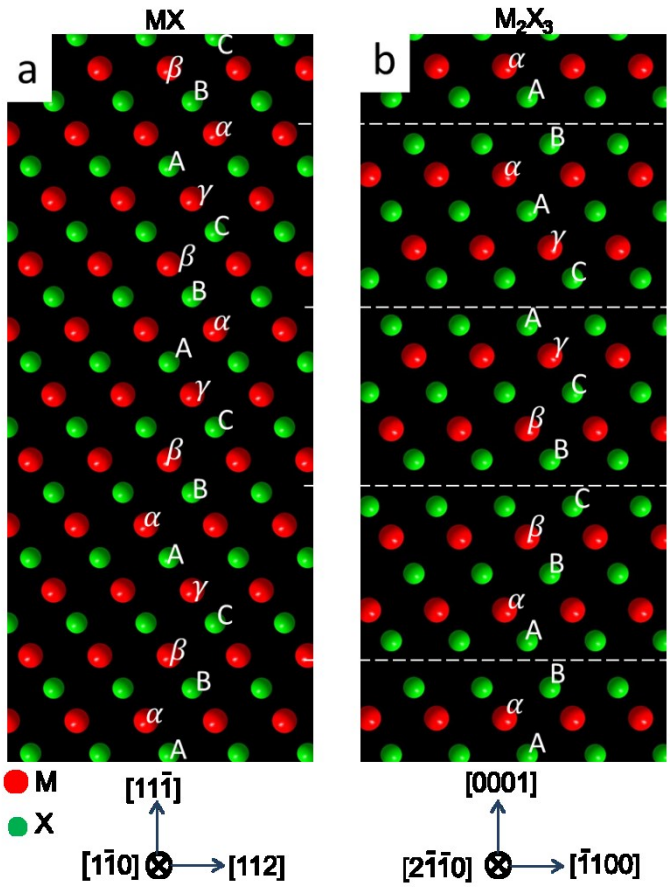


**Figure 2.5** Projected atomic models of (a) rock-salt structured MX and (b) rhombohedral structured $M_2X_3$.

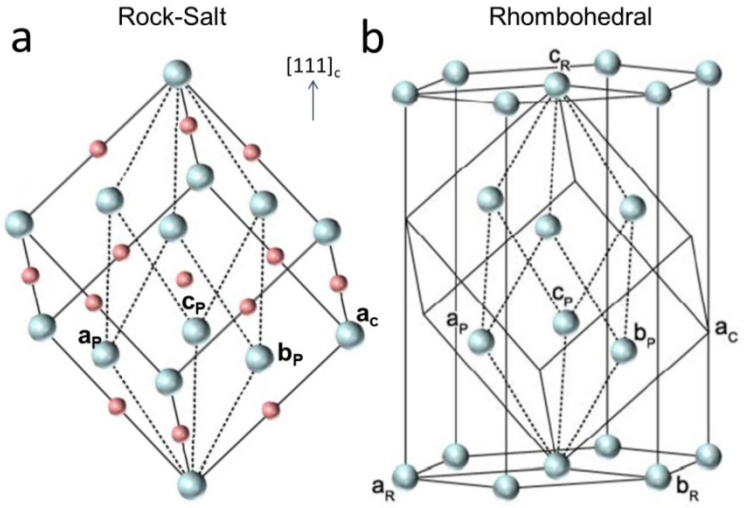


**Figure 2.6** (a) Unit cell, and primitive cell (denoted as P) of a rock-salt structured crystal. (b) Cubic unit cell (denoted as C), hexagonal unit cell (denoted as R), and primitive cell of a rhombohedral structured crystal.[35]

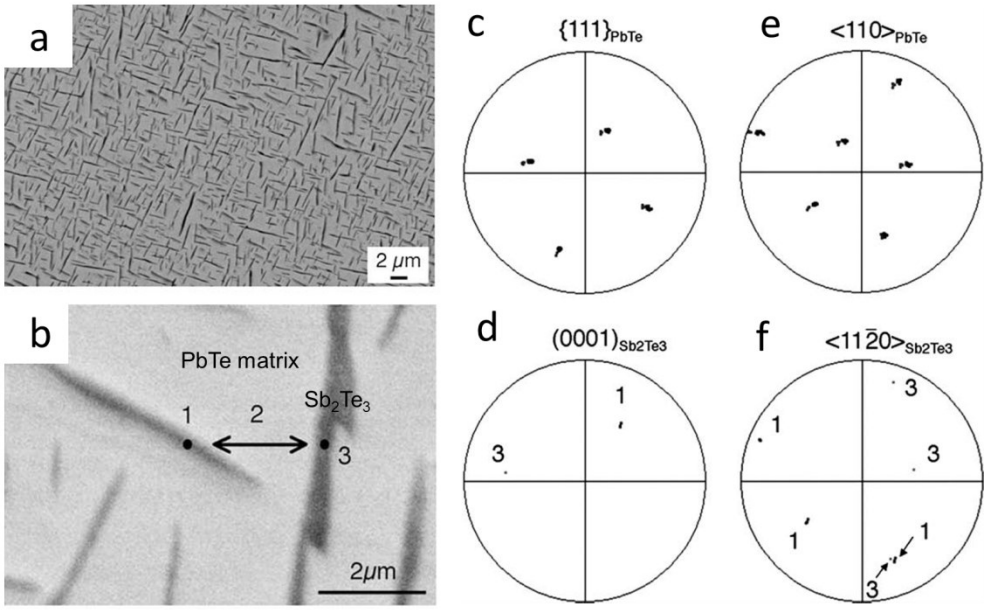


**Figure 2.7** (a) BSE image showing microstructure of PbTe matrix with $Sb_2Te_3$ precipitates. (b) BSE image showing two precipitates, labelled as "1" and "3", and the line between them in the matrix labelled as "2" were analysed in EBSD. (c-f) EBSD pole figures for (111) planes (c) and <110> directions (e) in PbTe, and for (0001) plane (d) and <$11\bar{2}0$> directions (f) in $Sb_2Te_3$.[36]

*2.1.3.2 $n(A^{IV}Te)\cdot m(B^{V}{}_2Te_3)$ phases*

In this section, we focus on ternary IV-V-VI phases. Similar to binary V-VI phases, they contain many-layered and long-period structures, and the stoichiometry is featured by $nA^{IV}Te\cdot mB^{V}{}_2Te_3$, where *n* and *m* are integers, and $A^{IV}$=Ge, Sn, Pb, $B^{V}$ =Bi, Sb. For example, $Ge_2BiTe_4$ can be described as $GeTe\cdot Bi_2Te_3$, with *m*=1 and *n*=1. Table 2.2 listed the lattice parameters of $n(A^{IV}Te)\cdot m(B^{V}{}_2Te_3)$ compounds, from which the average atomic-layer thickness c/*N* can be calculated as 0.18~0.21nm. Figure 2.8 shows the schematic atomic models of $A^{IV}B^{V}{}_2Te_4$ (*n*=1, *m*=1, including $GeSb_2Te_4$, $SnSb_2Te_4$, $PbSb_2Te_4$, $GeBi_2Te_4$, $SnBi_2Te_4$ and $PbBi_2Te_4$), $A^{IV}B^{V}{}_4Te_7$ (*n*=1, *m*=2), $A^{IV}B^{V}{}_6Te_{10}$ (*n*=1, *m*=3) compounds. The unit cells of these compounds comprise of seven-layer (Te-MII-Te-MI-Te-MII-Te) or five-layer (Te-MII-Te-MII-Te) slabs ordered along *c* axis, connected to one another by VDW force. Metal atom sites are denoted as MI and MII, in which MI site is a perfect octahedral interstice similar to the cation sites in rock-salt structure, whereas MII site is a distorted one similar to the cation sites of $M_2X_3$ structure. The layered feature of these compounds can be clearly revealed by their electron diffraction patterns. Figure 2.9a-c shows the

selective-area electron diffractions (SAED) patterns from ternary Ge-Sb-Te crystals in phases of $GeSb_2Te_4$, $Ge_2Sb_2Te_5$ and $Ge_3Sb_2Te_6$.[37] From the diffraction spots along {0001} direction, the periodic bright spots show a period of 7 for $GeSb_2Te_4$, 9 for $Ge_2Sb_2Te_5$ and 11 for $Ge_3Sb_2Te_6$, in consistency with the number of atomic layers in their unit cells (*N* or *N*/3, Table 4).

**Table 2.2** Number of atomic layers each unit cell (*N*), space group (S. G.), and lattice parameter of.$n(A^{IV}Te)\cdot m(B^{V}{}_2Te_3)$ compounds.

| System | Compound | *n* | *m* | S. G | *N* | *a*(Å) | *c*(Å) | PDF# | Ref. |
|---|---|---|---|---|---|---|---|---|---|
| Ge-Sb-Te | $GeSb_6Te_{10}$ | 1 | 3 | $R\bar{3}m$ | 51 | 4.26 | 101.51 | 00-063-0699 | [38] |
| | $GeSb_4Te_7$ | 1 | 2 | $P\bar{3}m1$ | 12 | 4.25 | 23.85 | 01-076-8867 | [39] |
| | $GeSb_2Te_4$ | 1 | 1 | $R\bar{3}m$ | 21 | 4.27 | 41.68 | 01-074-7389 | [40] |
| | $Ge_2Sb_2Te_5$ | 2 | 1 | $P\bar{3}m1$ | 9 | 4.23 | 17.28 | 01-082-8889 | [41] |
| | $Ge_3Sb_2Te_6$ | 3 | 1 | $R3m$ | 33 | 4.20 | 62.02 | 01-075-9746 | [42] |
| Ge-Bi-Te | $GeBi_6Te_{10}$ | 1 | 3 | $R\bar{3}m$ | 51 | 4.35 | 101.87 | 00-063-0700 | [43] |
| | $GeBi_4Te_7$ | 1 | 2 | $P\bar{3}m1$ | 12 | 4.35 | 23.92 | 01-089-1932 | [44] |
| | $GeBi_2Te_4$ | 1 | 1 | $R\bar{3}m$ | 21 | 4.32 | 41.27 | 00-048-1340 | [43] |
| | $Ge_2Bi_2Te_5$ | 2 | 1 | $P\bar{3}m1$ | 9 | 4.29 | 17.35 | 01-076-4258 | [45] |
| | $Ge_3Bi_2Te_6$ | 3 | 1 | $R3m$ | 33 | 4.27 | 62.59 | 00-050-0375 | [38] |
| Sn-Sb-Te | $SnSb_2Te_4$ | 1 | 2 | $R\bar{3}m$ | 21 | 4.30 | 41.57 | 01-080-8952 | [46] |
| Sn-Bi-Te | $SnBi_4Te_7$ | 1 | 2 | $R\bar{3}m$ | 12 | 4.40 | 24.07 | 01-082-3172 | [47] |
| | $SnBi_2Te_4$ | 1 | 1 | $R\bar{3}m$ | 21 | 4.44 | 41.60 | 01-082-3171 | [47] |
| Pb-Sb-Te | $PbSb_2Te_4$ | 1 | 1 | $R\bar{3}m$ | 21 | 4.35 | 41.71 | 01-073-4301 | [48] |
| Pb-Bi-Te | $PbBi_6Te_{10}$ | 1 | 3 | $R\bar{3}m$ | 12 | 4.40 | 102.54 | 01-070-9250 | [48] |
| | $PbBi_4Te_7$ | 1 | 2 | $R\bar{3}m$ | 12 | 4.41 | 24.07 | 01-073-4300 | [48] |
| | $PbBi_2Te_4$ | 1 | 1 | $R\bar{3}m$ | 21 | 4.44 | 41.77 | 01-038-1232 | [48] |

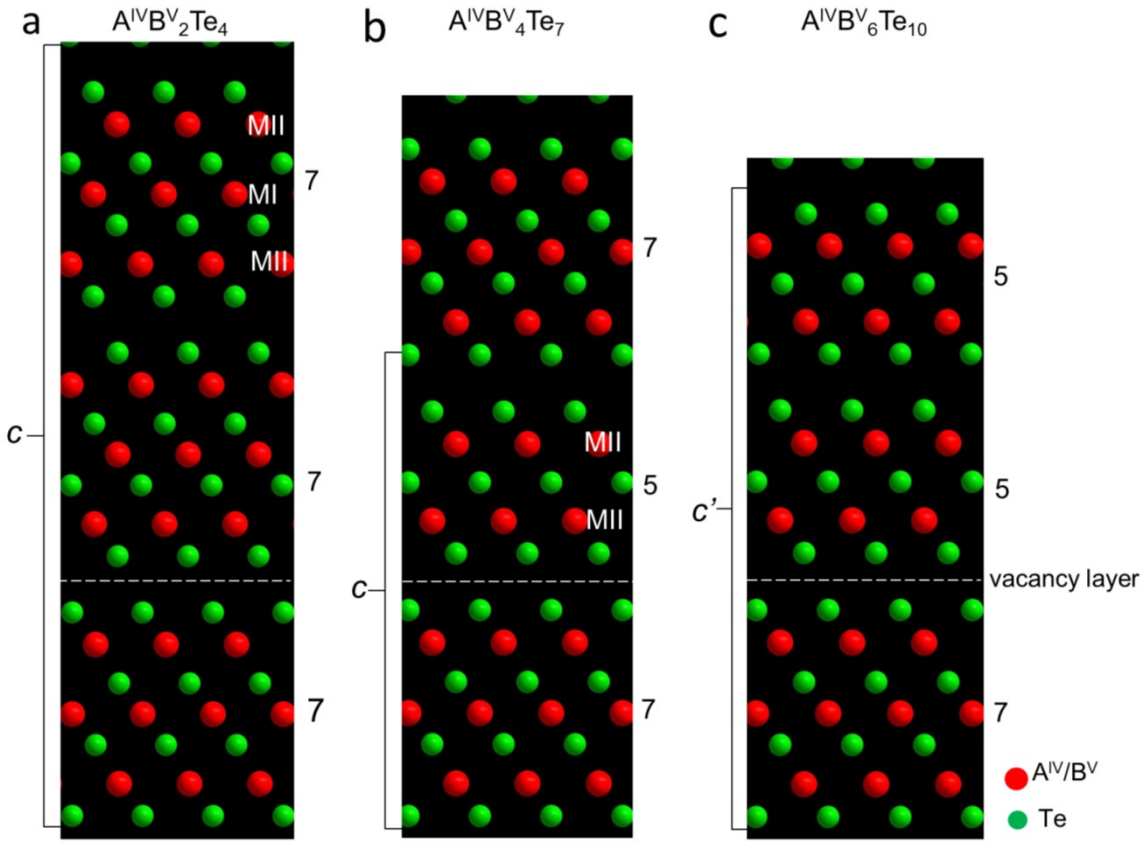


**Figure 2.8** Schematic atomic models of $A^{IV}B^{V}_2Te_4$, $A^{IV}B^{V}_4Te_7$, $A^{IV}B^{V}_6Te_{10}$ compounds projected onto $(01\bar{1}0)$ plane. *c*'= *c* /3.

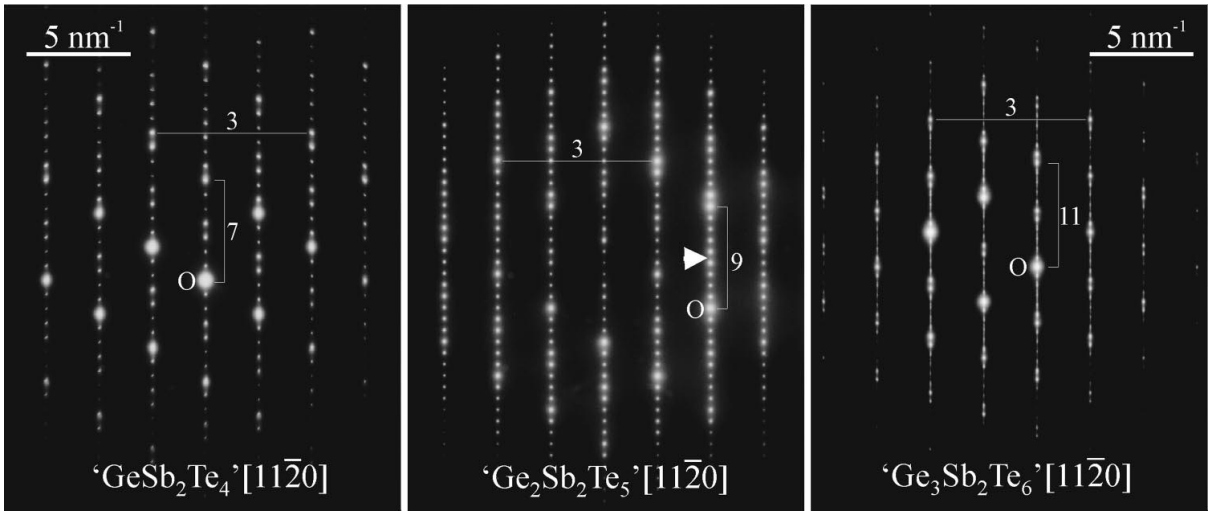


**Figure 2.9** SAED patterns from $GeSb_2Te_4$, $Ge_2Sb_2Te_5$ and $Ge_2SbTe_6$ crystals.[37]

*2.1.3.3 Defect in IV-V-VI compound*

2.1.3.3.1 Vacancy Disorder

Sections 2.1.3.1 and 2.1.3.2 have shown that the existence of metal vacancy layer is an intrinsic structure feature in ternary IV-V-VI compounds. For a $n(A^{IV}Te)\cdot m(B^{V}_2Te_3)$ phase with perfect crystal structure, the vacancy layers are expected to be distributed with an ordered manner and same spacing. However, this is not always the case in ternary IV-V-VI compounds, particularly for those samples with $A^{IV}Te$-riched compositions. Figure 2.10 takes $Ge_{18}Bi_2Te_{21}$ as an example, HRTEM imaging shows that vacancy layers are always found to be randomly distributed in the structure, with varying spacing between each other (21, 17, 15, 20, 23 atomic layers).[50] The arrangement of the vacancy layers is also dependent on sample preparation method. It has been found that heat treatments, such as annealing and quenching, can effectively manipulate the vacancy arrangement in IV-V-VI compounds. For example, in $(GeTe)_{12}\cdot(Sb_2Te_3)$, annealing can increase the ordering degree in vacancy arrangement in the crystal structure, which further influences their thermal conductivities.[51]

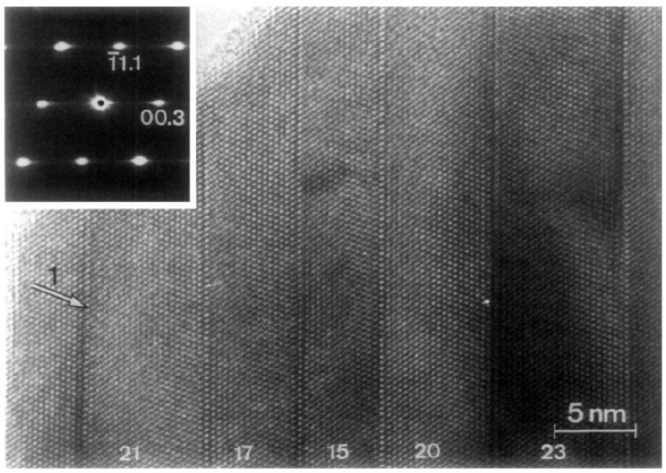


**Figure 2.10** HRTEM image taken from a $Ge_{18}Bi_2Te_{21}$ sample along $[11\bar{2}0]$, showing the presence of slabs with strongly varying width, indicating the random arrangement of vacancy layers.[50]

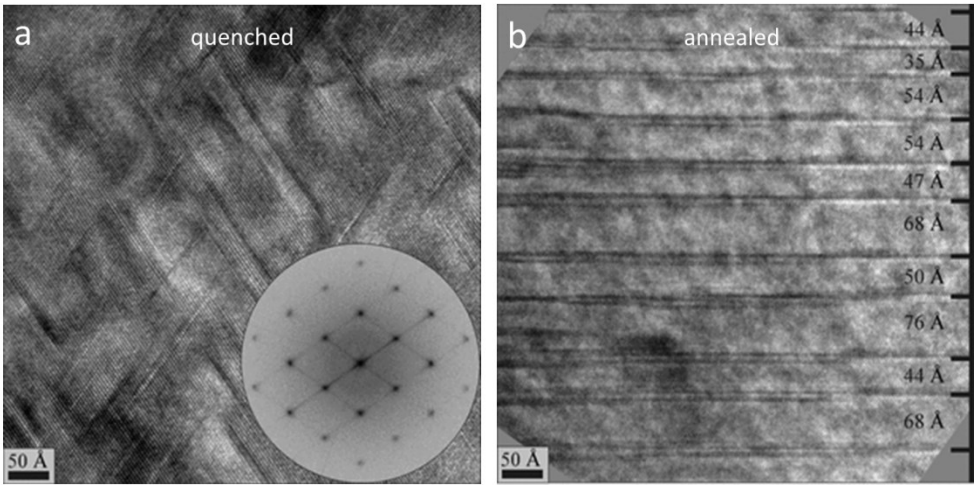


**Figure 2.11** TEM images showing the vacancy layer arrangements of $(GeTe)_{12}(Sb_2Te_3)$ samples from different heat treatments: (a) quenched from 500°C and (b) annealed at 400 °C for 20 h.[51]

The metal vacancies play an important role in phase-change IV-V-VI materials. Table 4 has shown that stable ternary IV-V-VI phases have a hexagonal crystal structure. In fact, metastable $n(A^{IV}Te)\cdot m(B^{V}{}_2Te_3)$ compounds may also have a rock-salt structure, in which metal vacancies are distributed randomly. When these compounds are undergoing heating or laser instantaneous irradiation, phase transition between hexagonal and cubic rock-salt phases is prone to happen. In this transition, vacancy diffusion was assumed to play an important role.[52] Figure 2.12 gives a sketch showing the possible processes happened during the phase transition of $GeSb_2Te_4$ from rock-salt to hexagonal: (A) Cation atom diffuses from site 2 to the vacancy at site 1, and a vacancy is formed at site 2. (B) Cation atom diffuses from site 3 to 2 and a vacancy is formed at site 3. With the repeating of process (A) and (B), a vacancy layer is formed at site 3. (C) Te atoms nearby sites 3 shift towards the vacancy layer.

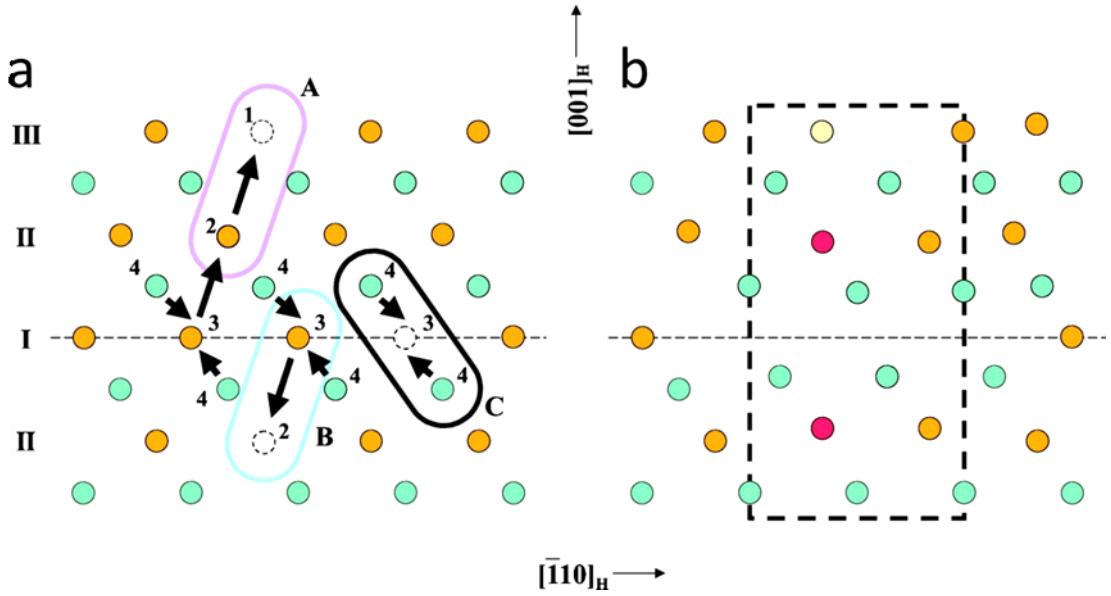


**Figure 2.12** Structural phase transition caused by vacancy diffusion. (a) Atomic model of the rock-salt structured $GeSb_2Te_4$, showing three processes of atomic displacements happened near the dash line for the transition to (b). (b) Atomic model of the hexagonal structured $GeSb_2Te_4$, with an ordered arrangement of the vacancies at the dash line. Cation vacancies, Te atoms and cation atoms, are respectively denoted by hollow circles, green filled circles and orange circles.[52]

Density functional theory (DFT) calculations have been widely employed to understand the vacancy formation in IV-V-VI compounds. Zhang *et al.* studied the impact of vacancy disorder on the phase stability of $GeSb_2Te_4$.[53] Figure 2.13 shows the four configurations they calculated for the comparison of total energies. The concentration of vacancies in the vacancy layers is denoted as $l_{vac}$, both cubic and hexagonal arrangements were considered. They start from a cubic $GeSb_2Te_4$ phase with Poisson distribution of Ge, Sb and vacancies in cation layers (25%), and then gradually reduce the disorder by depleting the number of atoms in every fourth cation layer, until vacancies fully occupy the sites at the depleting layer (100%). From Fig. 2.13, 100-*d* configuration with perfect vacancy planes has the lowest energy, indicating that the decrease in vacancy and compositional disorder with the change from cubic to hexagonal stacking lead to a large reduction in system energy.

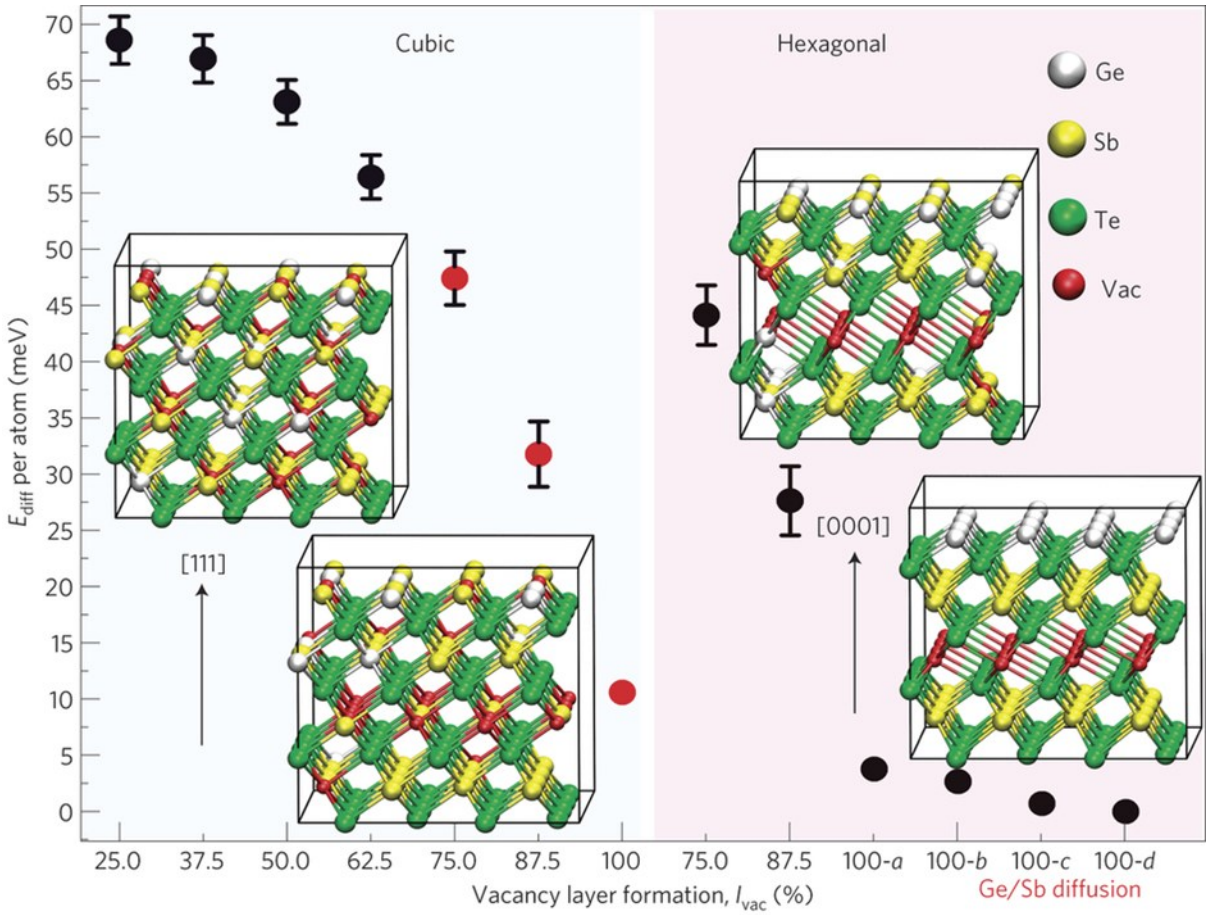


**Figure 2.13** Total energy per atom, $E_{diff}$, of the models of cubic $GeSb_2Te_4$, hexagonal $GeSb_2Te_4$ and intermediate structures studied. In the plot the zero of the energy coincides with the energy of the most favourable structure, hexagonal 100%-*d*. Insets show the starting random cubic phase, the final hexagonal phase 100%-*d* and two intermediate phases (cubic-$l_{Vac}$=50% and hexagonal-$l_{Vac}$=75%). The last four points (100%-*a*~*d*) correspond to hexagonal structures containing completely formed vacancy layers, which differ in the distribution of Ge and Sb atoms in the Ge/Sb layers.[53]

2.1.3.3.2 Metal-Atom Disorder

In the structure of $n(A^{IV}Te)\cdot m(B^{V}{}_2Te_3)$ compounds, there are two kinds of cation sites, one is adjacent to the vacancy layer, and the other is inside the cubic close packed slabs, respectively defined as MI and MII, as shown in Fig. 2.8. The fact that there are two kinds of cations ($A^{IV}$, $B^{V}$) in the compounds gives rise to the question of how these cations distribute in the MI and MII sites. To resolve this question, many methods have been employed to understand the real arrangement of metal atoms in

$n(A^{IV}Te)\cdot m(B^{V}_2Te_3)$ compounds, including X-ray diffraction, Mossbauer measurements and energetic calculations. However, the subject of metal arrangement is still under disputation, where both ordered and mixing models were proposed to describe the metal-atom arrangement. For example, $A^{IV}B^{V}_2Te_4$ comprises of seven atom-layer units that can be described as Te-MII-Te-MI-Te-MII-Te. The ordered model considers that Bi and Sn atoms respectively occupy MII and MI, and the atomic sequence is of Te-$B^{V}$-Te-$A^{IV}$-Te-$B^{V}$-Te. While the mixing model considers that $B^{V}$ and $A^{IV}$ coexist in each site and they are randomly distributed in the cation sites.

For $Bi_2SnTe_4$ phase, Bryan *et al.* studied the sites of Bi and Sn atoms by XRD experiments in combination with Rietveld refinements.[53] Table 2.3 shows the refinement results, using the powder data and models with different occupation ratios of Sn or Bi in MI and MII sites. Three different refinement scenarios converged successfully with $R_P/R_B$ values between 0.066/0.064 and 0.049/0.046 with both tellurium sites fixed at 100% occupancy. The best $R_P/R_B$ values were achieved when higher quantities of Sn occupy MI site (80%), defined as the 'partial mixing' model in Table 2.3. This result demonstrates that in $Bi_2SnTe_4$, M sites exhibit preference for Sn on the MI site and Bi on MII sites, but are not likely perfectly ordered.[54]

**Table 2.3** Rietveld refinements on $SnBi_2Te_4$ polycrystalline samples.[54]

| | Ordered | Even mixing | Partial mixing |
|---|---|---|---|
| Formula | $SnBi_2Te_4$ | $SnBi_2Te_4$ | $SnBi_2Te_4$ |
| $R_P/R_B$ | 0.066/0.064 | 0.053/0.048 | 0.051/0.054 |
| Sn[*M*(1)] | 1 | 1/3 | 0.8 |
| Sn[*M*(2)] | 0 | 1/3 | 0.1 |
| *z*[*M*(2)] | 0.4303(1) | 0.43093(8) | 0.4295(1) |
| *z*[Te(1)] | 0.13886(8) | 0.13719(7) | 0.13813(7) |
| *z*[Te(2)] | 0.2908(1) | 0.2842(1) | 0.2903(1) |

The partial mixing of metal atoms has also been observed in other systems like $GeSbTe_4$. Table 2.4 shows reported refined structural parameters for $GeSbTe_4$ derived from synchrotron XRD results. The refined results indicate that, in the three cation sites, Sb atoms prefer to occupy cation site (1) and (2) but Sb and Ge still coexist in all the three cation sites. [55] Therefore, the metal atom disordering may be a general phenomenon that can be observed in the crystal structure of ternary IV-V-VI

phases. Further theoretical and experimental investigations are required in order to pain a clearer picture of the metal-atom arrangement in ternary IV-V-VI compounds.

**Table 2.4** Refined structural parameters for $GeSb_4Te_7$ polycrystalline samples.[55]

| atom | site | *g* | *x* | *y* | *z* | *B* (Å$^2$) |
|---|---|---|---|---|---|---|
| Te(1) | 1:1*a* | 1.0 | 0 | 0 | 0 | 0.21 (2) |
| Ge/Sb(1) | 2:2*d* | 0.153/0.847(17) | 1/3 | 2/3 | 0.08365(21) | 1.05 (4) |
| Te(2) | 3:2*d* | 1.0 | 2/3 | 1/3 | 0.15490(14) | 0.21 |
| Te(3) | 4:2*c* | 1.0 | 0 | 0 | 0.27122(12) | 0.21 |
| Ge/Sb(2) | 5:2*d* | 0.155/0.845(15) | 1/3 | 2/3 | 0.34002(18) | 1.05 |
| Te(4) | 6:2*d* | 1.0 | 2/3 | 1/3 | 0.42508(14) | 0.21 |
| Ge/Sb(3) | 7:1*b* | 0.331/0.617 | 0 | 0 | 1/2 | 1.05 |

## 2.2 Physical Properties

Bismuth selenides, bismuth tellurides and tin tellurides are semiconductors with narrow bandgaps (~0.15eV in $Bi_2Te_3$, ~0.35eV in $Bi_2Se_3$, and ~0.18eV in SnTe). They have shown exotic physical properties, such as superconductivity, topological surface states, and high-efficiency thermoelectricity performances.

### 2.2.1 Electronic Structure

SnTe has a rock-salt structure (Fig. 2.14a) with face-centred-cubic Brillouin zone (Fig. 2.14b).[56] Figure 2.14c shows the calculated bulk electronic structure of SnTe, in which the valence band maximum and conduction band minimum both are located at the *L* points. As shown in the grey region, the orbitals are switched near *L* points, in which the conduction band edge is derived from Te and the valence band edge from Sn, suggesting that SnTe has an intrinsically inverted band structure. In SnTe, surface states exist on any crystal surface symmetric about {110} mirror plane, including {001}, {111}, and {110}. {100} surface Brillouin zone has been shown in Fig. 2.14b, in which four $\Gamma L_1 L_2$ plane in the bulk Brillouin zone projects into four $\overline{\Gamma X_1}$ lines in the surface Brillouin zone. Figure 2.14d plots the band dispersion of {001} surface, indicating that {001} surface states have four Dirac points located on the four equivalent $\overline{\Gamma X}$ lines (Fig. 2.14d).

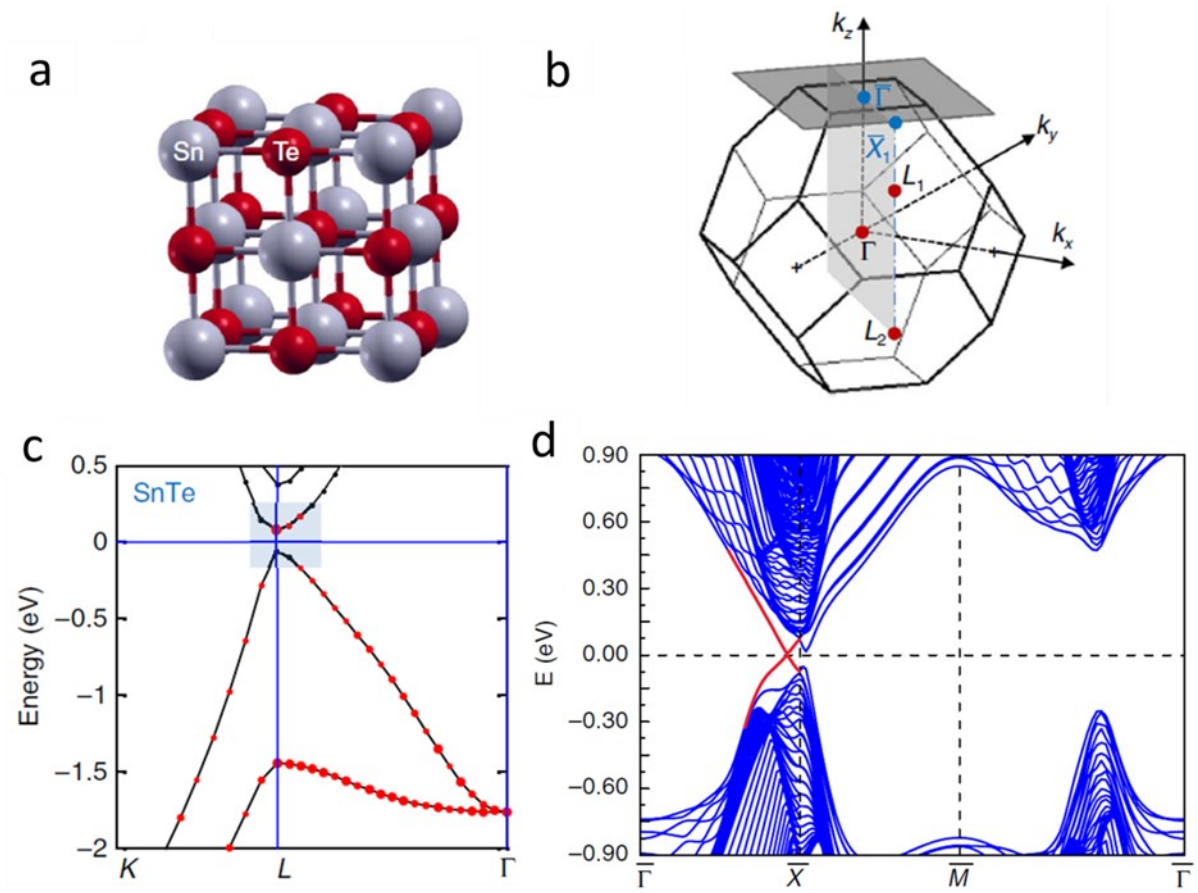


**Figure 2.14** (a) The rock-salt crystal structure of SnTe. (b) Corresponding face-centered-cubic (FCC) Brillouin zone, showing the plane $\Gamma L_1 L_2$, which is invariant under reflection about the (110) axis and projects onto the $\overline{\Gamma X_1}$ line in the [001] surface. (c) Calculated band structures of bulk SnTe. The size of the red dots represents the fraction of electronic charge residing on Te atoms. The exchange of the band character at *L* point as highlighted in the grey area indicates the intrinsic band inversion of SnTe. (d) Band dispersion of (001) surface.[56]

$Bi_2Se_3$, $Bi_2Te_3$, and $Sb_2Te_3$ have the same rhombohedral crystal structure. We take $Bi_2Se_3$ as an example, and show its unit cell and Brillouin zone in Fig. 2.15a. Figure 2.15b and c present the calculated band structure for $Bi_2Se_3$ without and with SOC, respectively.[5] By comparing these two figures, one can see that by turning on SOC, the only qualitative change induced is an anti-crossing feature around the $\Gamma$ point, indicating that SOC effects would induce an inversion between the valence band and conduction band.[5] Figure 2.15 d presents the calculated surface local density of states (LDOS) on the [111] surface for $Bi_2Se_3$. The surface states can be clearly

seen around the *Γ* point as red lines dispersing in the bulk gap that forms a single Dirac cone at *Γ* point.[5]

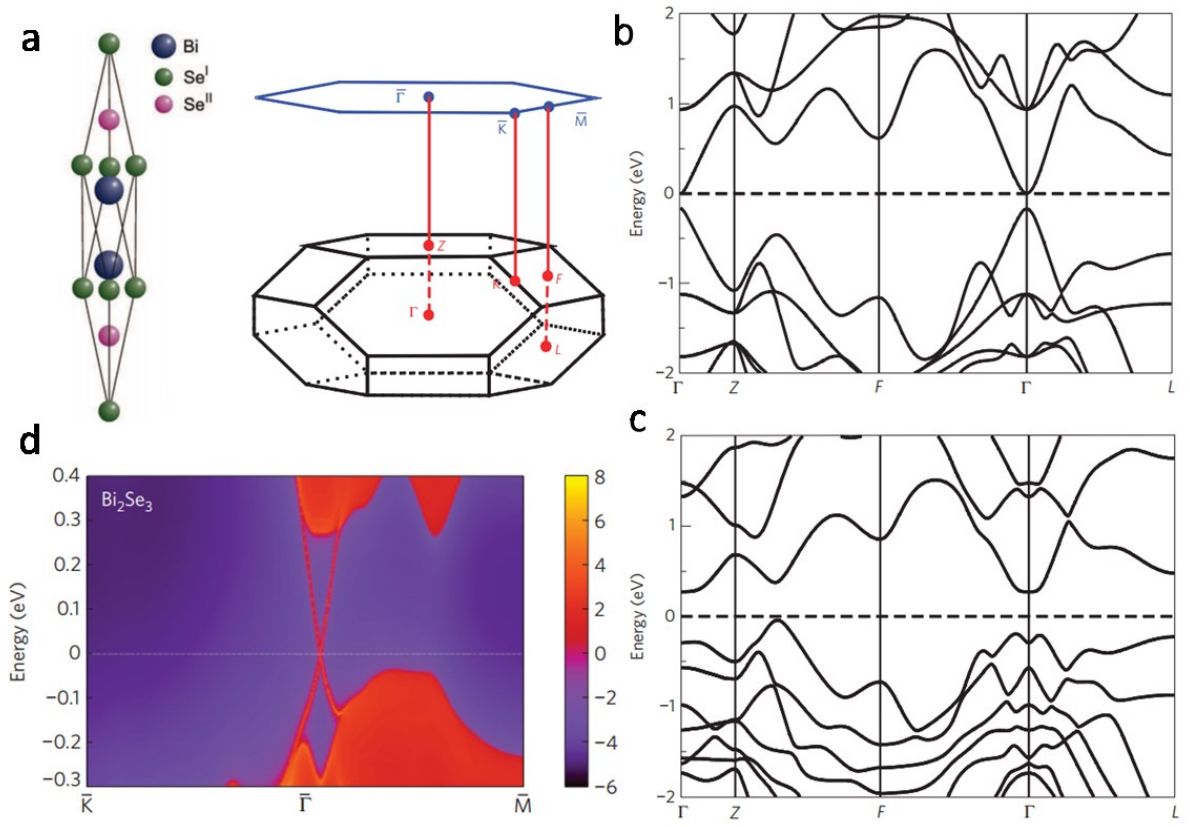


**Figure 2.15** (a) Primitive unit cell (left) and Brillouin zone (right) for $Bi_2Se_3$ with space group $R\bar{3}m$. The blue hexagon shows the 2D Brillouin zone of the projected (111) surface. (b, c) Calculated and structure for $Bi_2Se_3$ without considering SOC (b) and with SOC (c). (d) Energy and momentum dependence of the LDOS for $Bi_2Se_3$ on the (111) surface. The red regions indicate bulk energy bands and the blue regions indicate bulk energy gaps.[5]

### 2.2.2 Properties and Applications

#### *2.2.2.1 Thermoelectricity*

Two fundamental effects used in thermoelectricity are Seebeck Effect and Peltier Effect. Seebeck Effect refers to the phenomenon that the heat flow between two different conductor junctions can generate electrical field. The generated electrical voltage ($\Delta V$) from this effect is proportional to the difference of temperature ($\Delta V = S\Delta T$),[2] and the proportional coefficient S is known as the Seebeck coefficient, or

the thermopower. Peltier Effect refers to the phenomenon that a current would cause the heating or cooling at the junction of two different conductors.[2] The amount of the heat produced is proportional to the electric current ($Q = \Pi \Delta T$) and the proportional coefficient $\Pi$ is known as the Peltier coefficient. Equation $S = \Pi T$ can show the close relationship between Peltier Effect and Seebeck Effect.

TE modules can be used in two ways, as illustrated in Fig. 2.16: thermoelectric power generator and thermoelectric cooling device. When a voltage or current is applied from C to A, the module acts as a refrigerator due to Peltier Effect. Alternatively, when a resistive load is connected between A and C, which means that a heat removal is being processed from B to AC, the thermocouple would drive an electric current around the load and the circuit and acts as a generator due to the Seebeck Effect.

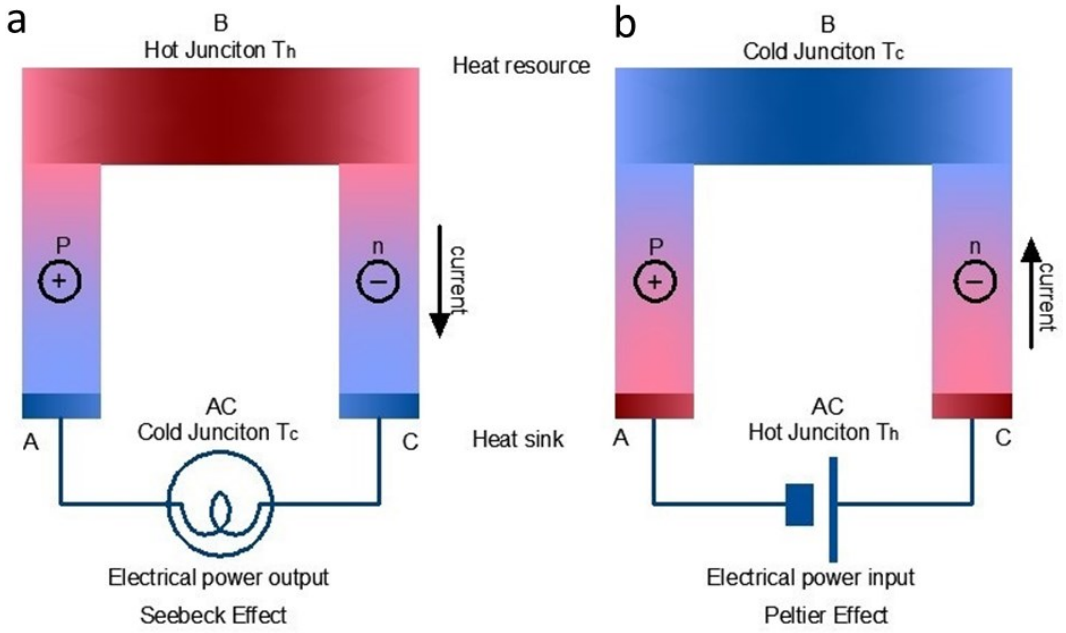


**Figure 2.16** Thermoelectric modules: (a) power generator by the Seebeck Effect, (b) cooling refrigerator by the Peltier Effect.

Figure of Merit *ZT* evaluates the maximum efficiency of a TE material, and is defined as:

$$ZT = \frac{S^2 \sigma T}{k} \tag{2.1}$$

where $S$ is the Seebeck coefficient, $\sigma$ is the electrical conductivity and $k$ is the thermal conductivity. In Eq. 2.1, the quantity $S^2\sigma$ is defined as the power factor (PF)

and the higher PF value suggests a larger voltage and current can be achieved from the TE device.

*ZT* of the thermoelectric couple in Fig. 2.16 is given by as below:[2]

$$ZT = \frac{(S_p - S_n)^2 T}{(k_n/\sigma_n)^{1/2} + (k_p/\sigma_p)^{1/2}} \quad (2.2)$$

And its efficiency in heat-to-electricity converting energy is as below:

$$\emptyset = \frac{T_H - T_C}{T_H} \left[\frac{(1+ZT_M)^{1/2} - 1}{(1+ZT_M)^{1/2} + (T_C/T_H)}\right] \quad (2.3)$$

As shown in Eq. 2.2, the *ZT* value depends on the Seebeck coefficients of the p-doped and n-doped semiconductors, $S_p$ and $S_n$; their electrical conductivities, $\sigma_p$ and $\sigma_n$; and thermal conductivities, $k_p$ and $k_n$. Eq. 2.3 gives the positive relationship between the converting efficiency $\emptyset$ and $(1 + ZT_M)^{1/2}$. For a given operating temperature or a temperature difference, a higher *ZT* leads a higher efficiency in power generation or refrigeration.

Eq. 2.1 provides the solutions to obtain high *ZT* TE materials, which is to simultaneously achieve a high $S$, high $\sigma$ and a low $k$. The thermal conductivity $k$ contains contributions from lattice and carrier thermal conductivities, and its value can be calculated from

$$k = k_e + k_l \quad (2.4)$$

where $k_e$ is the carrier thermal conductivity, $k_l$ is the lattice thermal conductivity. Thus, although a higher $\sigma$ is desirable for improving PF, it will not always increase the *ZT* since a higher $\sigma$ would lead to a considerable increase in $k_e$, which may further increase the total thermal conductivity $k$.

One of the practical approaches to reduce $k_l$ of the samples is nanostructuring, which creates extensive interfaces between the nanostructures and increase the phonon scattering at the grain boundaries. Meanwhile, with the quantum confinement and phonon scattering effect in nanostructures, they may show enhanced *ZT* value, The quantum confinement of the carriers increases the density-of-states (DOS) near the Fermi level in quantum well and correspondingly increases the Seebeck coefficient. In 1990s, Hicks and Dresselhaus have reported the calculation results for the *ZT* values of the 2D quantum $Bi_2Te_3$ layers compared to the 3D bulk $Bi_2Te_3$, which shows that *ZT* value in the 2D quantum layer is ~13 times

higher than that of its 3D bulk counterpart.[9] Therefore, it is very desirable to develop low-dimensional chalcogenides for TE applications.

SnTe based TE materials and have shown a promising *ZT* value over 1, as shown in Table 2.5, In fact, pure SnTe only has a *ZT* ~0.4 at 900K, which is attributed to (a) a low Seebeck coefficient and a high electronic thermal conductivity due to the high carrier concentration from intrinsic Sn vacancies, (b) bipolar transport from the low energy band gap (0.18 eV) at room temperature, and (c) a large separation in energy between heavy and light valence bands that hinders the contribution of the heavier holes to the Seebeck coefficients. To overcome these disadvantages, several strategies for enhancing *ZT* of SnTe have been proposed, include (i) suppressing the hole concentration by doping, enhance the Seebeck coefficient by (ii) supressing the bipolar effect, (iii) band convergence or (iv) valence resonance, and reduce the thermal conductivity with pronounced phonon scattering by introducing (v) lattice distortion from precipitates, or (vi) defects or grain boundaries.

**Table 2.5** Enhanced TE properties of SnTe based materials using different strategies.

| System | Strategy | T | *ZT* | Ref. |
|---|---|---|---|---|
| Ca - SnTe | i, iii, v | 873 | 1.35 | [57] |
| Cd - SnTe | i, iii, v, vi | 923 | 1.3 | [58] |
| In - SnTe | i, iv | 873 | 1.1 | [59] |
| Mg - SnTe | i, ii | 923 | 1.3 | [60] |
| Hg and Bi- SnTe | ii, iii, v, vi | 910 | 1.35 | [61] |
| $AgBiTe_2$-SnTe | i, vi | 775 | 1.1 | [62] |
| $AgBiTe_2$-SnTe | i, v | 710 | 1 | [63] |
| MnTe-SnTe | iii, iv | 900 | 1.3 | [64] |
| MnTe-SnTe | ii, iii, v, vi | 900 | 1.3 | [65] |

$Bi_2Te_3$ based materials have been recognized as a high-efficiency TE system at room temperature. The highest reported *ZT* value until now is 2.4 from $Bi_2Te_3$-$Sb_2Te_3$ thin film devices.[66] For bulk TE materials, the highest reported *ZT* value is 1.86 from a Te-riched $Bi_{0.5}Sb_{1.5}Te_3$.[68] Strategies used for further improvement of *ZT* in $Bi_2Te_3$ system includes based on grain boundary and defect engineering, doping and nanostructuring. [67-73]

*2.2.2.2 Topological Surface States*

Section 2.2.1 presented the exotic surface band structures of SnTe and $Bi_2Se_3$, in which their surface band dispersions form Dirac cones at the bulk gap region. This indicates that their surface states are metallic, which are known as the topological surface states. In the recent decade, the topological surface states have been found in $Bi_2Se_3$, $Bi_2Te_3$ and SnTe. $Bi_2Se_3$ and $Bi_2Te_3$ belong to a group of topological insulators (TI), where the metallic surface states are protected by the time-reversal symmetry.[74] SnTe belongs to a group of topological crystalline insulators (TCI), where the surface states are protected by the mirror symmetry of the crystal.

Figure 2.17a shows an idealized band structure of TI. The Fermi level falls within the bulk band gap which is traversed by topologically –protected surface states.[74] The metallic surface of TI is in a helical spin texture, where the electron spin is oriented perpendicularly to its orbital momentum. Figure 2.17b shows the wire-like metallic edges around 2D TI, a quantum well or thin film. Such edge states have the important “spin filtered” property that the up spins propagate in one direction, while the down spins propagate in the other. Figure 2.17c (left) shows the metallic surface states of a 3D TI. The spin texture on such surfaces is illustrated in momentum space as a “spin-resolved” band structure (right panel of Fig. 2.17c). Another attractive feature of TI is the inherent robustness of the metallic surface properties against almost any surface modification (Fig. 2.17d). In contrast, for a normal semiconductor, the surface states are usually easily modified or destroyed (Fig. 2.17e).

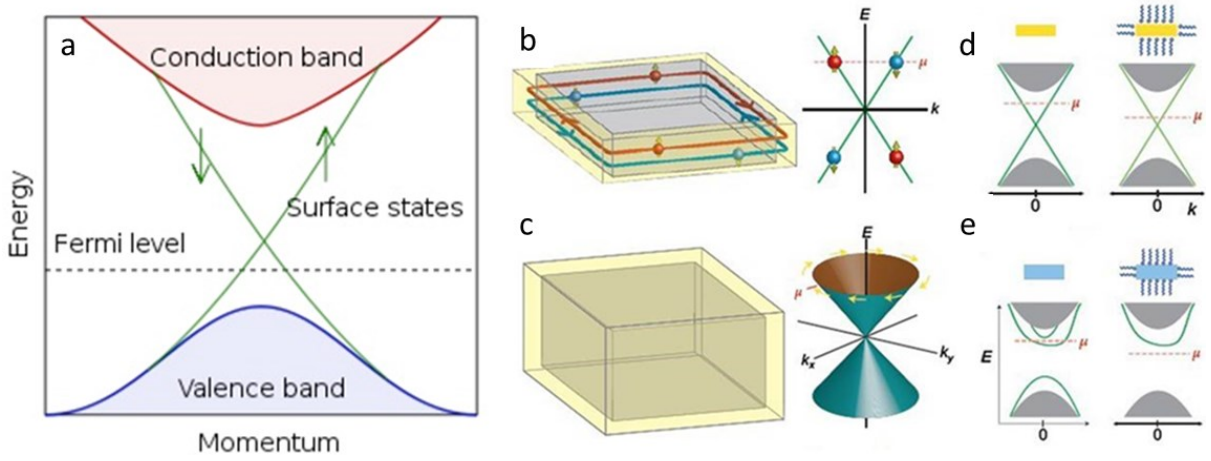


**Figure 2.17** (a) Idealized band structure of TI with metallic edge states (green lines) in the bulk bandgap, in which up and down spins propagate in opposite directions. (b) Metallic edge of a 2D TI (left), and the corresponding spin-resolved surface band structure (right). (c) Metallic surface of 3D TI (left) and the corresponding spin-resolved surface band structure (right). (d) Band diagram of a TI before surface modification (left) and after surface modification (right), in which the grey area denotes the bulk states. (e) Band structures of an ordinary semiconductor before surface modification (left) and after surface modification (right).[74]

The surface band structures of TI and TCI can be directly confirmed by angle-resolved photoemission spectroscopy (ARPES).[75] Figure 2.18 shows the ARPES measurements of surface electronic band dispersion on $Bi_2Se_3$(111), revealing the helical nature of the surface electrons.[8,76] As $Bi_2Se_3$ has comparative large band gap (~0.3eV at 360K) compared to other the current TI materials, its surface states and band structure can be tuned with proper doping and be observed at room temperature, as shown in Fig. 2.18c-d. In the case of SnTe, in contrast to $Bi_2Se_3$ with single Dirac cone at the surface band structure, surface electronic states of SnTe consist of four Dirac cones in the first surface Brillouin zone (Fig. 2.19).

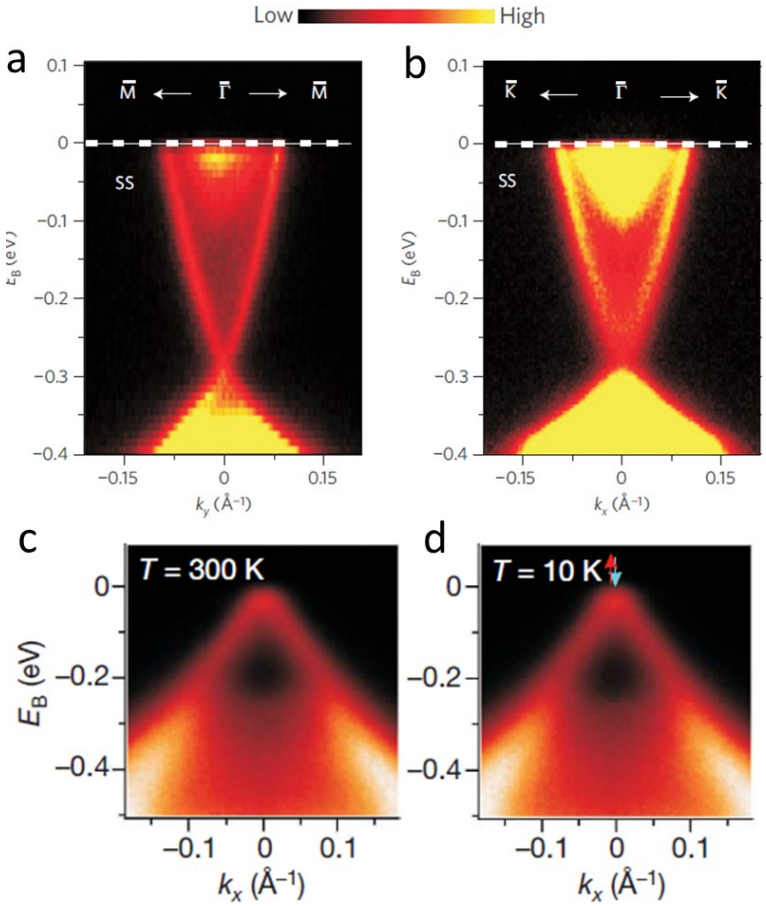


**Figure 2.18** (a, b) High-resolution ARPES measurements of the surface electronic band dispersion of $Bi_2Se_3$(111) near the $\bar{\Gamma}$ point along the $\bar{\Gamma}-\bar{M}$ (a) and $\bar{\Gamma}-\bar{K}$ (b) momentum-space cuts. (c, d) ARPES map of the surface band dispersion of $Bi_{2-x}Ca_xSe_3$ (111) after a 2 L dosage of $NO_2$, taken at 300K (c) and 10K (d).[8,76]

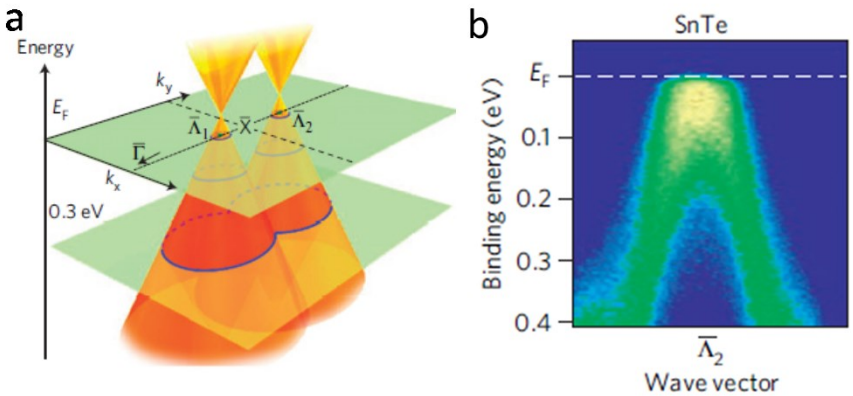


**Figure 2.19** (a) Schematic 2D band dispersions near Fermi level $E_F$ depicting the evolution of the surface Dirac cones. (b) Near-$E_F$ energy distribution curves around the $\bar{\Lambda}$ point for SnTe.[77]

A direct probing of the topological surface state in TI and TCI by transport experiments is challenging, because the contribution from the bulk carriers is likely to outnumber that from the surface carriers. Low-dimensional nanostructures, on the other hand, with enhanced surface-to-bulk ratio, provide attractive systems for surface transport property study, since a much higher contribution from surface carriers is expected. For example, in SnTe system, bulk sample always has a high hole concentration because of the intrinsic Sn vacancies, making it challenging to realize the probing of surface states. In contrast, in SnTe nanowires (NWs), transport experiments have realized the observation of topological surface states by quantum oscillation measurement, including Aharonov–Bohm (AB) interference and Shubnikov-de Haas (SdH) oscillations.[78-79] Figure 2.20 a shows a four terminal device of SnTe NW, from which a pronounced AB oscillation was observed under magnetic field at 20 K (Fig. 2.20 b-c). The derived prominent oscillation frequency of *h/e* is shown in Fig. 2.20C.[78] The above experiment result shows that low-dimensional TI and TCI nanostructures are excellent systems for understanding the topological surface states.

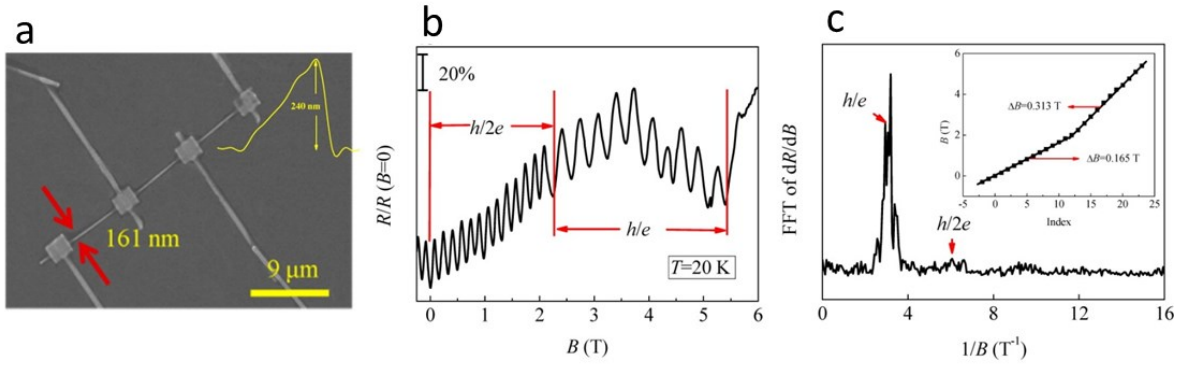


**Figure 2.20** (a) SEM image showing a Hall bar device fabricated for SnTe NW transport measurement. (b) Normalized magnetoresistance under magnetic field. (c) Fast Fourier transform of the derivate dR/dB, showing a prominent AB oscillation frequency of *h/e* at high magnetic field.[78]

## 2.3 Growth and Characteristics of Nanostructures

The fabrication techniques of low-dimensional chalcogenide nanomaterials can be classified as the solution-phase method (2.3.1) and the vapour deposition methods (2.3.1). The advantage and disadvantages of these two methods are listed in Table 2.6.

**Table 2.6** Advantages and disadvantages of the synthesis methods for low-dimensional chalcogenide nanostructures.

| Fabrication techniques | | Advantages | Disadvantages |
|---|---|---|---|
| Vapour-deposition methods | MBE | High-crystalline and purity products.<br>Controllability on product morphology and structure.<br>In-situ monitoring of the growth process.<br>Capability of growing high quality thin films. | Expensive and complex growth procedures.<br>Low product output |
| | CVD | High-crystalline and purity products<br>Controllability on the product morphology and structure<br>Simple growth procedure. | Low product output |
| Solution-phase methods | Electrochemical Deposition | Controllability on product morphology and scale. | Toxic electrolytes.<br>Complex growth procedure.<br>Chemical residues on product surface.<br>Low-crystalline products. |
| | Solvothermal Synthesis | Low cost and high product output | Chemical residues on product surface.<br>Time-consuming. |

### 2.3.1 Solution-Phase Method

Figure 2.21 shows a electrochemical deposition method to synthesize bismuth chalcogenide NWs using the anodic aluminium oxide (AAO) as the template, acid solution with precursors (such as Bi, $Bi_2(SO_4)_3$, Te, Se, $H_2SeO_3$) as the electrolyte. [80, 81] The template with products is then removed by dissolving it in NaOH to get the final product, as illustrated in Fig. 2.21a and b.

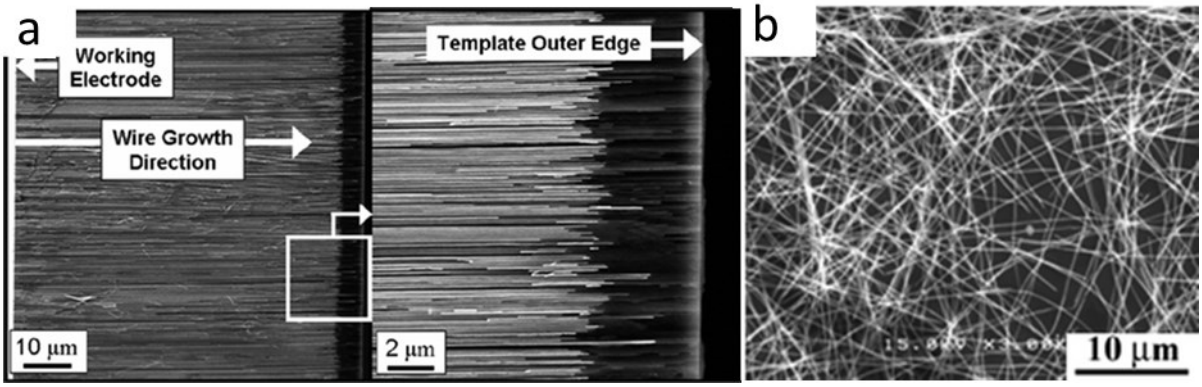


**Figure 2.21** SEM images of electrodeposition grown $Bi_2Te_3$ NWs. (a) Cross-section back-scattered SEM images of the NWs embedded in AAO templates. (b) NWs after the removal of the template.[80, 81]

In the synthesis by solvothermal method, the precursors (metal chlorides, oxides, nitrates and acetates) are mixed and dissolved in an organic (for example, ethanol and amine) or aqueous solvent with a reductant (for example PVP and EDTA).[82, 83] The mixture is then sealed, pressured and heated to certain temperature to enable the precursors react with each other to form bismuth chalcogenide. After the mixture is cooled down, the products are collected from the solution by washing and drying. Figure 2.22 shows the typical morphologies of solvothermal synthesised $Bi_2Te_3$ nanostructures.

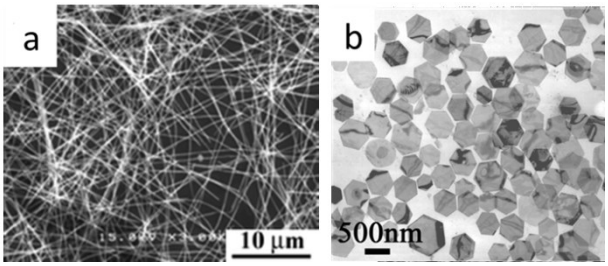


**Figure 2.22** TEM images of solvothermal method synthesised products. (a) $Bi_2Te_3$ ultrathin NWs (~8nm).[82] (b) $Bi_2Te_3$ nanoplates.[83]

Solution-phase method can be used to fabricate metal chalcogenide nanomaterials with controllable shapes. Guo *et. al* demonstrate the growth of monodisperse SnTe nanocubics, elongated NRs with controlled aspect ratio, and long, straight NWs by solution-phase method.[84] High-temperature growth (240°C) results in monodisperse SnTe nanocubes (Fig. 2.23a-b), whereas a lower-temperature synthesis (180 °C) produces SnTe NRs with aspect ratio tunable from 1.5 to >100 (Fig. 2.23c-d).

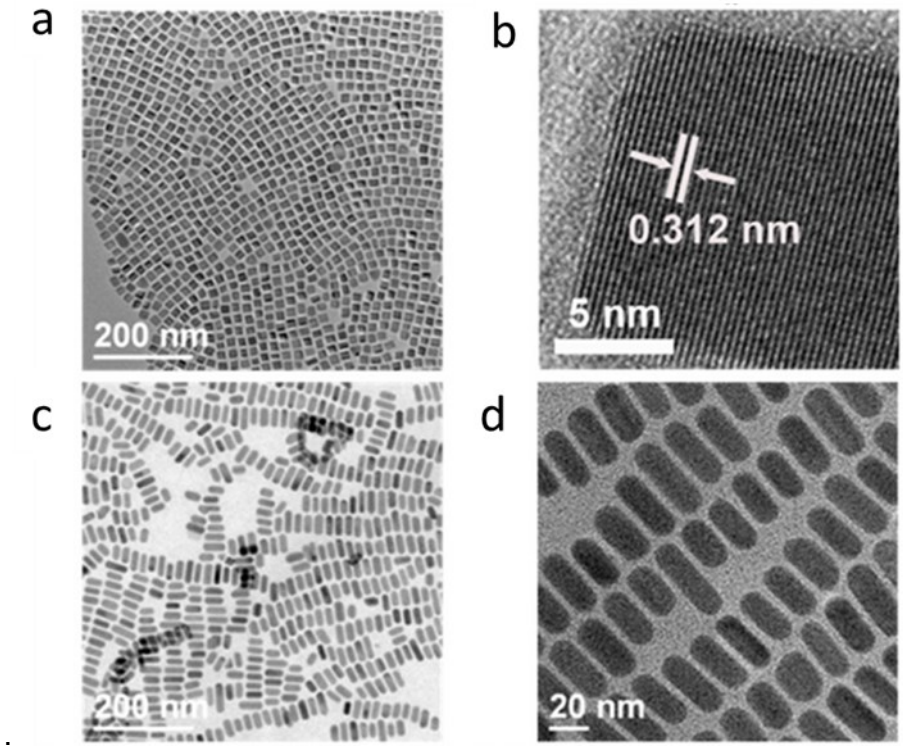


**Figure 2.23** TEM images of solution-based synthesised monodisperse cubic SnTe nanocubic (a-b), and NRs (c-d).[84]

Solution-phase method has been used widely for the synthesis for TE applications because its considerable product output that enables the assembly of nanocomposites for TE property tests. However, the residual surfactants or impurities from the reactants can hardly be removed completely, which may affect the TE performances of the final nanocomposites, In this regard, vapour-deposition grown method shows advantages in product quality, and therefore has been developed for synthesis of device-quality nanostructures.

### 2.3.2 Vapour-Deposition Method

The vapour-deposition method, as illustrated in its name, the growth of the solid products is initiated by vapour species. Widely used vapour-deposition growth methods include molecular beam epitaxy (MBE), metal organic chemical vapour deposition (MOCVD), and chemical vapour deposition (CVD), MBE and MOCVD show advantages in thin-film growth and precise growth control. However, CVD has become the most widely used method because of its low cost and convenience in operation. In a typical vapour-deposition growth, a substrate is exposed to the vapour constitutes of the desired products, which react with each other under certain temperature and the products are deposited on the substrate. For chalcogenide nanostructures, various substrates, such as Si ($Si/SiO_2$), $Al_2O_3$ and GaAs, have been used.[85-88] Figure 2.24a,b,c respectively shows the HAADF STEM image of $Bi_2Te_3$ nanostructure grown on GaAs (001),[85] Si (100),[86] and $Al_2O_3$ (mica) substrate.[87] The growth on GaAs substrate shows evident feature of lattice-matching epitaxy (Figure 2.24a), while for mica grown $Bi_2Te_3$, the growth is van der Waals epitaxy.[86] In the case of silicon or $SiO_2$/Si(100) substrate, it has been found that amorphous $SiO_x$ interface layer always exist when growing $Bi_2Te_3$ on silicon, even with HF treatment.[86,88] One of the growth mechanisms for $Bi_2Te_3$ growth on silicon is proposed as Te-seeded (Figure 2.24a), where a Te or Te-rich interface is responsible for the initiation of the nanostructure growth.[86,88] Since silicon substrates have been commonly adopted for depositing metal chalcogenide nanostructures with low cost and good visual/optical contrast, and $SiO_2$/Si substrates are favourable for device fabrication, we use the silicon substrates for nanostructure growth in this thesis.

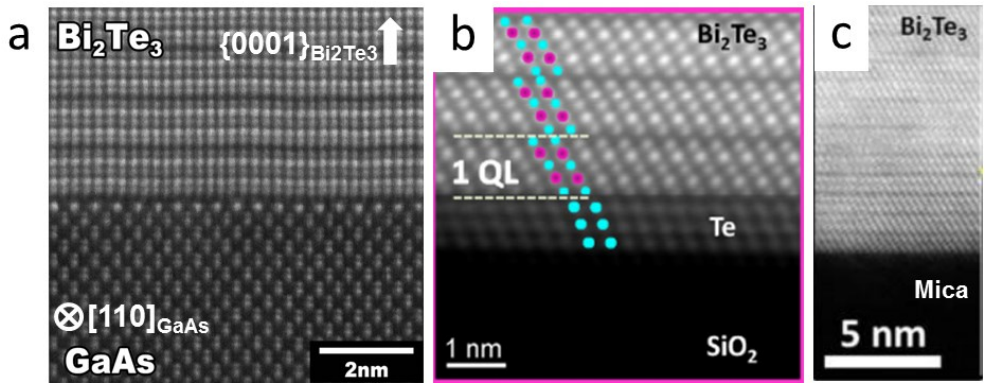


**Figure 2.24** (a) HAADF STEM image of the atomically abrupt $Bi_2Te_3$/GaAs interface viewed along $\langle 110 \rangle_{GaAs}$ axis.[85] (b) HAADF STEM image of the interface between

$Bi_2Te_3$ and $SiO_2$/Si substrate.[86] (c) HAADF STEM image of the interface between $Bi_2Te_3$ and mica substrate.[87]

However, when the substrates are covered with metallic catalysts, one-dimensional (1D) nanostructures with variable facets can grow, driven by a vapour-liquid-solid (VLS) or vapour-solid-solid (VSS) mechanism. The growth mechanisms of 1D nanostructures will be discussed in Chapter 3.

*2.3.2.1 CVD*

In this thesis, CVD method is used for the nanostructure growth, which has been widely used as for growth of high-quality nanostructures. The CVD vapour resources are directly using the elemental powders (Bi, Sn, Se, Te) or the compound powders ($Bi_2Te_3$, $Bi_2Se_3$ or SnTe). As illustrated in Fig. 2.25, in a typical CVD growth, the solid resources are put at the hot centre of the tube furnace, while the substrates are put at the downstream cooler area for product collection. After heating the furnace centre to certain temperature, vapour atomic species evaporate from the solid resources, moving to the downstream area by the carrier gases. When reach the substrates with proper growth temperature, they react with each other and form the solid product.

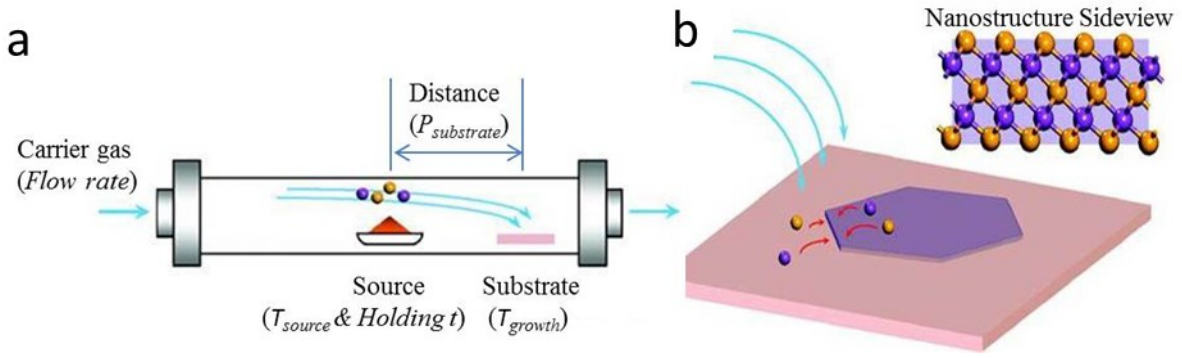


**Figure 2.25** (a) Scheme of a typical CVD reactor and the CVD growth parameters used for controlling the products. (b) Schematic diagram showing the vapour-solid growth process using bismuth chalcogenide nanoplate as an example.[89]

CVD growth parameters contain the temperature of the resource $T_{source}$, temperature of the substrates $T_{growth}$, which can be adjusted by the distance between the

substrate and the hot center ($P_{substrate}$), and the flow rate of the carrier gas. Especially, for the growth of 1D nanostructures, metallic catalysts may be used, and the choice and modification of the metallic catalyst can influence the final products. Table 2.7 and 2.8 summarized the reported CVD growth parameters for $Bi_2Te_3$, $Bi_2Se_3$ and SnTe based nanomaterials.

**Table 2.7** Growth parameters for CVD growth of $Bi_2Te_3$ and $Bi_2Se_3$ based nanomaterials (Para.=Parameters; NB=nanobelt; N=no catalyst or no carrier gas) .

| Para. / Product | Source | Catalyst | Carrier gas<br>*Flow rate* (sccm) | *$T_{source}$*<br>*Holding t* | *$P_{substrate}$ (cm)*<br>*$T_{growth}$* | Ref. |
|---|---|---|---|---|---|---|
| **$Bi_2Se_3$ NR** | $Bi_2Se_3$ | 20nm Au | Ar | 450~580 °C | 8~12 | 11 |
| | | | 30~120 | 1~5h | *NA* | |
| **$Bi_2Se_3$ NR** | $Bi_2Se_3$ | *N* | *N* | 680 °C | *NA* | 13 |
| | | | | 72h | 560 °C | |
| **Fe/Ni doped $Bi_2Se_3$ NR** | $Bi_2Se_3$ | 5nm Fe/Au<br>5nm Ni/Au | Ar | 430 °C | *NA* | 10 |
| | | | 135~145 | 1~3h | 350~450 °C | |
| **$Bi_2Te_3$ NW** | $Bi_2Te_3$ | 30nm Au | Ar | 470°C | 20~23 | 14 |
| | | | 30 | 1h | 432-355°C | |
| **Sn-doped $Bi_2Te_3$ NW** | $Bi_2Te_3$ | Sn Film &<br>13nm Au | $H_2$&Ar | 480℃ | 16 | 90 |
| | | | 25&25 | 5 min | *NA* | |
| **$Bi_2Se_3$ NP** | $Bi_2Se_3$ | *N* | Ar | 460~500 °C | 12 | 89 |
| | | | 50 | 5min | 320~360 °C | |
| **$Bi_2Te_3$ NP** | $Bi_2Te_3$ | *N* | Ar | 450~480 °C | 12 | 89 |
| | | | 20 | 5min | 320~360 °C | |

| | | | | | | |
|---|---|---|---|---|---|---|
| **$(Bi_xSe_{1-x})Te_3$ NP/NR** | $Bi_2Se_3$ $Bi_2Te_3$ | 10nm Au film | Ar | 480 °C | 6-15 | 12 |
| | | | 30-150 | 2h | *NA* | |
| **$(Bi_xSb_{1-x})Te_3$** | $Bi_2Sb_3$ $Bi_2Te_3$ | *N* | Ar | 490 °C | 12 | 91 |
| | | | 15 | 10min | 300 °C | |

**Table 2.8** Growth parameters for CVD growth of SnTe nanomaterials.

| Para. / Product | Source | Catalyst | Carrier gas | $T_{source}$ ($^oC$) | $P_{substrate}$ (cm) | Ref. |
|---|---|---|---|---|---|---|
| | | | *Flow rate* (sccm) | *Holding t* | $T_{growth}$ ($^oC$) | |
| **{100}SnTe NP/NR** | SnTe | Au film | Ar | 600 | *NA* | 92 |
| | | | 40~50 | 10 min | 350~450 | |
| **{111}SnTe NP/NR** | SnTe | Au film | Ar | 600 | *NA* | 92 |
| | | | 40~50 | 10 min | 300 | |
| **{100}SnTe NW** | SnTe | 20nm Au | Ar | 700 | *NA* | 93 |
| | | | 5~15 | 30min | 675 | |
| **SnTe NW** | SnTe | 20nm Au | Ar | 700 | *NA* | 93 |
| | | | 5~15 | 30min | 500 | |
| **SnTe NW** | SnTe | 10nm Au | Ar | 900 | 10~20 | 90 |
| | | | 100 | 1h | *NA* | |
| | | | 15 | 10min | 300 °C | |

Figure 2.26 shows the morphology and structure of the catalyst-free CVD grown $Bi_2Te_3$ or $Bi_2Se_3$ NPs. A-few layer NPs can be obtained with uniform sizes and morphology, mostly exhibit triangular and hexagonal morphologies, with {0001} as the surface facet and {1000} as side facet.

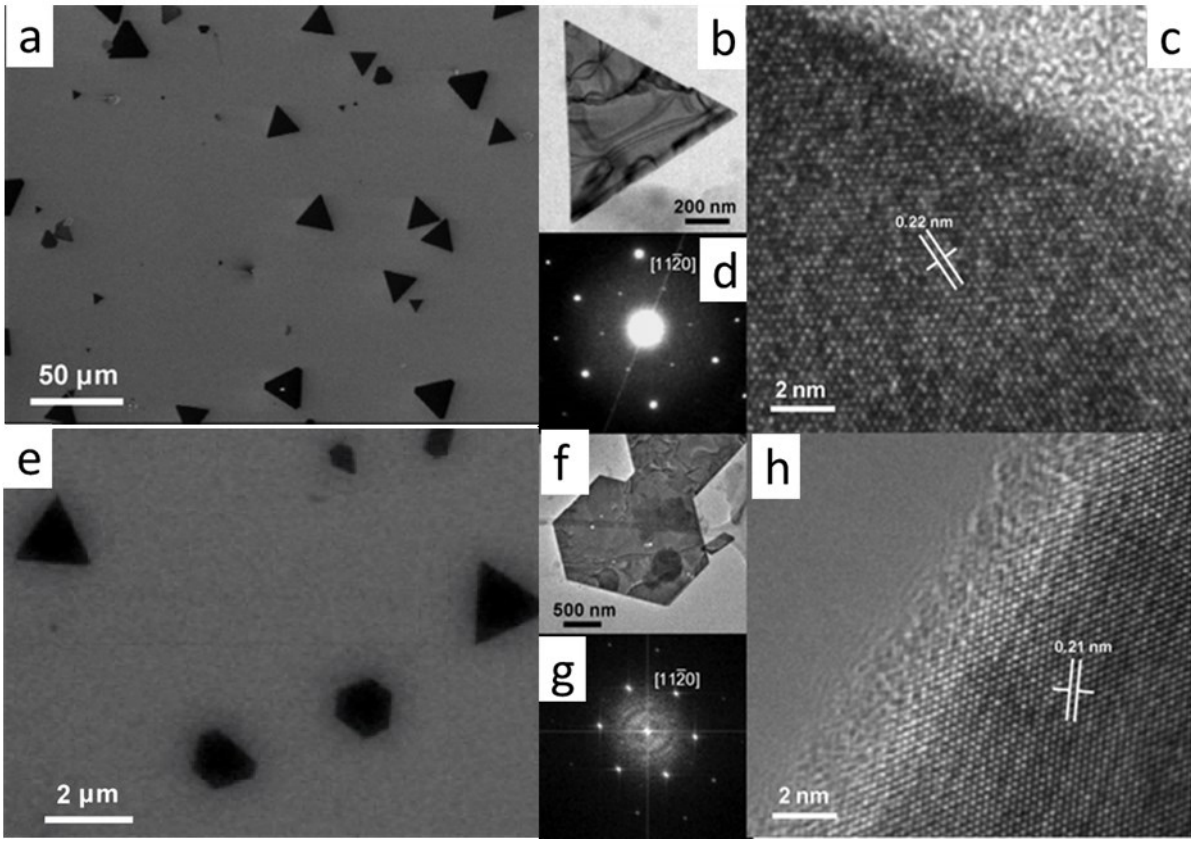


**Figure 2.26** Morphology and structure of CVD-grown $Bi_2Te_3$ and $Bi_2Se_3$ NPs. (a) SEM image of the CVD-grown $Bi_2Se_3$ NPs; (b) TEM image of a $Bi_2Se_3$ NP and (c) HRTEM image, with (d) SAED pattern taken from the NP; (e) SEM image of CVD-grown $Bi_2Te_3$ NPs, and the corresponding (f) TEM image, (g) FFT and (h) HRTEM images.[89]

When substrates are coated with proper metallic catalysts, 1D $Bi_2Te_3$ and $Bi_2Se_3$ NWs nanostructures can be grown. Figure 2.27 shows the morphologies of the gold-assisted CVD grown $Bi_2Se_3$ NWs and NRs, which generally exhibit a preferred growth direction along [11$\bar{2}$0]. For each NW and NR, gold catalyst nanoparticle can be found at the tip, suggesting the VLS growth mechanism. $Bi_2Se_3$ NW shows a rough surface facet and a growth direction along [0001] (Fig. 2.27d). In contrast, $Bi_2Se_3$ NRs, have smooth {0001} surfaces facet (Fig. 2.27c)

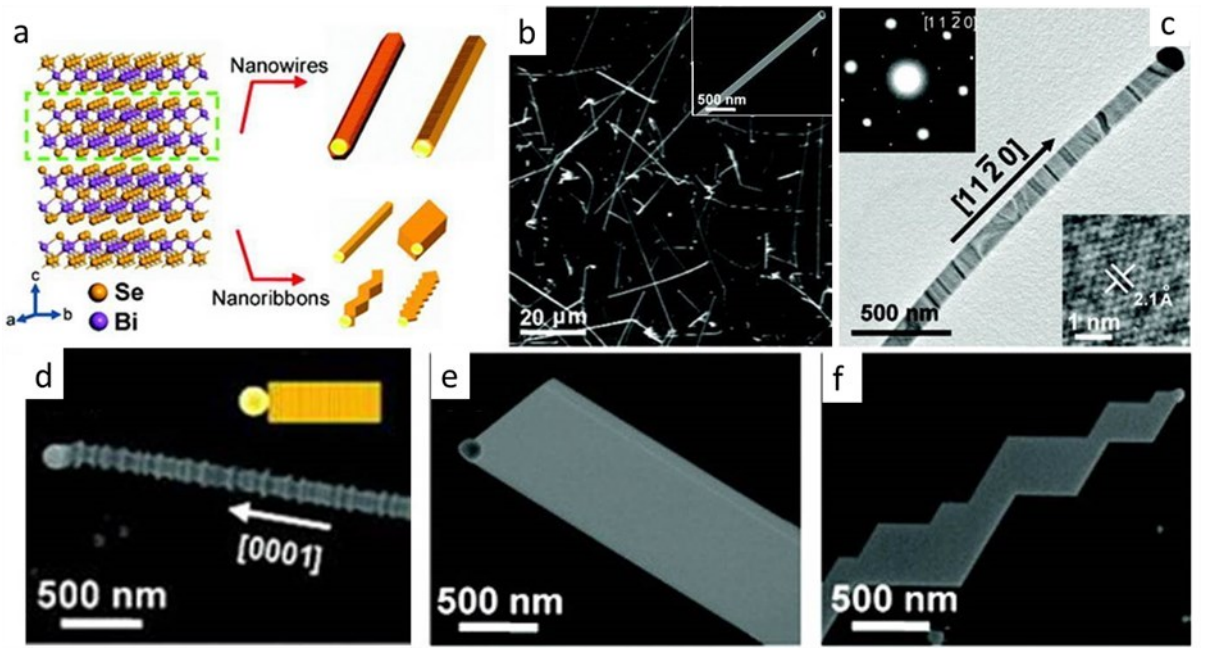


**Figure 2.27** Morphology and structure of Au-catalysed CVD-grown $Bi_2Se_3$ nanostructures. (a) Crystal structure of $Bi_2Se_3$ and schematic diagram of different morphologies of synthesized nanostructures. (b) SEM image of synthesised NRs, with an inset showing its catalyst NR tip. (c)TEM image of an individual NR, with an inset the SAED taken from the NR. (d, e, f) SEM images showing the different morphologies of individual nanostructures.[11]

For the growth of SnTe nanostructures, CVD was found to be an effective method to tune their surface facets. One of the controlling factors is found to be the growth temperature, which control the surface energy by adjusting the Te stoichiometry in the product. Figure 2.28a shows the calculated surface energies of SnTe as a function of Te chemical potential. Low-energy surface facets of SnTe include {100}, $\{111\}_{Te}$ and {110}. In general growth conditions, {100} facet has the lowest surface energy. However, when the growth condition is Te-rich, $\{111\}_{Te}$ facet may exhibit lower surface energy than that of {100} facet. This suggests a way of controlling the surface facet of SnTe through stoichiometry, and was proved by the experiments conducted by Li *et al.*. They demonstrated that by reducing the growth temperature, $\{111\}_{Te}$ surface facet can be found in SnTe nanostructures, as lower growth temperature induces a Te-rich growth condition.[93] Figure 2.28b,c,f show that the surface of high-temperature grown NWs are dominated by {100} facets, whereas {111} facets can be found in the low growth-temperature products (Fig. 2.28d,e,g).

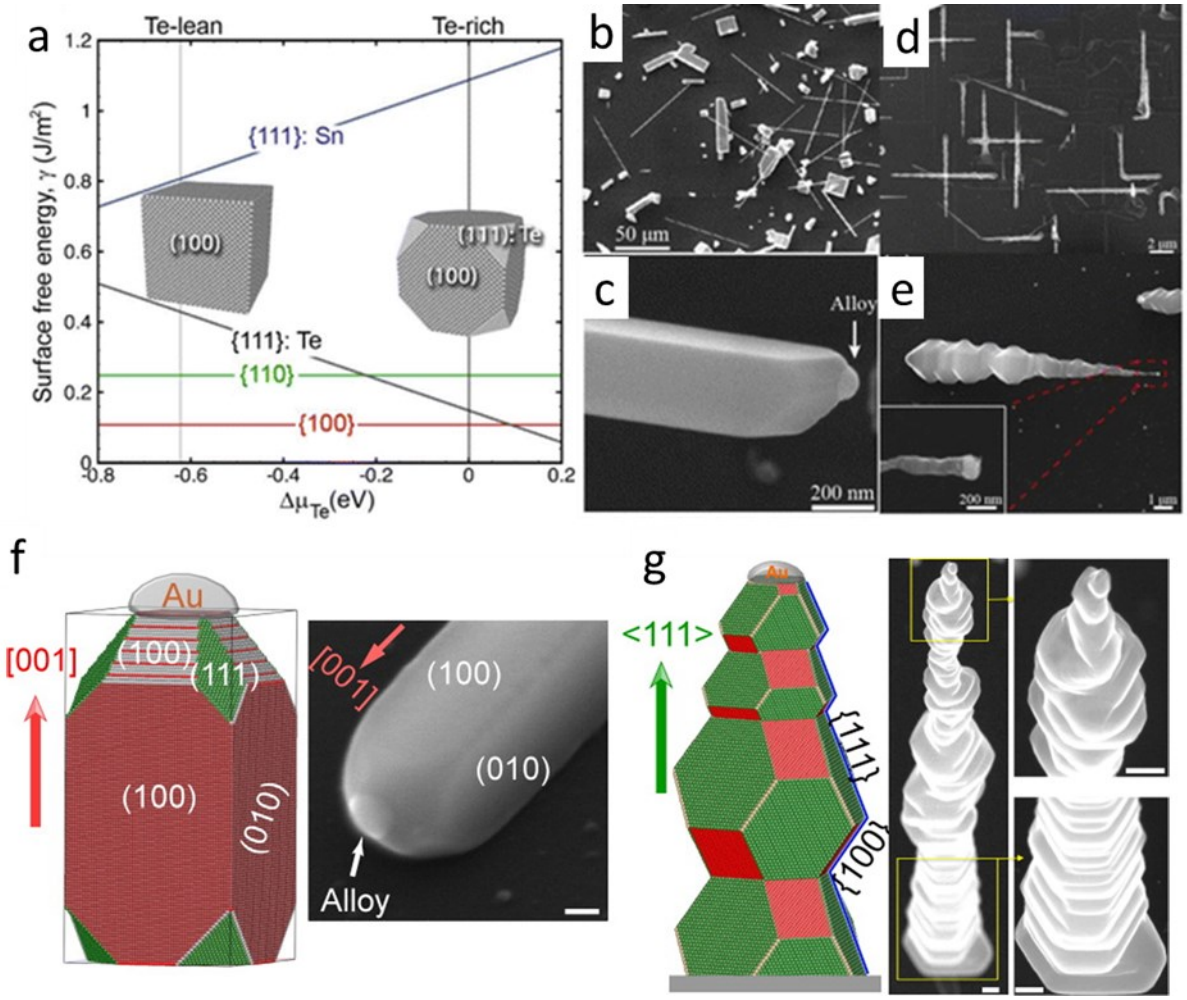


**Figure 2.28** Morphology control of Au-catalysed CVD-grown SnTe NWs by growth temperature in CVD. (a) Calculated free energies of surface facets in SnTe. (b, c) SEM images of the high-temperature grown {100} faceted NWs. (d, e) SEM images of the low-temperature NWs with both {100} and {111} facets. (f, g) Atomic models showing the {100}-faceted NWs (g) and the NWs with {111} and {100} surface facets (g).[93]

In spite of the extensive reports of semiconductor nanostructure growth, the controllable growth of high-quality IV-VI and V-VI chalcogenide nanostructures has achieved very limited success in CVD. Further experimental and theoretical analysis is highly demanded to develop the growth techniques and to understand the related growth mechanisms.

## 2.4 Growth Mechanisms of 1D Nanostructures

In this section, the detail growth mechanisms (VLS, VSS, self-catalysed and VS) of 1D nanostructures by vapour deposition are introduced. Through applying these growth mechanisms, successful examples of growth of metal chalcogenide nanomaterials have been already shown in Section 2.3.2.

### 2.4.1 Vapour-Liquid-Solid Mechanism

VLS mechanism is a classical growth mechanism to understand the catalyst-assisted growth of 1D nanostructures. It was firstly proposed by Wagner *et al.* to explain the growth of Au catalysed Si whisker.[94] The VLS growth consists of three main steps: (i) mass transport of NW growth species in the vapour to the catalyst, (ii) alloy reaction between the catalyst and the vapour phase on the vapour-liquid interface, resulting in a liquid alloy, (iii) the continuing dissolution and diffusion of the vapour atoms through the liquid alloy, and their solid precipitation on the liquid-solid interface. Figure 2.29 takes Au-assisted sI NW as an example to describe the VLS growth process. The substrates are coated with Au nanoparticles prior to the growth. During the growth, the substrate is heated to the growth temperature (~500$^{o}$C), and catalyst particles keep absorbing of the silicon vapour species, which makes the composition of Au-Si nanoparticles become silicon-rich phase and enter the liquid phase area shown as the step (ii) in Figure 2.29. As the Si content in the alloy particle is increased and reaches the saturated point, the solid precipitation of the excess Si leads to the 1D growth of Si NWs (step (iii)).

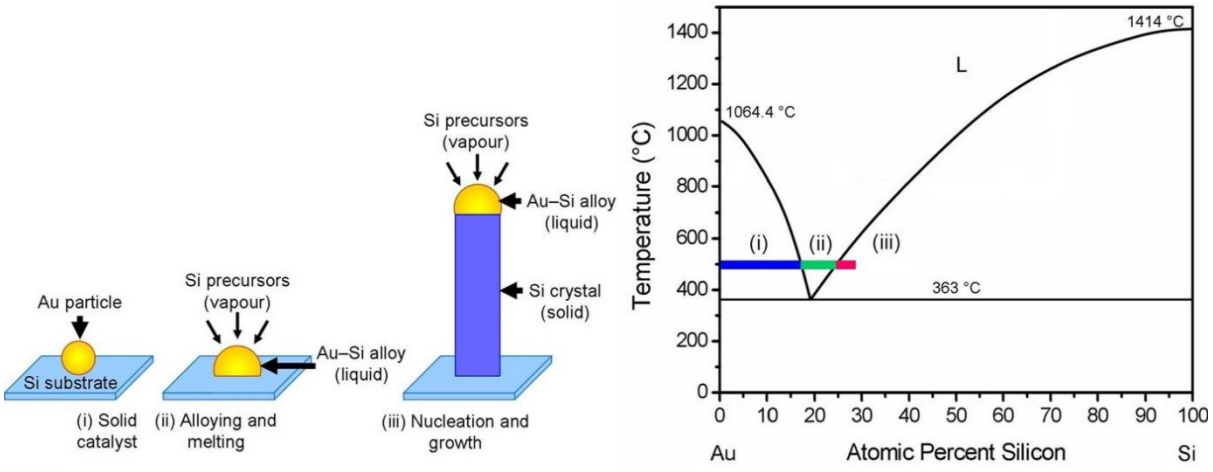


**Figure 2.29** VLS growth mechanism (Au-assisted silicon NW).[95]

### 2.4.2 Vapour-Solid-Solid Mechanism

Similar with the VLS growth mechanism, the 1D nanostructure growth by VSS is also induced by the saturation and precipitation of the grow species in the catalyst. But the growth of VSS can happen below the liquidus/eutectic point, during which the catalyst keeps the solid form. This mechanism is a comparatively new explanation for low-temperature catalyst assisted NW growth. Figure 2.30 illustrates the process of Al-assisted growth of silicon NW, which happens at the temperature below the eutectic point. As shown in Figure 2.30, the growth temperature is 470$^{o}$C while the eutectic temperature of Al-Si is 577 $^{o}$C, based on which Al and Si are not likely to form liquid alloys during the NW growth. But a quasi-liquid or solid alloy particle can still be formed by surface diffusion to initiate the nanostructure growth, which is the VSS mechanism. VSS growth process can be proposed as the following: (i) silicon vapour is absorbed by Al catalysts and form Au-Si solid solution by Si atom diffusion. (ii) After Si concentration reaches the saturation point, Si precipitates from the alloy particles to form the NW.

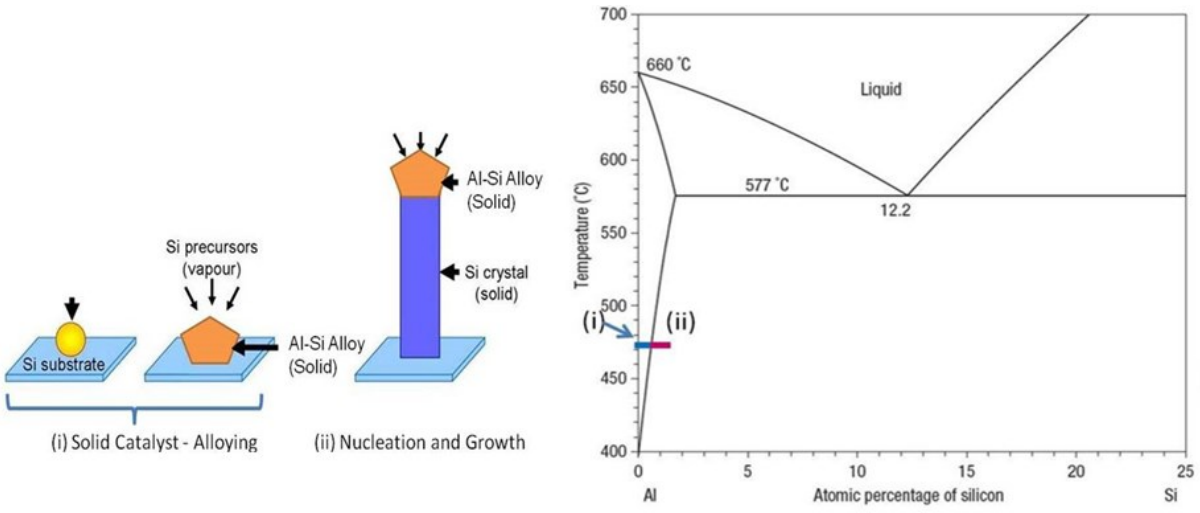


**Figure 2.30** VSS growth mechanism (Al-assisted silicon NW).[95]

### 2.4.3 Catalyst-Free Growth Mechanisms

The growth of 1D nanostructure without foreign catalyst is widely explained by self-catalysed and/or vapour-solid (VS) mechanisms.[96-100] In a typical self-catalysed growth, one of the reactants (normally the one with low melting point) agglomerates

first to form nuclei (droplet), which then absorbs vapour reactants to grow unidirectional nanostructure by VS/VLS mechanism. Such self-catalysed mechanism has been widely observed and adopted in III-V NW growth. Figure 2.31a shows the growth model and SEM images of Ga-catalysed GaAs NWs, where a Ga droplet can clearly be observed at the NW tip, indicating the catalyst role of Ga and the VLS growth of the NW.[96]

However, in many catalyst-free cases, absence of catalyst droplet can be observed at NW tip, suggesting the VLS-free growth. Figure 2.31b shows such a case, using the growth of InAs based NWs as an example.[97] These NWs show flat top surface after growth. To explain the disappearance of catalyst particles, researchers have proposed two models. The first one is that the catalyst particle was dissolved into the nanostructure at the early growth stage (Figure 2.31c).[98] The second is that the nucleation is so fast that no droplet was actually formed during the growth, and the growth is completely governed by VS mechanism (Figure 2.31d), where the unidirectional growth direction is attributed to the competition in growth rate among different crystallographic planes.[99-100] Nevertheless, for both models, the nanostructure growth needs assistance of heterogeneous nucleation, such as dislocation,[99] strain,[99] impurity(*e.g.* silicon oxides)[100] and selective area pattern.[97]

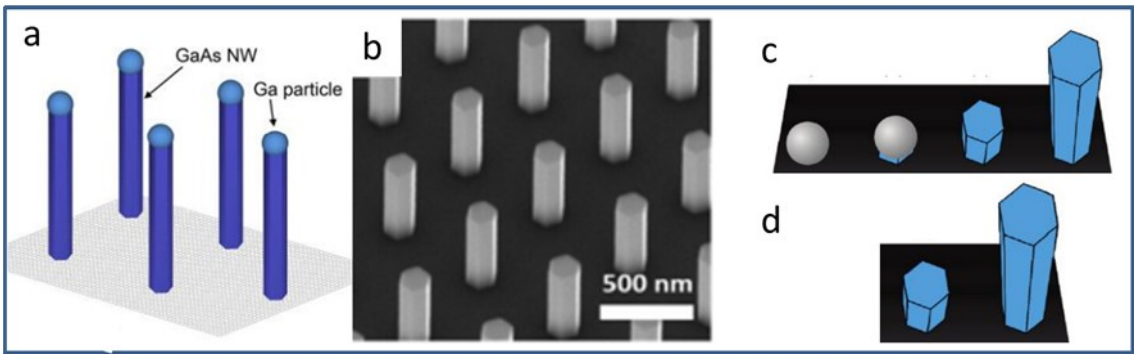


**Figure 2.31** (a) Self-catalysed growth model of GaAs NWs.[96] (b) SEM image of catalyst-free grown InAsSb NWs on InAs substrate by selective-area patterning.[97] (c) Catalyst-free growth model for catalyst-free InAs NW on Si substrate proposed by Dimakis *et al.*,[98] in which In-rich droplet forms first as nucleation followed by VS growth of NW. (d) VS growth model of NWs.[98]

## 2.5 Summary

In summary, low-dimensional chalcogenide nanomaterials are promising candidates for TE and TI applications. Among the current fabrication methods, CVD has been widely used for growing high-quality chalcogenide nanomaterials. However, insights into the growth mechanism and controllable growth of CVD grown nanomaterials are still limited, which will be investigated in our work.

## 2.6 References


1. Vining, C. B. An Inconvenient truth about thermoelectrics. *Nat. Mater.* **2009**. 8, 83-85.
2. Nolas, G. S.; Poon, J.; Kanatzidis, M. Recent developments in bulk thermoelectric materials. *Mrs Bulletin* **2006,** 31, 199-205.
3. Koumoto, K.; Terasaki, I.; Funahashi, R. Complex oxide materials for potential thermoelectric applications. *Mrs Bulletin* **2006,** 31, 206-210.
4. Yu, R.; Zhang, W.; Zhang, H.-J.; Zhang, S.-C.; Dai, X.; Fang, Z. Quantized anomalous hall effect in magnetic topological insulators. *Science* **2010**, 329, 61-64.
5. Zhang, H.; Liu, C.-X.; Qi, X.-L.; Dai, X.; Fang, Z.; Zhang, S.-C. Topological insulators in $Bi_2Se_3$, $Bi_2Te_3$ and $Sb_2Te_3$ with a single Dirac cone on the surface. *Nat. Phys.* **2009,** 5, 438-442.
6. Wang, M.-X.; Liu, C.; Xu, J.-P.; Yang, F.; Miao, L.; Yao, M.-Y.; Gao, C. L.; Shen, C.; Ma, X.; Chen, X., et al. The coexistence of superconductivity and topological order in the $Bi_2Se_3$ thin films. *Science* **2012**, 336, 52-55.
7. Hor, Y. S.; Williams, A. J.; Checkelsky, J. G.; Roushan, P.; Seo, J.; Xu, Q.; Zandbergen, H. W.; Yazdani, A.; Ong, N. P.; Cava, R. J. Superconductivity in $Cu_xBi_2Se_3$ and its implications for pairing in the undoped topological insulator. *Phys. Rev. Lett.* **2010**, 104, 057001.
8. Xia, Y.; Qian, D.; Hsieh, D.; Wray, L.; Pal, A.; Lin, H.; Bansil, A.; Grauer, D.; Hor, Y. S.; Cava, R. J., et al. Observation of a large-gap topological insulator class with a single Dirac cone on the surface. *Nat. Phys.* **2009**, 5, 398-402.

9. Dresselhaus, M. S.; Chen, G.; Tang, M. Y.; Yang, R. G.; Lee, H.; Wang, D. Z.; Ren, Z. F.; Fleurial, J. P.; Gogna, P. New directions for low-dimensional thermoelectric materials. *Adv. Mater.* **2007**, 19, 1043-1053.
10. Cha, J. J.; Williams, J. R.; Kong, D.; Meister, S.; Peng, H.; Bestwick, A. J.; Gallagher, P.; Goldhaber-Gordon, D.; Cui, Y. Magnetic doping and Kondo effect in $Bi_2Se_3$ nanoribbons. *Nano Lett.* 2**010**, 10, 1076-1081.
11. Kong, D. S.; Randel, J. C.; Peng, H. L.; Cha, J. J.; Meister, S.; Lai, K. J.; Chen, Y. L.; Shen, Z. X.; Manoharan, H. C.; Cui, Y. Topological insulator nanowires and nanoribbons. *Nano Lett.* 2**010**, 10, 329-333.
12. Cha, J. J.; Kong, D.; Hong, S.-S.; Analytis, J. G.; Lai, K.; Cui, Y. Weak antilocalization in $Bi_2(Se_xTe_{1-x})_3$ nanoribbons and nanoplates. *Nano Lett*. **2012**, 12, 1107-1111.
13. Fang, L.; Jia, Y.; Miller, D. J.; Latimer, M. L.; Xiao, Z. L.; Welp, U. Crabtree, G. W.; Kwok, W. K., Catalyst-free growth of millimeter-long topological insulator $Bi_2Se_3$ nanoribbons and the observation of the π-Berry phase. *Nano Lett.* **2012**, 12, 6164-6169.
14. Hamdou, B.; Kimling, J.; Dorn, A.; Pippel, E.; Rostek, R.; Woias, P.; Nielsch, K. Thermoelectric characterization of bismuth telluride nanowires, synthesized via catalytic growth and post-annealing. *Adv. Mater.* **2013**, 25, 239-244.
15. Zhao, Y.; Hughes, R. W.; Su, Z.; Zhou, W.; Gregory, D. H. One-step synthesis of bismuth telluride nanosheets of a few quintuple layers in thickness. *Angew. Chem. Int. Edit.* **2011**, 50, 10397-10401.
16. He, L.; Xiu, F.; Wang, Y.; Fedorov, A. V.; Huang, G.; Kou, X.; Lang, M.; Beyermann, W. P.; Zou, J.; Wang, K. L. Epitaxial growth of $Bi_2Se_3$ topological insulator thin films on Si (111). *J. Appl. Phys.* **2011**, 109, 103702-103706.
17. Wang, G.; Lok, S. K.; Wong, G. K. L.; Sou, I. K. Molecular beam epitaxy-grown $Bi_4Te_3$ nanowires. *Appl. Phys. Lett.* **2009**, 95, 263102.
18. Chen, C.-L.; Chen, Y.-Y.; Lin, S.-J.; Ho, J. C.; Lee, P.-C.; Chen, C.-D.; Harutyunyan, S. R. Fabrication and characterization of electrodeposited bismuth telluride films and nanowires. *J. Phys. Chem. C* **2010**, 114, 3385-3389.
19. Zhang, G.; Kirk, B.; Jauregui, L. A.; Yang, H.; Xu, X.; Chen, Y. P.; Wu, Y. Rational synthesis of ultrathin n-Type $Bi_2Te_3$ nanowires with enhanced thermoelectric properties. *Nano Lett.* **2011**, 12, 56-60

20. Kuznetsov V.L. System Sn-Te: critical evaluation and optimization of data on the thermodynamic properties and phase diagram. *Inorg. Mater.* **1996**, 32, 231-242
21. Sharma, R. C.; Chang, Y. A., The Sn−Te (tin-tellurium) system. *Bull. Alloy Phase Diagr.* **1986**, *7*, 72-80.
22. Okamoto, H. Phase Diagrams for Binary Alloys, Desk Handbook, 2000.
23. Cook, N. J.; Ciobanu, C. L.; Wagner, T.; Stanley, C. J. Minerals of the system Bi-Te-Se-S related to the tetradymite archetype: review of classification and compositional variation. *Can. Mineral.* **2007**, 45, 665-708.
24. Okamoto, H. The Bi-Se (bismuth-selenium) system. *J. Phase Equilib.* **1994**, 15, 195-201.
25. Nakajima, S. The crystal structure of $Bi_2Te_{3-x}Se_x$. *J. Phys. Chem. Solids* **1963,** 24, 479-485.
26. Semiletov S. A. Electron diffraction investigation of the structure of sublimated layers of composition Bi-Se and Bi-Te. *Trudy Instituta. Kristallografii, Akademiya Nauk SSSR* **1954,** 10, 76-83
27. Yamana, K.; Kihara, K.; Matsumoto, T. Bismuth tellurides: BiTe and $Bi_4Te_3$. *Acta Crystallogr. Section B* **1979,** 35, 147-149.
28. Bayliss, P. Crystal chemistry and crystallography of some minerals in the tetradymite group. *Am. Mineral* **1991,** 76, 257-265.
29. Stasova, M. M. Crystal structure of bismuth selenides and bismuth and antimony tellurides. *J. Struct. Chem.* 8, 584-589.
30. Imamov R.M., Semiletov S.A. The crystal structure of the phases in the systems Bi-Se, Bi-Te, and Sb-Te. *Sov. Phys. Crystallogr.* **1971,** 15, 845-850.
31. Teramoto, I.; Takayanagi, S. Relations between the electronic properties and the chemical bonding of $Sb_xBi_{2-x}Te_{3-y}Se_y$ system. *J. Phys. Chem. Solids* **1961,** 19, 124-129.
32. Jiang, Y.; Wang, Y.; Sagendorf, J.; West, D.; Kou, X.; Wei, X.; He, L.; Wang, K. L.; Zhang, S.; Zhang, Z. Direct atom-by-atom chemical identification of nanostructures and defects of topological insulators. *Nano Lett.* **2013**, 13, 2851-2856.
33. Medlin, D. L.; Snyder, G. J. Atomic-scale interfacial structure in rock salt and tetradymite chalcogenide thermoelectric materials. *JOM* **2013,** 65, 390-400.

34. Eremeev, S. V.; Landolt, G.; Menshchikova, T. V.; Slomski, B.; Koroteev, Y. M.; Aliev, Z. S.; Babanly, M. B.; Henk, J.; Ernst, A.; Patthey, L.; Eich, A.; Khajetoorians, A. A.; Hagemeister, J.; Pietzsch, O.; Wiebe, J.; Wiesendanger, R.; Echenique, P. M.; Tsirkin, S. S.; Amiraslanov, I. R.; Dil, J. H.; Chulkov, E. V. Atom-specific spin mapping and buried topological states in a homologous series of topological insulators. *Nat. Commun.* **2012,** *3*, 635.
35. Jung, C. S.; Kim, H. S.; Im, H. S.; Seo, Y. S.; Park, K.; Back, S. H.; Cho, Y. J.; Kim, C. H.; Park, J.; Ahn, J.-P. Polymorphism of GeSbTe superlattice nanowires. *Nano Lett.* **2013,** 13, 543-549.
36. Ikeda, T.; Ravi, V. A.; Snyder, G. J. Formation of $Sb_2Te_3$ Widmanstätten precipitates in thermoelectric PbTe. *Acta Mater.* **2009,** 57, 666-672.
37. Kooi, B. J.; De Hosson, J. T. M. Electron diffraction and high-resolution transmission electron microscopy of the high temperature crystal structures of $Ge_xSb_2Te_{3+x}$(x=1, 2, 3) phase change material. *J. Appl. Phys.* **2002,** 92, 3584-3590.
38. Shelimova, L. E.; Karpinskii, O. G.; Zemskov, V. S.; Konstantinov, P. P. Structural and electrical properties of layered tetradymite-like compounds in the GeTe-$Bi_2Te_3$ and GeTe-$Sb_2Te_3$ systems. *Inorg. Mater.* **2000,** 36, 235-242.
39. Matsunaga, T.; Kojima, R.; Yamada, N.; Kifune, K.; Kubota, Y.; Takata, M. Structural features of $GeSb_4Te_7$, an intermetallic compound in the GeTe-$Sb_2Te_3$ homologous series. *Chem. Mater.* **2008,** 20, 5750-5755.
40. Oeckler, O.; Matsunaga, T.; Yamada, N. Structural investigation of $GeSb_2Te_4$: A high-speed phase-change material. *Phys. Rev. B* **2004,** 69, 104111.
41. Urban, P.; Schneider, M. N.; Erra, L.; Welzmiller, S.; Fahrnbauer, F.; Oeckler, O. Temperature dependent resonant X-ray diffraction of single-crystalline $Ge_2Sb_2Te_5$. *CrystEngComm* **2013,** 15, 4823-4829.
42. Matsunaga, T.; Kojima, R.; Yamada, N.; Kifune, K.; Kubota, Y.; Takata, M. Structural investigation of $Ge_3Sb_2Te_6$, an intermetallic compound in the GeTe–$Sb_2Te_3$ homologous series. *Appl. Phys. Lett.* **2007,** 90, 161919.
43. Matsunaga, T.; Kojima, R.; Yamada, N.; Fujita, T.; Kifune, K.; Kubota, Y.; Takata, M. Structural investigation of $GeSb_6Te_{10}$ and $GeBi_6Te_{10}$ intermetallic compounds in the chalcogenide homologous series. *Acta Cryst.* **2010,** *B*66, 407-411.

44. Shelimova, L. E.; Karpinskii, O. G.; Konstantinov, P. P.; Avilov, E. S.; Kretova, M. A.; Zemskov, V. S. Crystal structures and thermoelectric properties of layered compounds in the ATe–$Bi_2Te_3$ (A = Ge, Sn, Pb) systems. *Inorg. Mater.* **2004,** 40, 451-460.
45. Zhukova, T.B., Zaslavskii, A.I. Crystal structures of the compounds $PbBi_4Te_7$, $PbBi_2Te_4$, $SnBi_4Te_7$, $SnBi_2Te_4$, $SnSb_2Te_4$, and $GeBi_4Te_7$. *Kristallografiya* **1972,** 16, 918.
46. Matsunaga, T.; Kojima, R.; Yamada, N.; Kifune, K.; Kubota, Y.; Takata, M. Structures of stable and metastable $Ge_2Bi_2Te_5$, an intermetallic compound in a GeTe-$Bi_2Te_3$ pseudobinary system. *Acta Cryst.* **2007,** B63, 346-352.
47. Schneider, M. N.; Fahrnbauer, F.; Vaughan, G. Atom distribution in $SnSb_2Te_4$ by resonant X-ray diffraction. *Solid State Sci.* **2011,** 13, 1157-1161.
48. Kuropatwa, B. A.; Kleinke, H. Thermoelectric properties of stoichiometric compounds in the $(SnTe)_x(Bi_2Te_3)_y$ system. *Z. Anorg. Allg. Chem.* **2012,** 638, 2640-2647.
49. Shelimova, L. E.; Karpinskii, O. G.; Svechnikova, T. E.; Avilov, E. S.; Kretova, M. A.; Zemskov, V. S. Synthesis and structure of layered compounds in the PbTe-$Bi_2Te_3$ and PbTe-$Sb_2Te_3$ systems. *Inorg. Mater.* **2004,** 40, 1264-1270.
50. Kuypers, S.; van Tendeloo, G.; van Landuyt, J.; Amelinckx, S. Electron microscopic study of the homologous series of mixed layer compounds $R_2Te_3(GeTe)_n$ (R = Sb, Bi). *J. Solid State Chem.* **1988,** 76, 102-108.
51. Schneider, M. N.; Urban, P.; Leineweber, A.; Döblinger, M.; Oeckler, O. Influence of stress and strain on the kinetic stability and phase transitions of cubic and pseudocubic Ge-Sb-Te materials. *Phys. Rev. B* **2010,** 81, 184102.
52. Matsunaga, T.; Yamada, N. Structural investigation of $GeSb_2Te_4$: A high-speed phase-change material. *Phys. Rev. B* **2004,** 69, 104111.
53. Zhang, W.; Thiess, A.; Zalden, P.; Zeller, R.; Dederichs, P. H.; Raty, J. Y.; Wuttig, M.; Blügel, S.; Mazzarello, R. Role of vacancies in metal–insulator transitions of crystalline phase-change materials. *Nat. Mater.* **2012,** 11, 952-956.
54. Kuropatwa, B. A.; Kleinke, H. Thermoelectric properties of stoichiometric compounds in the $(SnTe)_x(Bi_2Te_3)_y$ system. *Z. Anorg. Allg. Chem.* **2012,** 638, 2640-2647.

55. Matsunaga, T.; Kojima, R.; Yamada, N.; Kifune, K.; Kubota, Y.; Takata, M. Structural features of $Ge_1Sb_4Te_7$, an intermetallic compound in the GeTe-$Sb_2Te_3$ homologous series. *Chem. Mater.* **2008,** 20, 5750-5755.
56. Hsieh, T. H.; Lin, H.; Liu, J.; Duan, W.; Bansil, A.; Fu, L. Topological crystalline insulators in the SnTe material class. *Nat. Commun.* **2012,** 3, 982.
57. Al Rahal Al Orabi, R.; Mecholsky, N. A.; Hwang, J.; Kim, W.; Rhyee, J.-S.; Wee, D.; Fornari, M. Band degeneracy, low thermal conductivity, and high thermoelectric figure of merit in SnTe–CaTe alloys. *Chem. Mater.* **2016,** 28, 376-384.
58. Tan, G.; Zhao, L.-D.; Shi, F.; Doak, J. W.; Lo, S.-H.; Sun, H.; Wolverton, C.; Dravid, V. P.; Uher, C.; Kanatzidis, M. G. High thermoelectric performance of p-type SnTe via a synergistic band engineering and nanostructuring approach. *J. Am. Chem. Soc.* **2014,** 136, 7006-7017.
59. Zhang, Q.; Liao, B.; Lan, Y.; Lukas, K.; Liu, W.; Esfarjani, K.; Opeil, C.; Broido, D.; Chen, G.; Ren, Z. High thermoelectric performance by resonant dopant indium in nanostructured SnTe. *Proc. Natl. Acad. Sci. U.S.A.* **2013,** 110, 13261-13266.
60. Banik, A.; Shenoy, U. S.; Anand, S.; Waghmare, U. V.; Biswas, K. Mg alloying in SnTe facilitates valence band convergence and optimizes thermoelectric properties. *Chem. Mater.* **2015,** 27, 581-587.
61. Tan, G.; Shi, F.; Doak, J. W.; Sun, H.; Zhao, L.-D.; Wang, P.; Uher, C.; Wolverton, C.; Dravid, V. P.; Kanatzidis, M. G. Extraordinary role of Hg in enhancing the thermoelectric performance of p-type SnTe. *Energy Environ. Sci.* **2015,** 8, 267-277.
62. Tan, G.; Shi, F.; Sun, H.; Zhao, L.-D.; Uher, C.; Dravid, V. P.; Kanatzidis, M. G. SnTe-$AgBiTe_2$ as an efficient thermoelectric material with low thermal conductivity. *J. Mater. Chem. A* **2014,** 2, 20849-20854.
63. Han, M.-K.; Androulakis, J.; Kim, S.-J.; Kanatzidis, M. G. Lead-free thermoelectrics: high figure of merit in p-type $AgSn_mSbTe_{m+2}$. *Adv. Energy Mater.* **2012,** 2, 157-161.
64. Tan, G.; Shi, F.; Hao, S.; Chi, H.; Bailey, T. P.; Zhao, L.-D.; Uher, C.; Wolverton, C.; Dravid, V. P.; Kanatzidis, M. G. Valence band modification and high

thermoelectric performance in SnTe heavily alloyed with MnTe. *J. Am. Chem. Soc.* **2015,** 137, 11507-11516.

65. Wu, H.; Chang, C.; Feng, D.; Xiao, Y.; Zhang, X.; Pei, Y.; Zheng, L.; Wu, D.; Gong, S.; Chen, Y.; He, J.; Kanatzidis, M. G.; Zhao, L.-D. Synergistically optimized electrical and thermal transport properties of SnTe via alloying high-solubility MnTe. *Energy Environ. Sci.* **2015,** 8, 3298-3312.
66. Venkatasubramanian, R.; Siivola, E.; Colpitts, T.; O'Quinn, B. Thin-film thermoelectric devices with high room-temperature figures of merit. *Nature* **2001**, 413, 597-602.
67. Mehta, R. J.; Zhang, Y.; Karthik, C.; Singh, B.; Siegel, R. W.; Borca-Tasciuc, T.; Ramanath, G. A new class of doped nanobulk high-figure-of-merit thermoelectrics by scalable bottom-up assembly. *Nat. Mater.* **2012,** 11, 233-240.
68. Kim, S. I.; Lee, K. H.; Mun, H. A.; Kim, H. S.; Hwang, S. W.; Roh, J. W.; Yang, D. J.; Shin, W. H.; Li, X. S.; Lee, Y. H.; Snyder, G. J.; Kim, S. W. Dense dislocation arrays embedded in grain boundaries for high-performance bulk thermoelectrics. *Science* **2015,** 348, 109-114.
69. Cao, Y. Q.; Zhao, X. B.; Zhu, T. J.; Zhang, X. B.; Tu, J. P. Syntheses and thermoelectric properties of $Bi_2Te_3/Sb_2Te_3$ bulk nanocomposites with laminated nanostructure. *Appl. Phys. Lett.* **2008,** 92, 143106.
70. Hu, L.; Zhu, T.; Liu, X.; Zhao, X. Point defect engineering of high-performance bismuth-telluride-based thermoelectric materials. *Adv. Funct. Mater.* **2014,** 24, 5211-5218.
71. Poudel, B.; Hao, Q.; Ma, Y.; Lan, Y.; Minnich, A.; Yu, B.; Yan, X.; Wang, D.; Muto, A.; Vashaee, D.; Chen, X.; Liu, J.; Dresselhaus, M. S.; Chen, G.; Ren, Z. High-thermoelectric performance of nanostructured bismuth antimony telluride bulk alloys. *Science* **2008,** 320, 634-638.
72. Fan, S.; Zhao, J.; Guo, J.; Yan, Q.; Ma, J.; Hng, H. H. P-type $Bi_{0.4}Sb_{1.6}Te_3$ nanocomposites with enhanced figure of merit. *Appl. Phys. Lett.* **2010,** 96, 182104.
73. Hu, L.-P.; Zhu, T.-J.; Wang, Y.-G.; Xie, H.-H.; Xu, Z.-J.; Zhao, X.-B. Shifting up the optimum figure of merit of p-type bismuth telluride-based thermoelectric materials for power generation by suppressing intrinsic conduction. *NPG Asia Mater.* **2014,** 6, e88.

74. Kong, D. S.; Cui, Y. Opportunities in chemistry and materials science for topological insulators and their nanostructures. *Nat. Chem.* **2011**, 3, 845-849.
75. Moore, J. Topological insulators: the next generation. *Nat. Phys.* **2009**, 5, 378-380.
76. Hsieh, D. et al. A tunable topological insulator in the spin helical Dirac transport regime. *Nature* **2009**,460, 1101-1105.
77. Tanaka, Y.; Ren, Z.; Sato, T.; Nakayama, K.; Souma, S.; Takahashi, T.; Segawa, K.; Ando, Y. Experimental realization of a topological crystalline insulator in SnTe. *Nat. Phys.* **2012**, *8*, 800-803.
78. Safdar, M.; Wang, Q.; Mirza, M.; Wang, Z.; Xu, K.; He, J. Topological surface transport properties of single-crystalline SnTe nanowire. *Nano Lett.* **2013,** 13, 5344-5349.
79. Shen, J.; Xie, Y.; Cha, J. J. Revealing surface states in In-doped SnTe nanoplates with low bulk mobility. *Nano Lett.* **2015,** 15, 3827-3832.
80. Trahey, L.; Becker, C. R.; Stacy, A. M. Electrodeposited bismuth telluride nanowire arrays with uniform growth fronts. *Nano Lett.* **2007,** 7, 2535-2539.
81. Chen, C.-L.; Chen, Y.-Y.; Lin, S.-J.; Ho, J. C.; Lee, P.-C.; Chen, C.-D.; Harutyunyan, S. R. Fabrication and characterization of electrodeposited bismuth telluride films and nanowires. *J. Phys. Chem. C* **2010**, 114, 3385-3389.
82. Zhang, G.; Kirk, B.; Jauregui, L. A.; Yang, H.; Xu, X.; Chen, Y. P.; Wu, Y. Rational synthesis of ultrathin n-Type $Bi_2Te_3$ nanowires with enhanced thermoelectric properties. *Nano Lett.* **2011,** *12*, 56-60
83. Zhang, G.; Wang, W.; Lu, X.; Li, X. Solvothermal synthesis of V−VI binary and ternary hexagonal platelets: the oriented attachment mechanism. *Cryst. Growth Des.* **2008**, 9, 145-150.
84. Guo, S.; Fidler, A. F.; He, K.; Su, D.; Chen, G.; Lin, Q.; Pietryga, J. M.; Klimov, V. I. Shape-controlled narrow-gap SnTe nanostructures: from nanocubes to nanorods and nanowires. *J. Am. Chem. Soc.* **2015**, 137, 15074-15077.
85. Houston Dycus, J.; White, R. M.; Pierce, J. M.; Venkatasubramanian, R.; LeBeau, J. M. Atomic scale structure and chemistry of $Bi_2Te_3$/GaAs interfaces grown by metallorganic van der Waals epitaxy. *Appl. Phys. Lett.* **2013,** *102*, 081601.

86. Zhao, Y.; de la Mata, M.; Qiu, R. L. J.; Zhang, J.; Wen, X.; Magen, C.; Gao, X. P. A.; Arbiol, J.; Xiong, Q. Te-seeded growth of few-quintuple layer $Bi_2Te_3$ nanoplates. *Nano Res.* **2014,** *7*, 1243-1253.
87. Jiang, Y.; Zhang, X.; Wang, Y.; Wang, N.; West, D.; Zhang, S.; Zhang, Z. Vertical/planar growth and surface orientation of $Bi_2Te_3$ and $Bi_2Se_3$ topological insulator nanoplates. *Nano Lett.* **2015,** *15*, 3147-3152.
88. He, L.; Xiu, F.; Wang, Y.; Fedorov, A. V.; Huang, G.; Kou, X.; Lang, M.; Beyermann, W. P.; Zou, J.; Wang, K. L. Epitaxial growth of $Bi_2Se_3$ topological insulator thin films on Si (111). *J App. Phys.* **2011,** *109*, 103702.
89. Kong, D.; Dang, W.; Cha, J. J.; Li, H.; Meister, S.; Peng, H.; Liu, Z.; Cui, Y. Few-layer nanoplates of $Bi_2Se_3$ and $Bi_2Te_3$ with highly tunable chemical potential. *Nano Lett*. **2010**, 10, 2245-2250.
90. Mi, G.; Li, L.; Zhang, Y.; Zheng, G. Sn-doped bismuth telluride nanowires with high conductivity. *Nanoscale* **2012**, 4, 6276-6278.
91. Kong, D.; Chen, Y.; Cha, J. J.; Zhang, Q.; Analytis, J. G.; Lai, K.; Liu, Z.; Hong, S. S.; Koski, K. J.; Mo, S.-K., et al. Ambipolar field effect in the ternary topological insulator $(Bi_xSb_{1-x})_2Te_3$ by composition tuning. *Nat. Nanotech.* **2011**, 6, 705-709.
92. Shen, J.; Jung, Y.; Disa, A. S.; Walker, F. J.; Ahn, C. H.; Cha, J. J. Synthesis of SnTe nanoplates with {100} and {111} surfaces. *Nano Lett.* **2014,** 14, 4183-4188.
93. Li, Z.; Shao, S.; Li, N.; McCall, K.; Wang, J.; Zhang, S. X. Single crystalline nanostructures of topological crystalline insulator SnTe with distinct facets and morphologies. *Nano Lett.* **2013,** 13, 5443-5448.
94. Wagner, R. S.; Ellis, W. C. Vapour-liquid-solid mechanism of single crystal growth. *Appl. Phys. Lett.* **1964** 4, 89-90
95. Xu, H.-Y. Role of catalysts in the growth of one-dimensional III-V semiconductor nanowires. Doctor of Philosophy Thesis, University of Queensland, (2013).
96. Munshi, A. M.; Dheeraj, D. L.; Fauske, V. T.; Kim, D.-C.; van Helvoort, A. T. J.; Fimland, B.-O.; Weman, H. Vertically aligned GaAs nanowires on graphite and few-layer graphene: generic model and epitaxial growth. *Nano Lett.* **2012,** *12*, 4570-4576.

97. Farrell, A. C.; Lee, W.-J.; Senanayake, P.; Haddad, M. A.; Prikhodko, S. V.; Huffaker, D. L. High-quality InAsSb nanowires grown by catalyst-free selective-area metal–organic chemical vapor deposition. *Nano Lett.* **2015,** *15*, 6614-6619.
98. Dimakis, E.; Lähnemann, J.; Jahn, U.; Breuer, S.; Hilse, M.; Geelhaar, L.; Riechert, H. Self-assisted nucleation and vapor–solid growth of InAs nanowires on bare Si(111). *Cryst. Growth Des.* **2011,** *11*, 4001-4008.
99. Shin, J. C.; Choi, K. J.; Kim, D. Y.; Choi, W. J.; Li, X. Characteristics of strain-induced $In_xGa_{1-x}As$ nanowires grown on Si(111) substrates. *Cryst. Growth Des.* **2012,** *12*, 2994-2998.
100. Kim, B.-S.; Koo, T.-W.; Lee, J.-H.; Kim, D. S.; Jung, Y. C.; Hwang, S. W.; Choi, B. L.; Lee, E. K.; Kim, J. M.; Whang, D. Catalyst-free growth of single-crystal silicon and germanium nanowires. *Nano Lett.* **2009,** *9*, 864-869.

# 3

# Methodology

This project is focused on the CVD growth for low dimensional metal chalcogenide nanostructures, and their structural and compositional characterizations. In this chapter, the procedures of CVD growth for nanostructures will be presented, and the working principles of various structural characterization techniques including SEM, TEM, aberration-corrected STEM and XRD will be described in detail. Since part of the understanding of the nanostructure facets and atomic structure was based on DFT calculations, the theoretical background of DFT is also introduced.

## 3.1 CVD Growth Method

Figure 3.1 shows a schematic diagram of CVD reactor. Prior to the growth experiment, types of the chemicals for the solid source (precursor), the carrier gases and the substrates need to be predesigned. The precursor chemicals used in the growth experiments are listed in Table 3.1.

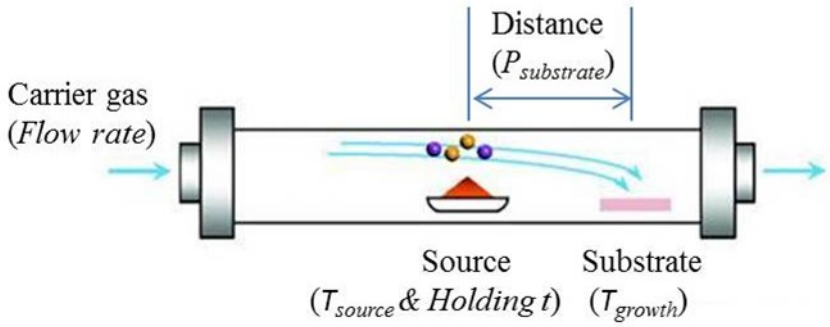


**Figure 3.1** A schematic diagram of the CVD reactor.

**Table 3.1** Chemicals for the CVD growth for chalcogenide nanostructures.

| Quality / Content | Purity | Particle Size | Supplier | Treatment Before Use |
|---|---|---|---|---|
| Bismuth Selenide | 99.9% | Beads 1~6mm | Sigma Aldrich | Grinding |
| Bismuth Telluride | 99.99% | Powder ~325mesh | Sigma Aldrich | N |
| Tin Telluride | 99.99% | NA | Sigma Aldrich | N |
| Bismuth | 99.99% | ~100 mesh | Sigma Aldrich | N |
| Telluride | 99.99% | ~50 mesh | Sigma Aldrich | N |
| Tin | 99.99% | ~50 mesh | Sigma Aldrich | N |
| Silicon Wafer | NA | NA | MTI | Soniclean |
| Silicon Wafer With 300nm Silica Layer | NA | NA | MTI | Soniclean |
| Argon Gas | 99.999% | NA | Coregas | N |
| Hydrogen Gas | 99.9995 | NA | Coregas | N |

The general procedures of the CVD experiments can be summarized as the below.

(i) Preparation of the wafers

Silicon wafer (Si or $Si/SiO_2$) is cleaned first in acetone and then in distilled deionized water using sonicator. For catalyst-assisted growth, the substrates are coated with Au films using a SPI module sputtering coater with a gold target.

(ii) Nanostructure growth

Weigh the precursor with predesigned amount. Put the precursor and substrates into the tube furnace, in which precursor are put at the centre while the substrates are put at the downstream of the tube. Flush the furnace chamber with mixed $Ar/H_2$ gas to prevent the oxygen contamination and then adjust the flow rates for the gases to predesigned value. Heat the furnace to temperature with predesigned program.

(iii) Sample collection

After a natural cool down to the room temperature, the substrates are removed from the furnace chamber. Samples are collected from the substrates for further characterization.

(iv) Controllable growth by tuning the growth parameters

After the characterization of the products, further experiments will be conducted to improve or modify the quality and morphology of the as-grown products by tuning the growth parameters, which include the composition of the precursor, the holding temperature of the hot centre (source), the holding time, the composition and the flow rate of the carrier gases, and the positions of the wafers (growth temperature).

## 3.2 Morphological and Structural Characterization

### 3.2.1 Scanning Electron Microscopy (SEM)

SEM produces the images through the scanning of sample surface using a focused electron beam. The interaction of the electron beam with the sample produces signals that contain the topography and composition information of the sample. Fig. 3.2a shows the major components of a SEM. The incident electron beam is collimated by the electromagnetic condenser lens, focused by an objective lens and scanned across the surface by electromagnetic scanning coils. After incident electron beam interacts with the surface of the specimen, the interaction signals, including the secondary electrons (SEs) and backscattered electrons (BSEs), will be generated and collected by multiple detectors. Figure 3.2b shows the interaction volume between the electrons and the specimen surface, and it can be seen that the SEs interact with the sample surface (5~50nm) with a much smaller volume than the BSEs. This suggests that SEs reflect the most surface information of the sample while the BSEs reflect the information from a deeper area of the sample. Since the volume of escaped SEs from protruded surface are theoretically larger than from a flat one, and more SE signals induce an increased brightness in the final image (edge effect), the SE imaging mode can be used to study the topography of the specimen. On the other hand, BSE signals are generated from the high-energy (>50eV) elastic scattered electrons, and their intensity is increased with an increase

of the average atomic number in the sample. BSE imaging mode is thereby used to reflect the composition difference across the specimen.

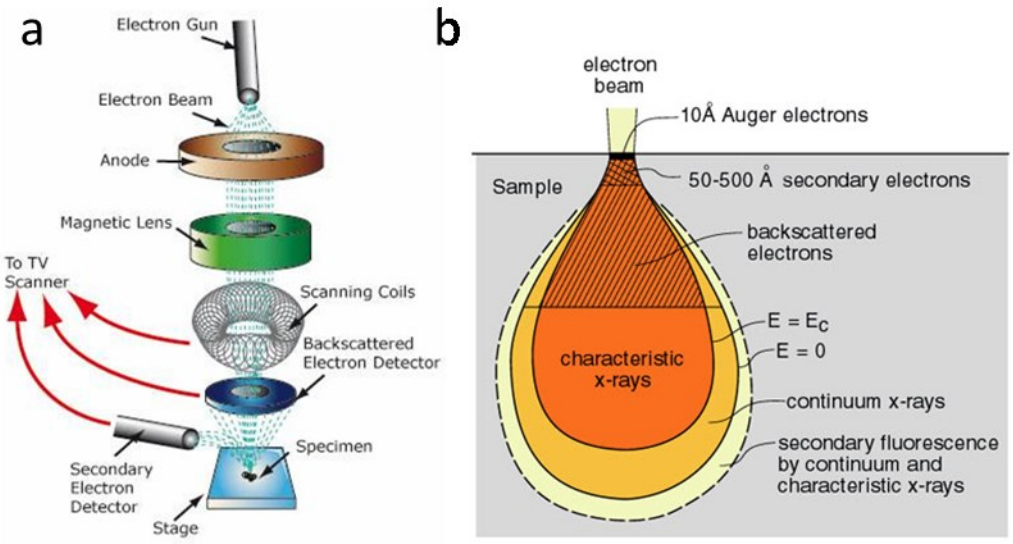


**Figure 3.2** (a) A schematic diagram showing the components of a SEM. (b) A schematic diagram showing the interactions between the electron beam and the sample, and the corresponding interaction volumes and emitted signals.[1]

### 3.2.2 Transmission Electron Microscopy (TEM)

Figure 3.3a shows a TEM facility and its major components are shown in Fig. 3.3b. Similar to SEM, an electron gun generates the electron beam with an acceleration voltage of 80~400 kV that is able to penetrate through thin samples. The electron beam is further modulated by series of condenser lenses and its interaction with the sample will further create signals for imaging.

Figure 3.4 shows the two modes in TEM. In general, when the intermediate lens is placed at the objective plane of the objective lens, the TEM is in an imaging mode (left panel of Fig. 3.4), and an enlarged image will be formed in the image plane of the objective lens. When the transmitted beam is selected by the objective aperture to pass through, a bright-field (BF) image is generated, in which thicker and heavier samples tend to be darker in the BF image. On the other hand, when the scattered beam is allowed by the aperture to generate the image, a dark-field image can be obtained. The bright contrast suggests that the imaging area contains atomic planes that satisfy the Bragg condition. When the intermediate lens is placed at the back focal plane of objective lens, the TEM is in a diffraction mode (right panel of Fig. 3.4).

If the sample is a single crystal, a set of well-defined electron diffraction spots can be obtained which can be used to determine the crystal structure. If the sample region under imaging contains polycrystals, diffraction rings are expected to be obtained; while when the imaging region contains amorphous materials, diffused diffraction rings may be obtained.

In this project, TEM is applied to obtain BF image, HRTEM images and diffraction patterns from the as-grown nanostructures. The EDX attached to the TEM is used to determine the chemical compositions of the as-synthesized nanostructures.

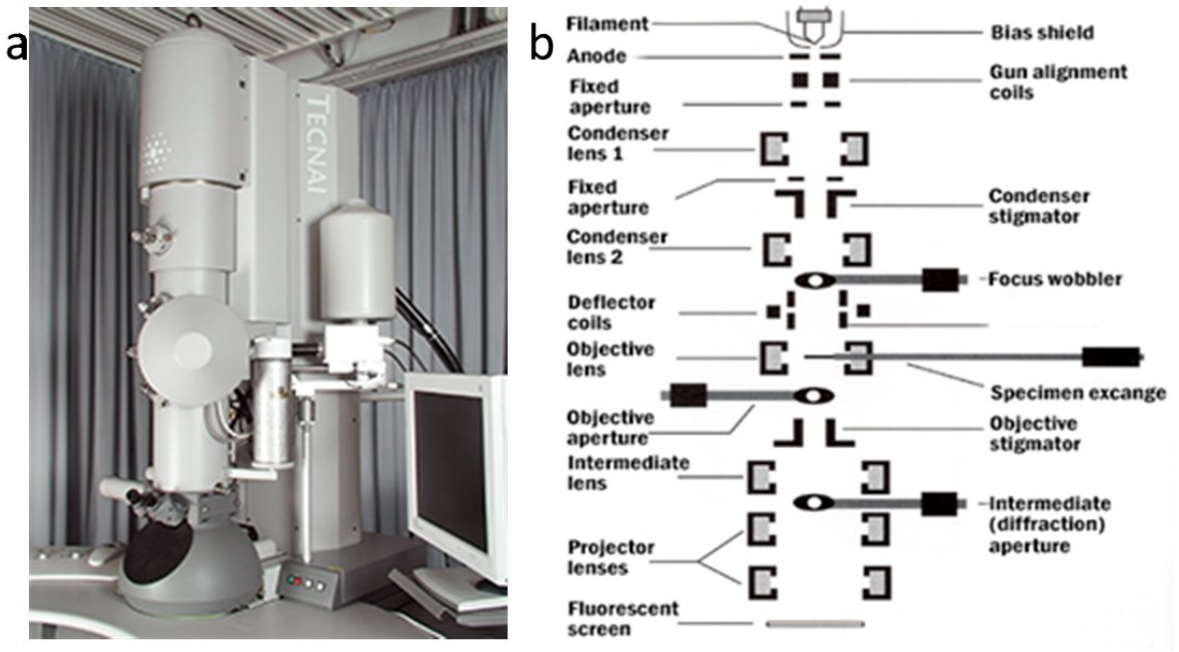


**Figure 3.3** (a) A photograph of a TEM instrument and (b) a schematic diagram showing its major components.[2]

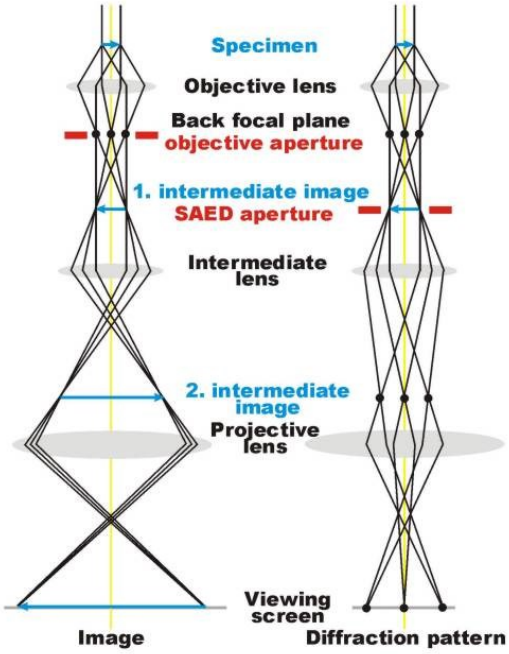


**Figure 3.4** The ray diagrams of the electron beams in the diffraction mode and in the imaging mode of TEM.[3]

### 3.2.3 Scanning Transmission Electron Microscopy (STEM)

The major components of a STEM are shown in Fig. 3.5. In STEM, a field-emission gun provides a highly coherent electron source, with an acceleration voltage arrange of 60~300 kV. The electron beam is further focused by the following lenses and optics until the diameter is reduced to be smaller than lattice spacing of the sample to be imaged. The focused electron beam is then used to scan over a sample with a thin thickness up to 100nm. The optimal thickness of the sample is neither too thin, to avoid the surface dominated signal, nor too thick, so that electron spot would not spread largely in the sample. After the beam is scanning across the sample, signals generated from scattered electrons and ionized atoms are recorded to build up a two-dimensional mapping image, and the electron-scattering differences between different atomic columns at the samples will be reflected as the image contrast.[4] By using a STEM detector with a large inner radius, an annular dark-field (ADF) detector, electrons that are not Bragg scattered are collected. The intensity of these high angle scattering depends only on the atomic number (Z) of the column atom, and is roughly proportional to the atomic number $Z^{1.7}$, where a larger Z induces greater the loss of energy. Therefore, high-angle ADF imaging mode can provide 'Z-contrast' imaging.

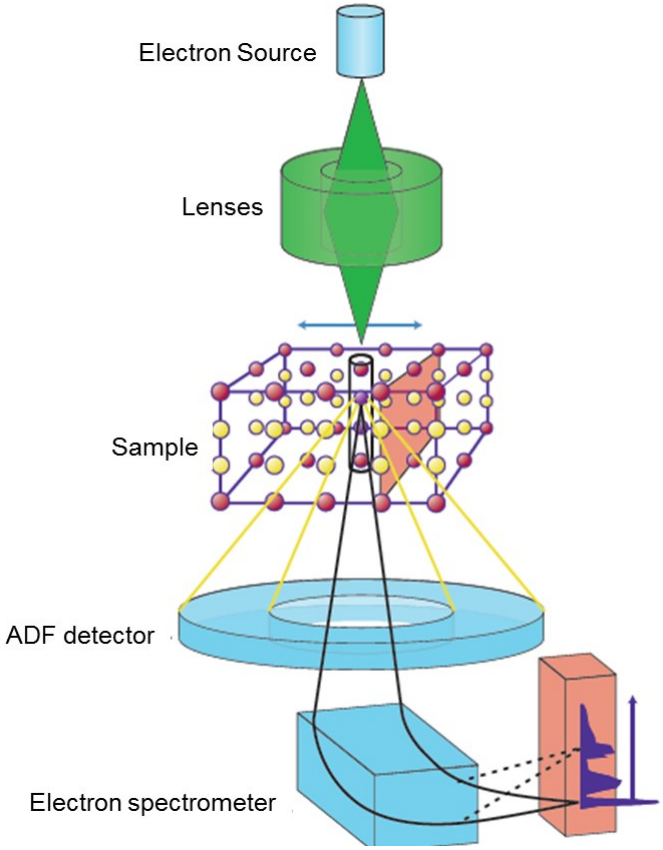


**Figure 3.5** Major components of a STEM.[4]

To improve the microscope resolution, one important approach is through reducing the spherical aberration. The limitation to the microscope resolution ($d_s$) is resulted from the spherical aberration, which can be described by the following formula:

$$d_s = 0.67 C_s^{1/4} \lambda^{3/4} \tag{3.1}$$

in which $C_s$ is the coefficient of spherical aberration and $\lambda$ is the wavelength of the incident electrons.

The appearance of $C_s$ is caused by the imperfect electromagnetic lenses, where the off-axial rays experience a greater bending than those close to the axis, leading to premature focus, which converts a point object into a disk of radius $r_s$ (Fig. 3.6),

$$r_s = C_s \alpha^3 \tag{3.2}$$

in which $\alpha$ is the objective lens collection angle.

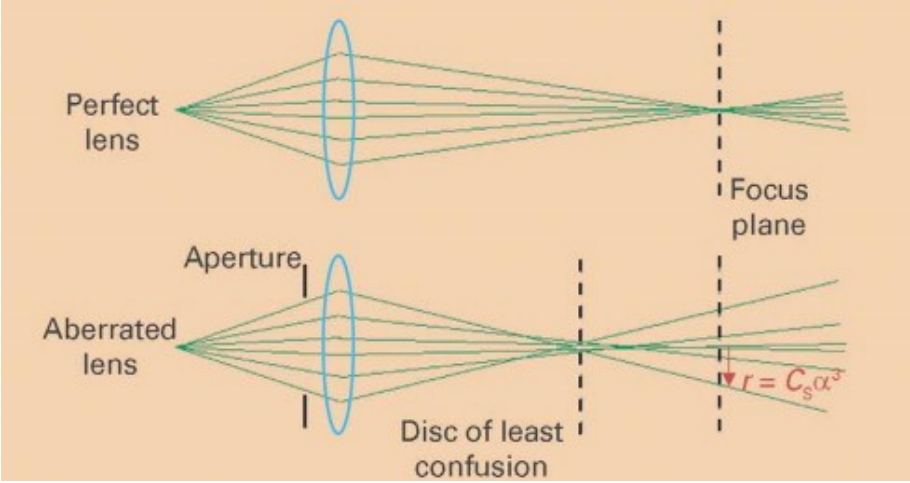


**Figure 3.6** A spherically aberrated lens causes higher angle rays to come to a premature focus (bottom) when compared with a perfect lens (top).[5]

The current $C_s$ corrector uses multipole lenses that can produce negative aberration to compensate the positive $C_s$. Once the spherical aberration has been compensated, the presence of chromatic aberration ($C_c$) becomes more significant. Chromatic aberration comes into play as a consequence of an energy spread in the electron beam produced by the electron source, resulting in longer focal distances for rays with higher energies and shorter distances for lower energies (Fig. 3.7). The effect of $C_c$ on the resulting spot size (disc of least confusion) can be expressed as[6]:

$$d_c = C_c \alpha \frac{\Delta E}{E} \tag{3.3}$$

where $C_c$ is chromatic aberration coefficient, $\Delta E/E_0$ is the energy spread with respect to the primary beam energy, and α is the convergence angle. The spot size dependence on *1/E* suggests stronger effect of chromatic aberration as accelerating voltage is lowered. The effect of chromatic aberration can be minimized by employing a $C_c$ corrector or by using a monochromator.

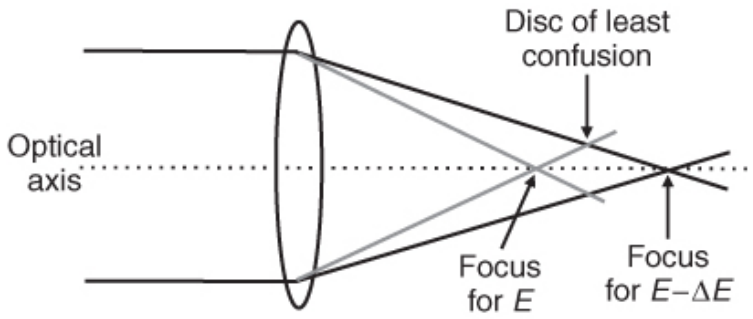

**Figure 3.7** A Schematic representation of chromatic aberration effects.[6]

### 3.2.4 X-Ray Diffraction (XRD)

There are two basic XRD techniques that can be used to study materials, single-crystal XRD apparatus and powder diffraction apparatus. The single-crystal XRD is used to solve the crystal structures of crystalline materials. The powder XRD is generally used to understand the crystal structure, as well as other information including grain size, and preferred crystal orientation in powder or polycrystalline sample.

X-ray diffractometers have three basic components: an X-ray tube to generate the X-ray source, a sample holder to hold the testing samples, and an X-ray detector, as illustrated in Fig. 3.8. X-rays are generated by heating a filament in a cathode ray tube. When electrons have sufficient energy to bounce out inner shell electrons from the X-ray generating material, characteristic X-rays can be produced, which provide the X-ray sources. The most widely used target material to generate X-ray is copper, with the wavelength of λ=1.5418 Å from Cu Kα radiation. The generated X-rays are collimated and fired onto the sample. During the testing, both sample and X-ray detector are rotated, and the intensity of the reflected X-rays is recorded. When the incident X-rays are rotated to a position that satisfies the Bragg equation when impinging the sample ($2d \sin \theta = \lambda$, where d is the interplanar spacing, λ is the wavelength of incidental electrons, and θ the Bragg angle), constructive interference occurs in a form of a peak at the position of 2θ, where 2θ is generally in a range of ~$5^{o}$ to $70^{o}$. In this project, powder XRD is employed for analysis of the crystalline phases of synthesized products. Substrates after product growth are directly used for X-ray diffraction characterization. XRD result will be compared with the stand PDF cards from the database by the International Center of Diffraction Data. The information from the substrates will be excluded to determine the phase composition of the products.

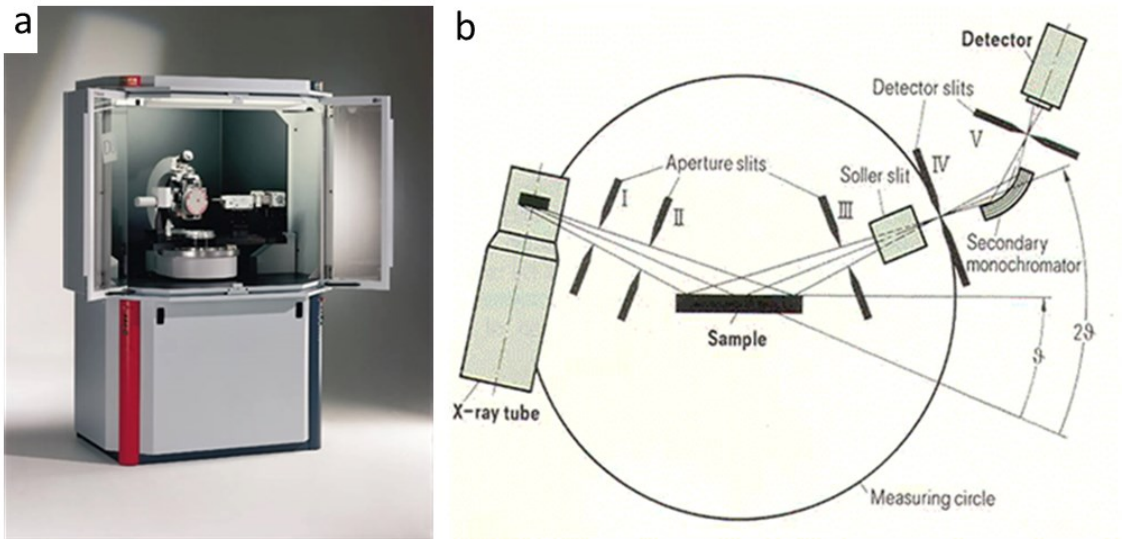


**Figure 3.8** (a) A photograph of a XRD instrument and (b) the schematic diagram of its components.[7]

## 3.3 Sample Preparation for Electron Microscopy

### 3.3.1 Sample Preparation for SEM

As the incident electrons with negative charges will continuously interact with the sample, it is very necessary to get rid of the negative charges accumulated on the sample. Thus, all the SEM samples need to be electrically conductive. For insulating samples, a thin layer of conductive agent, such as carbon, platinum or gold, will be coated on the surface. Since all the SEM samples in this thesis are semiconducting nanostructures, the nanostructured samples were not pre-coated with any conductive layer. Therefore, as-grown nanostructure on the substrate is directly used as the SEM samples. The substrate bottom is then sticked to the metallic sample stub to get plain views and side views of the sample.

### 3.3.2 Sample Preparation for TEM/STEM

In this thesis, there are two types of nanostructure sample, the first is individual NWs, and the other is the nanostructures with the supporting substrate. The corresponding sample prepare methods are listed as below.

**Table 3.2** Preparation processes of TEM/STEM samples.

| Sample type | Preparation process |
|---|---|
| Individual nanostructures | A small substrate with as-grown nanostructures is cut and placed in a small container with a tiny amount of pure ethanol. Then the container is put into a ultrasonicator for 10~40 min to break the NWs from the substrate. The NW-ethanol dispersion is then dropped onto a holy carbon film coated copper grid. |
| Cross-section TEM sample | Substrates with nanostructure were glued with clean silicon substrates, and form sandwiched TEM sample. Mechanically grinding the sandwich substrate till thin enough (by tripod or Disc Grinder, or polishing machine). Glue the thinned sandwich to a copper grid. Further thinning the sample till electron transparent by ion-milling via PIPS. |

## 3.4 Density Functional Theory (DFT)

DFT provides a powerful tool for computations of the quantum state of atoms, molecules and solids, and of *ab-initio* molecular dynamics. Its first version was conceived by Thomas and Fermi immediately after the foundation of quantum mechanics in 1927.[8] In the middle of 1960s, Hohenberg, Kohn and Sham established a logically rigorous DFT of the quantum ground state on the basis of quantum mechanics, and introduced an approximatively explicit theory called the local-density approximation (LDA), after which DFT grows vastly in popularity.[9-11]

Accurate description of electronic structure of atoms, molecules and solids is complex, since there are large numbers of electrons that must be treated following quantum mechanics rather than classical physics. To obtain the energy of the electron system, early quantum mechanics was by solving stationary (time-independent) Schrodinger equation[10]:

$$\hat{H}\,\Psi_k(\mathbf{r}_1,\mathbf{r}_2,\mathbf{r}_3,\cdots\mathbf{r}_{\mathrm{N}}) = E_k\Psi_k(\mathbf{r}_1,\mathbf{r}_2,\mathbf{r}_3,\cdots\mathbf{r}_{\mathrm{N}}) \tag{3.4}$$

where $\hat{H}$ is called Hamiltonian which operates on the wave function $\Psi_k$ and give corresponding energies (eigenvalues) $E_k$. When the function $\Psi$ is known, the corresponding energy of the system can be calculated as an expectation value of the Hamiltonian $\hat{H}$ as:

$$E = \frac{\int\int\cdots\int \Psi^*(\mathbf{r}_1, \mathbf{r}_2, \mathbf{r}_3, \cdots \mathbf{r}_\mathrm{N})\hat{H}\Psi(\mathbf{r}_1, \mathbf{r}_2, \mathbf{r}_3, \cdots \mathbf{r}_\mathrm{N})\boldsymbol{d}_{\mathbf{r}1}, \boldsymbol{d}_{\mathbf{r}2}, \boldsymbol{d}_{\mathbf{r}3}, \cdots \boldsymbol{d}_{\mathbf{r}\mathrm{N}}}{\int\int\cdots\int \Psi^*(\mathbf{r}_1, \mathbf{r}_2, \mathbf{r}_3, \cdots \mathbf{r}_\mathrm{N})\Psi(\mathbf{r}_1, \mathbf{r}_2, \mathbf{r}_3, \cdots \mathbf{r}_\mathrm{N})\boldsymbol{d}_{\mathbf{r}1}, \boldsymbol{d}_{\mathbf{r}2}, \boldsymbol{d}_{\mathbf{r}3}, \cdots \boldsymbol{d}_{\mathbf{r}\mathrm{N}}} \tag{3.5}$$

For an electronic system like atom or bulk materials, the total Hamiltonian operator can be written as:

$$\hat{H}_{tot} = \hat{T}_{nucl} + \hat{U}_{nucl} + \hat{T}_e + \hat{U}_{ee} + \hat{V}_{ext} \tag{3.6}$$

where $\hat{T}_{nucl}$ is the operator of kinetic energy of nuclei, $\hat{U}_{nucl}$ is the interaction energy of nuclei, $\hat{T}_e$ represents the kinetic energy of electrons, $\hat{U}_{ee}$ denotes the interaction energy between electrons, and $\hat{V}_{ext}$ is an external potential. Since nuclei are much heavier than electrons, we can consider that the movement of electrons depends on positions of nuclei in a parametric way, which is Born-Oppenheimer approximation.[12] It allows us to use describe electron Hamiltonian $\hat{H}_{el}$ as

$$\hat{H}_{el}=\hat{T}_e + \hat{U}_{ee} + \hat{V}_{ext}=\sum_{i=1}^{N} -\frac{1}{2}\nabla_i^2 + \sum_{i=1}^{N-1}\sum_{j=i+1}^{N-1}\frac{1}{|\mathbf{r}_i-\mathbf{r}_j|} + \sum_{i=1}^{N}\left(\sum_{\alpha=1}^{N_{nucl}}\frac{-Z_\alpha}{|\mathbf{r}_i-\mathbf{R}_\alpha|}\right) \tag{3.7}$$

in which energy is in Hartree unit, atomic units are used for mass of electron $m_e$= 1; $\hbar$= 1; length in bohrs; $|\mathbf{r}_i - \mathbf{r}_\mathrm{j}|$ is the distance between $i^{th}$ and $j^{th}$ electron. The $Z_\alpha$ is the charge of an $\alpha^{th}$ nucleus (atomic number), $|\mathbf{r}_i - \mathbf{R}_\alpha|$ is the distance between electron $i$ and nucleus $\alpha$, $N_{nucl}$ is the total number of nuclei in the molecule.

The essence of DFT is to describe a many-body interacting system via its particle density but not many-body wavefunction. This reduces the 3N degrees of freedom of N-body system to three spatial coordinates. The Thomas-Fermi (TF) model is predecessor of DFT concepts.[8] The TF model was proposed by Thomas and Fermi at around 1928, in which they use the electron density $n(r)$ as the basic variable instead of wave function. The total energy of a system in an external potential $V_{ext}(r)$ can be written as a functional of the electron density n(r) as:

$$E_{TF}[n(r)] = C_1 \int n(r)^{5/3}\, dr + \int n(r)^{\frac{5}{3}} V_{ext}(r) dr + \frac{1}{2}\int \frac{n(r)n(r\prime)}{|r-r'|}\, dr dr' \tag{3.8}$$

where the first term represents the kinetic energy of the non-interacting electrons in a homogeneous electron gas with $C_1 = \frac{3}{10}\,(3\pi^2)^{2/3}$ in atomic units ( $\hbar = m_e = e =$

$4\pi/\epsilon_0$=1). The kinetic energy density of a homogenous electron gap is obtained by adding up all of the free-electron energy state $\epsilon_0$=k$^2$/2 up to Fermi wave vector $k_F = [3\pi^2 n(r)]^{1/3}$. The second term represents the classical nucleus-electron Coulomb electrostatic interaction energy. The third term represents the classical Hartree energy with the classical Coulomb repulsion between electrons. As in TF method, the exchange and correlation among electrons was ignored, Dirac extended the TF method by adding a local exchange term $C_2 Rn(r)^{4/3}$dr with $C_2$=$\int 34(\frac{3}{\pi})^{1/3}$, which results new equation[13]:

$$E_{TFD}[n(r)] = C_1 \int n(r)^{5/3}\, dr + \int n(r)^{\frac{5}{3}} V_{ext}(r) dr + \frac{1}{2}\int \frac{n(r)n(r\prime)}{|r-r'|} drdr' + C_2 \int n(r)^{4/3}\, dr \quad (3.9)$$

The ground state density and energy can be obtained by minimizing the TF equation subject to conservation of the total number (*N*) of electrons. By using the technique of Lagrange multipliers, the solution can be found in the stationary condition:

$$\delta\{E_{TFD}[n(r)] - \mu(\int n(r)dr - N)\} = 0 \quad (3.10)$$

where $\mu$ is a Lagrange multiplier, which denotes the chemical potential (or Fermi energy at T=0K). Combining Eq. 3.5 and 3.6, the Thomas-Fermi-Dirac (TFD) equation can be described as:

$$\frac{5}{3} C_1 n(r)^{2/3} + V_{ext}(r) + \int \frac{n(r)}{|r-r'|} dr' + \frac{4}{3} C_2 n(r)^{4/3} - \mu = 0 \quad (3.11)$$

which can be solved directly to obtain the ground state density. The approximations used in the TFD approach fails to describe the atomic bonding, and thereby cannot give accurate description for molecules and solids. Nevertheless, it has given a path to application of DFT method.

Modern DFT is based on the Hobenberg-Kohn (HK) theorem,[14] which contains following conventional formulations:

Theorem 1: The external potential $V_{ext}[r]$, and hence the total energy is a unique functional of electron density $n(r)$.

Theorem 2: The ground state total energy functional $E_{V_{ext}}[\rho_0]$ reaches its minimal value at the ground state electron density $\rho_0$ corresponding to $V_{ext}$: the density that minimises the total energy is the exact ground state density.

$$E[\rho] \geq E[\rho_0] \quad (3.12)$$

For every trial electron density $\rho$, $E_{V_{ext}}[\rho_0]$ can be written as

$$E_{V_{ext}}[\rho_0] =< \Psi|T_e + V_{ee}|\Psi >+< \Psi|V_{ext}|\Psi >=F_{HK}[\rho] + \int \rho V_{ext} d\vec{r} \quad (3.13)$$

where $F_{HK}[\rho]$ is universal for a many-electron system. Then, the one-to-one correspondence $\rho_0 \leftrightarrow V_{ext}$, and ground state total energy functional $E_{V_{ext}}[\rho_0]$ are explained.

Theorem 1 demonstrates that the density contains as much information as the wave function. Hence, all the observable can be written as functional of electron density.

The HK theorem only shows that it is possible to obtain ground state density, but does not tell a way to find the ground state density. This difficulty was overcome by Kohn-Sham (KS) equations,[9] which rewrite the total energy as:

$$E[\rho] = T[\rho] + E_H[\rho] + E_{xc}[\rho] + \int n(r) V_{ext}(r) dr \quad (3.14)$$

where $T_0$, $V_H$ and $V_{xc}$ are the kinetic energy, Hartree potential, and exchange-correlation functional. The corresponding Hamiltonian is called the KS Hamiltonian:

$$\hat{H}_{KS} = \hat{T}_0 + \hat{U}_H + \hat{V}_{xc} + \hat{V}_{ext} \quad (3.15)$$

The exchange-correlation potential is given by the functional derivative of the exact ground state density:

$$\hat{V}_{xc} = \frac{\delta E_{xc}[\rho]}{\delta_\rho} \quad (3.16)$$

Now the KS equation can be described as

$$\hat{H}_{KS}\phi_i = \epsilon_i \phi_i \quad (3.17)$$

where the single particle wave functions $\phi_i$ fulfils $\sum_{i=1} \phi_i^* \phi_i = \rho$ and $\epsilon_i$ is orbital energy of the $i^{th}$ particle. KS equation simply needs the solution of single-particle Schrödinger equations to find the ground-state density $n(r)$ for non-interacting system.[15]

However, the crucial quantity i exchange correlation energy $E_{XC}[n]$ is still unknown in KS method. Since there is no way to know the exact exchange correlation, approximate exchange correlation functionals were used, such as local density approximation (LDA),[16] generalized gradient approximation (GGA)[17] and hybrid functionals.

In LDA, the exchange correlation energy is compared to homogeneous electron gas, [16]

$$E_{xc}^{LDA}[\rho] = \int \rho(\vec{r})\, \epsilon_{xc}^{hom}(\rho(\vec{r})) d^3(\vec{r}) \quad (3.18)$$

where $\epsilon_{xc}^{hom}(\rho(\vec{r}))$ is the exchange-correlation energy density. The many-electron system is divided into infinitesimally small regions located at positions $r$, each containing a homogeneous interacting electron gas with a constant local density $\rho$.

The LDA fails in system where there is a rapid variation in the electron density, such as surfaces and strongly correlated electron systems. The well-known example is the underestimation of bandgap in semiconductors and insulators.[10] To overcome this deficiency, other approximation methods have been proposed, in which the most widely used is GGA, where the exchange-correlation functional depends on both electron density and its gradient $|\nabla\rho(\vec{r})|$[17]:

$$E_{xc}^{GGA}[\rho(\vec{r})] = \int \rho(\vec{r})\, \epsilon_{xc}(\rho(\vec{r}), \nabla\rho(\vec{r}))d^3(\vec{r}) \quad (3.19)$$

The KS equations can be solved numerically through self-consistent iterations. The typical steps to solve KS equations follow the steps[9, 10]:

1, Start with a density, For the 1st iteration, superposition of atomic densities is usually taken;

2, Establish grid for charge density and exchange correlation potential;

3, Compute KS matrix;

4, Solve the equations for expansion coefficients to obtain KS orbits.

5, Calculate new density $\rho = \sum_{i=occ} |\phi_i(\mathbf{r})|^2$

6, If density or energy changed substantially, go to step 1.

7, If SCF cycle converged and geometry optimization is not requested, go to step 10.

8, Calculate derivatives of energy *vs.* atom coordinates, and update atom coordinates;

9, If gradients are still large, or positions of nuclei moved appreciably, go to step 1,

10, Calculate ground state properties and analyse the results.

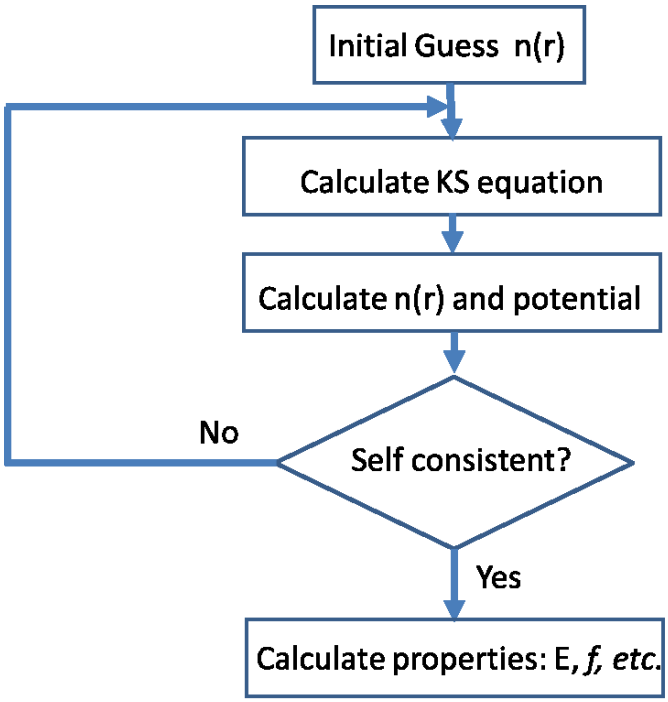


**Figure 3.9** A flow chart of the iteration scheme to solve KS equation.[9, 10]

In this thesis, Calculations of energies and electronic structures were performed using the Vienna *ab initio* simulation package (VASP) within the framework of DFT. The projector augmented wave (PAW) method was employed for electron-ion interactions, and the GGA from Perdew *et al.* (PW91) was used to describe the exchange-correlation functional.[16]

## 3.5 References


1. http://129.89.58.197/mediawiki/index.php/Scanning_Electron_Microscopy(SEM).
2. http://cmrf.research.uiowa.edu/transmission-electron-microscopy.
3. http://www.microscopy.ethz.ch/TEMED.htm.
4. Muller, D. A. Structure and bonding at the atomic scale by scanning transmission electron microscopy. *Nat. Mater.* **2009**, 8, 263-270.
5. Bleloch, A.; Lupini, A. *Mater. Today* **2004**, 7, 42-48.
6. Bell, D. C.; Erdman, N. *Low voltage electron microscopy: principles and applications*. John Wiley & Sons, 2012.
7. http://www.ksanalytical.com/theory/.
8. Thomas, L. H. The calculation of atomic fields. *Math. Proc. Cambridge* **1927,** 23, 542-548.

9. Kohn, W.; Sham, L. J. Self-consistent equations including exchange and correlation effects. *Phys. Rev.* **1965,** 140, A1133-A1138.
10. K. C. Santosh. First-principles study of novel interfaces for electronic devices and energy storage applications. Doctor of Philosophy Thesis, The University of Texas at Dallas (2014).
11. Eschrig. H. *The Fundamentals of Density Functional Theory*. Vieweg+Teubner Verlag | Springer, 1996.
12. Born, M.; Oppenheimer, R. Zur quantentheorie der molekeln. *Ann Phys-berlin **1927,*** 389, 457-484.
13. Dirac, P. A. M. Note on Exchange phenomena in the Thomas atom. *Math Proc Cambridge **1930,*** 26, 376-385.
14. Hohenberg, P.; Kohn, W. Inhomogeneous electron gas. *Physical Review **1964,*** 136, B864-B871.
15. Hartree. D. R. The wave mechanics of an atom with a non-coulomb central field. part II. some results and discussion. *Math. Proc. Cambridge* **1928,** 01, 111-132.
16. Perdew, J. P.; Zunger, A. Self-interaction correction to density-functional approximations for many-electron systems. *Phys. Rev. B* **1981,** *23*, 5048-5079.
17. Perdew, J. P.; Burke, K.; Ernzerhof, M. Generalized gradient approximation made simple. *Phys. Rev. Lett.* 1996, 77, 3865-3868.

# 4

# Morphological Variation of $Bi_2Se_3$ Nanostructures by Catalyst-Nanostructure Interface Effect

## 4.1 Introduction

Au-catalyzed chemical vapor deposition (CVD) has become the most widely employed approach for growth of $Bi_2Se_3$ and $Bi_2Te_3$ nanostructures. However, their growth mechanism is still far from understanding. Here, we use $Bi_2Se_3$ as a case system to study the growth mechanism, and to understand the impact of catalyst-nanostructure interface on the growth directions of nanostructures. We have achieved the growth of 1D $Bi_2Se_3$ nanostructures with different growth directions using Au film as catalyst. $Bi_2Se_3$ nanostructures with various orientations, including $< 11\bar{2}0 >$ NRs, <0001> NWs and NR-NW junctions, were found to be induced by faceted Au catalysts via VSS mechanism. It has been found that a {0001} interface between the catalyst/nanostructure induces the growth of NWs. While when the interface is not sharp, NRs were induced. We further correlate the electrical properties with the growth directions of individual $Bi_2Se_3$ nanostructures by *in-situ* TEM, and a large conductivity anisotropy ratio (~250) was observed.

## 4.2 Journal Publication

These results in Chapter 4 are included as it appears in ***Journal of Physical Chemistry C,*** 2014, 118, 20620-20626.
http://pubs.acs.org/doi/abs/10.1021/jp505407j

**Anisotropic Electrical Properties from Vapor-Solid-Solid Grown $Bi_2Se_3$ Nanoribbons and Nanowires**

Yichao Zou,[†] Zhi-Gang Chen,[†] Yang Huang,[†] Lei Yang,[†] John Drennan,[‡] and Jin Zou[†, ‡]

[†]Materials Engineering and [‡]Centre for Microscopy and Microanalysis, The University of Queensland, Brisbane, QLD 4072, Australia

**Abstract**

High-quality $Bi_2Se_3$ nanoribbons and NWs were synthesized by a Au-catalyzed chemical vapor deposition method. Detailed structural and chemical characterizations show that the growth of both $Bi_2Se_3$ nanoribbons and NWs are governed by the vapor-solid-solid growth mechanism, in which the nanoribbons grow along <$11\bar{2}0$> and NWs grow along <0001> directions. *In-situ* scanning tunneling microscope-transmission electron microscopy electrical measurements show that the nanoribbons are much more conductive than the NWs with a conductivity anisotropy ratio of ~2.5 x$10^2$ at room temperature.

**Key words:** Bismuth Selenide, Topological Insulators, NWs, Chemical Vapor Deposition, *In-situ* TEM, Thermoelectrics

## Introduction

As an ideal candidate for applications in thermoelectrics and topological insulators, $Bi_2Se_3$ has been a globally focused material system, from which various unique physical phenomena, such as quantum anomalous Hall effect, superconductivity and topological magnetoelectric effect, have been observed.[1-8] For the bulk topological insulators, the direct observation and manipulation of their metallic edge/surface states are relatively difficult due to the significant outnumbering of the bulk carriers.[9-11] The 1D topological insulator nanostructures, on the other hand, have become an excellent alternative system for understanding the metallic surface properties because of the enhanced surface-to-volume ratio.[10, 12-19] For example, single-crystalline $Bi_2Se_3$ NRs show unambiguous transport properties through the periodic quantum interference effect.[18] Therefore, engineering $Bi_2Se_3$ at the nanoscale is exciting for developing topological insulators for future spintronic applications.

From the structural point of view, a rhombohedral layered structured $Bi_2Se_3$ has a strongly covalent bonding within the quintuple layers and a weak van der Waals bonding between the quintuple layers.[20] Such a strong structural anisotropy is expected to result in a strong electrical anisotropy, which may be enhanced when the sample size is reduced to nanoscale.[21] For example, hexagonal layer-structured $In_2Se_3$ NWs (NWs) also have such anisotropic structural feature, and have shown much stronger anisotropy ratio in electrical properties that from their bulk materials (10~$10^3$ times).[21] Therefore, it is desirable to investigate the electrical anisotropy in 1D $Bi_2Se_3$ nanostructures with different growth directions, and hence a desire for their growth.

Metal-catalyzed chemical vapor deposition (CVD) is a common method for growing 1D $Bi_2Se_3$ nanostructures, by which the growth of $Bi_2Se_3$ nanostructures was generally believed to be governed by the vapour-liquid-solid (VLS) mechanism,[1, 9, 16, 18, 22] although it needs demonstration for the possibility of the vapour-solid-solid (VSS) growth mechanism, which has been also constantly found in other metal-catalysed 1D nanostructures.[23-27] Growth of $Bi_2Se_3$ nanostructures with different morphologies, including NRs and NWs,[9-10, 16, 18, 28] was realized by CVD. However, achieving high-quality $Bi_2Se_3$ nanostructures with different growth directions remains challenging and requires further investigations to understand the fundamental growth mechanism.

In this study, we have achieved the growth of 1D $Bi_2Se_3$ nanostructures with different growth directions using Au film as catalyst. $Bi_2Se_3$ nanostructures with various orientations, including < $11\bar{2}0$ > NRs, <0001> NWs and NR-NW junctions, were induced by faceted Au catalysts, which were proposed to be grown via the VSS mechanism. The physical reasons of this observation have been discussed. We further correlate the electrical properties with the growth directions of individual $Bi_2Se_3$ nanostructures, and a large conductivity anisotropy ratio (~250) was observed.

**Experimental**

*Material Synthesis.* The $Bi_2Se_3$ nanostructures were grown in a horizontal tube furnace under atmospheric pressure. $SiO_2$/Si (001) substrates were firstly cleaned by acetone and distilled water and then dried with high-purity $N_2$ gas. Prior to the nanostructure growth, the substrates were coated with a thin Au film (~9 nm thickness) using the SPI Module sputtering coater. The $Bi_2Se_3$ powders (99.999 %, 0.2 g per growth from Sigma Aldrich) were placed in the hot centre of the furnace while the Au-coated substrates were placed in the downstream of the tube at a distance ranging from 9-12 cm away from the central furnace, as schematically shown in Figure 1a. The alumina tube was firstly flushed with Ar gas to minimize the oxygen contamination, and then was heated to 700 $^{o}$C with a heating rate of 8 $^{o}C \cdot min^{-1}$ and kept at this temperature for 1.5 h under the mixed carrier gas of Ar (100 $sccm \cdot min^{-1}$) and $H_2$ (40 $sccm \cdot min^{-1}$), followed by cooling-down naturally. When the furnace center was heated to 700 $^{o}$C, the temperature distribution along the downstream were measured by an external thermocouple, in which the substrate temperature for collecting samples are found to be varied from 490 to 580 $^{o}$C (defined as the growth temperature - $T_{growth}$), as schematically illustrated in Fig.1a.

*Material Characterizations.* The morphological, structural and chemical characteristics of as-grown products were investigated by scanning electron microscopy (SEM, JEOL JEM 7800, operated at 15 kV) and transmission electron microscopy (TEM, Philips Tecnai F20 and F30, operated at 200 kV) equipped with energy-dispersive X-ray spectroscopy (EDS) for compositional analysis.

*Electrical Measurements.* Electrical measurements of individual nanostructures were performed using a Nanofactory *in-situ* scanning tunneling microscope (STM)-TEM

electrical probing system inside the F20 TEM. Individual nanostructures for electrical measurements were prepared by scratching the surface of the sample substrates with home-made Cu grids. As illustrated in Figure 1b, during the electrical measurement, the Cu grid acts as the top electrode and the bottom electrode is a W tip that is movable via the control of a piezo tube.

**Results and discussion**

Figure 2a shows a typical overview SEM image of the products grown on the substrate and shows many 1D nanostructures. Detailed SEM characterization suggests that the majority of these nanostructures are NRs with lengths of several tens of μm. Figure 2b shows a side-view SEM image of a typical NR, in which a faceted catalyst can be observed at the NR tip (refer to its inset). Figure 2c shows a SEM image taken from the bottom section of a typical NR, indicating that the NRs grow from the nanoplates stacked on the substrate. Apart from NRs, NWs were also found and an example is shown in Fig. 2d. As can be seen, the NW is relatively short with rough sidewalls. Figure 2e is an enlarged SEM image to show details of the NW tip, in which the faceted catalyst can be observed. In addition, NW-NR junctions were occasionally observed, as shown in Fig. 2f.

To understand the detailed structural and chemical characteristics of the as-grown NRs and NWs, TEM was employed. Figures 3a and 3e are bright-field (BF) TEM images of a typical NR and a typical NW. Figures 3b and 3f are their corresponding EDS spectra taken from both the catalysts and nanostructures. EDS results indicate that the NR and the NW have identical chemical composition with a Bi:Se atomic ratio of 2:3 and the catalysts are pure Au (the Cu peaks shown in the EDS spectra are due to the Cu grids). Selected area electron diffraction (SAED) patterns and high-resolution TEM (HRTEM) were used to evaluate the structures of the NR and the NW. Their corresponding results are shown in Fig. 3c-d and Fig. 3g-h, from which, the structures of the NR and NW are confirmed to be rhombohedral $Bi_2Se_3$ phase with $a$ = 4.1 Å and $c$ = 28.6 Å (fitted well with JCPDS file no. 33-0214). As can be seen in Fig. 3c, a set of weak diffraction patterns can be observed, which is faint kinematically forbidden $\{10\bar{1}0\}$ in the zero Laue zone but can be constantly observed in rhombohedral nanostructured samples.[9,16, 29] The appearance of such spots may be resulted from (1) the projection of the diffractions from higher Laue zone caused

by the intrinsic large *c*-axis lattice parameter in rhombohedral $Bi_2Se_3$ with the thin feature (<50nm) of the NR along *c*-axis;[30] (2) the antisite defects in the NR.[31] By carefully correlating the SAED patterns and corresponding TEM images, the axial direction of the NRs can be determined as < $11\bar{2}0$> while the NW has the axial direction of <0001> with few stacking faults (refer to Fig. 3h).

Figure 4a presents a typical BF TEM image taken from a NR-NW junction where the electron beam is perpendicular the axial directions of the NR section and the NW section. The corresponding SAED pattern (inset of Fig. 4a) shows that the NW section grows along the <0001> direction while the NR section grows along the < $11\bar{2}0$ > direction, similar to those individual NRs and NWs. Figure 4b shows an HRTEM image taken from the NW section, confirming that the axial direction of the NW section is along <0001>. Figure 4c shows a HRTEM image taken from the NW/catalyst interface and shows a sharp {0001} NW/catalyst interface. Figure 4d is a BF TEM image taken from the NR-NW junction and inset is the corresponding HRTEM image, showing a sharp {0001} junction. Interestingly, during the electron beam irradiation, the NW section was cleaved along the {0001} plane (possibly due to the weak van der Waals bonding between the quintuple layers), from which a hexagonal cross-section can be seen (refer to Fig. 4e). By correlating the TEM view direction and the cleaved morphology, the side facets of the NW section can be determined as $\{1\bar{1}00\}$, and the atomic structure of the NW can be schematically illustrated, as shown in Fig. 4f.

To understand the growth mechanism of our 1D $Bi_2Se_3$ nanostructures, we note that the post-growth catalysts for both NRs and NWs are faceted, suggesting that the catalysts were in solid form during the 1D nanostructure growth.[26, 32] Accordingly, the growth of our 1D $Bi_2Se_3$ nanostructures should be governed by the VSS mechanism. To understand whether the Bi and Se atoms in vapor can form a liquid alloy with Au particles (formed after the thin Au film being broken due to the heating[26]), we investigate the possible eutectic reactions in the Au-Se and Au-Bi phase diagrams. Based on the Au-Se phase diagram, we found that the eutectic point in Au-Se is ~755 $^{o}$C ($T_{eu\ (Au\text{-}Se)}$), which is much higher than the $T_{growth}$, suggesting that such eutectic reaction is unlikely to happen in our growth temperature.[33] In the Au-Bi case, there is an eutectic point at 241 $^{o}$C ($T_{eu(Au2Bi\text{-}Bi)}$), which is 200 $^{o}$C lower than $T_{growth}$. [33] To investigate whether such a eutectic reaction can happen in our growth

environment, we correlated the Au-Bi binary phase diagram (refer to Fig. 5a) with our experimental results. As can be seen in Figure 5a, the $Au_2Bi$-Bi eutectic reaction requires the Bi concentration to be as high as 86.8 atom% in Au solid, which is impossible for Au particles with sizes of ~300 nm to absorb sufficient Bi to reach such a eutectic point.[31,33] As a consequence, we consider the possibility that Au formed a liquid alloy with Bi is unlikely during the nanostructure growth. From the above discussion, the catalysts should be in the solid form during the growth of the $Bi_2Se_3$ nanostructures. Therefore, the Au-induced 1D $Bi_2Se_3$ nanostructures should be governed by the VSS growth.

To understand how the Au particles absorb and collect the vapour species during the VSS growth of 1D $Bi_2Se_3$ nanostructures, we examined the solubility of Bi and Se in Au. From Au-Se and Au-Bi phase diagrams, Se is not soluble in solid Au,[33] while Bi can form a solid solution with Au in a solubility range of 0~0.06% under the temperature of 500-1064 $^{o}$C, as shown in the inset of Fig. 5a.[34] Therefore, under our $T_{growth}$ (490-580 $^{o}$C), a small amount of Bi can be penetrated into the Au particles by solid diffusion mechanism.[35-36] After growth, Bi is not soluble in Au at room temperature and will be expelled entirely from the Au catalyst, which is in consistence with our post-growth catalyst composition (only Au can be detected in the catalyst, as shown in Fig. 3b and 3f). Regarding how the Se reaction during the growth of the nanostructures, we note that the growth of III-IV semiconductor NWs only needs the penetration of single component into the catalyst, and the other component can react with the penetrated one to form the compound at the energy-favorable catalyst-nuclei interfaces.[35,37] Therefore, Se vapor may react with Bi to induce the growth of $Bi_2Se_3$ compound at the catalyst/nanostructure interface, as illustrated in Fig. 5b.[35-36, 38]

To understand the growth difference of NRs and NWs, as well as NR-NW junctions, we note that the interfaces between catalyst and these nanostructures are significant different according to our extensive SEM and TEM investigations. In the case of NWs and NR-NW junctions, NW sections and the catalysts always have the {0001} interfaces (refer to Fig. 3h and 4c), while the NRs and their catalysts always have multi-faceted interfaces. Taking these experimental results and the VSS growth mechanism into accounts, the solid-form catalysts makes it difficult to form specific interfaces with their underlying nuclei,[26] and the variety in the nuclei/catalyst

interfaces can induce nanostructures with different morphologies.[26, 39] Thus, we propose that when the catalyst/nuclei interfaces are not {0001} interfaces, NRs will be induced by the catalysts,[39] while if the catalyst/nuclei interfaces are {0001} interfaces, both NRs and NWs can be induced and the NR-NW junctions are very likely to be formed from the formal case (NRs that have {0001} NR/catalyst interfaces), as shown in Fig. 5b.

Since a strong anisotropy in transport properties is expected in the rhombohedral structured $Bi_2Se_3$ nanostructures due to their nature of layered structure, we accordingly measured the conductivities of our NRs and NWs using the STM-TEM electrical probing system. Figure 6a shows a BF TEM image with an inset SAED showing a typical $< 11\bar{2}0 >$ NR connected by two electrodes. Corresponding measured *I-V* curve is shown in Figure 6b. Figure 6c shows a BF TEM image with an inset SAED pattern of a typical <0001> NW. Figure 6d shows the corresponding *I-V* curve from the NW. In Fig. 6b and 6d, both *I-V* curves are linear, indicating that the contacts between the electrodes and the nanostructures are ohmic-type contacts. The contact area between the electrodes and the nanostructures was found to have very little effect on the resistance measurement results (Fig. S1), which means we can use the two-terminal resistance to estimate the intrinsic nanostructure conductivity. The resistances (*R*) of the NR and the NW can be calculated as 0.167 MΩ and 12.50 MΩ, respectively. To calculate the electrical conductivity (*C*), we use $C = l / (R \cdot A)$,[21] where *l* is the length of the wire and *A* is the cross-sectional area. Given that the NR has a length of 3.0 μm and a quasi-rectangular cross section with a width of 304 nm and a thickness of ~30 nm (estimated by the statistical thickness to width ratio ~1:10), and the NW has a length of 1.2 μm and a quasi-hexagonal cross section with a diagonal length of 140 nm, the conductivities of the NR and NW can be calculated as ~19.44 $S \cdot cm^{-1}$ and ~0.078 $S \cdot cm^{-1}$. The electrical conductivity of the $<11\bar{2}0>$ NR is about $2.5 \times 10^2$ times higher than that of the <0001> NW. The anisotropic value is much higher than that of the $Bi_2Se_3$ bulk single crystal (up to ~40).[40] Based on the measurements of different NW and NR samples, we obtained an anisotropic ratio value large than 250 (refer to Fig. S2 and Table S1). We found that the conductivities of our NRs are marginally comparable to the reported conductivity values of undoped $Bi_2Se_3$,[41-42] while the conductivities of our NWs are much lower (>2 orders of magnitude) than that from the single crystal measured

along the [0001] direction.[40] From the native structural characteristics of $Bi_2Se_3$ crystal, the weak van der Waals bonding interaction between the layers along <0001> directions can cause structural defects such as stacking faults more easily (refer to Fig. 3h),[21] while strong covalent bonding within the layer along <$11\bar{2}0$> is free of defects, which increases the conductivity anisotropy in our 1D $Bi_2Se_3$ nanostructures. Since many physical properties of $Bi_2Se_3$ are directly related to their transport properties, we expect that the large electrical anisotropy in our 1D $Bi_2Se_3$ nanostructures with different growth directions must bring more possibilities for their practical applications.

**Conclusion**

We have fabricated high-quality $Bi_2Se_3$ NRs and NWs by a CVD method using Au thin film as catalyst. Through detailed structural and chemical characterizations using electron microscopy, we found that the growth of both $Bi_2Se_3$ <$11\bar{2}0$> NRs and <0001> NWs are governed by the VSS growth mechanism. From detailed *in-situ* STM-TEM electrical measurements, the correlation of transport properties with the growth directions of 1D $Bi_2Se_3$ NRs and NWs was built, which shows that <$11\bar{2}0$> NRs have a much higher electrical conductivity than <0001> NWs. The large conductivity anisotropy (with a ratio of ~ $2.5x10^2$) in nano-form 1D $Bi_2Se_3$ will allow for new opportunities in many $Bi_2Se_3$-based advanced device applications.

**Figure Captions**

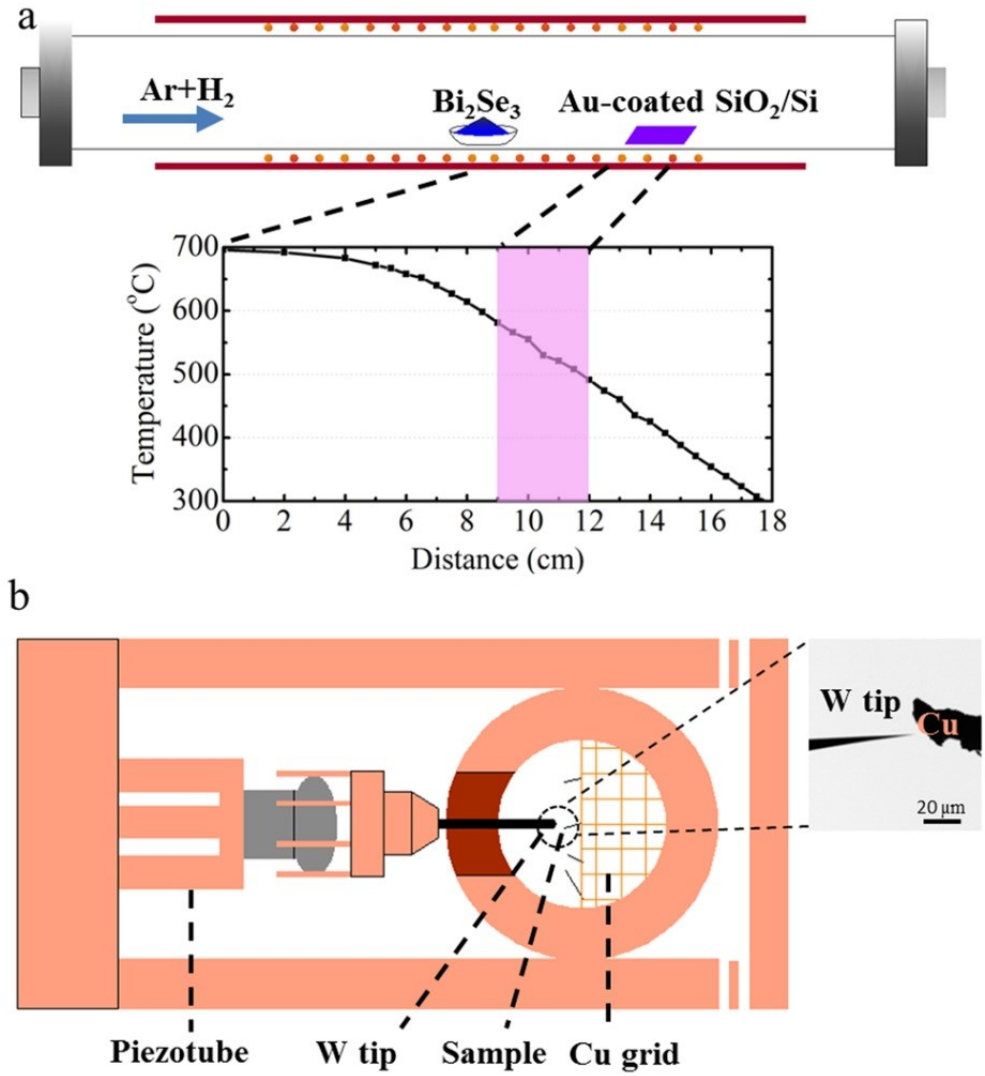


**Figure 1. (**a) Schematics of the tube furnace for growing $Bi_2Se_3$ nanostructures (upper panel) and the temperature as a function of position (lower panel). (b) Schematics of the *in-situ* STM-TEM electrical probing system, with the inset of a TEM image showing the W tip, and the Cu grid for electrically connecting the sample.

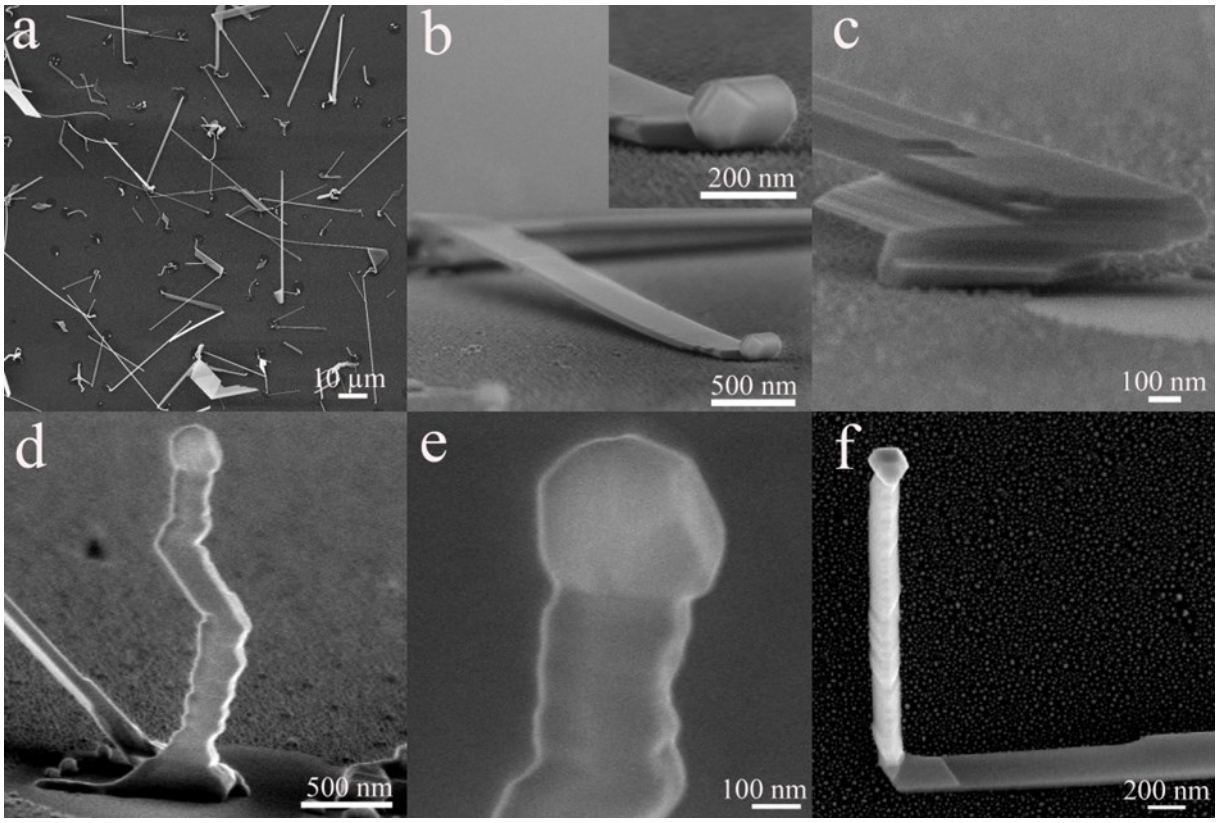


**Figure 2.** SEM images of the nanostructures grown on substrate. (a) Plain-view image of the as-grown products. (b) Side-view image of a typical NR with an inset showing the NR tip with a faceted catalyst particle. (c) Side-view image showing the bottom of a NR. (d) Side-view image of a short NW. (e) High-magnified side-view image of the NW tip with a faceted catalyst. (f) Side-view image of a NW-NR junction.

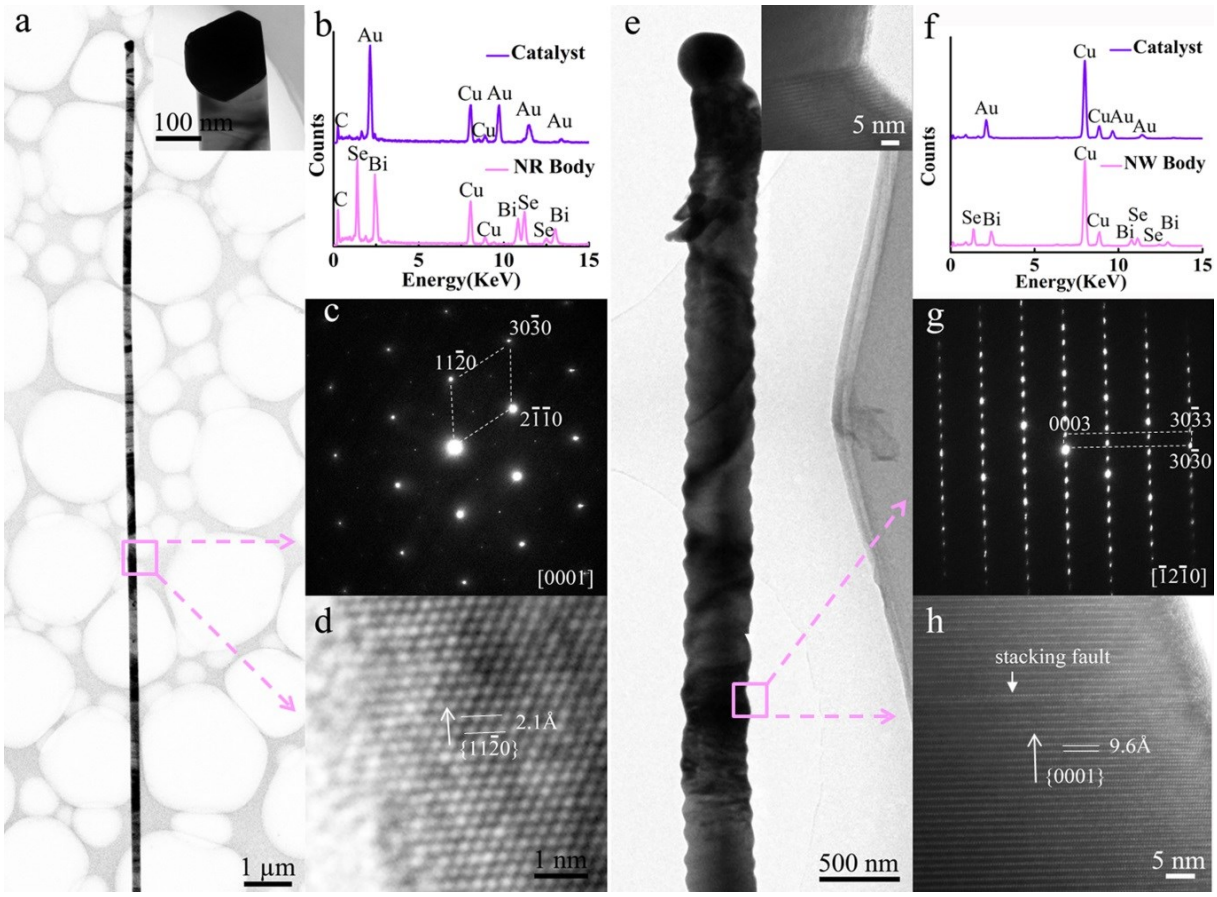


**Figure 3.** TEM characterization results of a NR and a NW. (a) BF image of a NR with an inset showing the catalyst tip. (b) EDS spectra taken at the catalyst and body of the NR. (c) Corresponding SAED pattern taken along [0001] zone axes from the area indicated by the square in a). (d) The corresponding HRTEM image. (e) BF image of a NW with an inset of HRTEM image showing a sharp {0001} catalyst/NW interface. (f) EDS spectra taken at the catalyst and the body of the NW. (g) Corresponding SAED pattern taken along $[\bar{1}2\bar{1}0]$ zone axis from the area indicated by the square in (e). (h) Corresponding HRTEM image of the NW section showing a stacking fault.

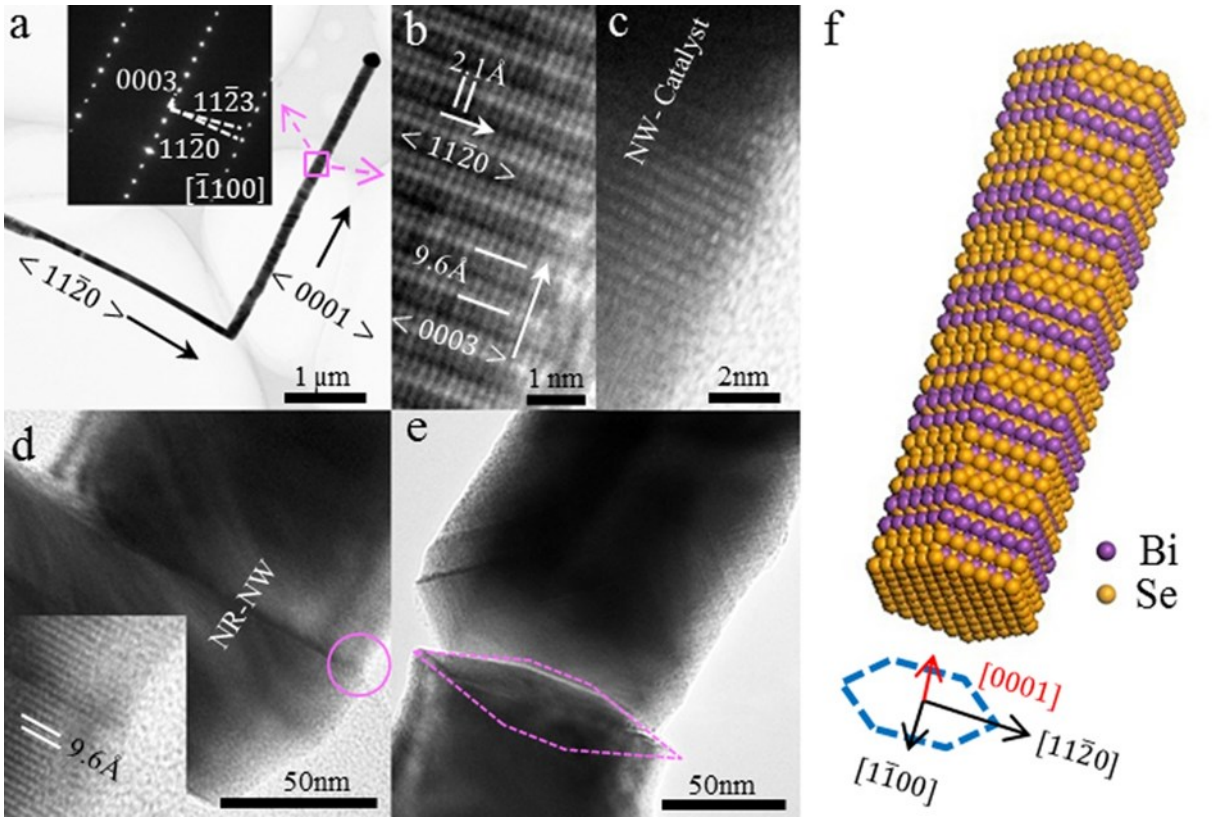


**Figure 4.** TEM images and the atomic model of a NR-NW junction. (a) BF image with the inset of SAED pattern taken along $[\bar{1}100]$ zone axis from the area indicated by the square. (b) Corresponding HRTEM image from the NW section. (c) Corresponding HRTEM image from the catalyst-NW interface. (d) BF image showing the NR-NW interface with an inset of the HRTEM image. (e) BF image taken along $[\bar{1}100]$ zone axis from the cleaved area of the NW. (f) An atomic model of a NW section, the black vectors are within the *a-b* plane while the red vectors are along the *c*-axis.

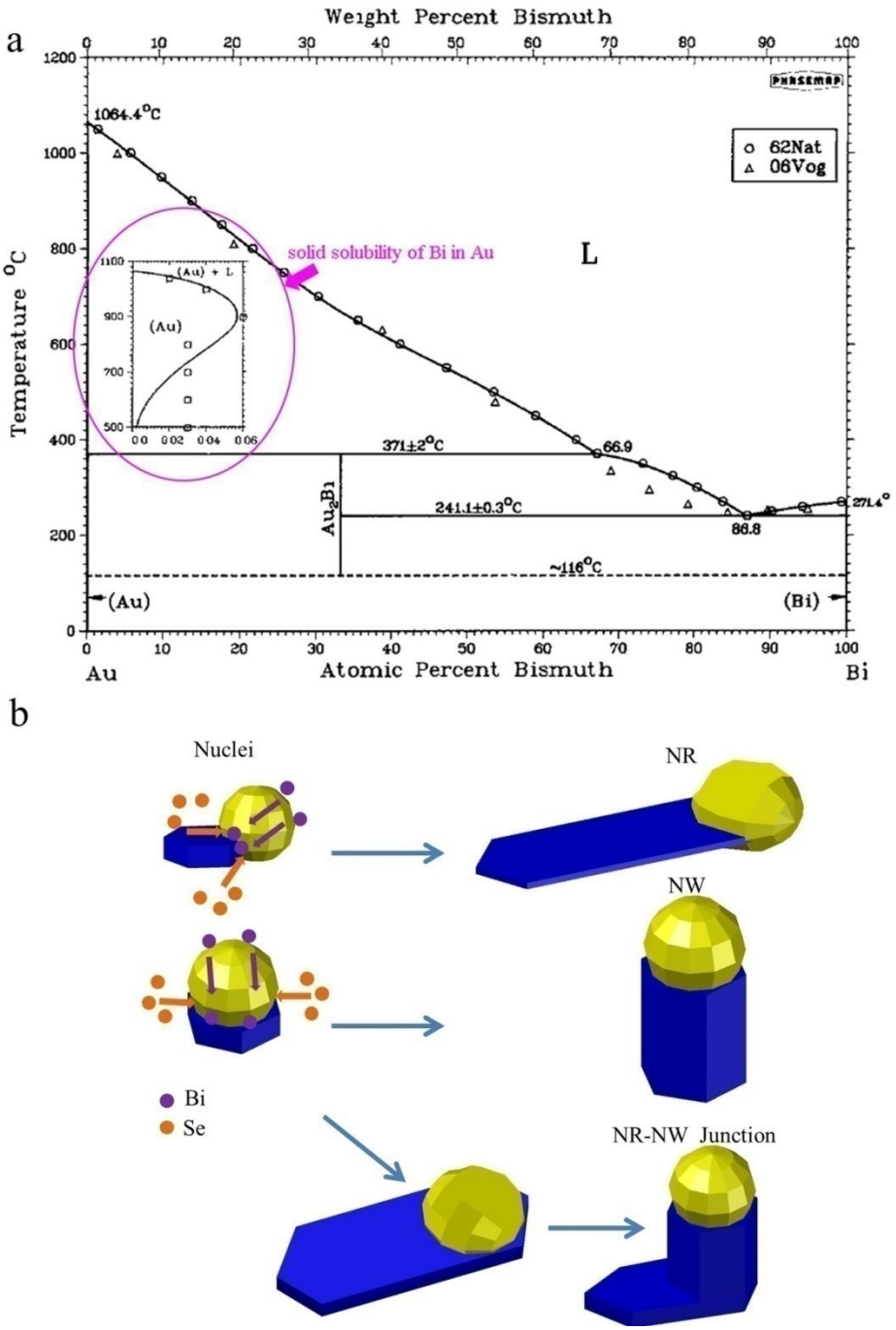


**Figure 5 (**a) Au-Bi binary phase diagram, with an inset to illustrate the solid solubility of the Bi in Au.[34] (b) Proposed growth models for the $Bi_2Se_3$ nanostructures with different morphologies.

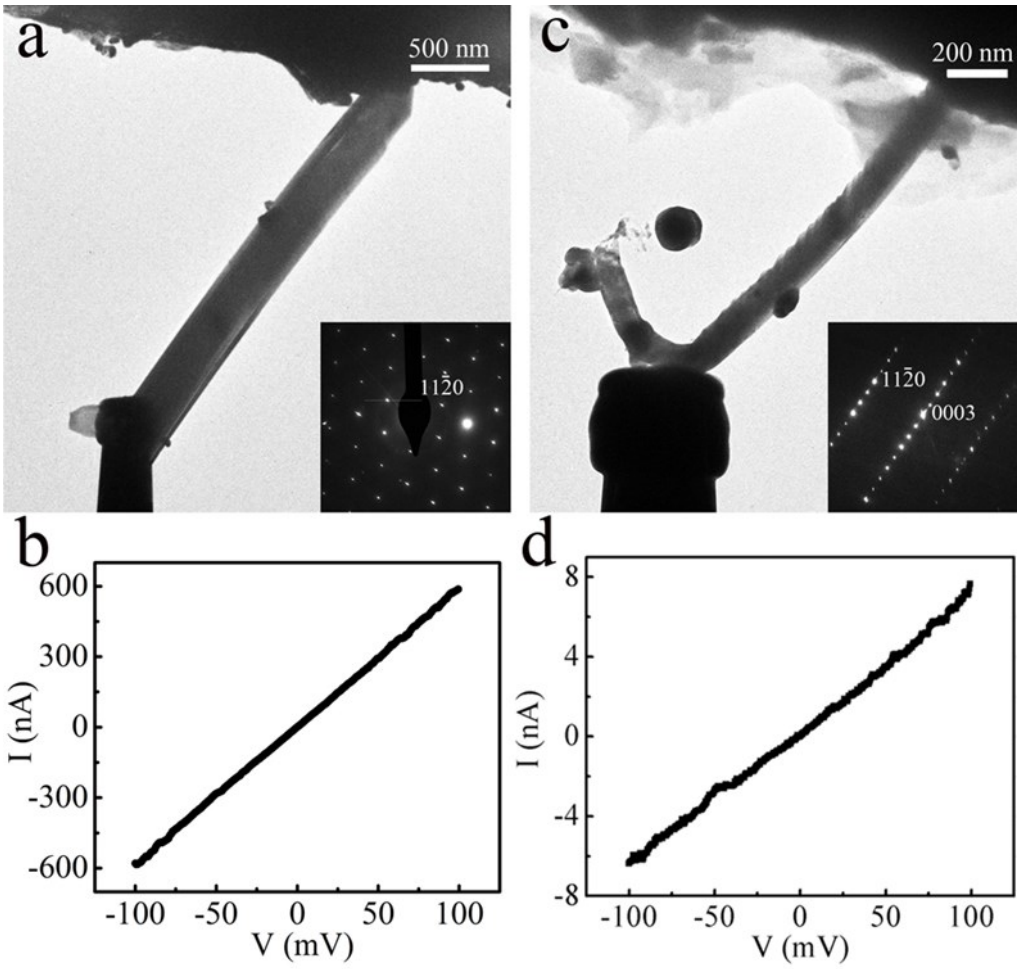


**Figure 6**. (a) A BF TEM image of a NR contacted by the electrodes with an inset of SAED. b) Two-probe *I-V* characteristics for the NR. (c) A BF TEM image of a NW contacted by the electrodes with a SAED inset. (d) Two-probe *I-V* characteristics for the NW.

**Supporting Information**

Figures S1a-c shows the variation of the contact area between the electrodes. Figure S1d shows the corresponding *I-V* measurement results. It can be seen that the *I-V* curves are not evidently changed when the contact area is varied.

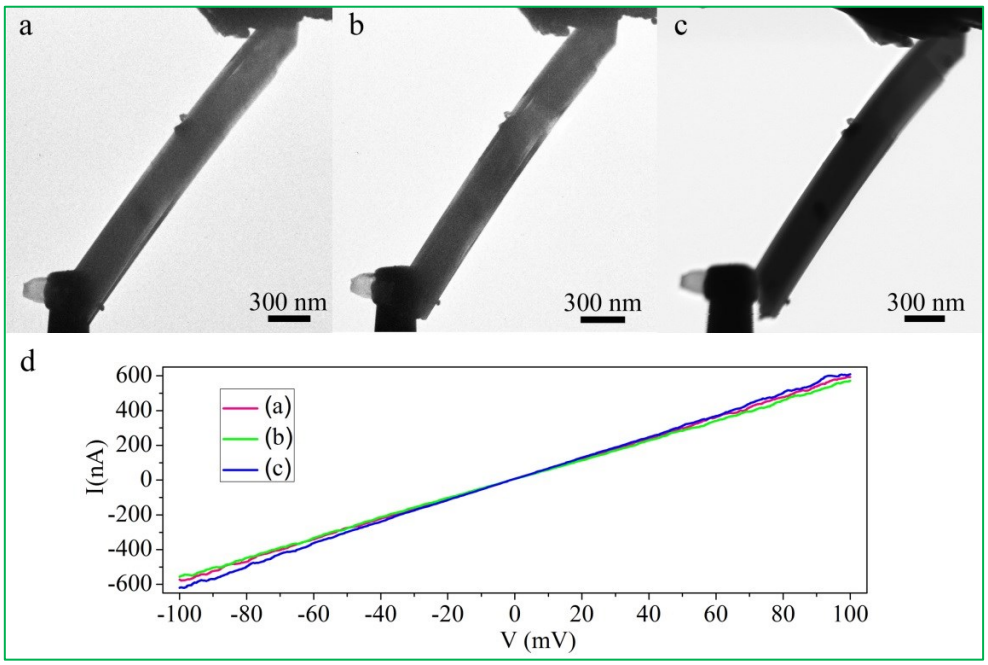


**Figure S1** Effects of the contact area between the W tip and the $Bi_2Se_3$ NR on its conductivity. (a-c) Variation in the contact area. (d) I-V curves corresponding to different contact areas.

Figure S2 shows the I-V curves from 6 samples, in which the NW#0 and NR# 0 are the samples presented in the main manuscript. The corresponding calculated geometrical features, resistances and electrical conductivities of these samples are presented in Table S1, which shows that the conductivity variation range is 19.74~44.00 $s \cdot cm^{-1}$ for the NRs and is 0.008~0.078 $s \cdot cm^{-1}$ for the NWs, resulting in an anisotropy ratio varying in a range of 250~5500.

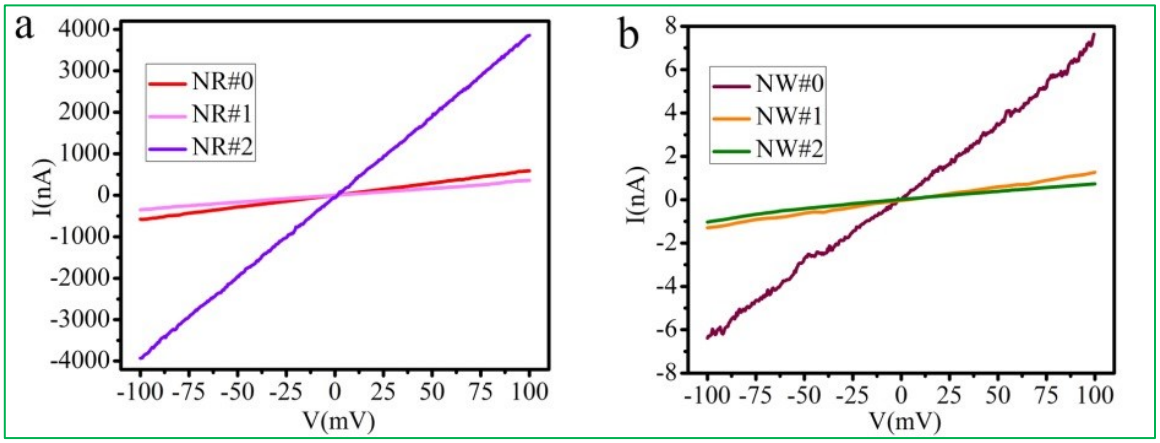


**Figure S2** (a) *I-V* curves obtained from the NR samples. (b) *I-V* curves obtained from the NW samples.

Table S1 Geometrical and electrical characterization results from the NR and NW samples.

| No. | Cross-Section Area($m^2$) | Channel Length (m) | R（MΩ） | C($s \cdot cm^{-1}$) |
|---|---|---|---|---|
| NW0 | $9.1 \times 10^{-15}$ | $3.0 \times 10^{-6}$ | 0.167 | 19.44 |
| NR1 | $4.0 \times 10^{-15}$ | $3.4 \times 10^{-6}$ | 0.277 | 30.07 |
| NR2 | $1.0 \times 10^{-14}$ | $1.1 \times 10^{-6}$ | 0.025 | 44.00 |
| NW0 | $1.7 \times 10^{-14}$ | $1.2 \times 10^{-6}$ | 12.5 | 0.078 |
| NW1 | $3.5 \times 10^{-14}$ | $6.5 \times 10^{-6}$ | 76.9 | 0.024 |
| NW2 | $5.4 \times 10^{-14}$ | $4.2 \times 10^{-6}$ | 97.0 | 0.008 |

**References**


1. Kong, D.; Cui, Y. Opportunities in chemistry and materials science for topological insulators and their nanostructures. *Nat. Chem.* **2011**, *3*, 845-849.
2. Yu, R.; Zhang, W.; Zhang, H.; Zhang, S.; Dai, X.; Fang, Z. Quantized anomalous Hall effect in magnetic topological insulators. *Science* **2010**, *329*, 61-64.
3. Wang, M.-X.; Liu, C.; Xu, J.-P.; Yang, F.; Miao, L.; Yao, M.-Y.; Gao, C. L.; Shen, C.; Ma, X.; Chen, X., et al. The coexistence of superconductivity and topological order in the $Bi_2Se_3$ thin films. *Science* **2012**, *336*, 52-55.
4. Chen, Z. G.; Han, G.; Yang, L.; Cheng, L. N.; Zou, J. Nanostructured thermoelectric materials: current research and future challenge. *Prog. Nat. Sci.* **2012**, *22*, 535-549.
5. Sun, Y.; Cheng, H.; Gao, S.; Liu, Q.; Sun, Z.; Xiao, C.; Wu, C.; Wei, S.; Xie, Y. Atomically thick bismuth selenide freestanding single layers achieving enhanced thermoelectric energy harvesting. *J. Am. Chem. Soc.* **2012**, *134*, 20294-20297.
6. Zhang, H.; Liu, C.-X.; Qi, X.-L.; Dai, X.; Fang, Z.; Zhang, S.-C. Topological insulators in $Bi_2Se_3$, $Bi_2Te_3$ and $Sb_2Te_3$ with a single Dirac cone on the surface. *Nat. Phys.* **2009**, *5*, 438-442.
7. Liu, Y.; Li, Y. Y.; Rajput, S.; Gilks, D.; Lari, L.; Galindo, P. L.; Weinert, M.; Lazarov, V. K.; Li, L. Tuning Dirac states by strain in the topological insulator $Bi_2Se_3$. *Nat. Phys.* **2014**, *10*, 294-299.
8. Zhang, J.; Chang, C.-Z.; Tang, P.; Zhang, Z.; Feng, X.; Li, K.; Wang, L.-l.; Chen, X.; Liu, C.; Duan, W., et al. Topology-driven magnetic quantum phase transition in topological insulators. *Science* **2013**, *339*, 1582-1586.
9. Kong, D. S.; Randel, J. C.; Peng, H. L.; Cha, J. J.; Meister, S.; Lai, K. J.; Chen, Y. L.; Shen, Z. X.; Manoharan, H. C.; Cui, Y. Topological insulator NWs and nanoribbons. *Nano Lett.* **2010**, *10*, 329-333.
10. Hong, S. S.; Zhang, Y.; Cha, J. J.; Qi, X. L.; Cui, Y. One-dimensional helical transport in topological insulator NW interferometers. *Nano Lett.* **2014**, *14*, 2815-2821.
11. Peng, H.; Lai, K.; Kong, D.; Meister, S.; Chen, Y.; Qi, X.-L.; Zhang, S.-C.; Shen, Z.-X.; Cui, Y. Aharonov-Bohm interference in topological insulator nanoribbons. *Nat. Mater.* **2010**, *9*, 225-229.

12. Safdar, M.; Wang, Q.; Mirza, M.; Wang, Z.; Xu, K.; He, J., Topological surface transport properties of single-crystalline SnTe NW. *Nano Lett.* **2013**, *13*, 5344-5349.
13. Safdar, M.; Wang, Q.; Mirza, M.; Wang, Z.; He, J. Crystal shape engineering of topological crystalline insulator SnTe microcrystals and NWs with huge thermal activation energy gap. *Cryst. Growth & Des.* **2014**, *14*, 2502-2509.
14. Cha, J. J.; Koski, K. J.; Cui, Y. Topological insulator nanostructures. *Phys. Status Solidi RRL* **2013**, *7*, 15-25.
15. Fang, L.; Jia, Y.; Miller, D. J.; Latimer, M. L.; Xiao, Z. L.; Welp, U.; Crabtree, G. W.; Kwok, W. K. Catalyst-free growth of millimeter-long topological insulator $Bi_2Se_3$ nanoribbons and the observation of the π-Berry phase. *Nano Lett.* **2012**, *12*, 6164-6169.
16. Cha, J. J.; Williams, J. R.; Kong, D.; Meister, S.; Peng, H.; Bestwick, A. J.; Gallagher, P.; Goldhaber-Gordon, D.; Cui, Y. Magnetic doping and Kondo effect in $Bi_2Se_3$ nanoribbons. *Nano Lett.* **2010**, *10*, 1076-1081.
17. Li, Z.; Shao, S.; Li, N.; McCall, K.; Wang, J.; Zhang, S. X. Single crystalline nanostructures of topological crystalline insulator SnTe with distinct facets and morphologies. *Nano Lett.* **2013**, *13*, 5443-5448.
18. Tang, H.; Liang, D.; Qiu, R. L. J.; Gao, X. P. A. Two-dimensional transport-induced linear magneto-resistance in topological insulator $Bi_2Se_3$ nanoribbons. *ACS Nano* **2011**, *5*, 7510-7516.
19. Xiu, F.; He, L.; Wang, Y.; Cheng, L.; Chang, L.-T.; Lang, M.; Huang, G.; Kou, X.; Zhou, Y.; Jiang, X., et al. Manipulating surface states in topological insulator nanoribbons. *Nat. Nano.* **2011**, *6*, 216-221.
20. an, G.; Chen, Z.-G.; Ye, D.; Yang, L.; Wang, L.; Drennan, J.; Zou, J. In-doped $Bi_2Se_3$ hierarchical nanostructures as anode materials for Li-ion batteries. *J. Mater. Chem. A* **2014**, *2*, 7109-7116.
21. Peng, H.; Xie, C.; Schoen, D. T.; Cui, Y. Large anisotropy of electrical properties in layer-structured $In_2Se_3$ NWs. *Nano Lett.* **2008**, *8*, 1511-1516.
22. Lee, C. H.; He, R.; Wang, Z.; Qiu, R. L. J.; Kumar, A.; Delaney, C.; Beck, B.; Kidd, T. E.; Chancey, C. C.; Sankaran, R. M., et al. Metal-insulator transition in variably doped $(Bi_{1-x}Sb_x)_2Se_3$ nanosheets. *Nanoscale* **2013**, *5*, 4337-4343.

23. Hofmann, S.; Sharma, R.; Wirth, C. T.; Cervantes-Sodi, F.; Ducati, C.; Kasama, T.; Dunin-Borkowski, R. E.; Drucker, J.; Bennett, P.; Robertson, J. Ledge-flow-controlled catalyst interface dynamics during Si NW growth. *Nat. Mater.* **2008**, *7*, 372-375.
24. Kodambaka, S.; Tersoff, J.; Reuter, M. C.; Ross, F. M. Germanium NW growth below the eutectic temperature. *Science* **2007**, *316*, 729-732.
25. Dick, K. A.; Deppert, K.; Mårtensson, T.; Mandl, B.; Samuelson, L.; Seifert, W. Failure of the vapor-liquid-solid mechanism in Au-assisted MOVPE growth of InAs NWs. *Nano Lett.* **2005**, *5*, 761-764.
26. Xu, H.-Y.; Guo, Y.-N.; Liao, Z.-M.; Sun, W.; Gao, Q.; Hoe Tan, H.; Jagadish, C.; Zou, J. Catalyst size dependent growth of Pd-catalyzed one-dimensional InAs nanostructures. *Appl. Phys. Lett.* **2013**, *102*, 203108.
27. Wang, Y.; Schmidt, V.; Senz, S.; Gosele, U. Epitaxial growth of silicon NWs using an aluminium catalyst. *Nat. Nano.* **2006**, *1*, 186-189.
28. Kong, D.; Dang, W.; Cha, J. J.; Li, H.; Meister, S.; Peng, H.; Liu, Z.; Cui, Y. Few-layer nanoplates of $Bi_2Se_3$ and $Bi_2Te_3$ with highly tunable chemical potential. *Nano Lett.* **2010**, *10*, 2245-2250.
29. Mehta, R. J.; Zhang, Y.; Karthik, C.; Singh, B.; Siegel, R. W.; Borca-Tasciuc, T.; Ramanath, G. A new class of doped nanobulk high-figure-of-merit thermoelectrics by scalable bottom-up assembly. *Nat. Mater.* **2012**, *11*, 233-240.
30. Chen, Z.-G.; Yang, L.; Ma, S.; Cheng, L.; Han, G.; Zhang, Z.-d.; Zou, J. paramagnetic Cu-doped $Bi_2Te_3$ nanoplates. *Appl. Phys. Lett.* **2014**, *104*, 053105.
31. Okamoto, H., *Desk Handbook: Phase Diagrams for Binary Alloys*; ASM international: Materials Park, Ohio, 2000.
32. Wen, C.-Y.; Reuter, M. C.; Bruley, J.; Tersoff, J.; Kodambaka, S.; Stach, E. A.; Ross, F. M. Formation of compositionally abrupt axial heterojunctions in silicon-germanium NWs. *Science* **2009**, *326*, 1247-1250.
33. Prince, A.; Raynor, G. V.; Evans, D. S. Phase diagrams of ternary gold alloys. In *Handbook of Ternary Alloy Phase Diagrams*, The Institute of Metals: London, 1990; Vol. 4, pp 158-165.
34. Okamoto, H.; Massalski, T. B. The Au−Bi (Gold-Bismuth) system. *Bulletin of Alloy Phase Diagrams* **1983**, *4*, 401-407.

35. Persson, A. I.; Larsson, M. W.; Stenstrom, S.; Ohlsson, B. J.; Samuelson, L.; Wallenberg, L. R. Solid-phase diffusion mechanism for GaAs NW growth. *Nat. Mater.* **2004**, *3*, 677-681.
36. Helveg, S.; Lopez-Cartes, C.; Sehested, J.; Hansen, P. L.; Clausen, B. S.; Rostrup-Nielsen, J. R.; Abild-Pedersen, F.; Norskov, J. K. Atomic-scale imaging of carbon nanofibre Growth. *Nature* **2004**, *427*, 426-429.
37. Lin, P. A.; Liang, D.; Reeves, S.; Gao, X. P. A.; Sankaran, R. M. Shape-controlled Au particles for InAs NW growth. *Nano Lett.* **2011**, *12*, 315-320.
38. Liao, Z.-M.; Chen, Z.-G.; Lu, Z.-Y.; Xu, H.-Y.; Guo, Y.-N.; Sun, W.; Zhang, Z.; Yang, L.; Chen, P.-P.; Lu, W., et al. Au impact on GaAs epitaxial growth on GaAs (111)B substrates in molecular beam epitaxy. *Appl. Phys. Lett.* **2013**, *102*, 063106.
39. Fan, H. J.; Bodo, F.; Roland, S.; Cameliu, H.; Andreas, B.; Hartmut, L.; Armin, D.; Alois, K.; Silke, C.; Ulrich, G., et al. Vapour-transport-deposition growth of ZnO nanostructures: Switch between *c*-axial wires and *a*-axial belts by indium doping. *Nanotechnology* **2006**, *17*, S231.
40. Hashimoto, K. Galvanomagnetic effects in bismuth selenide $Bi_2Se_3$. *J. Phys. Soc. Jpn.* **1961**, *16*, 1970-1979.
41. Wang, Z.-Y.; Wei, P.; Shi, J. Tuning the fermi Level in $Bi_2Se_3$ bulk materials and transport devices. *Front. Phys.* **2012**, *7*, 160-164.
42. Lin, Y.-F.; Chang, H.-W.; Lu, S.-Y.; Liu, C. W. Preparation, characterization, and electrophysical properties of nanostructured $BiPO_4$ and $Bi_2Se_3$ derived from a structurally characterized, single-source precursor $Bi[Se_2P(OiPr)_2]_3$. *J. Phys. Chem. C* **2007**, *111*, 18538-18544.

# 5

# Morphological Control of SnTe Nanostructures by Catalyst Engineering

## 5.1 Introduction

Au-catalyzed chemical vapor deposition (CVD) has become the most widely employed approach for growth of SnTe nanostructures. However, growth mechanism is still far from well understanding, and the controllable growth technique reported is still limited. Therefore, in this work, we investigate into the detail growth mechanism of how Au induces the growth of SnTe nanostructures. We further demonstrate a morphological control of SnTe nanostructures using a facile chemical vapor deposition approach, in which Au containing catalysts with different Au concentrations were used to induce the nanostructure growth. Through electron-microscopy analysis, Au-Sn catalysts with different compositions were found to induce SnTe nanostructures with different morphologies.

## 5.2 Journal Publication

These results in Chapter 4 are included as it appears in ***Nano Research*****,** 2015, 8, 3011-3019.

http://link.springer.com/article/10.1007%2Fs12274-015-0806-y

**Morphological Control of SnTe Nanostructures by Tuning Catalyst Composition**

Yi-Chao Zou[1], Zhi-Gang Chen[1]*, Jing Lin[1], Xiaohao Zhou[2], Wei Lu[2], John Drennan[3], and Jin Zou[1,3]

[1]Materials Engineering, The University of Queensland, Brisbane, QLD 4072, Australia
[2]National Laboratory for Infrared Physics, Shanghai Institute of Technical Physics, Chinese Academy of Sciences, 500 Yu-Tian Road, Shanghai 200083, China
[3]Centre for Microscopy and Microanalysis, The University of Queensland, Brisbane, QLD 4072, Australia

**Abstract**

A method of controlling the morphology of SnTe nanostructures produced by a simple chemical vapor deposition is presented, in which Au-containing catalysts with different Au concentrations are used to induce specific growth behavior. Triangular SnTe nanoplates with a {100} dominated surface and {100}, {111} and {120} side facets were induced by AuSn catalysts, whereas <010> SnTe NWs with four nonpolar {100} side-facets were produced using $Au_5Sn$ catalysts. Through detailed structural and chemical characterization, coupled with surface energy calculations, it is found that NW growth is thermodynamically controlled via a vapor-solid-solid growth mechanism, whereas nanoplate growth is kinetically controlled via a vapor-liquid-solid growth mechanism. Therefore, this study provides a fundamental understanding of the catalyst's role in the growth of IV-VI compound nanostructures.

**Key words:** Tin Telluride, Chemical Vapor Deposition, Morphology, Catalyst Composition, Topological Insulator, Thermoelectrics

## Introduction

As a new type of topological insulators(TI), topological crystalline insulator (TCIs), SnTe owns exotic electronic properties, such as superconductivity,[1] and ferromagnetism,[2] which makes it as a promising candidate for applications in low-dissipation quantum computation,[3] and spintronics devices.[4,5] The direct observation and manipulation of the SnTe surface states remain challenging since the bulk carriers often mask the contribution from the surface carriers.[6] A major approach to reveal the surface states of SnTe is to reduce their size to nanoscale. To realize the growth of high-quality nanoscaled SnTe, Au-catalyzed chemical vapor deposition (CVD) has become the most widely employed approach.[5-8] However, the growth mechanism of the Au-catalyzed SnTe nanostructures is still far from clear, which deserve detailed understanding in order to effectively direct the controllable growth of SnTe nanostructures.

In contrast to the TIs that possess a single surface state, TCIs possess multiple surface states.[6] In SnTe, topological surface states exist on {100}, {110} and {111} surfaces, and each surface has its own unique topological surface states.[4] Therefore, the facet control of SnTe is crucial to secure the specific surface state.[6] Previous studies showed that SnTe nanostructures with different morphologies, such as NWs,[7] nanoplates,[6] and nanocubes,[6] can be obtained by CVD approach.[5-7] Variation of the growth temperature can be employed to obtain different products with varied morphologies, in which higher growth temperature facilitates {100} facet dominated SnTe nanostructures, while growth of {111} dominated SnTe is favored under a low growth temperature.[5-8] However, it is still far to realize the facet control in the growth of highly-uniform SnTe nanostructures.

Catalyst composition has been widely recognized as a key parameter to tailor the structures of semiconductor nanomaterials.[9-12] For examples, binary metallic catalysts with varied compositions, such as $Ni_xFe_{1-x}$ and $W_xCo_y$, can manipulate the chirality of carbon nanotubes.[13,14] On the other hand, Au-Ni catalysts, with Au-rich or Ni-rich composition, can result in $<1\bar{1}00>$ or $<12\bar{1}0>$ grown GaN NWs.[15] Different compositional Au-Ga or Au-In catalysts can tune the phase and growth direction of III-V NWs.[16,17] Fundamentally, catalyst compositions influence the catalyst chemical potential, the surface energy and interface energy of the catalyst and the nucleus, which in turn drives the formation of specific morphology and structures. Therefore,

we anticipate catalyst composition and status engineering as effective approach to alter the morphology of synthesized nanostructures.

In this study, growth of SnTe with two different morphologies: nanoplates and NWs with specific facets have been realized using a facile CVD approach using Au catalysts. The grown nanoplates and the NWs are found to be induced by catalyst with different status and different Sn concentrations. The fundamental reasons behind such phenomena were investigated by electron microscopy analysis, coupled with the surface energy calculation.

**Experimental**

SnTe nanostructures were grown in a multi-zone horizontal tube furnace under atmospheric pressure using SnTe powders as the precursor (Fig. 1a). $SiO_2$(300nm thick)/Si(001) substrates, labelled as sample A and B, were used for the growth.[18] The substrates are firstly coated with a ~1 nm thick Au film prior to the nanostructure growth. During the growth, substrate A was placed at the 500$^{o}$C zone in the downstream near to the precursor, and substrate B was placed at the 450$^{o}$C zone, comparatively farther away from the precursor, as illustrated in Fig. 1a. The morphological, structural and chemical characteristics of the as-grown nanostructures was investigated by scanning electron microscopy (SEM, JEOL 7800), and transmission electron microscopy (TEM, FEI F20, F30) equipped with energy-dispersive X-ray spectroscopy (EDS) for compositional analysis.

**Results and Discussion**

In this study, two kinds of nanostructures were obtained. Figure 1b shows a typical plain-view SEM image taken from sample A, in which triangular nanoplates with a lateral dimension of up to 6 μm and a thickness of up to 200 nm are seen. Figures 1c and 1d show a pair of SEM images taken from a typical triangular nanoplate, viewed in plain-view and 45$^{o}$ tilted-view, respectively. From this pair of SEM images, the triangular feature of the nanoplate can be confirmed and the fine feature of its side-walls can be witnessed (details refer to the inset of the Fig. 1c). On this basis, the morphological feature of the nanoplate can be illustrated and shown in Fig. 1e, in which different facets are labels. Figure 1f shows a typical SEM image of sample B, in which NWs with an average length of 5 μm and a diameter of up to 120 nm are

seen. Figure 1g shows a SEM image of a typical NW in which a catalyst associates with one end of the NW. Figure 1h shows a tilted SEM image taken from the bottom of the NW, illustrating a faceted feature of the NW with the NW cross-section being a near squared shape.

To understand the morphological and structural characteristics of as-grown nanostructures, TEM was employed. Figure 2a shows a bright field (BF) TEM image of a triangular nanoplate obtained from sample A, in which a catalyst can be found at the tip of the triangular nanostructure. Since this TEM image was taken from un-tilted specimen, we anticipate that the surface normal of the plate is parallel to the electron beam. Therefore, the angles measured between different edges (as shown in Fig. 1a) reflect as the true crystallographic angles. Figure 2b presents the corresponding selected area electron diffraction (SAED) pattern, which can be index as [100] zone axis of cubic structured SnTe phase (JCPDS #. 65-0322, *a* = 6.304 Å and a space group of $\mathrm{Fm\bar{3}m}$). Accordingly, the facet A shown in Fig. 1e and inset of Fig. 2a can be indexed as the {100} plane. Since TEM images provide only two-dimensional projections of three-dimensional objects, SEM investigation was performed on the TEM specimens to gain three-dimensional information of the nanoplates, particular the side facets. Figure 2c shows such an example, where an inclined side facet associated with the catalyst (facet C) can be seen. Furthermore, the side facets of B and D can be found to be perpendicular to facet A, which can then be respectively indexed as {010} and {120} by correlating Figs. 2a–c. Since the projected plane of different C facets along the electron beam is {110} and the corresponding projected morphology is an inclined plane, the C facets can index as {11x} (x is an integer). Based on our surface energy modelling (see below), we found that C facets can be assigned as {111} planes. As a consequence, the structural model of our triangular nanoplates can be built, as shown in Figs. 1d-e.

TEM investigations were also performed to the NWs grown at the relevant low temperature, and the results are shown in Fig. 3. Figure 3a shows a BF TEM image of a typical NW, and the inset is a magnified TEM image taken from the NW tip, where the catalyst can be clearly seen. The corresponding SAED pattern is shown Fig. 3b. Correlating Figs. 3a,b, the axial direction of the NW can be determined to be along <010> direction. According to Fig. 1h, NWs grown at the relevant low temperature has near squared cross-sections. Taking this phenomenon with Figs.

3a,b into account, the four side-walls of the NWs can be determined to be {100} surfaces. The atomic model of the NW is shown in Fig. 3c.

Figures 4a and 4b show a pair of BF TEM images taken from the tip region of a triangular nanoplate, obtained by tilting along the [010] axis of SnTe. Figures 4c and 4d show the corresponding nanodiffraction patterns taken from the catalyst, which can be indexed as the $[01\bar{1}\bar{1}]$ and $[\bar{1}2\bar{1}0]$ zone-axes diffractions patterns of a hexagonal structured AuSn phase (JCPDS #. 08-0463, with a= 4.323Å, c=5.517Å and a space group of P63). Figure 4e shows the EDS profiles taken respectively from the catalyst and nanoplate, from which the composition of Au and Sn in the catalyst can be estimated as 1:1 and the nanoplate has a composition of 49 at.% Sn and 51 at.% Te with an uncertainty of ±3% (note that the Cu peaks are due to the Cu TEM grids). Figure 4f presents a nanodiffraction pattern taken from both the catalyst and its underlying nanoplate, which shows that two sets of diffraction patterns are superimposed, with one belonging to the [101]SnTe and the other belonging to the $[\bar{1}2\bar{1}0]$ AuSn. This diffraction pattern suggests that the catalyst and its underlying nanoplate have a certain crystallographic relationship. The crystallographic orientation relationship between the catalyst and the nanoplate can be determined as $\{10\bar{1}0\}_{AnSn}$ // $\{242\}_{SnTe}$ and $\{0001\}_{AuSn}$ // $\{111\}_{SnTe}$. To ensure the validity of such a crystallographic relationship in all nanoplates, we have examined over a dozen nanoplates and confirmed this crystallographic relationship does exist generally. To understand the existence of such a crystallographic relationship between AuSn and SnTe, we note the similarity of equilibrium lattice spacings of AuSn and SnTe: $d\{10\bar{3}0\}_{AnSn}$ (1.25Å ≈$d\{242\}_{SnTe}$ (1.29Å), and $d\{0003\}_{AnSn}$ (1.84Å) ≈ $d\{22\bar{2}\}_{SnTe}$ (1.83Å).

Similar analysis has also been performed on the catalysts of SnTe NWs. Figure 5a shows a BF TEM image of a tip section of a NW sample. Since this TEM image is taken without any titling, the axial direction of the NW should be perpendicular to the electron beam. Therefore, the observed sharp interface between the catalyst and NW must be perpendicular to the axial direction of the NW. EDS spectra taken from the catalysts and the NW, showing that the catalyst has the chemical composition of ~84 at.% Au and ~16 at.% Sn with an uncertainty of ± 2% and the NW is SnTe as expected (Fig. 5b). Figures 5c and 5d show a pair of nanodiffraction patterns taken from the catalyst shown in Fig. 5a, which can be respectively indexed as diffraction patterns along [0001] and $[01\bar{1}0]$ zone axes of a rhombohedral structured $Au_5Sn$

phase (JCPDS#. 65-2188, *a*=5.09Å and *c*=14.33Å, with a space group of R3). Figure 5e shows the SAED pattern taken from both catalyst and NW, in which the superimposed diffraction patterns can be indexed as $[\ \bar{1}01\ ]_{SnTe}//[0001]_{Au5Sn}$, suggesting a crystallographic relationship between the catalysts and NW. According to Fig. 5e, both the diffraction spots of $\{03\bar{3}0\}_{An5Sn}$ and $\{220\}_{SnTe}$ and the diffraction spots of $\{11\bar{2}0\}_{Au5Sn}$ and $\{010\}_{SnTe}$ are parallel, indicating that the crystallographic orientation relationship of $\{01\bar{1}0\}_{AnSn}//\{101\}_{SnTe}$ and $\{11\bar{2}0\}_{Au5Sn}//\{010\}_{SnTe}$. We note that, in equilibrium conditions, $d\{01\bar{1}0\}_{Au5Sn}$ (4.41Å) ≈ $d\{101\}_{SnTe}$ (4.45Å) with a lattice mismatch of 0.9%. The atomic model is shown in Fig. 5(f). We further calculate the other (perpendicular) in-plane lattice mismatch between $5d\{\ \bar{1}01\ \}_{SnTe}$ and $4d\{0001\}_{An5Sn}$, which shows a lattice mismatch as small as 0.6%. Therefore, the interface between the NW and catalyst can be considered as an almost coherent interface, as schematically illustrated in Fig. 5g.

It is of interest to note that, in both cases, the catalysts and their underlying nanostructures have crystallographic relationships as a result of their similar lattice spacings, as outlined above. To understand the formation and impact of such relationships, it is necessary to clarify whether catalysts in both cases are in the liquid form or in the solid form during the nanostructure growth, as the formal leads to a vapor-liquid-solid (VLS) grown mechanism,[19] and the latter lead to a vapour-solid-solid (VSS) growth mechanism.[15, 16] Accordingly, we examine both Au-Sn and Au-Te phase diagrams.[20] Since Te is nearly not soluble in solid Au (<0.046 at.% Te), and since we did not find Te in the catalysts (refer to Figs. 4e, 5b), we only need to deal with the Au-Sn phase diagram for understanding the nature of catalysts. Figure 6 is the binary Au-Sn phase diagram,[21] from which the AuSn phase has a melting point of 418.7$^{o}$C, suggesting that the catalysts in sample A must be in the liquid form when inducing the nanoplate growth. As a consequence, the observed lattice matching between the catalysts and nanoplate must be formed during the cooling period of the nanoplate growth, in which the liquid catalysts solidifies and forms coherent interfaces with their precipitated nanostructures in order to reduce their interfacial energy.[22] On the other hand, in the case of sample B, the catalysts have a post-growth composition of ~16 at.% Sn. According to the Au-Sn diagram, alloy with such a Au-Sn composition can only be completely transformed to liquid at a temperature of as high as ~700$^{o}$C,[23] indicating that $Au_5Sn$ catalyst should be in solid

or quasi-solid form during the NW growth at 450$^{o}$C. This suggests that the formation of SnTe NWs is induced by the solid or quasi-solid $Au_5Sn$ catalysts. Since a tiny lattice mismatch was found between the $Au_5Sn$ catalyst and the NW at the {010} interface (refer to Fig. 5g), we anticipate that the coherent interface is the driving force for the formation of [010] NWs through the VSS growth mechanism.

To understand the evolution of these nanostructures, two issues need to be addressed: (1) why catalysts with different phases can be obtained at different synthesis zones; and (2) why different nanostructures can be obtained at different synthesis zones?

To answer the first question, we note that, at a high temperature zone of 500$^{o}$C, more Sn vapor species can be absorbed by the catalysts because nanostructural elements can be diffused into Au catalysts at a higher diffusion rate.[10] In addition, according to the experimental setup (refer to Fig. 1a), the facts that (1) the location of sample A is much closer to the precursors than that of sample B and (2) some Sn and Te vapors have been consumed in the location of sample A, leading to a relatively low Sn and Te vapor concentrations in the location of sample B. These synergetic effects result in a high diffusibility of Sn into the catalysts for sample A. On this basis, the catalysts at the 500$^{o}$C zone are expected to have a significantly higher Sn concentration than that at the 450$^{o}$C zone, which in turn results in different catalyst status and compositions.

To answer the second question, we need to consider the surface energies of obtained nanostructures and status of the catalysts during the nanostructure growth. Figure 7a plots the calculated surface energies of SnTe phase for low indexed surfaces, including {100}, {110}, {120}, $\{111\}_{Sn}$ and $\{111\}_{Te}$ planes. As can be seen, the surface energies of {100}, {120}, and $\{111\}_{Te}$ are all low, suggesting that they are relatively stable. Among them, the {100} surface has the lowest surface energy, which has a value of ~10.4 meV/Å$^2$, in consistency with previous literature results.[7] This can also be confirmed experimentally by (i) the plate normal of triangular nanoplates being {100} and (ii) {100} side-walls of NWs, as illustrated in Figs. 7b,c. As outlined above, the NWs are induced by the solid catalysts that require a coherent interface between the catalysts and NWs (parallel to the SnTe (010) plane) to lower the interfacial energy. Since {100} surfaces have the lowest surface energy, the fact that the sidewalls of NWs are {100} suggests that the formation of NWs (in

the low temperature zone) is thermodynamically dominated (by minimalizing the side-wall surface energy). In contrast, when compared with elemental diffusion in solid, elemental diffusion in liquid catalysts at the high temperature zone is much faster, resulting in a fast nanostructure growth rate of the nanoplate. Since all {100}, {120}, and $\{111\}_{Te}$ surfaces have relatively low surface energies, the formation of triangular nanostructures can be accordingly considered as a kinetically dominated process at the high temperature zone. To understand this phenomenon, we can consider the classical crystal growth theory, in which the crystal growth velocity (v) can be presented as:[24, 25]

$$v \propto [\Delta\mu/k_B T]^2 \quad (1)$$

where the $k_B$ is the Boltzmann constant, T is the growth temperature, and $\Delta\mu$ is the chemical potential difference between the catalyst and the nanostructure that can be expressed as:[26]

$$\Delta\mu = k_B T \ln\left[ C_{Sn} C_{Te} / C_{Sn,eq} C_{Te,eq} \right] \quad (2)$$

in which $C_{Sn}$ refers to the Sn concentration in the alloyed catalyst. $C_{Te}$ refers to the Te concentration in vapor during growth, $C_{Te,eq}$ and $C_{Sn,eq}$ denotes the Te and Sn concentration at equilibrium.

According to Eqs. (1) and (2), high $C_{sn}$ leads to a high $\Delta\mu$, and in turn promotes v. Compared to NWs, nanoplates have a much higher $C_{sn}$. Therefore, a higher growth rate of triangular nanoplates can be expected, as the synthesis can be easily dominated kinetically, leading to the formation of the {120}, $\{111\}_{Te}$ side facets via a VLS growth mode.

**Conclusion**

Through carefully controlling the catalyst compositions and statues at different synthesis zones in a CVD synthesis, we have successfully grown morphological-uniform SnTe triangular nanoplates and NWs at different zones, respectively. Our detailed characterisation indicates that (1) the SnTe triangular nanoplates are kinetically induced by liquid Au-Sn catalysts with high Sn concentrations, while (2) the SnTe NW growth is thermodynamically controlled by the solid or quasi-solid $Au_5Sn$ catalysts, in which the coherent {010} interfaces between the $Au_5Sn$ catalysts and NWs are the driving force for the NW growth. This study opens a pathway to realize the facet control of the crystalline nanostructures, which is critically important

for their applications, such as in the case of TCIs, where crystallographic facets determine the properties.

**Figure Captions**

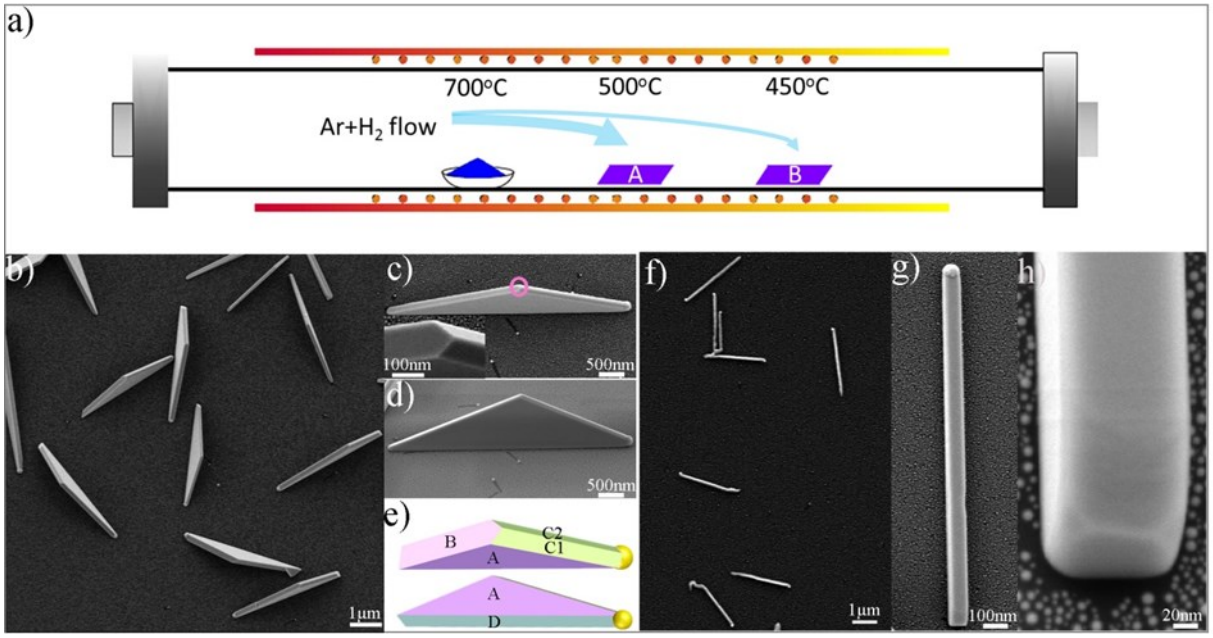


**Figure1.** (a) Schematic diagram of the CVD reactor for growing SnTe nanostructures. (b) SEM image of the nanoplates from sample A. (c) High-magnified SEM image of a typical nanoplate with an inset of a tip area marked by a circle. (d) 45$^{o}$-tilted side-view SEM image of the nanoplate. (e) Labels for the different facets of the triangular nanoplate (the dominant facet is defined as facet A, side facets are labelled as facet B, C1, C2 and D). (f) SEM image of the NWs from sample B. (g) Plain-view SEM image of a typical NW. (h) 45$^{o}$-tilted SEM image at the bottom part of the NW.

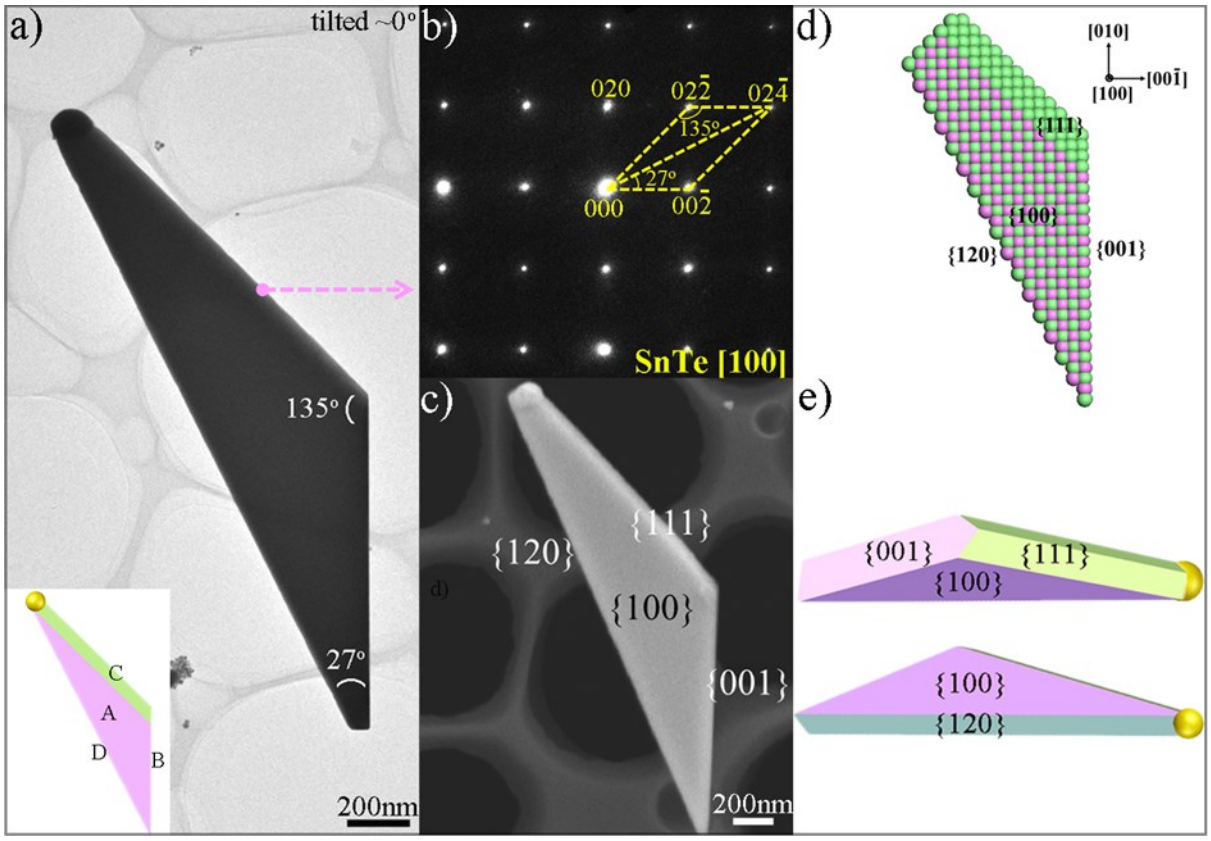


**Figure 2.** (a) Plain-view BF TEM image of a typical SnTe nanoplate with an inset model with facets labeled. (b) Corresponding [100] zone-axis SAED pattern. (c) SEM image of a typical nanoplate taken from a TEM sample with the electron beam perpendicular to the {100} nanoplate surface. (d) Atomic model of the nanoplate viewed along [100]. (e) Morphological models of a nanoplate with all determined crystallographic facets

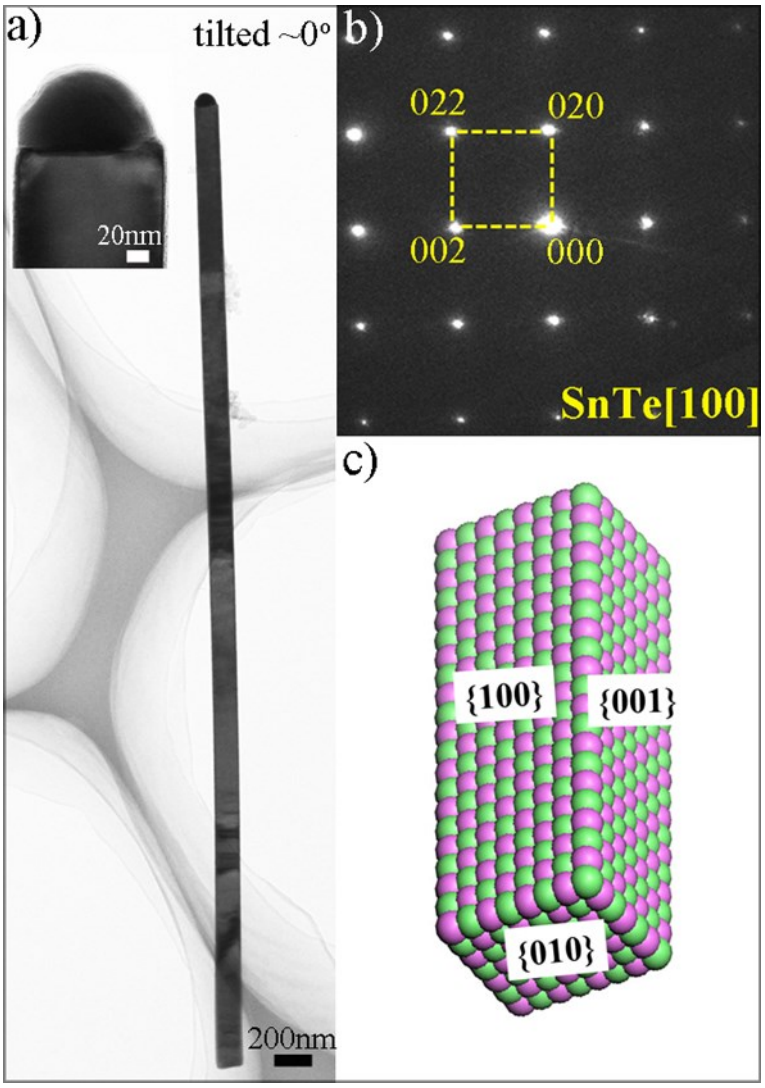


**Figure 3.** (a) A 0°-tilted BF TEM image of a typical NW; the upper inset is a magnified BF image of the NW tip region. (b) Corresponding SAED from the NW body area. (c) An atomic model of the NW with facets labeled.

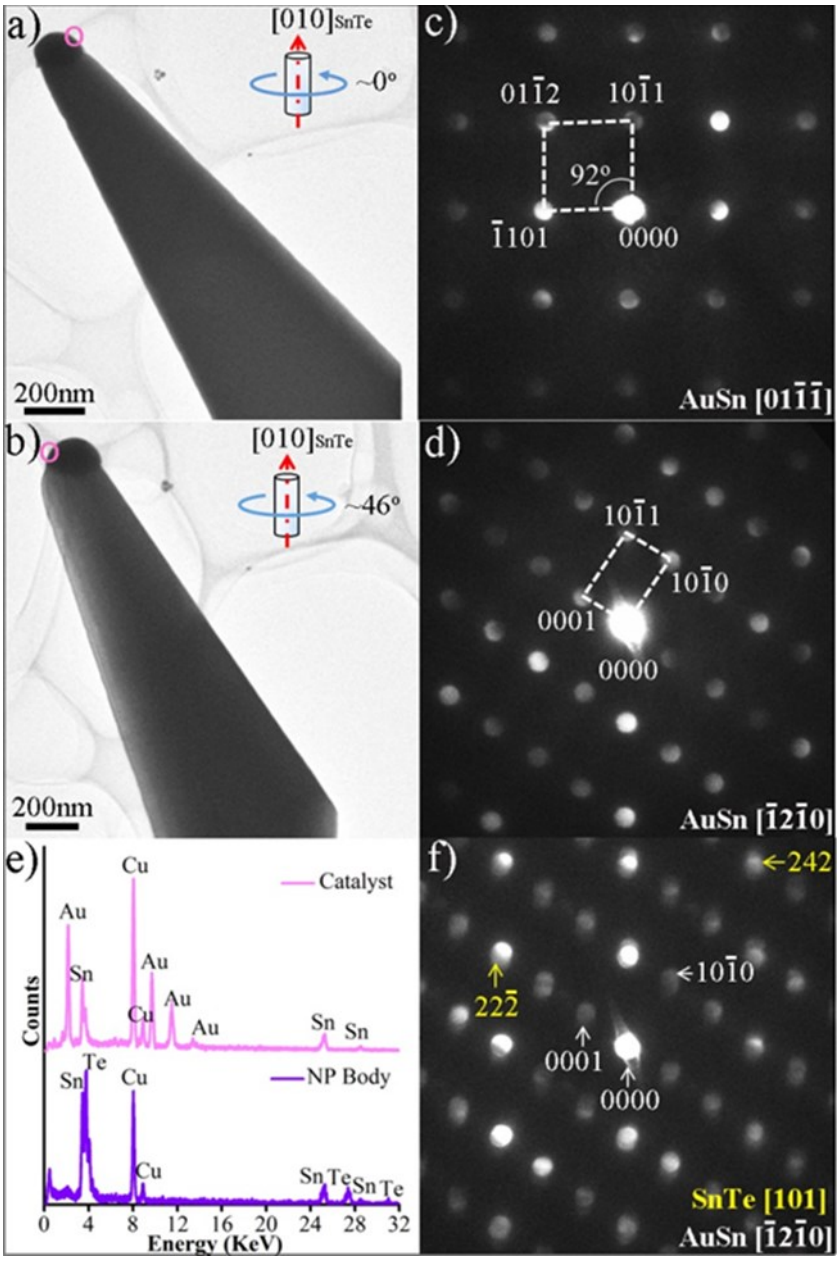


**Figure 4.** (a, b) BF TEM images of a section of a typical nanoplate near the catalyst with different tilting angles. (c, d) Corresponding nanodiffraction patterns of the catalyst taken along $[01\bar{1}\bar{1}]$ and $[\bar{1}2\bar{1}0]$ zone axes, respectively. (e) EDS spectra taken from the catalyst and the nanoplate. (f) Nanodiffraction pattern taken from the nanoplate-catalyst interface area showing overlapped diffraction patterns.

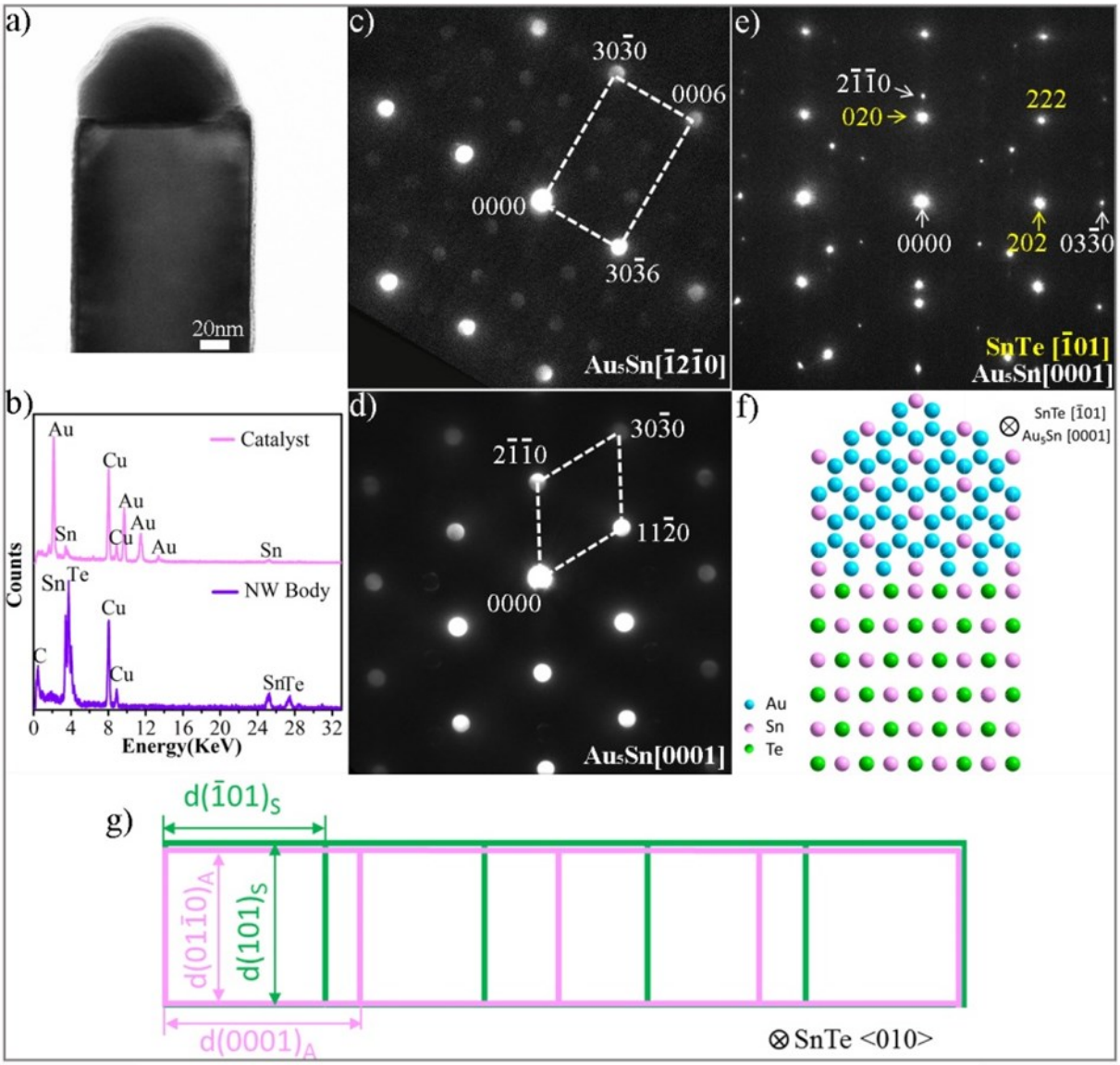


**Figure 5.** (a) BF TEM image of a typical NW section near the catalyst. (b) EDS spectra taken from the catalyst and NW. (c, d) Nanodiffraction patterns of the NW catalyst taken along $[\bar{1}2\bar{1}0]$ and [0001] zone axes, respectively. (e) SAED pattern taken from the NW-catalyst interface showing overlapped diffraction patterns. (f) Atomic model for $Au_5Sn$ catalyst-SnTe NW junction viewed along the SnTe $[\bar{1}01]$ direction. (g) Schematic diagram showing the almost coherence of the atomic planes at the catalyst/NW interface.

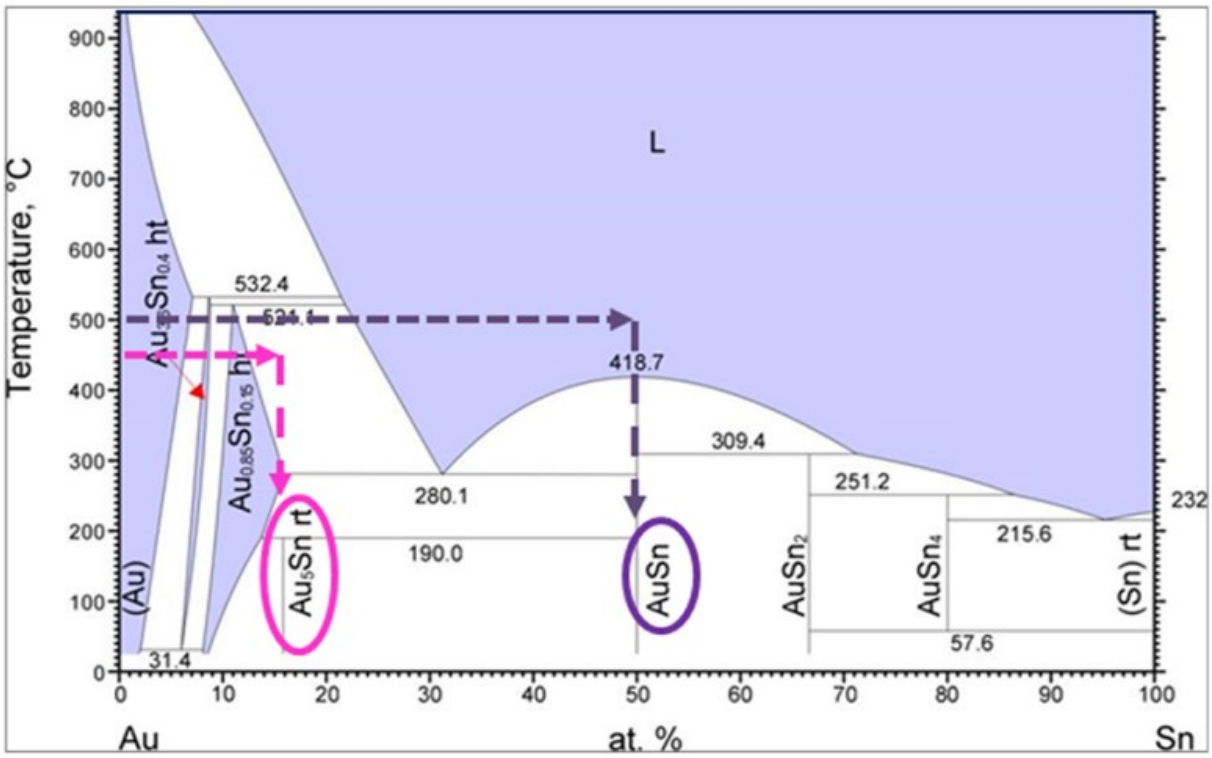


**Figure 6.** Au-Sn binary phase diagram with the purple and pink lines illustrating the formation of AuSn and $Au_5Sn$ catalyst particles.

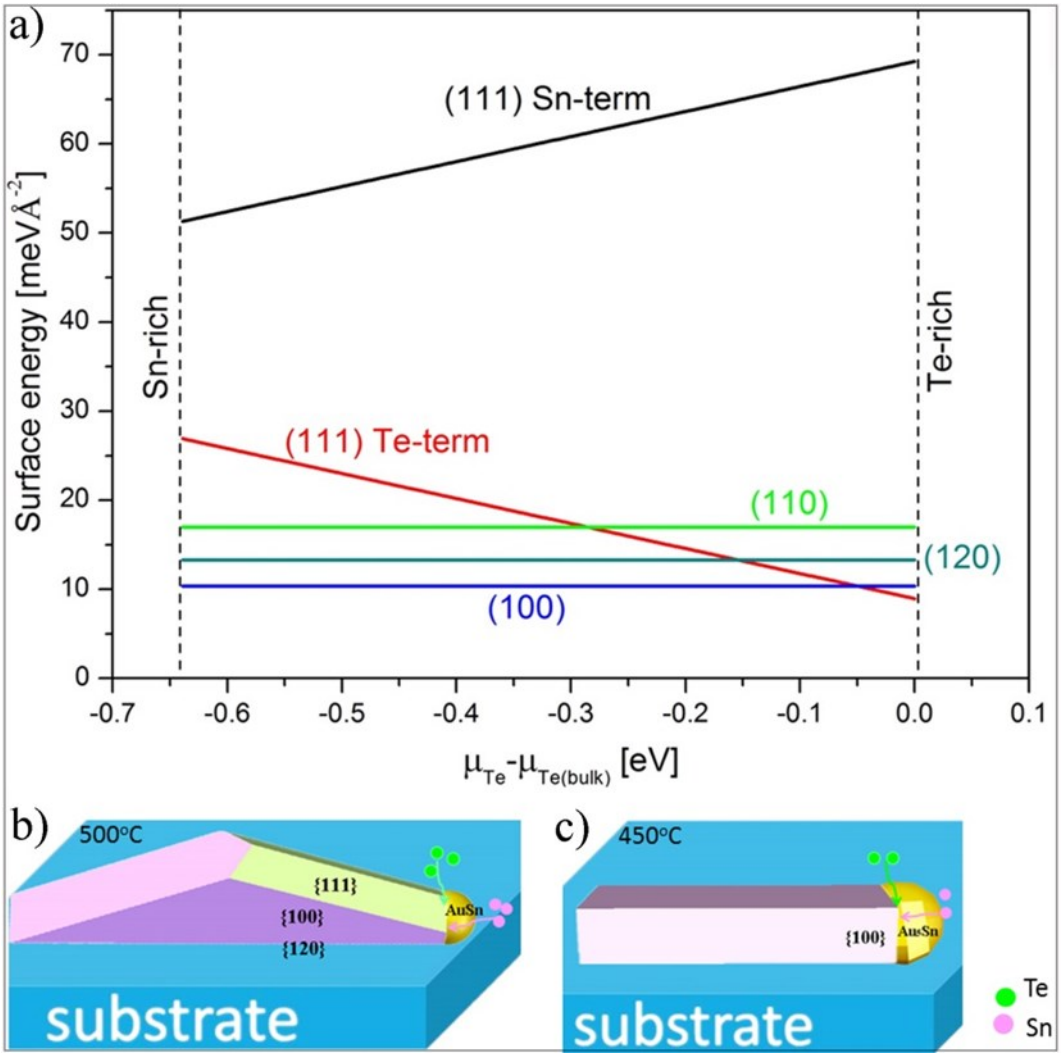


**Figure 7.** (a) Calculated surface energies for the {100}, {110}, {120}, $\{111\}_{Sn}$ and $\{111\}_{Te}$ surfaces as a function of the relative Te chemical potential $\Delta\mu_{Te}$. (b, c) Models of grown triangular nanoplate and NW

**References**


1. Erickson, A. S.; Chu, J. H.;Toney, M. F.; Geballe, T. H.; Fisher, I. R. Enhanced superconducting pairing interaction in indium-doped tin telluride. *Phys. Rev. B* **2009**, *79*, 024520.
2. Salje, E.; Safarik, D.; Modic, K.; Gubernatis, J.; Cooley, J.; Taylor, R.; Mihaila, B.; Saxena, A.; Lookman, T.; Smith, J.; Fisher, R.; Pasternak, M.; Opeil, C.;Siegrist, T.; Littlewood, P.; Lashley, J. Tin telluride: A weakly co-elastic metal. *Phys. Rev. B* **2010**, *82*, 184112.
3. Xia, Y.; Qian, D.; Hsieh, D.; Wray, L.; Pal, A.; Lin, H.; Bansil, A.; Grauer, D.; Hor, Y. S.; Cava, R. J.; Hasan, M. Z. Observation of a large-gap topological-insulator class with a single Dirac cone on the surface. *Nat. Phys.* **2009**, *5*, 398-402.
4. Tanaka, Y.; Ren, Z.; Sato, T.; Nakayama, K.; Souma, S.; Takahashi, T.; Segawa, K.; Ando, Y. Experimental realization of a topological crystalline insulator in SnTe. *Nat. Phys.* **2012**, *8*, 800-803.
5. Safdar, M.; Wang, Q.; Mirza, M.; Wang, Z.; Xu, K.; He, J. Topological surface transport properties of single-crystalline SnTe nanowire. *Nano Lett.* **2013**, *13*, 5344-5349.
6. Safdar, M.; Wang, Q.; Mirza, M.; Wang, Z.; He, J. Crystal shape engineering of topological crystalline insulator SnTe microcrystals and NWs with huge thermal activation energy gap. *Cryst. Growth & Des.* **2014**, *14*, 2502-2509.
7. Li, Z.; Shao, S.; Li, N.; McCall, K.; Wang, J.; Zhang, S. X. Single crystalline nanostructures of topological crystalline insulator SnTe with distinct facets and morphologies. *Nano Lett.* **2013**, *13*, 5443-5448.
8. Shen, J.; Cha, J. Topological crystalline insulator nanostructures. *Nanoscale* **2014**, *6*, 14133-14140.
9. Morales, A. M.; Lieber, C. M. A laser ablation method for the synthesis of crystalline semiconductor nanowires. *Science* 1**998**, *279*, 208-211.
10. Xu, H.; Wang, Y.; Guo, Y.; Liao, Z.; Gao, Q.; Tan, H. H.; Jagadish, C.; Zou, J. Defect-free <110> zinc-blende structured InAs NWs catalyzed by palladium. *Nano Lett.* **2012**, *12*, 5744-5749.
11. Lieber, C. M. Nanoscale science and technology: Building a big future from small things. *Mrs. Bull.* **2003**, *28*, 486-491.

12. Xu, H.-Y.; Guo, Y.-N.; Liao, Z.-M.; Sun, W.; Gao, Q.; Hoe Tan, H.; Jagadish, C.; Zou, J. Catalyst size dependent growth of Pd-catalyzed one-dimensional InAs nanostructures. *Appl. Phys. Lett.* **2013**, *102*, 203108.
13. Chiang, W.-H.; Mohan Sankaran, R. Linking catalyst composition to chirality distributions of as-grown single-walled carbon nanotubes by tuning $Ni_xFe_{1-x}$ nanoparticles. *Nat. Mater.* **2009**, *8*, 882-886.
14. Yang, F.; Wang, X.; Zhang, D.; Yang, J.; Luo, Da; Xu, Z.; Wei, J.; Wang, J.-Q.; Xu, Z.; Peng, F.; Li, X.; Li, R.; Li, Y.; Li, M.; Bai, X.; Ding, F.; Li, Y. Chirality-specific growth of single-walled carbon nanotubes on solid alloy catalysts. *Nature* **2014**, *510*, 522-524.
15. Kuykendall, T. R.; Altoe, M. V. P.; Ogletree, D. F.; Aloni, S. Catalyst-directed crystallographic orientation control of GaN nanowire growth. *Nano Lett.* **2014**, *14*, 6767–6773.
16. Han, N.; Wang, F.; Hou, J. J.; Yip, S.; Lin, H.; Fang, M.; Xiu, F.; Shi, X.; Hung, T.; Ho, J. C. Manipulated growth of GaAs nanowires: Controllable crystal quality and growth orientations via a supersaturation-controlled engineering process. *Cryst. Growth & Des.* **2012**, *12*, 6243-6249.
17. Zhang, Z.; Lu, Z.; Xu, H.; Chen, P.; Lu, W.; Zou, J. Structure and quality controlled growth of InAs NWs through catalyst engineering. *Nano Res.* **2014**, *7*, 1640-1649.
18. Zou, Y.; Chen, Z.-G.; Huang, Y.; Yang, L.; Drennan, J.; Zou, J. Anisotropic electrical properties from vapor–solid–solid grown $Bi_2Se_3$ nanoribbons and NWs. *J. Phys. Chem. C* **2014**, *118*, 20620-20626.
19. Wagner, R. S.; Ellis, W. C. Vapor-liquid-solid mechanism of single crystal growth. *Appl. Phys. Lett.* **1964**, *4*, 89-90.
20. Cabri, L. J. Phase relations in the Au-Ag-Te systems and their mineralogical significance. *Economic Geology* **1965**, *60*, 1569-1606.
21. Okamoto, H. Au-Sn (gold-tin). *Journal of Phase Equilibria and Diffusion* **2007**, *28*, 490-490.
22. Porter, D. A.; Easterling, K. E. *Phase transformations in metals and alloys, (revised reprint)*; CRC press: London, 1992.
23. Ciulik, J.; Notis, M. R. The Au-Sn phase diagram. *J. Alloy. Compd.* **1993**, *191*, 71-78.

24. Biswas, S.; O'Regan, C.; Petkov, N.; Morris, M. A.; Holmes, J. D. Manipulating the growth kinetics of vapor–liquid–solid propagated Ge nanowires. *Nano Lett.* **2013**, *13*, 4044-4052.
25. Givargizov, E. I. Fundamental aspects of VLS growth. *J. Cryst. Growth* **1975**, *31*, 20-30.
26. Joyce, H. J.; Wong-Leung, J.; Gao, Q.; Tan, H. H.; Jagadish, C. Phase perfection in zinc blende and wurtzite III-V nanowires using basic growth parameters. *Nano Lett.* **2010**, *10*, 908-915.

# 6

# Crystal-Structure Control of $Sn_{1-x}Bi_xTe$ Nanoribbons by Doping

## 6.1 Introduction

In this work, we investigate into the effect of Bi doping on the crystal structure of SnTe nanostructures. We found that in highly doped SnTe, the incorporation of Bi dopants promote the formation of Sn planar vacancies. The density of the planar vacancies can be engineered in $Sn_{1-x}Bi_xTe$ NRs by using Bi dopants via a facile chemical vapour deposition. Through combination of sub-ångström-resolution imaging and calculation within density functional theory, these planar vacancies are found to be associated with Bi segregations, which significantly lower the formation energies of the vacancies. The planar vacancies exhibit polymorphic structures with local variations in lattice relaxation level, determined by their proximity to NR surface. Such polymorphic planar vacancies, in conjunction with Bi dopants, trigger distinct localized electronic states, offering new device platforms for ternary chalcogenide materials.

## 6.2 Journal Publication

These results in Chapter 6 have been published in ***ACS Nano,*** 2016, 10, 5507-5515.

http://dx.doi.org/10.1021/acsnano.6b01953

**Planar Vacancies in $Sn_{1-x}Bi_xTe$ Nanoribbons**

Yi-Chao Zou,[†] Zhi-Gang Chen,[†] Fantai Kong,[§] Jing Lin,[†] John Drennan,[‖] Kyeongjae Cho,[§] Zhongchang Wang,[‡] Jin Zou[†,‖]

[†] Materials Engineering, and [‖]Centre for Microscopy and Microanalysis, University of Queensland, Brisbane, QLD 4072, Australia
[‡] WPI, Advanced Institute for Materials Research, Tohoku University, 2-1-1 Katahira, Aoba-ku, Sendai 980-8577, Japan
[§] Department of Materials Science & Engineering, The University of Texas at Dallas, Richardson, TX 75080, USA.

**Abstract**

Vacancy engineering is a crucial approach to manipulate physical properties of semiconductors. Here, we demonstrate that planar vacancies are formed in $Sn_{1-x}Bi_xTe$ nanoribbons by using Bi dopants *via* a facile chemical vapour deposition. Through combination of sub-ångström-resolution imaging and density functional theory calculations, these planar vacancies are found to be associated with Bi segregations, which significantly lower their formation energies. The planar vacancies exhibit polymorphic structures with local variations in the lattice relaxation level, determined by their proximity to the nanoribbon surface. Such polymorphic planar vacancies, in conjunction with Bi dopants, trigger distinct localized electronic states, offering platforms for device applications of ternary chalcogenide materials.

**Keywords**: chalcogenides, nanoribbon, vacancy, scanning transmission electron microscopy, density functional theory

## Introduction

Vacancy engineering has been demonstrated as an effective approach to expand the practical applications of semiconductors in superconductors,[1] thermoelectrics,[2-4] optoelectronics,[5-7] and ferromagnetic devices.[8,9] The spatial arrangements of vacancies in crystal lattices have been recognized as a key factor to govern the electrical,[10-12] thermal,[2-4] and optical[5-7] properties of semiconductors. For example, manipulating the distribution of vacancy clusters in thermoelectric materials can greatly suppress the thermal conductivity and enhance their thermoelectric performances.[4] In light of the fundamental role, vacancies break the ordered arrangement of atoms in crystals and thus considerably shift the local electronic states and phonon scattering behaviours. Therefore, to fully understand the mechanism behind vacancy engineering and resultant physical/chemical properties, it is crucial to obtain a comprehensive atomic insight into the local vacancy-defect structure.[13,14]

For highly doped semiconductors, vacancies are likely to interact with impurities, leading to an increased complexity in local defect structures. The incorporation of donor (acceptor) impurities may cause the formation of compensating acceptor (donor) vacancies, resulting in vacancy-impurity defect complexes.[15-19] These defect complexes may induce unexpected physical phenomena in semiconductors, such as abnormal resistance switching memory,[18] superconductivity,[19] illuminances,[20] and ferromagnetism.[8] Although these defect complexes can be demonstrated by theoretical modellings and/or property measurements, no direct evidence of the atomic configuration of vacancy-impurity complex has been shown experimentally. On the other hand, aberration-corrected scanning transmission electron microscopy (STEM) has enabled the atomic-scale observation of vacancies associated with impurities.[13,14,21]

Metal chalcogenide nanostructures are important building blocks for semiconductor electronic devices.[22,23] Particularly, impurity doped SnTe nanomaterials have shown exotic physical properties including superconductivity,[24] enhanced topological surface states[24] and high thermoelectric performances.[25-31] SnTe is a *p*-type compound semiconductor with native Sn vacancies, in which the Sn vacancies significantly influence the property.[32] However, the atomic configurations of various defects in doped SnTe have not been studied experimentally, although theoretical

modelling have predicted that the point defects in SnTe have the tendency to form complex clusters.[32] To further clarify the defect structure in doped SnTe, here we conducted STEM imaging on Bi-doped SnTe NRs, from which we find that in the highly doped NRs, Bi promotes the formation of Sn planar vacancies, which are decorated by Bi dopants. In combination with synthesis experiments, we show that the density of the planar vacancy can be engineered by using Bi dopants. Density functional theory (DFT) calculations were further conducted to understand the energetic origin of the Bi segregation and the formation mechanism of the planar vacancies. By correlating the atomic modelling and the density of states (DOS) calculations, we are able to identify the distinct local electronic states arising from the complex planar vacancies.

**Results and Discussion**

$Sn_{1-x}Bi_xTe$ nanostructures doped with different Bi concentrations were synthesized by catalyst-free chemical vapour deposition (CVD). Their compositions were controlled by varying the weight ratios of elemental precursors in the CVD growth as the nominal compositions of x = 0.15, 0.2, and 0.3 (in mole fraction), respectively. Figure 1a-c show (scanning electron microscopy) SEM images of as-grown nanostructures with different Bi concentrations. Corresponding high-magnified SEM images are shown in Figure 1d-f, revealing that the nanostructures have the morphology of NRs with a lateral size of 70~300 nm and a thickness of 20~80 nm. The comparison of Figure 1a-c suggests that the growth rate of the NRs can be enhanced by increasing the Bi doping concentration. The NRs are dominated by {111} surface facets based on our TEM investigations.

Figure 2 presents the TEM investigations of the three samples with different Sn/Bi ratios. Figure 2a,e,i show their typical bright-field (BF) TEM images taken at a section of an individual NR. Their corresponding energy-dispersive spectroscopy (EDS) profiles (Figure 2b,f,j) confirm the presence of Bi, Sn and Te in all samples (note that the C and Cu peaks are attributed to the holly C film on the Cu grid for supporting NRs). Further quantitative analyses show that the compositions of obtained $Sn_{1-x}Bi_xTe$ NRs are very close to their nominal compositions. EDS line scan and mapping further confirm that the elemental composition of Sn, Bi and Te, and they are found throughout the entire NR (Figure S1). From Figure 2a,e,i, with

increasing the Bi concentration, an increased density of planar defects can be observed in the NRs. This is further confirmed by high-resolution TEM (HRTEM) images taken from the NRs (Figure 2c,g,k), in which the planar defects can be clearly seen (yellow arrows). Figure 2d,h,l show their corresponding selective-area electron diffraction (SAED) patterns taken along their [011] axis of rock-salt structured SnTe. By correlating the BF TEM and HRTEM images with SAED patterns, the axial direction of obtained NRs can be determined along the <110> direction and planar defects are lying on the {111} planes. Interestingly, streaks lying along the 111* diffraction spots can be seen in Figure 2k,l with pronounced streaks found in Figure 2l, reflecting the high-density of planar defects.

To understand the atomic configuration of planar defects, we employed aberration-corrected high-angle annular dark-field (HAADF) imaging technique in STEM. Figure 3a, 3b respectively shows typical HAADF STEM images showing the planar defects in $Sn_{0.8}Bi_{0.2}Te$ and $Sn_{0.7}Bi_{0.3}Te$ NRs, revealing the impact of the Bi doping level on the planar-defect density. Statistical analysis (from more than 10 NRs in each sample) further indicates that the averaged density of planar defect is increased from ~$9.1\times10^3\ \mu m^{-2}$ for the $Sn_{0.8}Bi_{0.2}Te$ sample to ~$2.9\times10^4\ \mu m^{-2}$ for the $Sn_{0.7}Bi_{0.3}Te$ sample, as plotted in Figure 3c.

Figure 4 presents a detail HAADF STEM analysis for an individual planar defect in a $Sn_{0.7}Bi_{0.3}Te$ sample. Figure 4a shows four horizontal planar defects in a very small area. Interestingly, brighter atomic columns can be constantly and regularly observed near the planar defects (Figure 3a,b and 4a). Since the intensity of an atomic column in the HADDF STEM imaging mode is approximately proportional to $Z^{1.7}$ (Z is atomic number),[13] and since Bi has a higher Z (83) value compared with Sn (50) and Te (52), brighter atomic columns should be Bi-rich. To further confirm this point, a detailed planar defect is analysed. Figure 4b shows a magnified image of the area marked as 'R' in Figure 4a, defined as individual R-type planar defect. Figure 4c plots the intensity profile between point I and II in Figure 4b, showing two highest peaks (red arrows) associated with brighter columns and they are symmetrical to the corresponding vacancies sites (denoted as Vs), indicating that the planar defect is composed of Sn vacancies condensed at {111} planes, with Bi atoms aggregated at the nearest cation sites next to Vs (denoted as S1, Figure 4d). To further verify the brighter columns being Bi atoms, we conducted DFT calculations and found that Bi

energetically prefers locating at S1 by saving at least 0.31 eV compared to that at bulk (S2 sites in Figure 4d). Using this energetically stable structural model, further HADDF STEM image simulation was performed, and the result is shown in Figure 4e, which is in an excellent agreement with experimental HAADF STEM image (Figure 4b).

By carefully examining the planar defects shown in Figure 4a, two structural types of planar vacancies can be observed and defined as R-type and U-type planar vacancy (marked as 'R' and 'U' in Figure 3a). To fully understand their structural similarity and difference, a HAADF STEM investigation on U-type planar defect was also conducted (Figure 5). Figure 5a shows a HAADF STEM image taken from the edge of a U-type defect, revealing that it is also composed of Sn vacancies at a {111} atomic plane, which is verified by DFT calculations (Figure 5b). The extracted intensity line profile further confirmed the abrupt drop of image intensity at the vacancy sites (Figure 5c). Interestingly, a small peak can still be detected at the vacancy site (marked by the yellow arrow). To understand this, we note that each "white dot" in a HAADF STEM image corresponds to the projection of an atomic column. When there exists a perfect region and a vacancy region along an atomic column, a weak "white dot" corresponding to the atomic column is expected. For this reason, the small peak found in the vacancy site in Figure 5c indicates there exists a small section of perfect region superimposed with the U-type planar vacancy. This is in agreement with features shown in Figure 5d, from which U-type defect terminate before reaching the NR surface and are surrounded by perfect regions, whereas the R-type defects extend to the NR surface (Figure 4a).

On a closer inspection of atomic configurations of R-type and U-type planar vacancies, we can find their difference in defect geometry, particularly on the structural relaxation levels in the vacancy plane. To evaluate the structural relaxation level, we define $(d_{T\text{-}T}\text{-}d_{T1\text{-}T1})/d_{T\text{-}T}$ as an index, where $d_{T\text{-}T}$ is the distance between the two nearby Te atoms on the {110} atomic plane in the bulk (white arrows, Figure 4b,5a), while $d_{T1\text{-}T1}$ is the distance between two nearby Te atoms at the vacancy region (blue arrows, Figure 4b,5a). $d_{T\text{-}T}$ of both types of vacancies can be measured as ~4.5Å, close to $d_{\{110\}}$ of a perfect SnTe (~4.46 Å), confirming that the host lattice has a SnTe rock-salt structure. $d_{T1\text{-}T1}$ of U-type vacancies can be measured as ~4.3Å (Figure 5a,c), with a relaxation level of ~4%, indicating that the formation of U-type

planar vacancies has little influence on the surrounding rock-salt structured lattice. In contrast, in R-type planar vacancies, $d_{T1\text{-}T1}$ is reduced to a much smaller value of ~2.8 Å (Figure 4b), with a large relaxation level of ~38%. This indicates that R-type vacancy structure has deviated from the rock-salt matrix, in which adjacent atoms have relaxed toward the vacancies, resulting in a significantly reduced spacing between T1-T1 layers. In fact, such a structural arrangement of lattice relaxed R-type planar vacancies is similar to the structure of rhombohedral-structured stable $Bi_2Te_3$ phase. The R-type vacancy structure exhibit a A($\alpha$)B(*V*)A($\alpha$)B stacking sequence (*V* denotes the vacancy layer) at the local vacancy region along its <111> direction, which shows similarity to that of the $Bi_2Te_3$ phase along the <0001> direction (Figure S3). The above results show that the R-type exhibit a larger degree in structural relaxation compared to the U-type. As the U-type vacancies are bounded by surrounding bulk, their structural relaxation is restricted, whereas the R-type vacancies located at the vicinity of the surface have larger freedom to relax.[33]

To understand the energetic origin of the Bi segregation nearby the planar vacancies, we performed DFT calculations for both R-type (Figure 6a-c) and U-type (Figure 6d-f) defects. Starting with pure Sn planar vacancies (0% cases shown in Figure 6a,d), we gradually introduce Bi that segregates to the S1 sites nearby, to simulate the defect configurations with different levels of Bi segregation (100% cases shown in Figure 6b,e).

To determine which defect configuration is stable, we further calculated the formation energy ($E_{form}$) of the planar vacancies as a function of the atomic chemical potentials ($\mu_{Sn}$, $\mu_{Bi}$, $\mu_{Te}$) of their constituents (Sn, Bi, Te), using the equation of[34]

$$E_{form} = \frac{1}{2A}[E_{tot}(defect) - E_{tot}(SnTe) + n_{Sn}\mu_{Sn} - n_{Bi}\mu_{Bi} + qE_F] \quad (1)$$

where $E_{tot}$(defect) and $E_{tot}$(SnTe) are total energies derived from a supercell calculation, with and without the planar vacancies, respectively; $n_{Sn}$ denotes the number of Sn atoms that have been removed from the pristine SnTe, and $n_{Bi}$ denotes the number of Bi atoms substituting Sn atoms; $\mu_{Sn}$ and $\mu_{Bi}$ are the chemical potentials of Sn and Bi atoms, respectively; $E_F$ is the electron Fermi energy, and A is the defective area. Charge neutrality is maintained in all calculations ($q$ = 0).

During the calculation, $\mu_{Sn}$, $\mu_{Bi}$, and $\mu_{Te}$ were estimated by adopting the following equations[28, 35]:

$$\mu_{Sn} + \mu_{Te} = E_{SnTe} \text{ , and} \quad (2)$$

$$2\mu_{Bi} + 3\mu_{Te} = E_{Bi_2Te_3}; \quad (3)$$

where $E_{SnTe}$ and $E_{Bi_2Te_3}$ denote the cohesive energies of one pair of Sn-Te in SnTe, and one pair of Bi-Te in $Bi_2Te_3$. Our DFT calculations shows that $E_{SnTe}$ and $E_{Bi_2Te_3}$respectively has a value of $E_{SnTe}$=-7.618 eV and $E_{Bi_2Te_3}$=-18.500eV.

According to the approach of atomistic thermodynamics,[28] the chemical potentials of Sn and Te cannot be higher than their cohesive energies in the elemental stable phases, namely:

$$\mu_{\mathrm{Te}} < E_{\mathrm{Te}} \text{ , and} \quad (4)$$

$$\mu_{Sn} < E_{Sn} \text{ ;} \quad (5)$$

where $E_{\mathrm{Te}}$ and $E_{Sn}$ are the total energy of Te (trigonal crystal structure) and Sn (tetragonal crystal structure), respectively. Total energies for Sn and Te were calculated by DFT as $E_{Te} = -3.163$ eV, and $E_{Sn} = -3.896$ eV. [28] Based on Eqs. 2,4,5, the chemical potential of Te is in the range of -3.722 $< \mu_{Te}$<-3.163 eV. Using Eqs 1-3 and the calculated $\mu_{Te}$ range, $E_{\mathrm{form}}$ can be calculated as a function of $\mu_{Te}$. In this study, the relative Te chemical potential $\Delta\mu_{Te}$ (= $\mu_{Te} - E_{Te}$) is applied as a variable, which has a range of -0.559eV<$\Delta\mu_{Te}$<0 eV calculated from the $\mu_{Te}$ range. Te-rich condition is reached when $\Delta\mu_{Te}$ =0 eV ($\mu_{Te}$=$E_{Te}$), and Te-lean condition is reached when $\Delta\mu_{Te}$ = -0.559 eV ($\mu_{Sn}$=$E_{Sn}$).[28]

Figure 6c,f show the calculated $E_{\mathrm{form}}$ for both R-type and U-type planar vacancies with different Bi segregation levels as a function of $\Delta\mu_{Te}$. From the energy profiles, one can clearly see that for both R-type and U-type, over the entire range of $\mu_{\mathrm{Te}}$, the planar vacancies segregated with Bi (25~75% cases) show lower formation energies than that without Bi (0% case). With increasing the Bi substitution concentration at S1 sites, $E_{\mathrm{form}}$ is gradually reduced over the whole range of $\mu_{\mathrm{Te}}$, indicating that Bi tends to substitute the Sn until a fully substitution at S1 sites (100% case). In all these cases, $E_{\mathrm{form}}$ of R-type planar vacancies with full Bi segregation has shown the lowest value, in consistent with our observation that R-type defects are statistically dominated (refer to Figure 4a). The above analysis indicates that Bi segregation at the planar vacancies assists the stability of planar vacancies, and a large lattice relaxation would further lower the formation energy.

For both R-type and U-type planar vacancies, the cases with 100% Bi occupying nearby cation sites have the lowest formation energy, which suggests that formation of defect clusters ($2Bi_{Sn}+V_{Sn}$) are more energy favourable than that of a single Sn

vacancy ($V_{Sn}$). To understand this, we note that each Bi atom has three 6*p* electrons, which has one more *p* electron compared with Sn ($5p^2$).[36] Bi can therefore act as a donor dopant in SnTe, as Bi is normally trivalent and Sn is divalent.[29–32] In our case where Bi is excessively doped in SnTe, the formation of Sn planar vacancies can effectively compensate the local unbalanced charge introduced by $Bi^{3+}$ impurities, and two of $Bi_{Sn}^{+}$ can be charge-compensated locally by one negatively charged Sn vacancy ($V_{Sn}^{2-}$). This is further supported by the DOS calculated for the planar vacancies with different Bi segregation levels (Supporting Information Figure S2). The DOS plots indicate that sole Sn vacancies act as deep *p*-type dopants in the system (0% case), and a further introduction of Bi dopants (25%~100% cases) right shifts the Fermi level and brings compensation with donor (*n*-type) doping. Consequently, the observed planar vacancies are compensating defect clusters formed between donor Bi impurities and the charged native Sn vacancies. In fact, the formations of the compensating vacancy-impurity clusters driven by formation energy minimization have also been reported in other material systems, such as Sb stabilized Si vacancies in Sb doped Si,[14] Li induced Zn vacancies in Li-doped ZnO, [9] and oxygen stabilized Ga vacancies in GaN.[20]

It is of interest to note that for improving the thermoelectric properties of SnTe, attempts have been devoted to suppress the native Sn vacancies in SnTe by doping cations (such as Ga, Sb, In and Bi).[30,31] In many cases, the incorporation of cation dopants didn't give an efficient compensation of Sn vacancies, particularly when the dopant concentration is high.[30,31] This issued can explained by our observation that: in Bi-doped SnTe, the incorporation of Bi dopants promote the formation of Sn planar vacancies, and the higher the Bi concentration, the more Sn vacancies are expected. To understand the impact of the Bi decorated planar vacancies on the electronic properties of our NRs, Figure 7a,b presents the calculated total DOS using the predicted stable atomic structures (100% cases in Figure 6b,e) of R-type and U-type defects. As a comparison, total DOS calculated for bulk SnTe is also presented (as the grey background), which shows consistent features with reported calculation results.[36-38] The calculated band gap ($E_g$) of pure SnTe (0.28 eV) is in good agreement with experimentally determined bandgap (0.3 eV at 4 K).[39] In contrast to bulk SnTe, the $E_g$ for the systems with R-type and U-type planar vacancies are relatively smaller, with a value of 0.12 and 0.19 eV, respectively. This is mainly

resulted from the shift of conduction band minimum (CBM) toward to the Fermi level (0.15 eV for R-type, 0.08 eV for U-type). Figure 7c and 7d show the partial DOS (PDOS) projected on specific valence orbitals (*d*, *s* and *p* states) of Sn, Bi and Te atoms, for R-type and U-type defects, respectively. The PDOS reveals that the CBM shift is mainly attributed to Sn-*p* and Bi-*p* states. In the total DOS of U-type defect, additional acceptor state at ~0.4eV above CBM can be found (red arrows, Figure 7b), which is not evident in the case of R-type defects and SnTe, indicating that these states originate from the local variation in the defect geometric features, such as the under-coordination of ions and local strain.[40] From Figure 7d, these acceptor states stem from the hybridization of Sn-*p* and Bi-*p* states. Meanwhile, localized valence states can also be found for both R-type and U-type defects, at ~0.3 eV below the valence band maximum (blue arrows, Figure 7a,b), which is induced by the strong interaction of the Bi-*p* sand Te-*p* states. Previous studies on SnTe related thermoelectric materials have shown that local increase of DOS near the Fermi level helps enhance the Seebeck coefficient and the thermoelectric performance.[26,41-43] Therefore we anticipate that the additional gap states brought by the planar vacancies may play a decisive role to the overall properties of the system.

**Conclusion**

In summary, we have demonstrated that Bi dopants promote the formation of planar vacancies in SnTe-based NRs. Detailed atomic-scale analysis indicates that Bi atoms preferentially occupy at the nearby cation sites of the planar vacancies, driven by the need of formation-energy minimization and the local charge balancing. These planar vacancies exhibit local variation in structural relaxation level. When terminating at the NR surface, the planar vacancies (R-type) exhibit large structural relaxation level, and are characterized by low formation energy. Determination of the atomic structure of these planar vacancies with such atomistic detail has enabled us to predict their corresponding electronic properties. Calculations show that the Bi segregated planar vacancies introduce localized DOS distortion into the system, which provides opportunities for the future applications of chalcogenide materials.

**Methods**

*Sample Growth.* $Sn_{1-x}Bi_xTe$ NRs with different Bi concentrations were grown by catalyst-free chemical vapour deposition method in a horizontal tube furnace, using Bi, Sn and Te elemental powders as precursors, coflow of Ar and $H_2$ as carrier gas and Si(100) as substrates. In a typical synthesis, Bi and Sn powders were put at the heating centre with a heating temperature of 750$^{o}$C, while Te powder was put 14 cm away at the upper-stream area from the center. NR samples were collected from Si substrates ~12 cm away from furnace centre, at a growth temperature of approximately 500$^{o}$C. The compositional control of the nanostructures was realized by varying the weight ratios of Bi and Sn powders.

*Microscopic Characterization.* Morphology of the samples supported by their substrates was characterized using SEM (JEOL 7800). Structural and chemical characteristics of the samples were characterized using 200-kV TEM (FEI Tecnai F20), equipped with energy-dispersive X-ray spectroscopy (EDS) for compositional quantification analysis. The HAADF images were obtained using a 200-kV STEM (JEOL 2100F) equipped with an aberration corrector (CEOS Gmbh). In the HAADF imaging, a probe convergence angle of ~22 mrad, and a HAADF detector with an inner semi-angle of over 60 mrad were adopted.

*Calculation Methodology.* Calculations of energies and electronic structures were performed using the Vienna *ab initio* simulation package (VASP) within the framework of DFT. The projector augmented wave (PAW) method was employed for electron-ion interactions, and the generalized gradient approximation (GGA) of Perdew *et al.* (PW91) was used to describe the exchange-correlation functional.[44] The Kohn-sham wave function was expanded in a plane wave basis with a cut-off energy of 400 eV. Potentials for Sn, Bi and Te contained the $5s^25p^2$, $6s^26p^3$ and $5s^25p^4$ electrons as valence, respectively. The *k*-point mesh was generated within Monkhorst Packscheme and applied for all calculations. Optimized grid for R-type and U-type defect supercells is 6×3×1 and 5×3×3, respectively, to guarantee the convergence of 1 meV/unit. R-type planar defects were modelled by periodic supercells with a dimension of 4.52×7.84×56.36 Å. U-type planar defects were modelled by periodic supercells with a dimension of 4.47×22.11×38.62 Å. The supercells were further doubled for examining the size effect. All atoms in the supercells were fully optimized until the magnitude of force on every atom fell below 0.05 eV/Å, and the total energy converged up to $10^{-4}$ eV. The self-consistent

calculations were performed using tetrahedron method with Blöchl corrections with energy convergence criteria of $10^{-5}$ eV.

## Figure Captions

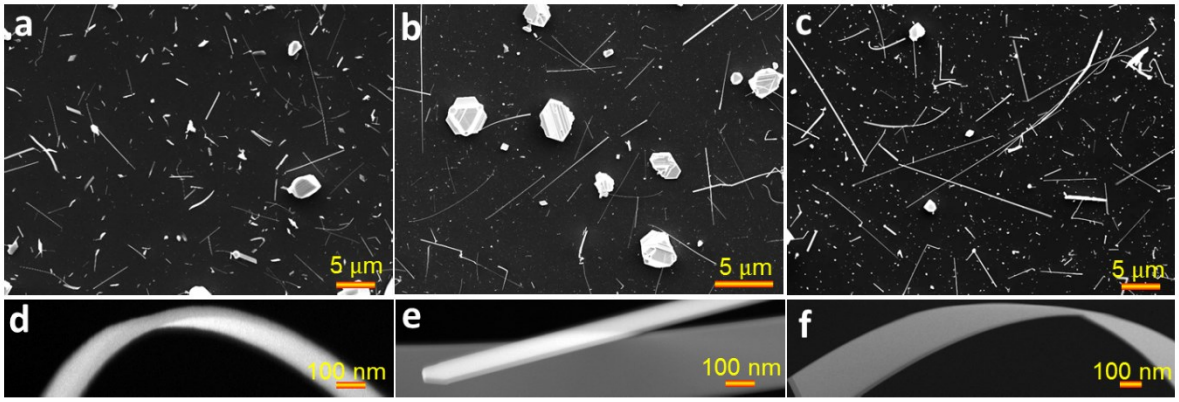


**Figure 1.** (a-c) Over-view SEM images taken from NRs with compositions of $Sn_{0.85}Bi_{0.15}Te$ (a), $Sn_{0.8}Bi_{0.2}Te$ (b), and $Sn_{0.7}Bi_{0.3}Te$ (c). (d-f) High-magnified SEM images taken from NRs with compositions of $Sn_{0.85}Bi_{0.15}Te$ (d), $Sn_{0.8}Bi_{0.2}Te$ (e), and $Sn_{0.7}Bi_{0.3}Te$ (f).

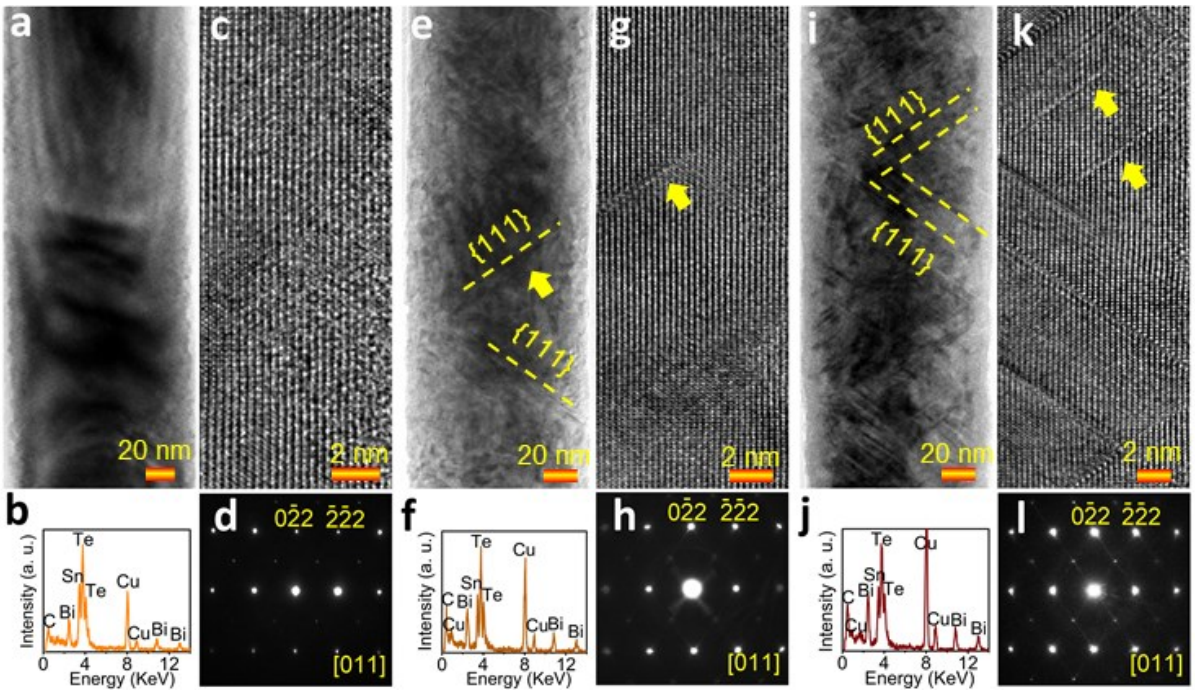


**Figure 2.** (a,e,i) BF TEM images, (b,f,j) EDS profiles, (c,g,k) HRTEM images, and (d,h,l) SAEDs of NRs with compositions of $Sn_{0.85}Bi_{0.15}Te$, (a-d) $Sn_{0.8}Bi_{0.2}Te$ (e-h), and $Sn_{0.7}Bi_{0.3}Te$. (i-l). Typical planar defects are marked with yellow dash lines and yellow arrows. All TEM images are taken along [011] axis.

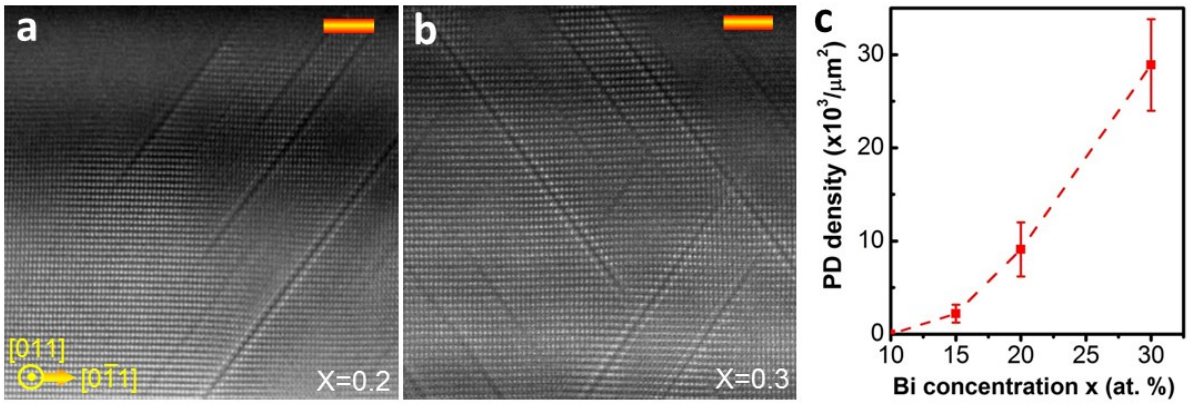


**Figure 3.** (a, b) Atomic-resolution HAADF STEM imaging showing planar defects in (a) $Sn_{0.8}Bi_{0.2}Te$ and (b) $Sn_{0.7}Bi_{0.3}Te$ NRs. (c) Planar defect (PD) density as a function of Bi concentration, counted from experimental images taken from NRs with different Bi concentrations. Scale bars are 2 nm.

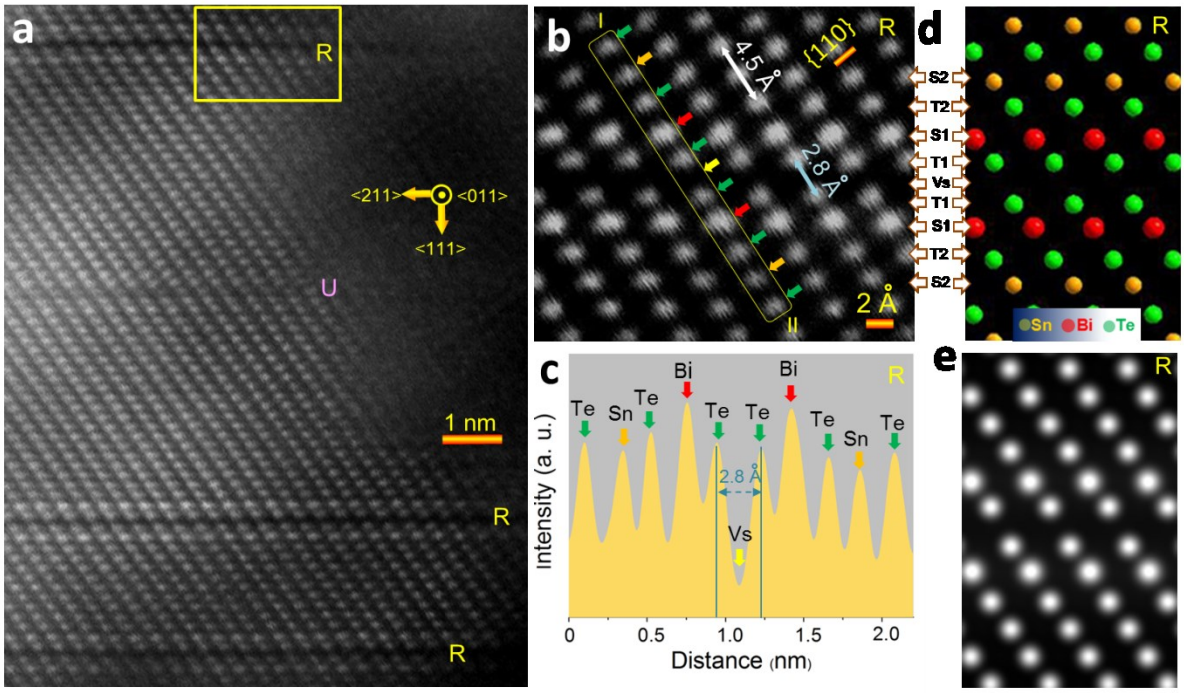


**Figure 4.** (a) HAADF STEM image showing four planar defects obtained from the edge of a $Sn_{0.7}Bi_{0.3}Te$ NR. (b) Magnified HAADF STEM image showing a section of the R-type planar vacancies. (c) Line profiles showing the image intensity along the line I-II defined in (b). (d) Corresponding atomic model calculated by DFT for R-type planar vacancies. (e) Simulated HAADF STEM image using the atomic model in (d).

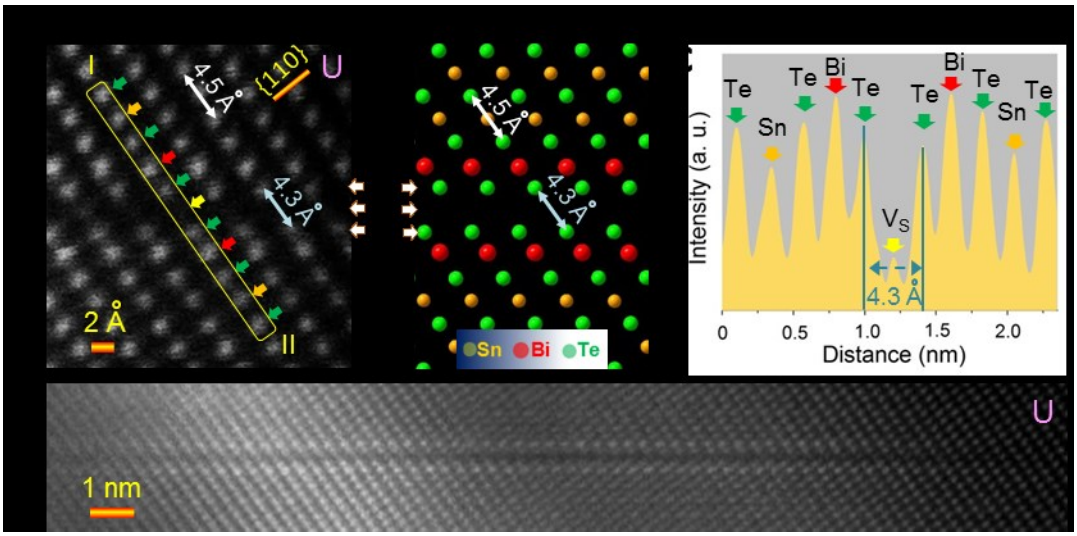


**Figure 5.** (a) HAADF STEM image taken from the edge of U-type planar vacancies. (b) Relaxed atomic models for U-type planar vacancies calculated by DFT. (c) Line profile showing image intensity along the line I-II in (a). (d) A HAADF STEM image of a U-type planar defect bounded with the bulk atoms.

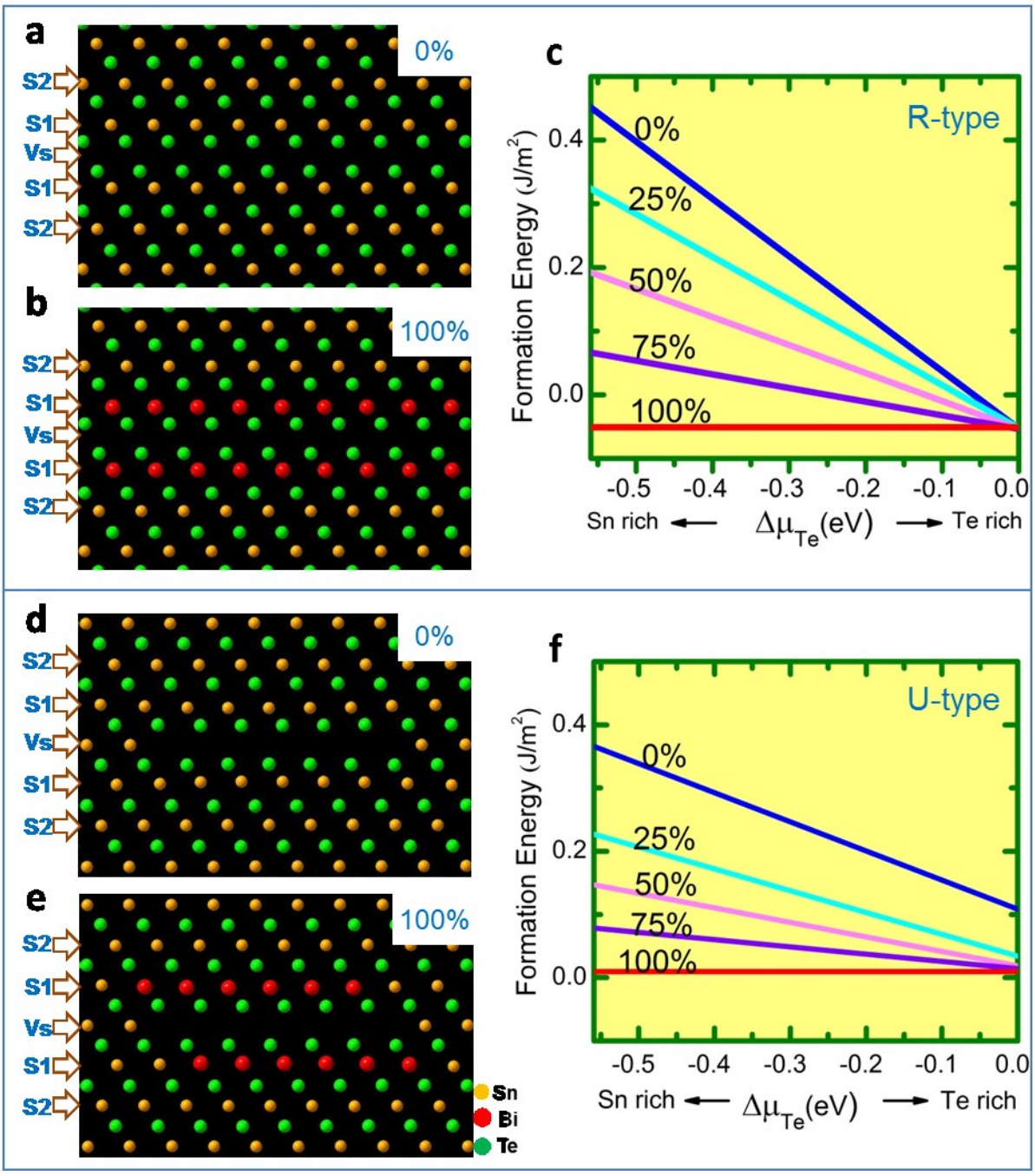


**Figure 6.** (a, b) Relaxed atomic models for R-type planar vacancies without Bi segregation (a) and with 100% Bi substitution (b) at S1. (c) Formation energies of R-type planar vacancies with different Bi substitution concentrations. (d, e) Relaxed atomic models for R-type planar vacancies without Bi segregation (d) and with 100% Bi substitution (e) at S1. (f) Formation energies of U-type planar vacancies with different Bi substitution concentrations.

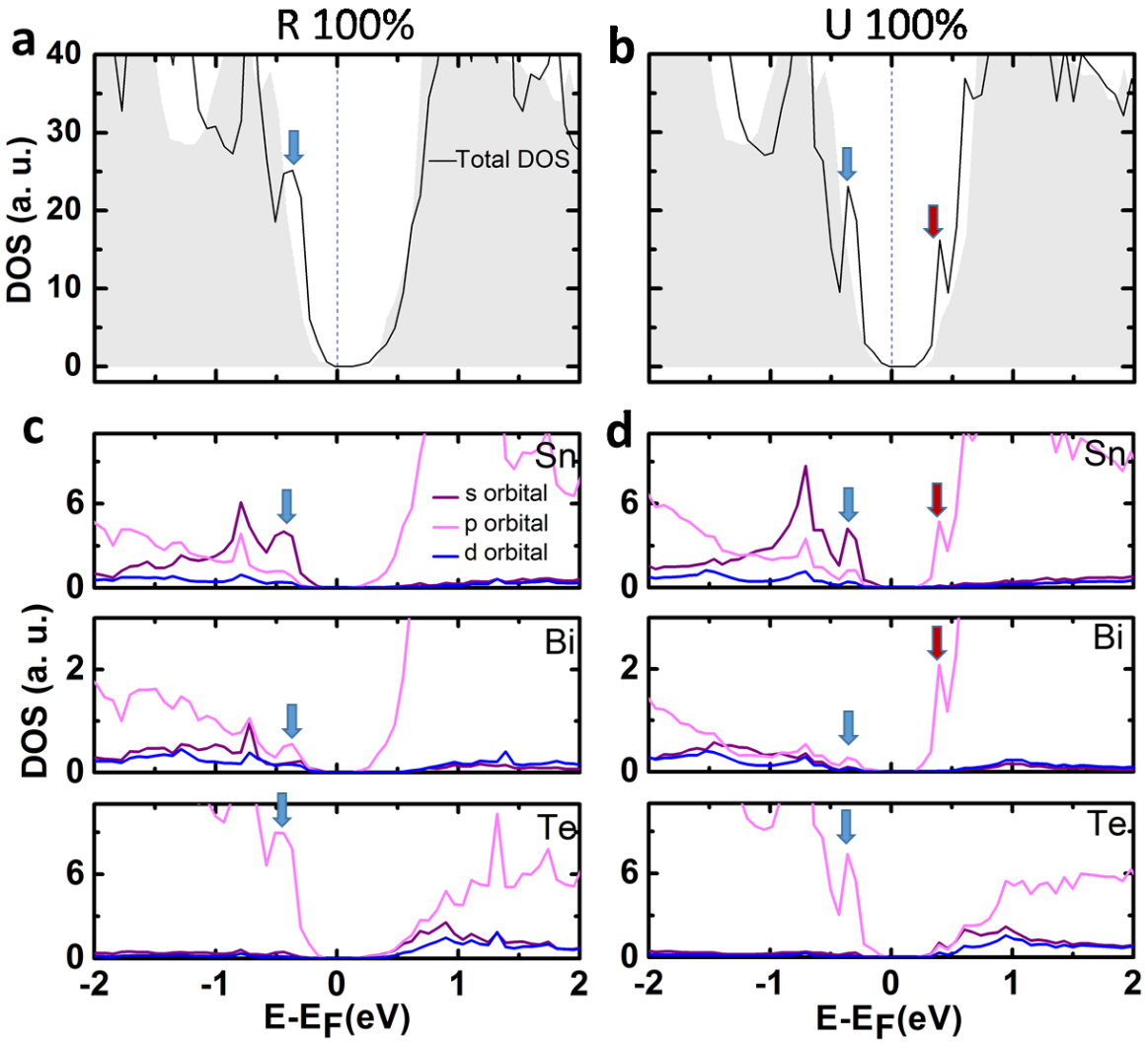


**Figure 7.** (a, b) Total DOS and PDOS for Sn, Bi and Te atoms for (a) R-type and (b) U-type planar vacancies with full Bi segregation, the total DOS for bulk SnTe is given as the grey shaded area. (c, d) PDOS plots of the *s, p, d* orbitals of Sn, Bi and Te atoms in (c) R-type and (d) U-type planar vacancies with full Bi segregation. The Fermi level is set to zero and indicated by a vertical dotted line.

## S1. EDS Line Scan and Mapping for $Sn_{1-x}Bi_xTe$ Nanoribbons

Figure S1 show a typical STEM-EDS line-scan and mapping analysis conducted on $Sn_{0.7}Bi_{0.3}Te$ NR, demonstrating its elemental composition across the entire sample.

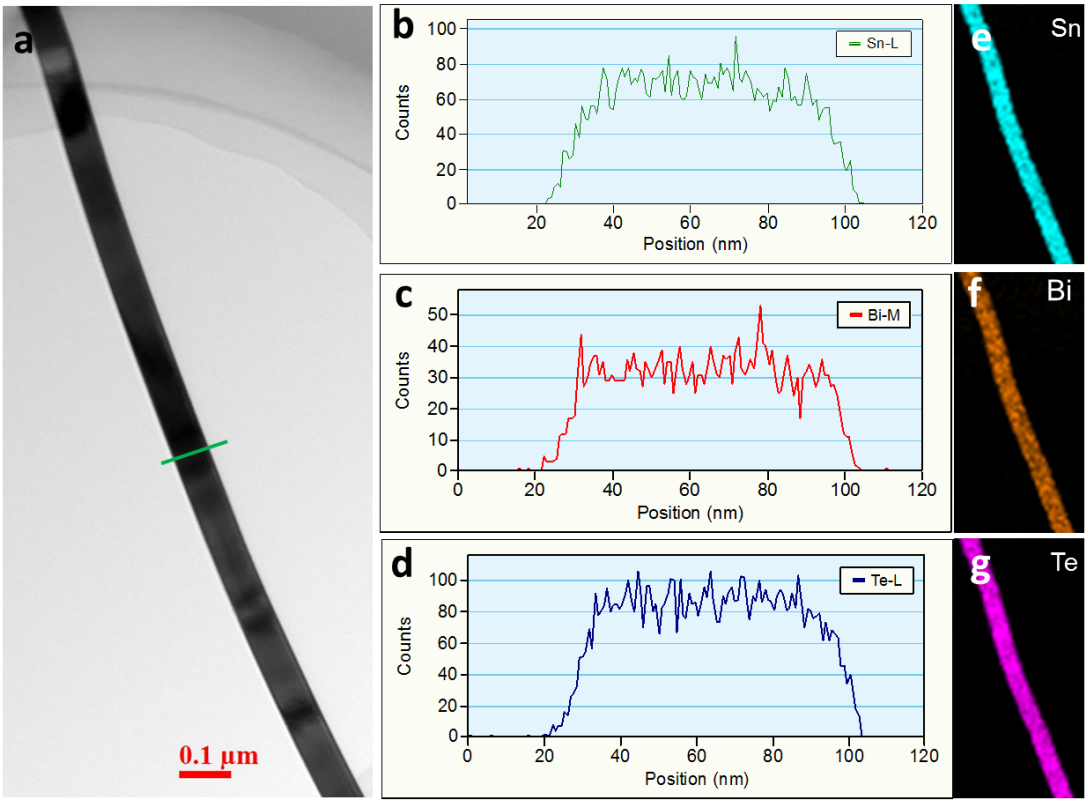


**Figure S1**. (a) A typical BF TEM of a $Sn_{0.7}Bi_{0.3}Te$ NR. (b-d) Corresponding EDS line scan profiles obtained along the green line in (a), for element Sn (b), Bi (c) and Te (d). (e-g) Corresponding EDS mapping images taken from the NR in (a), for element Sn (e), Bi (f) and Te (g).

**S2. Comparison of R-type vacancy structure with the rhombohedral structure of $Bi_2Te_3$**

Figure S2 shows the analogy diagram of R-type vacancy structure to rhombohedral structured $Bi_2Te_3$, in which their stacking sequences are labelled by Greek and Capital letters.[1] They both show a stacking sequence of A($\alpha$)B(*V*)A($\alpha$)B at the vacancy region, where *V* denotes the vacancy layer.

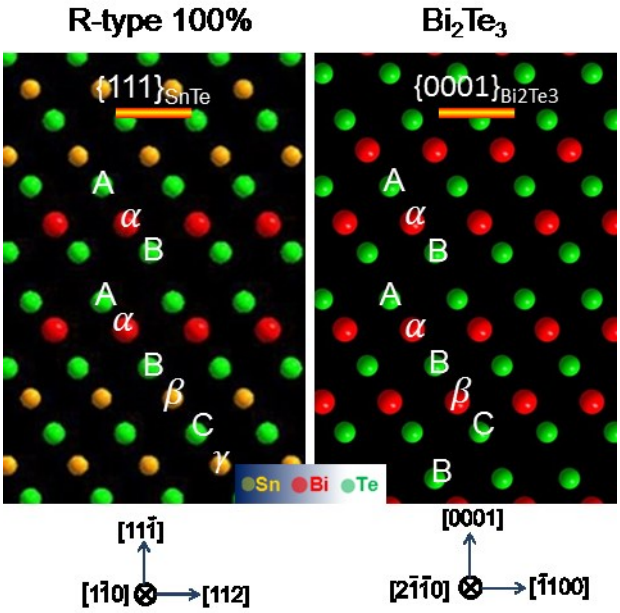


**Figure S2** Projected atomic models of R-type planar vacancies, and rhombohedral structured $Bi_2Te_3$, where the stacking sequences of cationic (Bi/Sn) and Te atomic planes are respectively denoted by Greek and Capital letters.

**S3. Total DOS of planar vacancies with different Bi segregation levels**

Figure S3 shows the total DOS calculated for both R-type and U-type planar vacancies with different Bi segregation levels at S1 sites. For 0~75% cases, the Fermi levels always lie in valence band, indicating the metallicity for the systems, and the role of Sn vacancies as deep *n*-type dopants. With an increasing Bi segregation level, the Fermi level shifts towards the conduction band, indicating that Bi dopants act as donor (*n*-type) dopants in the system.

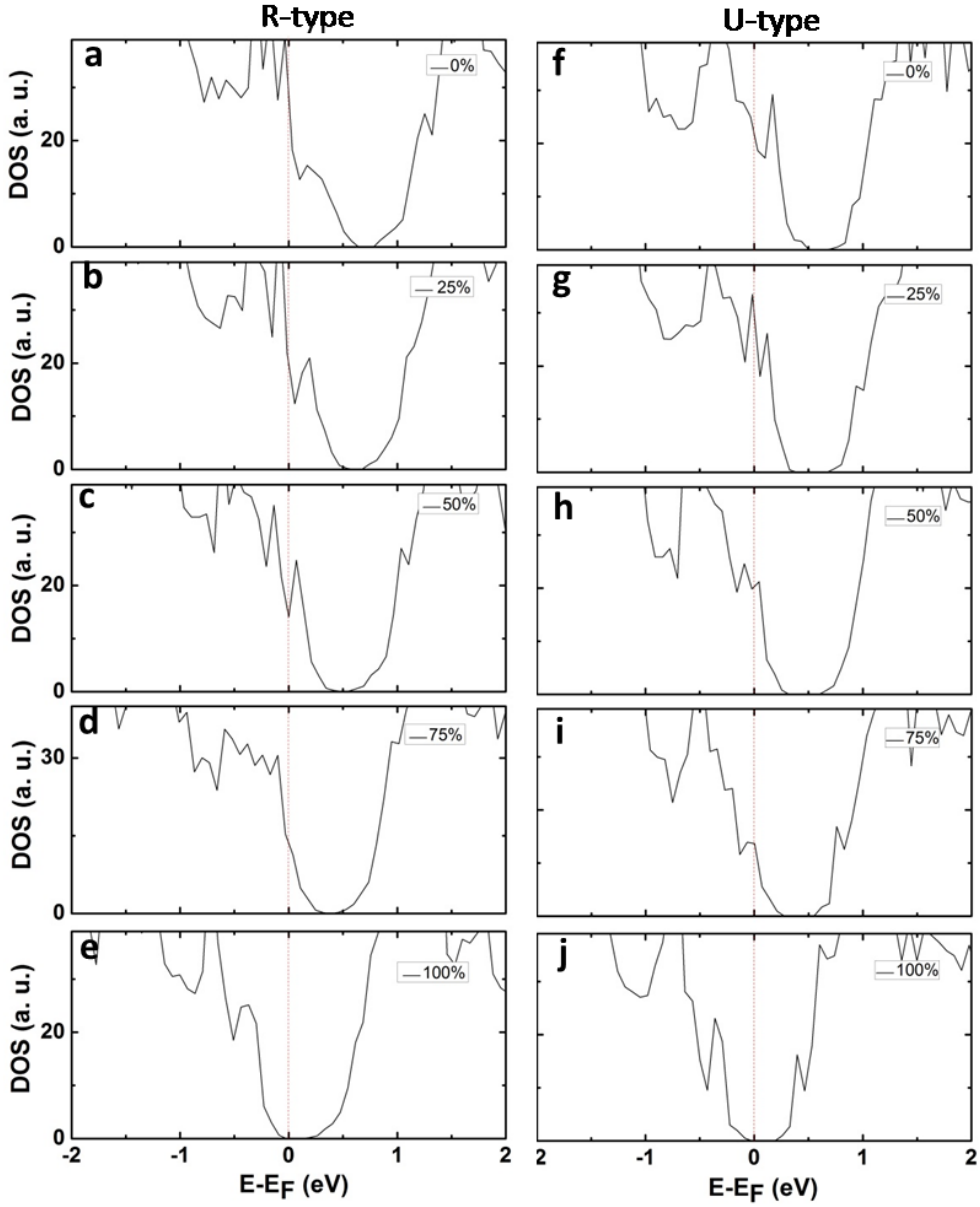

**Figure S3**. Total DOS calculated for R-type (a-e) and U-type (f-j) planar vacancies, with Bi substitution levels (at S1 sites) of 0% (a, f), 25% (b, g), 50% (c, h) 75% (d, i) and 100% (e, j).

## S4. Supercells of R-type and U-type planar vacancies with different Bi substitution levels

Figure S4 shows the supercells adopted for R-type planar defect calculations, which contain 60 atoms, with 28 cationic (Sn/Bi) atoms and 32 Te atoms.

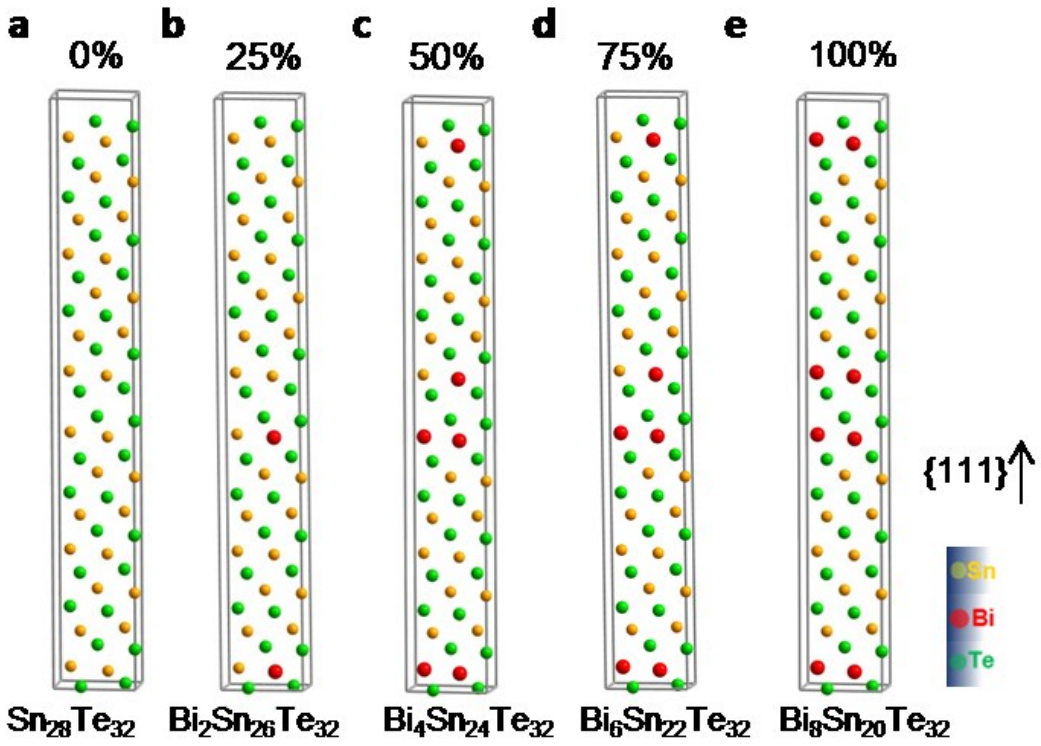


**Figure S4** Relaxed supercells for R-type planar vacancies with Bi segregation levels of (a) 0%, (b) 25%, (c) 50%, (d) 75% and (e) 100%.

Figure S5a-e show the supercells adopted for U-type planar defect calculations, which contain 114 atoms, with 54 cationic (Sn/Bi) atoms and 60 Te atoms. Figure S5f-g show that the energetic-favourable substitution sites for Bi dopants are 1-6#, in

which site 6# has the lowest substitution energy. Therefore, sites 1-6# were chosen for Bi substitution to build supercells for U-type planar vacancies with 25~100% Bi segregation (Figure S5b-e).

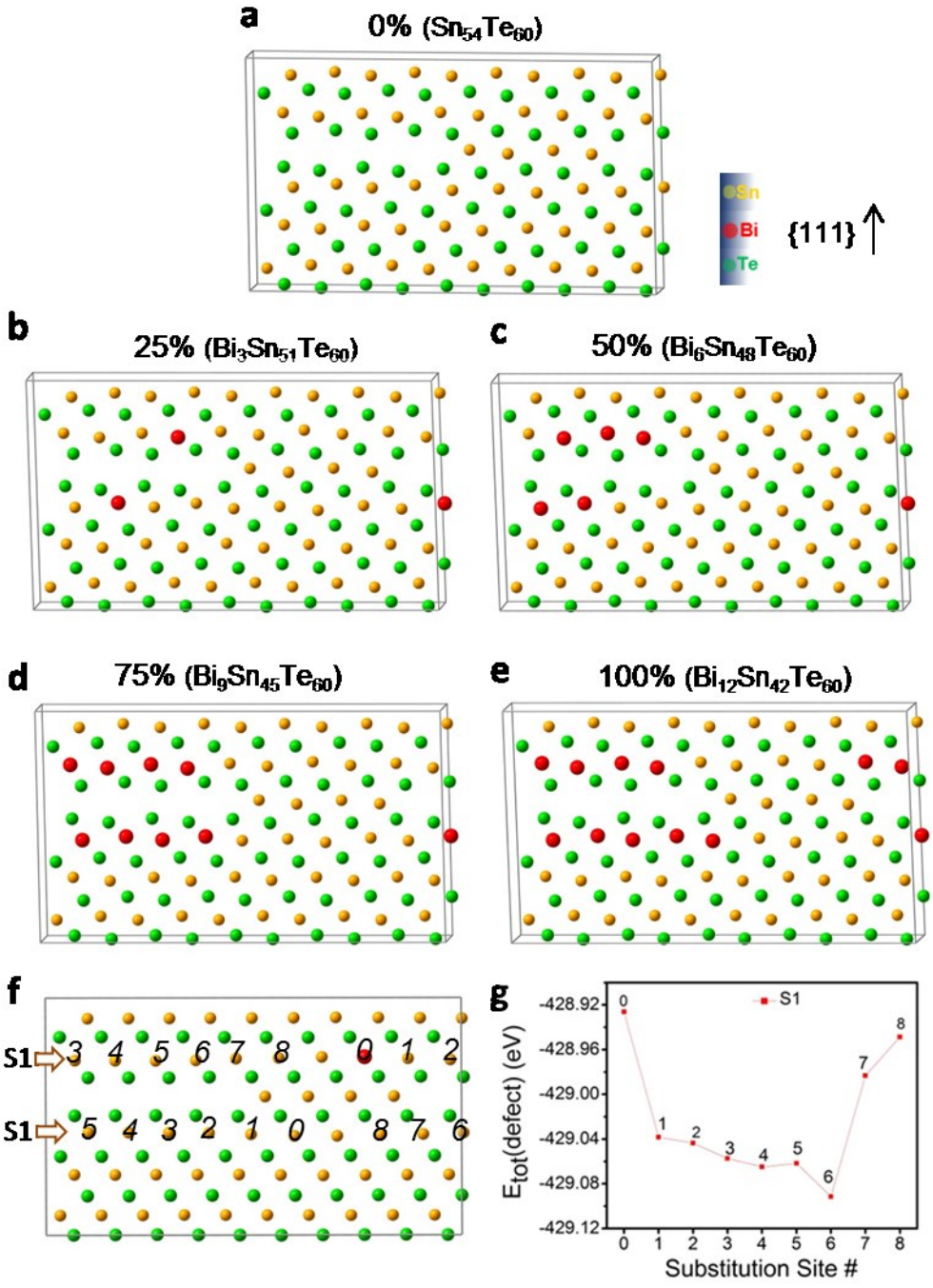


**Figure S5** Relaxed supercells for U-type planar vacancies with Bi segregation levels of (a) 0%, (b) 25%, (c) 50%, (d) 75% and (e) 100%. (f) Projected atomic model of a U-type planar vacancy supercell ($BiSn_{53}Te_{60}$) with Bi substituting one of the nine

possible substitution sites in S1 sites (labelled as 0 through 8). (g) Total energies of the supercells with Bi substituting at one of the sites labelled in (f), revealing that sites 1-6# are energy favourable for Bi substitution.

**References**


1. Li, W.; Ding, H.; Deng, P.; Chang, K.; Song, C.; He, K.; Wang, L.; Ma, X.; Hu, J.-P.; Chen, X.; Xue, Q.-K. Phase separation and magnetic order in K-doped iron selenide superconductor. *Nat. Phys.* **2012,** 8, 126-130.
2. Voneshen, D. J.; Refson, K.; Borissenko, E.; Krisch, M.; Bosak, A.; Piovano, A.; Cemal, E.; Enderle, M.; Gutmann, M. J.; Hoesch, M.; Roger, M.; Gannon, L.; Boothroyd, A. T.; Uthayakumar, S.; Porter, D. G.; Goff, J. P. Suppression of thermal conductivity by rattling modes in thermoelectric sodium cobaltate. *Nat. Mater.* **2013,** 12, 1028-1032.
3. Kim, C. E.; Kurosaki, K.; Ishimaru, M.; Jung, D. Y.; Muta. H.; Yamanaka, S. Effect of Periodicity of the Two-dimensional vacancy planes on the Thermal conductivity of bulk $Ga_2Te_3$. *Phys. Status Solidi RRL* **2009,** 3, 221-223.
4. Rosenthal, T.; Schneider, M. N.; Stiewe, C.; Döblinger, M.; Oeckler, O. Real Structure and thermoelectric properties of GeTe-rich germanium antimony tellurides. *Chem. Mater.* **2011,** 23, 4349-4356.
5. Inam, F. A.; Grogan, M. D. W.; Rollings, M.; Gaebel, T.; Say, J. M.; Bradac, C.; Birks, T. A.; Wadsworth, W. J.; Castelletto, S.; Rabeau, J. R.; Steel, M. J. Emission and nonradiative decay of nanodiamond NV centers in a low refractive index environment. *ACS Nano* **2013,** 7, 3833-3843.
6. Wang, Z.; Xu, K.; Li, Y.; Zhan, X.; Safdar, M.; Wang, Q.; Wang, F.; He, J. Role of Ga vacancy on a multilayer GaTe phototransistor. *ACS Nano* **2014,** 8, 4859-4865.
7. Balandin, A. A.; Nika, D. L. Phononics in low-dimensional materials. *Materials Today* **2012,** 15, 266-275.
8. Wang, Q.; Sun, Q.; Chen, G.; Kawazoe, Y.; Jena, P. Vacancy-induced magnetism in ZnO thin films and nanowires. *Phys. Rev. B* **2008,** 77, 205411.
9. Yi, J. B.; Lim, C. C.; Xing, G. Z.; Fan, H. M.; Van, L. H.; Huang, S. L.; Yang, K. S.; Huang, X. L.; Qin, X. B.; Wang, B. Y.; Wu, T.; Wang, L.; Zhang, H. T.; Gao, X. Y.; Liu, T.; Wee, A. T. S.; Feng, Y. P.; Ding, J. Ferromagnetism in dilute magnetic semiconductors through defect engineering: Li-doped ZnO. *Phys. Rev. Lett.* **2010,** 104, 137201.
10. Zhang, W.; Thiess, A.; Zalden, P.; Zeller, R.; Dederichs, P. H.; Raty, J. Y.; Wuttig, M.; Blügel, S.; Mazzarello, R. Role of Vacancies in metal–insulator

transitions of crystalline phase-change materials. *Nat. Mater.* **2012,** 11, 952-956.

11. Kittel, C. *Introduction to Solid State Physics*. Wiley: 2005.
12. Kobayashi, S.; Mizumukai, Y.; Ohnishi, T.; Shibata, N.; Ikuhara, Y.; Yamamoto, T. High electron mobility of Nb-doped $SrTiO_3$ films stemming from rod-type Sr vacancy clusters. *ACS Nano* **2015,** 9, 10769-10777.
13. Wang, Z.; Saito, M.; McKenna, K. P.; Gu, L.; Tsukimoto, S.; Shluger, A. L.; Ikuhara, Y. Atom-resolved imaging of ordered defect superstructures at individual grain boundaries. *Nature* **2011,** 479, 380-383.
14. Voyles, P. M.; Muller, D. A.; Grazul, J. L.; Citrin, P. H.; Gossmann, H. J. L. Atomic-scale imaging of individual dopant atoms and clusters in highly n-Type bulk Si. *Nature* **2002,** 416, 826-829.
15. Rummukainen, M.; Makkonen, I.; Ranki, V.; Puska, M. J.; Saarinen, K.; Gossmann, H. J. L. Vacancy-impurity complexes in highly Sb-doped Si grown by molecular beam epitaxy. *Phys. Rev. Lett.* **2005,** 94, 165501.
16. Look, D. C.; Leedy, K. D.; Vines, L.; Svensson, B. G.; Zubiaga, A.; Tuomisto, F.; Doutt, D. R.; Brillson, L. J. Self-compensation in semiconductors: the Zn vacancy in Ga-doped ZnO. *Phys. Rev. B* **2011,** 84, 115202.
17. Steiauf, D.; Lyons, J. L.; Janotti, A.; Van de Walle, C. G. First-principles study of vacancy-assisted impurity diffusion in ZnO. *APL Mater.* **2014,** 2, 096101.
18. Kwon, D.-H.; Kim, K. M.; Jang, J. H.; Jeon, J. M.; Lee, M. H.; Kim, G. H.; Li, X.-S.; Park, G.-S.; Lee, B.; Han, S.; Kim, M.; Hwang, C. S. Atomic structure of conducting nanofilaments in $TiO_2$ resistive switching memory. *Nat. Nanotech.* **2010,** 5, 148-153.
19. Goto, T.; Iwatsuki, T.; Takagi, Y. Infinite layer of solution-spun $(Ca_{1-x}Sr_x)YCuO_{2-Z}$ filaments. *J. Supercond.* **1994,** 7, 23-25.
20. Neugebauer, J.; Van de Walle, C. G. Gallium vacancies and the yellow luminescence in GaN. *Appl. Phys. Lett.* **1996,** 69, 503-505.
21. He, Z.; He, K.; Robertson, A. W.; Kirkland, A. I.; Kim, D.; Ihm, J.; Yoon, E.; Lee, G.-D.; Warner, J. H. Atomic structure and dynamics of metal dopant pairs in graphene. *Nano Lett.* **2014,** 14, 3766-3772.

22. Lin, J.; Pantelides, S. T.; Zhou, W. Vacancy-induced formation and growth of inversion domains in transition-metal dichalcogenide monolayer. *ACS Nano* **2015,** 9, 5189-5197.
23. Koski, K. J.; Cui, Y. The new skinny in two-dimensional nanomaterials. *ACS Nano* **2013,** 7, 3739-3743.
24. Shen, J.; Xie, Y.; Cha, J. J. Revealing surface states in In-Doped SnTe nanoplates with low bulk mobility. *Nano Lett.* **2015,** 15, 3827-2832.
25. Tanaka, Y.; Ren, Z.; Sato, T.; Nakayama, K.; Souma, S.; Takahashi, T.; Segawa, K.; Ando, Y. Experimental realization of a topological crystalline insulator in SnTe. *Nat. Phys.* **2012,** 8, 800-803.
26. Chen, Z. G.; Han, G.; Yang, L.; Cheng, L. N.; Zou, J. Nanostructured thermoelectric materials: current research and future challenge. *Prog. Nat. Sci.* **2012,** 22, 535-549.
27. Zou, Y.; Chen, Z.; Lin, J.; Zhou, X.; Lu, W.; Drennan, J.; Zou, J. Morphological control of SnTe nanostructures by tuning catalyst composition. *Nano Res.* **2015,** 8, 3011-3019.
28. Li, Z.; Shao, S.; Li, N.; McCall, K.; Wang, J.; Zhang, S. X. Single crystalline nanostructures of topological crystalline insulator SnTe with distinct facets and morphologies. *Nano Lett.* **2013,** 13, 5443-5448.
29. Zhang, Q.; Liao, B.; Lan, Y.; Lukas, K.; Liu, W.; Esfarjani, K.; Opeil, C.; Broido, D.; Chen, G.; Ren, Z. High thermoelectric performance by resonant dopant indium in nanostructured SnTe. *Proc. Natl. Acad. Sci. U.S.A.* **2013,** 110, 13261-13266.
30. Zhao, L.-D.; Zhang, X.; Wu, H.; Tan, G.; Pei, Y.; Xiao, Y.; Chang, C.; Wu, D.; Chi, H.; Zheng, L.; Gong, S.; Uher, C.; He, J.; Kanatzidis, M. G. Enhanced thermoelectric properties in the counter-doped SnTe system with strained endotaxial SrTe. *J. Am. Chem. Soc.* **2016,** 138, 2366-2373.
31. Tan, G.; Shi, F.; Hao, S.; Chi, H.; Bailey, T. P.; Zhao, L.-D.; Uher, C.; Wolverton, C.; Dravid, V. P.; Kanatzidis, M. G. Valence band modification and high thermoelectric performance in SnTe heavily alloyed with MnTe. *J. Am. Chem. Soc.* **2015,** 137, 11507-11516.

32. Hoang, K.; Mahanti, S. D.; Kanatzidis, M. G. Impurity clustering and impurity-induced bands in PbTe-, SnTe-, and GeTe-based bulk thermoelectrics. *Phys Rev. B* **2010,** 81, 115106.
33. Deng, B.; Luisa da Rosa, A.; Frauenheim, T.; Xiao, J. P.; Shi, X. Q.; Zhang, R. Q.; Van Hove, M. A. Oxygen vacancy diffusion in bare ZnO nanowires. *Nanoscale* **2014,** 6, 11882-11886.
34. Wang, Z.; Okude, M.; Saito, M.; Tsukimoto, S.; Ohtomo, A.; Tsukada, M.; Kawasaki, M.; Ikuhara, Y. Dimensionality-driven insulator–metal transition in A-site excess non-stoichiometric perovskites. *Nat. Commun.* **2010,** 1, 106.
35. Wang, N.; West, D.; Liu, J.; Li, J.; Yan, Q.; Gu, B.-L.; Zhang, S. B.; Duan, W. Microscopic origin of the p-type conductivity of the topological crystalline insulator SnTe and the effect of Pb alloying. *Phys. Rev. B* **2014**, 89, 045142.
36. Matsunaga, T.; Kojima, R.; Yamada, N.; Kifune, K.; Kubota, Y.; Tabata, Y.; Takata, M. Single structure widely distributed in a GeTe−$Sb_2Te_3$ pseudobinary system: a rock salt structure is retained by intrinsically containing an enormous number of vacancies within its crystal. *Inorg. Chem.* **2006,** 45, 2235-2241.
37. Chen, X.; Parker, D.; Singh, D. J. Importance of non-parabolic band effects in the thermoelectric properties of semiconductors. *Sci. Rep.* **2013,** 3, 3168.
38. Al Rahal Al Orabi, R.; Mecholsky, N. A.; Hwang, J.; Kim, W.; Rhyee, J.-S.; Wee, D.; Fornari, M. Band Degeneracy, Low thermal conductivity and high thermoelectric figure of merit in SnTe–CaTe alloys. *Chem. Mater.* **2016,** 28, 376-384.
39. Esaki, L.; Stiles, P. J. New type of negative resistance in barrier tunneling. *Phys. Rev. Lett.* **1966,** 16, 1108-1111.
40. Wang, Z.; Saito, M.; McKenna, K. P.; Ikuhara, Y. Polymorphism of dislocation core structures at the atomic scale. *Nat. Commun.* **2014,** 5, 3239.
41. Xiong, K.; Longo, R. C.; Wang, W.; Gupta, R. P.; Gnade, B. E.; Cho, K. Enhancement of the thermoelectric efficiency of PbTe by selective site doping: effect of group VA impurities. *Comp. Mater. Sci.* **2015,** 97, 159-164.
42. Heremans, J. P.; Jovovic, V.; Toberer, E. S.; Saramat, A.; Kurosaki, K.; Charoenphakdee, A.; Yamanaka, S.; Snyder, G. J. Enhancement of thermoelectric efficiency in PbTe by distortion of the electronic density of states. *Science* **2008,** 321, 554-557.

43. Heremans, J. P.; Wiendlocha, B.; Chamoire, A. M. Resonant levels in bulk thermoelectric semiconductors. *Energy Environ. Sci.* **2012,** 5, 5510-5530.
44. Perdew, J. P.; Burke, K.; Ernzerhof, M. Generalized gradient approximation made simple. *Phys. Rev. Lett.* **1996,** 77, 3865-3868.

# 7

# Morphological Control of SnTe Nanostructures by Bi Doping

## 7.1 Introduction

Chapter 5 and 6 have discussed the morphology of un-doped SnTe and Bi doped SnTe nanostructures. The un-doped SnTe nanostructures show morphologies of NW and nanoplate, which are all dominated by {100} surface facet, whereas the Bi doped SnTe nanostructures shows a distinct morphology of NR. To clarify the impact of Bi dopant on the morphology of SnTe nanostructures, in this chapter, we investigate into the surface-facet control of single-crystalline SnTe nanostructures by Bi doping. The nanostructured un-doped and Bi-doped SnTe samples were synthesized through catalyst-free CVD method. The surface-facet control is realized by surface energy engineering through the combination of CVD experiments with first-principles calculations.

## 7.2 Journal Publication

These results are to be submitted for publication soon.

**Bi-Doped SnTe Nanoribbons with {111} Surface Facets**

Yi-Chao Zou,[†] Zhi-Gang Chen,[†] Fantai Kong,[§] John Drennan,[‖] Kyeongjae Cho,[§] Enze Zhang,[‡] Faxian Xiu, [‡] Jin Zou[†,‖]

[†] Materials Engineering, University of Queensland, Brisbane, QLD 4072, Australia
[§] Department of Materials Science & Engineering, The University of Texas at Dallas, Richardson, TX 75080, USA.
[‡] Key Laboratory of Surface Physics and Department of Physics, and Collaborative Innovation Center of Advanced Microstructures, Fudan University, Shanghai 200433, China
[‖] Centre for Microscopy and Microanalysis, University of Queensland, Brisbane, QLD 4072, Australia

**Abstract**

Facet control of SnTe nanostructures is important for the realization of their property modifications. For pure SnTe nanocrystals, both theoretical and experimental studies found that {100} surface facets are the most stable, and it is challenging to realize the synthesis of uniform SnTe nanostructures with high percentage of {111} surface facet. In this work, through chemical vapour deposition experiments in combination with density functional calculations, we demonstrate that Bi doping is an effective method to control the surface facet of SnTe by surface-energy engineering. Using this method, we have realized the growth of Bi doped SnTe nanoribbons with {111} dominated surface facet.

**Keywords**: tin telluride, nanoribbon, surface facet, morphology control

## Introduction

As one of the new-emerging topological insulators, topological crystalline insulator (TCI) has recently attracted extensive attention, which possesses gapless surface states protected by crystalline symmetries rather than time-reversal symmetries.[1] TCIs were firstly discovered within the class of rock-salt structured IV-VI semiconductors, such as SnTe and $Pb_{1-x}Sn_xTe$.[2] Theoretical studies predicted that topological surface states exist on their high-symmetry surfaces, such as {100}, {110} and {111}.[2] Experimentally, the existence of Dirac surface states in {100} and {111} surfaces of SnTe has been confirmed by both angle-resolved photoemission spectroscopy measurements and scanning tunneling microscopy,[4,5] which also show that the modulation of the surface states can be achieved by strain or alloying.[5] The unique and tunable surface properties of SnTe have demonstrated its potential spintronic applications.

To manifest the surface states of SnTe, an important approach is to develop low-dimensional SnTe nanostructures.[6] In bulk TCIs, the direct observation and manipulation of the topological surface states are highly challenging due to the dominant bulk contributions.[6] This is because that in pristine SnTe, the intrinsic Sn vacancies largely contribute to the bulk hole concentration, which often masks the surface conductance.[6] On the other hand, low-dimensional SnTe nanostructures with high surface-to-volume ratio provide an excellent system for probing and tuning the surface states, which enables the observation of quantum oscillation effects, including Shubnikov-de Haas oscillations,[7] Aharonov–Bohm oscillations,[7] and weak antilocalization.[6] In addition, with introducing dopants, more exotic properties, such as superconducting[6] and quantum anomalous Hall effect,[8] are presented, making SnTe based nanostructures highly attractive for spintronic applications.

To access the specific surface state in SnTe, it is crucial to grow SnTe nanostructures with controlled surface facet,[9] since each surface facet has its own surface state.[2] For examples, on {100} surfaces, the surface states locate away from $\bar{X}$ points with a double-Dirac-cone structure.[2] In contrast, on {111} surfaces, four Dirac-cone surface states exist, with one centered at $\bar{\Gamma}$ and three centered at $\bar{M}$ points.[2] However, it is still a challenge to fabricate uniform low-dimensional SnTe nanostructures with {111} dominated surface facets, due to the coexistence of low-energy {100} facets.

In this study, we demonstrate that the growth of {111}-dominated SnTe NR can be achieved by Bi doping. We firstly investigated the effect of Bi dopant on the surface facet of SnTe crystals by density functional theory (DFT) calculations, which suggests that Bi doping can switch the relative surface stability between {100} and {111} facets in SnTe. Based on the theoretical predictions, we grow Bi-doped SnTe nanostructures by a facile catalyst-free chemical vapor deposition (CVD) method. Detailed electron microscopy analysis proved that Bi dopant can tune the morphology of SnTe nanostructures. Subsequent magnetotransport measurements conducted on the Bi-doped SnTe NRs show that weak antilocalization (WAL) effect can be observed.

To theoretically understand the effects of Bi doping on the surface energies of SnTe, Figure 1 shows the calculated {100}, {110} and {111} surface energies of SnTe with different Bi doping concentrations of 0 at.%, 4 at.% and 8 at.%. It should be pointed out that in pristine SnTe, {100} and {110} surfaces have equal numbers of Sn and Te atoms, while the {111} surfaces can either be Sn-terminated (denoted as $\{111\}_{Sn}$) or Te-terminated (denoted as $\{111\}_{Te}$). Surface energies ($\gamma$) were calculated as a function of the chemical potentials of the atomic species ($\mu_\alpha$)using the equation[10]:

$$\gamma = \frac{1}{2A}[E_{slab}^{surf} - E_{slab}^{refer} - \sum_\alpha \Delta n_\alpha \, \mu_\alpha] \quad (1)$$

where $A$ is the free surface area of the simulated slab supercell (fully relaxed); $E_{slab}^{surf}$ is the DFT total energy of the slab supercell with specific surface and $E_{slab}^{refer}$is the DFT total energy of reference slab which is derived from atomic energy of bulk SnTe; $\Delta n_\alpha$ are the differential numbers of atom species $\alpha$ (Sn, Te, Bi) relative to the reference slab. In this calculation, the relative Te chemical potential $\Delta\mu_{Te}$ (in the range of −0.559~0 eV) is applied as a variable. $\Delta\mu_{Te}$=0 denotes the Te-rich growth condition and the Te-poor condition corresponds to $\Delta\mu_{Te}$=-0.559 eV.

As can be seen from Figure 1a, for almost the entire range of $\Delta\mu_{Te}$ in un-doped SnTe, the {100} surface energy ($\gamma_{100}$) lies lowest with a value of 9.64 meV/A$^2$, which is in consistent with previous reported calculation results and experimental observation.[10] The surface energies of $\{111\}_{Sn}$ and {110} surfaces are higher than those of $\{111\}_{Te}$ and {100} surfaces, suggesting that only $\{111\}_{Te}$ ($\gamma_{111Te}$) and {100} facets could be presented in the facet configuration of un-doped SnTe nanostructures.[11,12] The comparisons of Figure 1a-c indicate that, with increased Bi

concentration, $\gamma_{111Te}$ gradually decreases while $\gamma_{100}$ increases. When the Bi concentration reaches 8 at.%, $\gamma_{111Te}$ (16.57~3.95 meV/A$^2$) becomes almost lower than $\gamma_{100}$ (14.94~18.26 meV/A$^2$). According to the surface energy profiles in Figure 1a-c, the equilibrium crystal facets (ECFs) were further predicted using the Gibbs-Wulff theory.[12] Figure 1d,f,e respectively show the ECFs of SnTe with different Bi dopant levels under the condition of $\Delta\mu_{Te}$=-0.25eV (ECFs of Te-poor or Te-rich conditions were also calculated, Figure S1). In such a condition, the ECF of pure SnTe is predicted to have the {100} as dominant surfaces (Figure 1d). With the incorporation of Bi dopant (Figure 1e-f), the $\{111\}_{Te}$ facets become dominant, and when the Bi doping level reaches to 8 at%, $\{111\}_{Te}$ facets become the preferred surfaces for the SnTe crystals. These calculation results suggest that the surface energy engineering in SnTe crystals can be achieved through effective Bi doping.

To verify above theoretical predictions, the synthesis of SnTe nanostructures with and without Bi dopants was conducted via CVD. Figure 2a shows a representative scanning electron microscopy (SEM) image of un-doped SnTe nanostructures, in which nanowires (NWs) with cubic cross-section can be seen (inset of Figure 2a). Figure 2b shows a bright-field (BF) transmission electron microscopy (TEM) image of an un-doped SnTe NW. Since this TEM image was taken from an un-tilted TEM specimen, the surface normal of a NW side-wall is anticipated to be parallel to the electron beam. Figure 2c shows the corresponding selective-area electron diffraction (SAED) pattern, which can be indexed as the [100] zone-axis of SnTe, indicating that the NWs are single-crystalline. Figure 2b and 2c indicate that the NWs have {100} facets as side-wall surfaces and a growth direction of [010], leading to a cubic cross-section when viewed along the [010] direction (Figure 2d). This experimental result is in excellent agreement with the theoretical prediction shown in Figure 1a that {100} is the most stable surface facet in un-doped SnTe.

Similar electron microscopic analyses were further conducted for Bi-doped nanostructures with doping levels of 4 at.% (Figure 2e-h) and 8 at.% (Figure 2i-l), respectively. For 4 at.% doped nanostructures, wire morphology can be witnessed (Figure 2e). However, this Bi-doped NW has a different cross-section geometry (slightly distorted hexagon, Figure 2e inset) compared with un-doped NWs (square, Figure 2a inset). Figure 2f,g show respectively a BF TEM image and the corresponding SAED pattern taken from a typical doped NW without tilting the NW.

The SAED pattern can be indexed as the [111] zone-axis of SnTe, and the comparison of Figure 2f,g indicates that the NW has its axial direction of [110]. Crystallographically, the possible side-walls are {mmn} atomic planes (where m and n are integers). Taking the [110] growth direction and cross-section geometries into account (Figure 2e inset), the side facets can be determined as four {111} planes and two {100} planes (all with low surface energies, refer to Figure 1e), as illustrated in Figure 2h. In the case of 8 at.% Bi-doped nanostructures, Figure 2i shows a representative SEM image, in which ribbon-like nanostructures can be seen. The zoom-in SEM image at one end of a ribbon-like nanostructure (Figure 2i inset) illustrates that those ribbon-like nanostructures are NRs with a cross-section geometry of a parallelogram. Further TEM investigation (Figure 2j-k) shows that the NRs grow along the <110> direction. Combining the cross-section morphology (Figure 2i) and the <110> growth direction, the side facets of the NRs can be determined as four {111} facets, as illustrated in Figure 2l.

These detailed electron microscopy results indicate that the dominant surface facet of SnTe were switched from {100} to {111} through the Bi doping, which is in excellent agreement with the theoretical predictions that the Bi incorporation can alter the surface stability between $\{111\}_{Te}$ and {100}.

To obtain the statistical analysis of surface facets, X-ray diffraction (XRD) was performed on the doped and un-doped SnTe nanostructures, and their results are shown in Figure 3a. All the XRD peaks can be indexed exclusively as the rock-salt structured SnTe phase. The comparison of their diffraction peak intensities indicates that, for un-doped SnTe nanostructures, the 200* diffraction peak is the dominating peak with a weak 222* diffraction peak; while with increasing the Bi concentration, the intensity of the 200* diffraction peak decreases but the intensity of the 222* diffraction peak increases. When the SnTe nanostructures doped with 8 at.% Bi, 222* diffraction peak becomes dominating, suggesting that {111} facets become dominated surface facets.

Since Bi atoms have different covalent radii (~1.48 Å) compared with Sn (~1.39 Å) and Te (~1.38 Å), the incorporation of Bi may cause a change of lattice parameters.[13] Figure 3b are XRD patterns to show the detailed positions of 222* diffraction peak for different nanostructures, from which 0.16% ($a$=6.305 Å) and 0.30% ($a$ = 6.314 Å) increase of $a$ can be found for 4 at.% and 8 at.% Bi-doped SnTe

when compared with those of the un-doped SnTe (a = 6.295 Å). This indicates that Bi has been indeed doped in SnTe. To examine the underlying reason for the increased lattice parameter, XPS analysis was performed to understand the chemical state of Bi dopant in Bi-doped nanostructures. Figure 3c shows a XPS survey spectrum taken from the 8 at.% doped NRs, in which Sn, Te and Bi peaks can be found (note that the Si peak is attributed to the Si substrate). Figure 3d shows the high-resolution scan for Bi 4f, in which two peaks, located at 156.8 eV and 158.8 eV, can be respectively attributed to the binding energies of the Bi-Te bonding and the Bi-O bonding (due to the surface oxidation of the sample).[13] This indicates that Bi has substituted Sn in SnTe,[14] which verifies our theoretical models in which the Bi dopants are incorporated to substitute Sn in SnTe. Since the covalent/ionic radius of Bi is slightly larger than that of Sn, the Bi substitution of Sn in the lattice leads to an increase in the lattice parameter of the Bi-doped SnTe.

As SnTe nanostructures are expected to have interesting magnetoresistance (MR) properties,[6] we measured the MR of our NRs by fabricating Hall bar devices. The optical image of the fabricated device is presented in the inset of Figure 4a, in which the current (I) is applied along the longitudinal direction of the NR and the magnetic field (B) is applied perpendicular to the NR surface. Figure 4a plots the temperature (T) dependent resistivity of the NR at zero magnetic field (denoted as $\rho_0$). The $\rho_0$−T curve reveals a metallic behaviour of the NR, similar with previous experiment oberservations.[6] Figure 4b displays the corresponding MR, defined as $\Delta\rho/\rho = (\rho_B - \rho_0)/\rho_B$, measured from 4K to 30K. Interestingly, at low temperatures (4K and 6K), a sharp dip in MR can be observed when the magnetic field is close to zero (denoted by arrow), implying the presence of a WAL effect.[6] Such WAL effect is due to strong spin-orbit coupling of Dirac electron, which can only be observed up to 20K, and is vanished at 30K (Figure 4b). WAL effect has been investigated in many 2D TCI nanostructures, where the subtracted magnetoconductance ($\Delta\sigma(B)$ ) can be fitted to the 2D Hikami-Larkin-Nagoka (HLN) equation as:

$$\Delta\sigma(B) = \sigma_B - \sigma_0 = \alpha \frac{e^2}{2\pi\hbar} \left[\Psi\left(\frac{\hbar}{4eBl_\phi{}^2} + \frac{1}{2}\right) - \ln\left(\frac{\hbar}{4eBl_\phi{}^2}\right)\right] \quad (2)$$

where $e$ is the charge of electron, $\hbar$ is the reduced Planck constant, $\Psi$ is the digamma function, $\alpha$ is a prefactor representing the number of conduction channels and $l_\phi$ is the phase coherence length. The WAL effect appears as a negative

$\Delta\sigma$(B).[10] Figure 4c shows the $\Delta\sigma$(B) curve measured at 4K. By fitting this curve to equation (2), the values of the fitting parameters of $\alpha$ and $l_\phi$ can be found to be -1.2 and 93.1 nm, respectively (Figure 4c). As $\alpha \approx$ -1 and the number of surface transport channels (A) can be calculated as A=2|$\alpha$|, A can obtained as ~2, suggesting that our {111} dominated Bi-doped SnTe NRs have multiple surface states, which is consistent with the theoretical band structure and other experiment observations.[2-4] Fundamentally, at the {111} surface of SnTe, since there exists four Dirac cones that can contribute eight valley transport channels,[15] the ideal value of $\alpha$ should be 4, larger than our experimental value ($\alpha$=1.2), which can be ascribed to the strong couplings among the eight different valley channels.[15] Therefore, the surface state may have remained intact in the Bi-doped SnTe NRs, which can further be corroborated by the linear MR behaviour observed at high magnetic field (Figure 4d).[6]

In summary, we demonstrate that SnTe NRs with {111} dominated surface facets can be achieved by Bi doping through surface-energy engineering under the prediction of DFT calculation. Bi dopants can effectively substitute the Sn in SnTe and significantly reverse the relative stability between {100} and {111} facets. WAL effect and linear MR at high magnetic field can be both observed in the Bi-doped SnTe NRs, which makes them promising for future applications in spintronic devices.

## Conclusion

In this work, we demonstrate a surface-facet control method for SnTe nanostructures through surface energy engineering by Bi doping. We first explore the effect of Bi dopant on SnTe surface energies by DFT calculation. Calculation results show that the incorporation of Bi dopant on the surface reverses the relative stability between {100} and $\{111\}_{Te}$ surface facet. On the basis of theoretical predictions, we have synthesized uniform Bi doped SnTe NRs with {111} dominant surface facet through chemical vapour deposition.

## Methods

*Sample Growth.* Bi doped SnTe NRs were grown by catalyst-free chemical vapour deposition method in a horizontal tube furnace, using elemental Bi, Sn, Te powders as precursors, coflow of Ar and $H_2$ as carrier gas and Si(100) as substrates. In a

typical synthesis, Sn and Bi powders were put at the heating centre with a heating temperature of 720 $^{o}$C, while Te powder was put 14 cm away at the upper-stream area from the center. The synthesised products samples were collected from Si substrates ~12 cm away from furnace centre, at a growth temperature of approximately 500 $^{o}$C. As a comparison, a synthesis without adding Bi powders was used to fabricate un-doped SnTe nanostructures.

*Microscopic Characterization.* Morphology of the samples supported by their substrates was characterized using SEM (JEOL 7800). Structural and chemical characteristics of the samples were characterized using 200-kV TEM (FEI Tecnai F20), equipped with energy-dispersive X-ray spectroscopy (EDS) for compositional quantification analysis, and X-ray photoelectron spectroscopy (XPS). Phase identification characterizations were carried out by using a Bruker D8 Advance powder X-ray diffractometer (XRD) with a Cu-Kα1 radiation.

*Calculation Methodology.* Calculations of surface energies and electronic structures were performed using the Vienna ab initio simulation package (VASP) within the framework of DFT. The projector augmented wave (PAW) method was employed for electron-ion interactions, and the generalized gradient approximation (GGA) was used to describe the exchange-correlation functional. The Kohn-sham wave function was expanded in a plane wave basis with a cut-off energy of 400 eV.

*Transport Measurement from Nanodevice*. Hall bar nanodevices were fabricated on Bi doped SnTe NR on 300 nm $SiO_2$/Si. Cr/Au electrodes were deposited by E-beam lithography. Quantum Design PPMS was used to measure the magnetotransport in magnetic fields up to 9 T at a temperature between 4~30 K.

**Figure Captions**

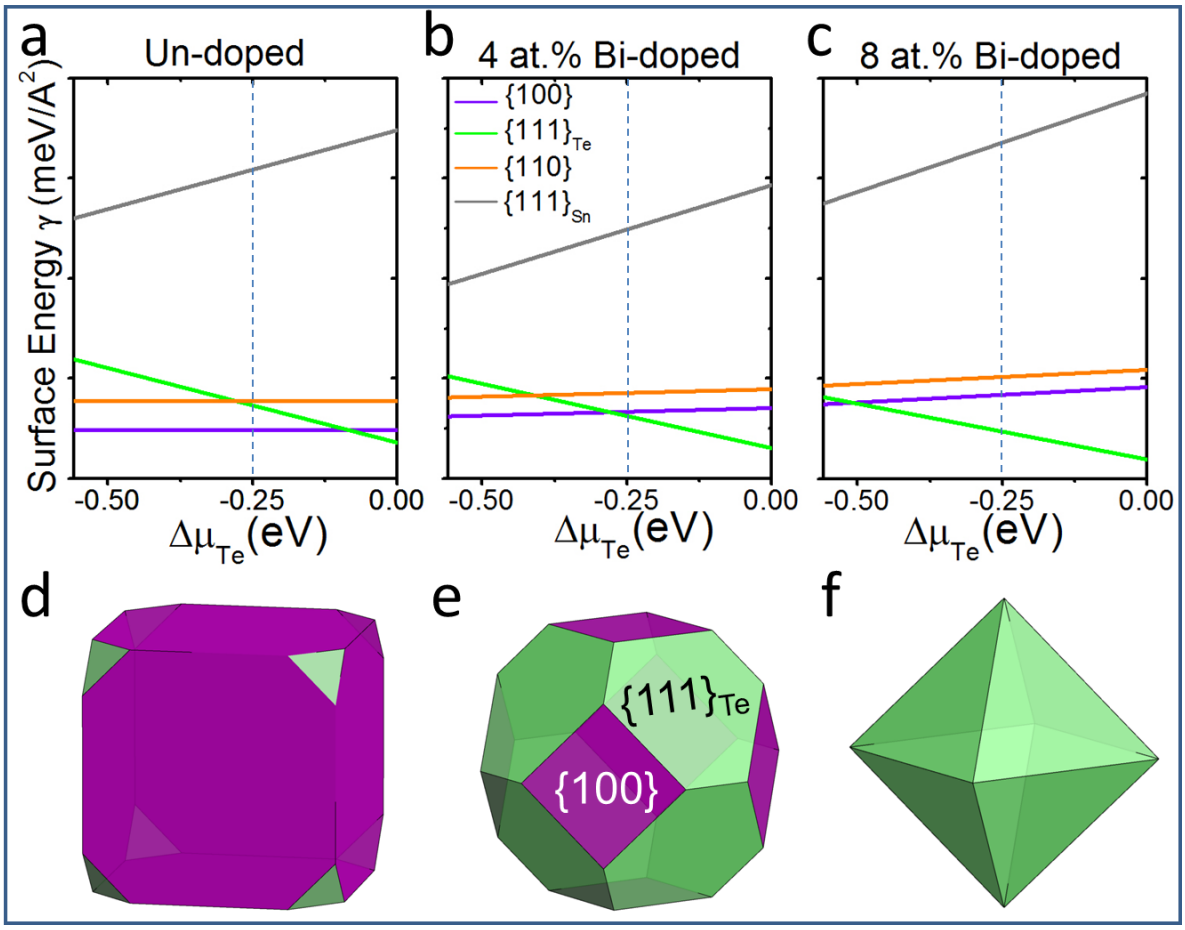


**Figure 1.** (a-c) Calculated surface energies as a function of $\Delta\mu_{Te}$ for un-doped SnTe (a), and Bi-doped SnTe with Bi concentrations of 4 at.% (b) and 8 at.% (c). (d-f) Wulff constructions of the thermodynamic equilibrium SnTe crystals when $\Delta\mu_{Te}$ =-0.25 eV (denoted by the vertical dash lines in a-c) with Bi concentrations of (d) 0 at.%, (e) 4 at.%, and (f) 8 at. %.

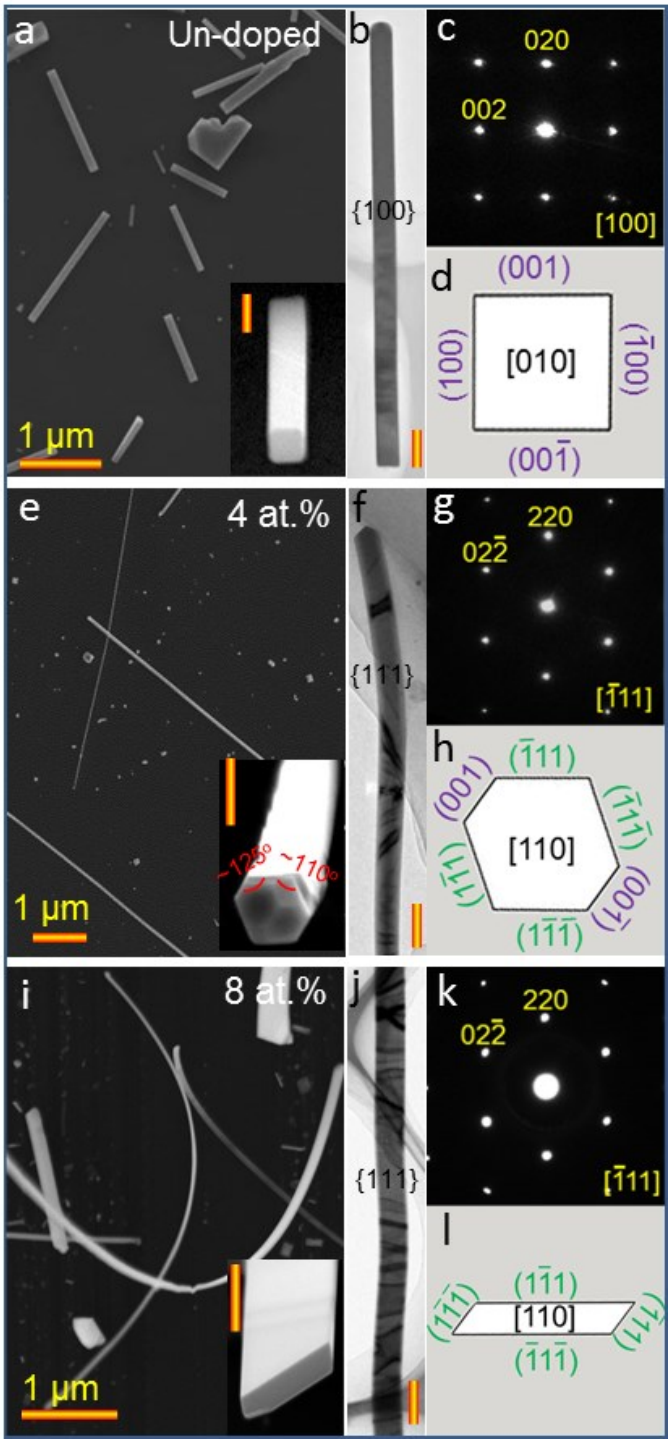


**Figure 2.** Surface-facet analysis for nanostructures of un-doped SnTe (a-d), 4 at.% Bi-doped (e-h), and 8 at.% Bi-doped SnTe (i-l), by SEM (a, e, i), BF TEM imaging (b, f, j) and SAED (c, g, k). (d, h, l) Schematic diagrams showing the cross-section geometry and side-facet configuration of the nanostructures. Scale bars are 100 nm.

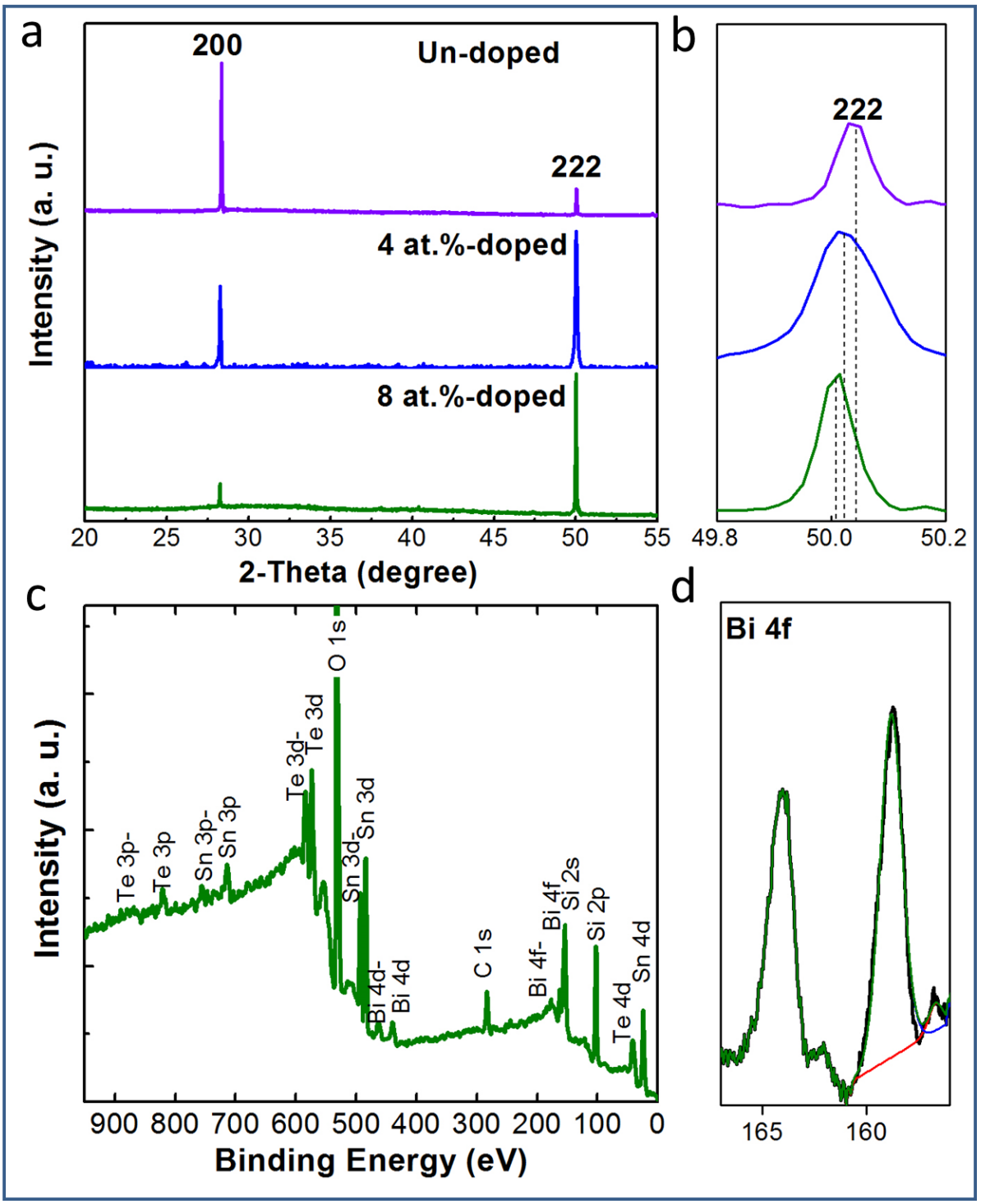


**Figure 3.** (a) Typical XRD patterns from the un-doped and doped SnTe samples, and (b) corresponding enlarged 222* peaks. (c) XPS spectra of Bi 4p from the 8 at.% Bi-doped SnTe sample, and (d) corresponding high-resolution scan of Bi 4f.

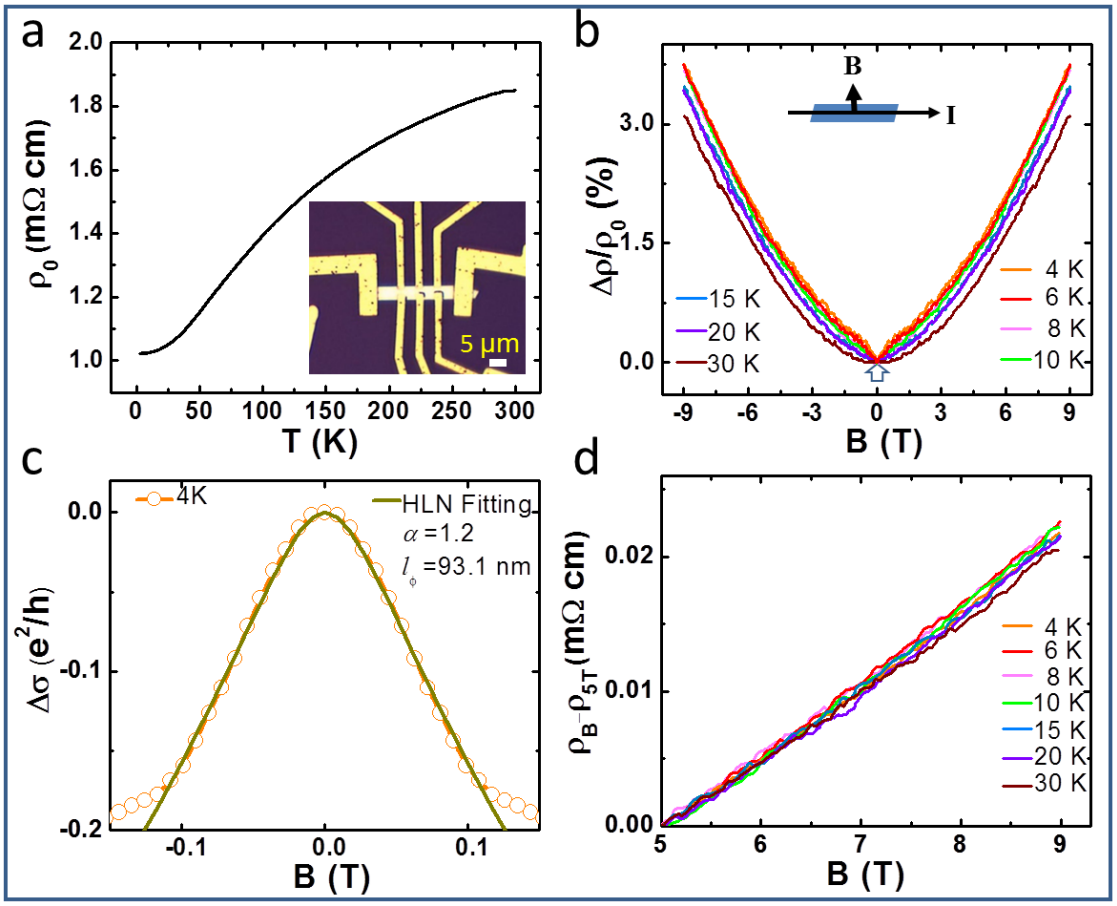


**Figure 4.** Magnetoresistance measurements for an individual Bi-doped SnTe NR. (a) $\rho_0$-T curve. The inset is an optical image of the device. (b) $\Delta\rho/\rho_0$-B curves measured from 4~30K, in which when B is near zero, WAL effect can be observed at low temperatures (denoted by arrow). (c) Subtracted magnetoconductivity $\Delta\sigma(B) = \sigma_B - \sigma_0$ measured at 4K, where $\sigma_B$ and $\sigma_0$ respectively denote the conductivities measured with and without the application of magnetic field. $\Delta\sigma(B)$ is normalized by $e^2/h$. Solid lines depict fitting to HLN equation. (d) $\rho_B$- $\rho_{5T}$ curves at a high magnetic field (5-9T), which are linear and overlapped below 30K.

**Supporting Information**

EDS analysis was conducted on individual SnTe nanostructures in TEM. Figure S1a, b, c respectively show the typical EDS spectrum taken from SnTe nanostructures with different nominal Bi concentrations of 0 at.% (Figure S1a), 4. at.% (Figure S1b) and 8 at.% (Figure S1c). In the EDS spectrum from un-doped sample (Figure S1a), only Sn and Te peaks can be found, from which the atomic ratio of Sn:Te is close to 1:1, indicating that the un-doped sample is indeed pure SnTe. In contrast, from the EDS spectrums of Bi-doped samples (Figure S1a,b), besides the Sn and Te peaks, presence of Bi peaks can be observed, and their peak intensities are increased with the increase of Bi concentration. Further quantification analysis shows that the Bi concentrations in the nanostructures are very close to their nominal doping concentrations.

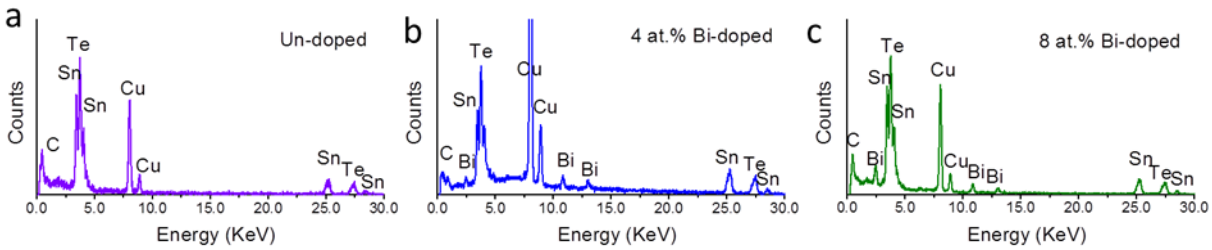


**Figure S1.** Typical EDS point profiles taken from SnTe nanostructures with Bi doping concentrations of (a) 0 at.%, (b) 4 at.%, and (c) 8 at. %.

**References**


1. Hsieh, T. H.; Lin, H.; Liu, J.; Duan, W.; Bansil, A.; Fu, L. A tunable topological insulator in the spin helical Dirac transport regime. *Nat Commun.* **2012,** 3, 982.
2. Tanaka, Y.; Shoman, T.; Nakayama, K.; Souma, S.; Sato, T.; Takahashi, T.; Novak, M.; Segawa, K.; Ando, Y. Two types of Dirac-cone surface states on the (111) surface of the topological crystalline insulator. *Phys. Rev. B* **2013**, 88, 235126.
3. Tanaka, Y.; Ren, Z.; Sato, T.; Nakayama, K.; Souma, S.; Takahashi, T.; Segawa, K.; Ando, Y. Experimental realization of a topological crystalline insulator in SnTe. *Nat. Phys.* **2012,** 8, 800-803.
4. Tanaka, Y.; Sato, T.; Nakayama, K.; Souma, S.; Takahashi, T.; Ren, Z.; Novak, M.; Segawa, K.; Ando, Y. Tunability of the k-space location of the Dirac cones in the topological crystalline insulator $Pb_xSn_{1-x}Te$. *Phys. Rev. B* **2013**, 87, 155105.
5. Zeljkovic, I.; Walkup, D.; Assaf, B. A.; Scipioni, K. L.; SankarR; Chou, F.; Madhavan, V. *Nat. Nanotechnol.* **2015**, 10, 849-853.
6. Shen, J.; Xie, Y.; Cha, J. J. Revealing surface states in In-doped SnTe nanoplates with low bulk mobility. *Nano Lett.* **2015,** 15, 3827-3832.
7. Safdar, M.; Wang, Q.; Mirza, M.; Wang, Z.; Xu, K.; He, J. Topological surface transport properties of single-crystalline SnTe nanowire. *Nano Lett.* **2013,** 13, 5344-5349.
8. Fang, C.; Gilbert, M. J.; Bernevig, B. A. Large-Chern-number quantum anomalous Hall effect in thin-film topological crystalline insulators. *Phys. Rev. Lett.* **2014,** 112, 046801.
9. Li, Z.; Shao, S.; Li, N.; McCall, K.; Wang, J.; Zhang, S. X. Single crystalline nanostructures of topological crystalline insulator SnTe with distinct facets and morphologies. *Nano Lett.* **2013,** 13, 5443-5448.
10. Deringer, V. L.; Dronskowski, R. Stability of pristine and defective SnTe surfaces from first principles. *ChemPhysChem* **2013,** 14, 3108-3111.
11. Wang, J.; Liu, J.; Xu, Y.; Wu, J.; Gu, B.-L.; Duan, W. Structural stability and topological surface states of the SnTe (111) surface. *Phys. Rev. B* **2014**, 89, 125308.

12. Zucker, R. V.; Chatain, D.; Dahmen, U.; Hagège, S.; Carter, W. C. New software tools for the calculation and display of isolated and attached interfacial-energy minimizing particle shapes. *J Mater. Sci.* **2012,** 47, 8290-8302.
13. Cheng, L.; Chen, Z.-G.; Ma, S.; Zhang, Z.-d.; Wang, Y.; Xu, H.-Y.; Yang, L.; Han, G.; Jack, K.; Lu, G.; Zou, J. High curie temperature $Bi_{1.85}Mn_{0.15}Te_3$ nanoplates. *J. Am. Chem. Soc.* **2012,** 134, 18920-18923.
14. Zou, Y.-C.; Chen, Z.-G.; Kong, F.; Lin, J.; Drennan, J.; Cho, K.; Wang, Z.; Zou, J. Planar vacancies in $Bi_xSn_{1-x}Te$ nanoribbons. *ACS Nano* **2016**, 10, 5507-5515.
15. Akiyama, R.; Fujisawa, K.; Yamaguchi, T.; Ishikawa, R.; Kuroda, S. Two-dimensional quantum transport of multivalley (111) surface state in topological crystalline insulator SnTe thin films. *Nano Res.* **2016,** 9, 490-498.

# 8

# Metal-Atom Disorder in $Bi_2SnTe_4$ Nanostructures

## 8.1 Introduction

In Bi-Sn-Te ternary system, $Bi_2SnTe_4$ has been recognized as the most stable phase. The unit cell of $Bi_2SnTe_4$ comprises of layers structures with ordered lamellae. Each lamella is composed of seven atomic layers (Te-MII-Te-MI-Te-MII-Te), where MI and MII sites are the octahedral interstices of Te atoms that are occupied by metallic atoms (Bi or Sn). Controversy still exists regarding the arrangement of Bi and Sn atoms in MI and MII sites. To address this issue, in this chapter, we investigate into the metal-atom arrangement in single-crystalline $Bi_2SnTe_4$ nanoplates synthesized through catalyst-free chemical vapour deposition method. The atomic structure was studied using Cs-corrected scanning transmission electron microscopy in combination with first-principles calculation.

## 8.2 Journal Publication

These results are to be submitted for publication soon.

# Direct observation of the partial ordering of metal atoms in $Bi_2SnTe_4$ Nanostructures

Yichao Zou[1], Zhigang Chen[1], Fantai Kong[3], John Drennan,[4] Kyeongjae Cho[3], Lihua Wang[1], Zhongchang Wang[2] and Jin Zou[1,4]

[1] Materials Engineering, University of Queensland, Brisbane, QLD 4072, Australia
[2] WPI, Advanced Institute for Materials Research, Tohoku University, 2-1-1 Katahira, Aobaku, Sendai 980-8577, Japan
[3] Department of Materials Science & Engineering, The University of Texas at Dallas, Richardson, TX 75080, USA.
[4] Centre for Microscopy and Microanalysis, University of Queensland, Brisbane, QLD 4072, Australia

**Abstract**

The debate is still on-going regarding the metal-atom arrangement in $Bi_2SnTe_4$, whether it is in a mixed or an ordered model. To give a precise identification of the metal-atom arrangement in $Bi_2SnTe_4$, we conduct Cs-corrected scanning transmission electron microscopy studies on nanostructured $Bi_2SnTe_4$ samples, synthesized through a chemical vapor deposition method. The STEM imaging observations, in combination with first-principles calculation, shows that a partial ordered metal-atom arrangement can be observed in the crystal structure. Further electronic calculation suggested that the small degree of metal-atom disordering we observed may lead to a semiconductor-to-metal transition in $Bi_2SnTe_4$.

**Keywords**: ternary compound, STEM, tin telluride, bismuth telluride, topological insulator, thermoelectric, atomic structure

## Introduction

Layered-structured $Bi_2Te_3$ compounds have attracted world-wide research interest because of their high thermoelectric performances at room temperature, and their exotic physical properties as a topological insulator.[1-8] Search for new thermoelectric materials and topological insulators with $Bi_2Te_3$-type crystal structures has led many researchers to focus on pseudobinary $(A^{IV}Te)_m(Bi_2Te_3)_n$ materials systems ($A^{IV}$ denoting the Group IV elements: Ge, Sn, Pb).[9-18] Through variation in m and n integers, one is able to obtain a series of tetradymite-like layer structured compounds,[9-18] i.e. $GeBi_2Te_4$, $SnBi_2Te_4$ and $PbBi_2Te_4$ (m=n=1). Experimental studies have shown that these compounds generally have a lower lattice thermal conductivity compared to their constituent tellurides, which makes them attractive for applications in thermoelectricity.[9-12] Meanwhile, most of these compounds, such as $GeBi_2Te_4$ and $PbBi_2Te_4$, have been both theoretically and experimentally proved to be 3D topological insulators with complicated surface electronic structures, revealing the potential for applications in novel quantum devices.[13-18]

To precisely predict and understand the properties of $(A^{IV}Te)_m(Bi_2Te_3)_n$ compounds, it is critical to give an accurate identification of their real atomic structure. In many of the compounds, structural unit cell contains a seven atomic-layer structure, which can be described as Te-MII-Te-MI-Te-MII-Te (Fig. 1a).[19] MI and MII are the octahedral interstice sites of Te atoms, occupied by metallic atoms (Bi or $A^{IV}$). The difference of MI and MII sites is that MI is a regular octahedral site while MII is a distorted one, as illustrated in Fig. 1a. It has been noted that such difference may induce different types of Bi and $A^{IV}$ atom arrangement, which further influences the surface state and overall properties of the compounds.[14] This prompts the important question of how Bi and $A^{IV}$ atoms are distributed in the cation sites of $(A^{IV}Te)_m(Bi_2Te_3)_n$ compounds.

However, the arrangement of Bi and $A^{IV}$ atoms in MI and MII sites is still a subject of controversy.[11,18,19] For example, in $Bi_2SnTe_4$ system, both an ordered (Fig. 1a) and random (Fig. 1b) models were proposed to describe the metal-atom arrangement, XRD results from Zhukova et al. show that Bi and Sn atoms are statistically randomly occupy the MI and MII sites.[20] This is in variance with the XRD results from Kuropatwa et al.,[11] who referred from Rietveld refinement results to indicate that Sn atoms exhibit preferences for MI sites. Mossbauer spectra results from Ledda et al.

also suggest that Sn and Bi in $SnBi_2Te_4$ should be arranged in an ordered manner,[12] as the Sn peak from $SnBi_2Te_4$ is similar with that of SnTe. Energetic calculations from Casula et al. further support that the ordered arrangement of Sn and Bi is preferred in $Sn_2BiTe_4$.[4] Despite of intensive diffraction, spectroscopy and simulation analysis, none of these methods gives a direct evidence of the metal-atom arrangement in $Sn_2BiTe_4$. On the other hand, aberration-corrected scanning transmission electron microscopy (STEM) with Z-contrast imaging technique has enabled us to give a precise identification of the atomic configuration of compounds with complicated compositions.

In this study, to clarify metal-atom distribution in $SnBi_2Te_4$, we report a direct atomic-scale observation on the atomic structure of $Sn_2BiTe_4$ nanostructures using aberration-corrected STEM imaging. We found that Bi and Sn atoms are partially ordered in the cation sites, where Bi atoms prefer to occupy MII sites and Sn atoms prefer to occupy MI sites, but they are not completely ordered. The result of the observation is further understood by structural modeling and energetic calculations using density functional theory.

**Experimental**

$Sn_2BiTe_4$ nanostructures were prepared by chemical vapor deposition method using the vapour-solid growth mechanism in a horizontal tube furnace, using elemental powders of Sn (Sigma Aldrich, 99.99%), Bi (Sigma Aldrich, 99.99%), Te (Sigma Aldrich, 99.99%) as the precursor, and mixture of Ar(100sccm) and $H_2$(40sccm) as the carrier gas. Silicon (100) with natural oxide layer was used as the substrate to collect the nanostructured samples. During the growth, precursors were put at the center of the furnace and heated to 700$^{o}$C, whereas substrates were put at the downstream area with a distance of ~12 cm from the furnace center.

Phase identification characterizations were carried out by using a Bruker D8 Advance powder X-ray diffractometer (XRD) with a Cu-K $\alpha$ 1 radiation. The morphological, structural and chemical characteristics of the samples were studied using scanning electron microscope (SEM, JEOL 7800) and transmission electron microscope (TEM, Philips Tecnai F20, 200kV), equipped with energy-dispersive X-ray spectroscopy (EDS) for compositional quantification analysis. Cross-sectional TEM specimens were prepared firstly by mechanical ground till their thickness

reached ~0.12mm, followed by a dimpling down to ~20um. To further make the specimen electron transparent, the dimpled slices were finally thinned by argon-ion polishing (PIPS 691, Gatan). For atomic-resolution imaging of TEM specimens, high-annular angle dark-field images (HAADF) were taken by scanning transmission electron microscope (ARM-200FC STEM, 200kV) equipped with a probe corrector (CEOS Gmbh).

Calculations of energies and electronic structures were performed using the Vienna ab initio simulation package (VASP) within the framework of DFT. The projector augmented wave (PAW) method was employed for electron-ion interactions, and the generalized gradient approximation (GGA) was used to describe the exchange-correlation functional. The Kohn-sham wave function was expanded in a plane wave basis with a cut-off energy of 400 eV. Potentials for Sn, Bi and Te, respectively used $5s^2 5p^2$, $6s^2 6p^3$ and $5s^2 5p^4$ orbitals as valence electrons.

**Results and Discussion**

Figure 2a shows the experimental XRD patterns obtained from the sample. The XRD experimental result agrees with the standard Bragg peaks from a rhombohedral structured $Bi_2SnTe_4$ (PDF# 65-3692), indicating that the crystals grown were single-phased $Bi_2SnTe_4$. Figure 2b,c present a pair of SEM images taken from the $Bi_2SnTe_4$ nanostructures grown on silicon substrate with a top view (Fig. 2b) and a side view (Fig. 2c). The nanostructures exhibit morphology as nanoplate, with a lateral size of 30-200 nm, and are grown free-standing on the substrate surface. In combination with the XRD results shown in Fig. 2a, the strong intensity of {0001} peaks suggested that the nanoplates have a dominated surface facet as {0001}.

To further understand the structural characteristics of the as-grown $Bi_2SnTe_4$ nanoplates, cross-sectional TEM analysis was conducted. Figure 2d shows a high-resolution TEM bright-field (BF) image of a typical nanoplate, clearly showing the layer-structured feature. The seven-layered structure is further confirmed by selective-area electron-diffraction patterns (SAED) taken from the nanoplate, which reveals seven spots between two adjacent [00021] spots, as shown in Fig. 2e. Figure 2f shows EDS point profile taken from the nanostructure (note that the C, O Si and Cu peaks are due to the superglue used for sample preparation, silicon

substrate, and Cu grid for supporting the sample). Quantitative analysis confirms that the atomic ratio of Bi, Sn and Te is approximately 2:1:4 in the sample.

To understand the atom arrangement in our $BiSn_2Te_4$ samples, the same nanoplate was further characterized under STEM imaging mode. Figure 3a shows a typical HAADF STEM image taken from the thin edge of the nanoplate, where slabs of Te-MII-Te-MI-Te-MII-Te atomic layers can be seen. Constantly, brighter atomic columns can be observed at the MII sites. Since the intensity of an atomic column in the HADDF STEM mode is roughly proportional to $Z^{1.7}$ (Z is atomic number), and Bi has a higher Z (83) value compared with Sn (50) and Te (52), brighter atomic columns can be classified as Bi-rich atomic columns. This was further confirmed by extracting the intensity profile along line I-II, as shown in Fig. 3b, revealing that atomic columns at MII sites show higher image intensity than other sites. This indicates that Bi atoms show preference to occupy MII sites, and Sn show preference for MI sites. Nevertheless, it should be noted that atomic columns at MI sites show slightly higher intensity than that of Te sites, suggesting that the metal atom arrangement is not perfectly ordered in the $Bi_2SnTe_4$ sample. Based on our examination on more than half a dozen of samples, the STEM imaging result shows that there exists certain degree of metal-atom disorder, and the metal arrangement can be considered as partial ordered.

To understand the degree of metal-atom disorder in our sample, image simulations using multi-slice method were conducted. The supercells used for image simulation was built and relaxed using DFT. As shown in Table 1, starting from supercells of the ordered model, in which the Sn occupancy at MII sites ($g_{Sn\text{-}MII}$) equals 0, we gradually exchange Sn with Bi, and increase the $g_{Sn\text{-}MII}$ to 1/10, 1/4, and 1/3. When gsn-MII reaches 1/3, the arrangement of metal atoms is completely mixed. Corresponding supercells and their projections are shown in Fig. 4a, b. Using these atomic models, the resulted simulated HAADF images are shown in Fig. 4c. In Fig. 4c, one can see that as the degree of exchange is increased, the difference of image contrast between atom column at MI and MII sites is largely reduced. By comparing the simulated images with our experimental one in Fig. 3a, the simulated image at $g_{Sn\text{-}MII}$ of 1/10 agrees the best, suggesting that in our sample, the exchange degree of Sn and Bi atoms is around 1/10.

To understand whether the 10% metal atom exchange we observed is energetically favourable, we calculate formation energies ($E_f$) using the $BiSn_2Te_4$ supercells shown in Fig. 4a. Figure 5a shows the calculated energy profiles as a function of $g_{Sn\text{-}MI}$, where the formation energy ($E_f$) of the ordered arrangement is set to zero. Figure 5a reveals that an increased disorder of metal atom arrangement leads to an increase of $E_f$. The 1/3 case, where Sn evenly occupy 1/3 of both MI and MII sites, has the highest $E_f$, suggesting that an evenly mixed arrangement of metal atoms is not likely to form. This is in agreement with our experimental results that Sn prefers MII rather that MI sites. Although the 1/10 and 1/4 cases show higher $E_f$ than the ordered one, their energy difference is quite low, which is below 0.1eV/f.u. The low $E_f$ suggests that although metal disorder is not predicted to be the most energy favourable at thermal-equilibrium conditions, a small fluctuation such as strain or chemical potential in the synthesis environment may easily induce the metal disorder, especially in our case of nanostructures where finite-size effects exist. [23]

To understand the impact of metal-atom disorder on the electronic property of $Bi_2SnTe_4$, Figure 5b compared the density of states (DOS) calculated for the ordered and 1/10 exchanged supercells. The DOS of the ordered model shows a band gap ~0.45 eV, with the Fermi level lying close to the valence band maximum (VBM), showing a *p*-type semiconducting feature. This is in consistency with previous calculations using the ordered model.[11] In contrast, in 1/10 exchanged case, the band gap is diminished, showing a metallic conducting feature. We further calculated DOS and band structures for other cases (Fig. S1), which suggests that the semiconductor-to-metal transition can always be observed. This transition is due to the left shift of conduction band minimum (CBM), stem from the valence *p* orbitals of Bi and Te atoms.

**Conclusion**

From CVD grown $Bi_2SnTe_4$ nanoplates, STEM imaging found that Bi and Sn atoms are partially ordered in the cation sites of $Bi_2SnTe_4$, where Bi prefer to stay in MII sites and Sn atoms prefer to stay at MI site, with certain degree of metal-atom disorder can be observed. Calculations show that metal-atom disorder may cause a semiconductor-to-metal transition in $Bi_2SnTe_4$.

## Figure Captions

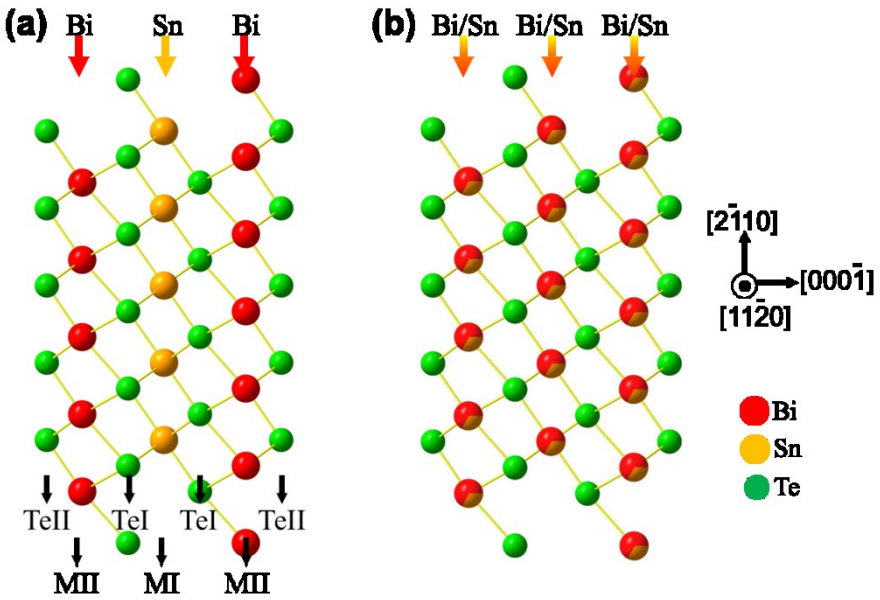


**Figure 1.** Projections along $[11\bar{2}0]$ of the structure models proposed for the rhombohedral $Bi_2SnTe_4$ phase with an ordered (a) and a random (b) metal atom arrangement. In the seven-layer structural unit, two types of octahedral cation sites exist, labelled as MI, MII in (a). In an ordered model, MI sites are occupied by Sn, while MII sites are occupied by Bi (a). In a random model, Bi and Sn are antisited compared to the ordered one. MI and MII are occupied by even mixing of Bi and Sn atoms, in which Sn has occupancy of 1/3 in both M sites (b).

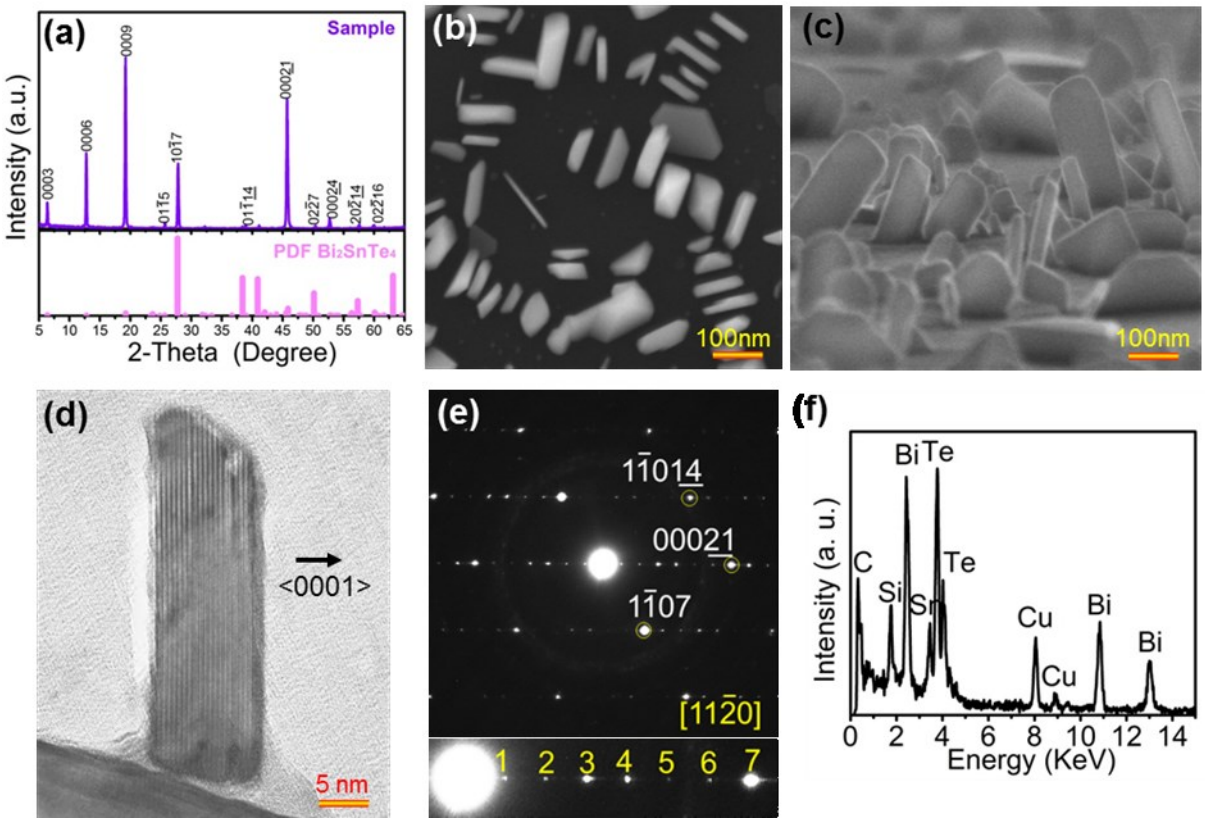


**Figure 2.** (a) XRD patterns from the as-grown sample, with the bottom panel showing standard peaks of a rhombohedral $Bi_2SnTe_4$ phase. (b-c) SEM images of $Bi_2SnTe_4$ nanoplates standing on the substrate surface, with a top view (b) and a side view (c). (d) TEM BF image of cross-section specimen taken from a $Bi_2SnTe_4$ nanostructure along [$11\bar{2}0$] axis, indicating the layered structure. (e) SAED patterns taken from the nanostructure along [$11\bar{2}0$] axis. (f) EDS point profile taken from the nanoplate.

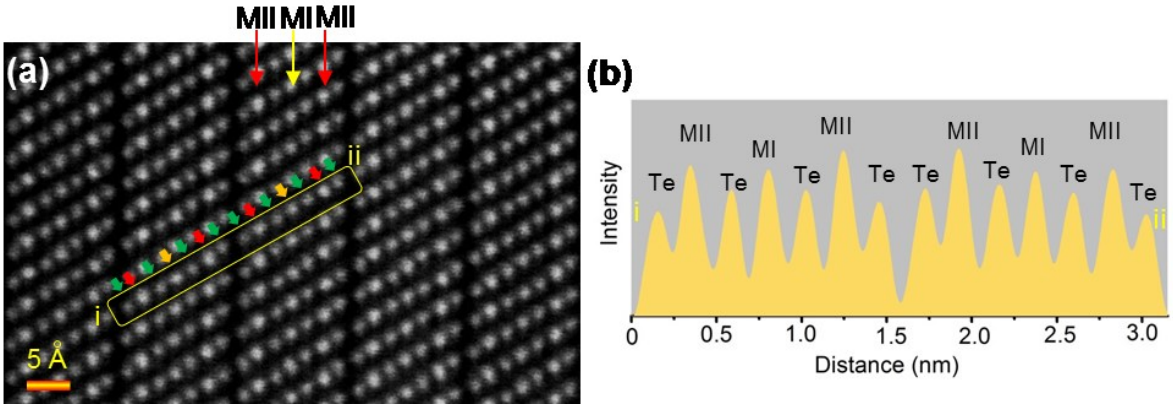


**Figure 3.** (a) Atomic-resolution HADDF image taken from the nanoplate sample, showing its seven-layer slabs. (b) Line profiles showing the image intensity along line i-ii in (a).

**Table 1** Occupancy of Sn in MI and MII sites in the four proposed atomic models to describe the exchange levels of metal atoms in $Bi_2SnTe_4$

| | 0 | 1/10 | 1/4 | 1/3 |
|---|---|---|---|---|
| | Completely ordered | Partial ordered | Partial ordered | Evenly mixed |
| $g_{Sn\text{-}MI}$ | 1 | 0.8 | 0.5 | 0.33 |
| $g_{Sn\text{-}MII}$ | 0 | 0.1 | 0.25 | 0.33 |

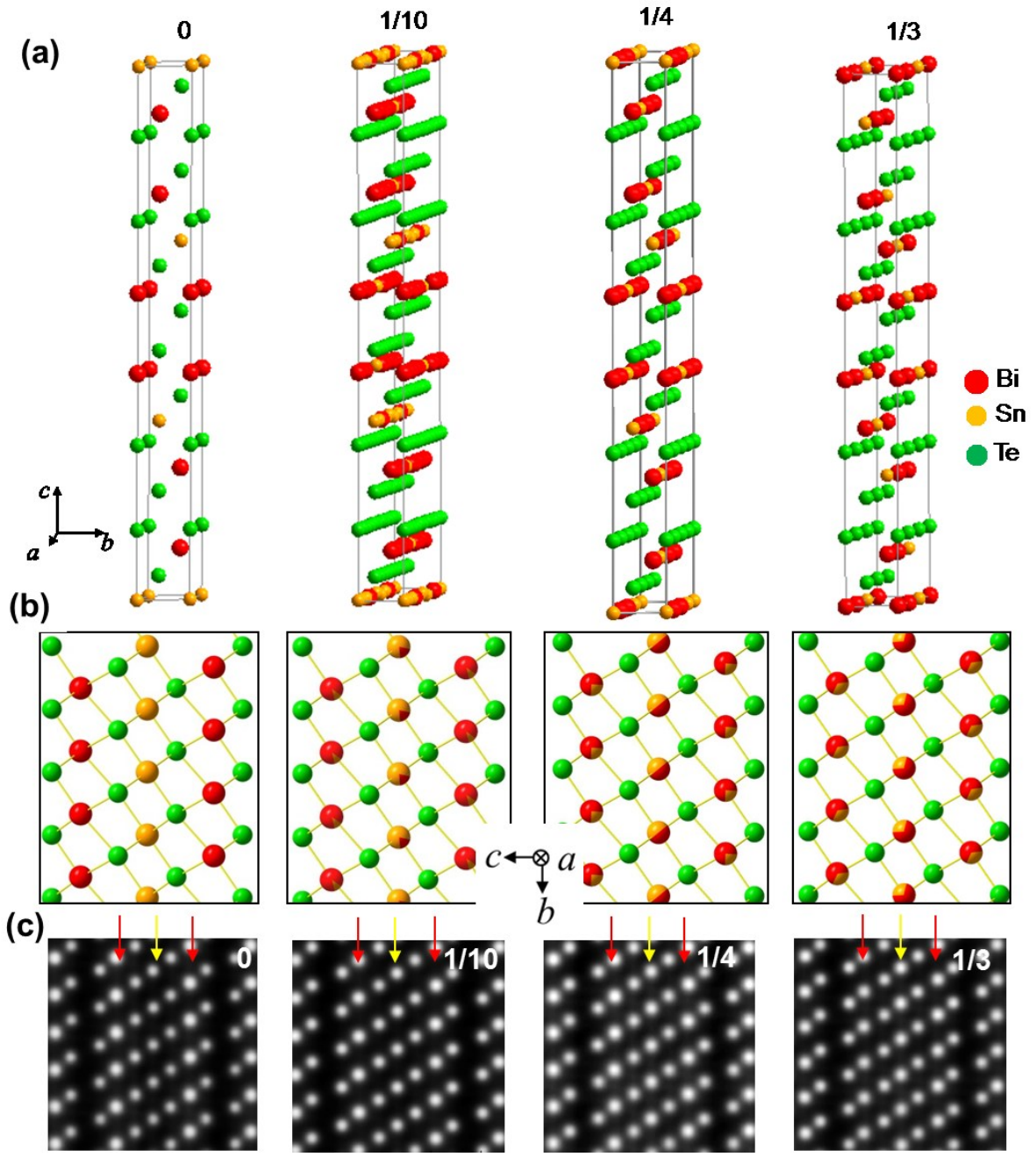


**Figure 4.** (a) $Bi_2SnTe_4$ supercells with different exchange degrees of Bi and Sn, supercells from left to right corresponding to a $g_{Sn\text{-}MII}$ value of 0%, 10%, 25% and 33.33%. (b) Corresponding schematic projections along [ $11\bar{2}$ 0] axis, (c) Corresponding simulated STEM images, atomic columns at MI and MII sites are denoted by yellow and red arrows, respectively.

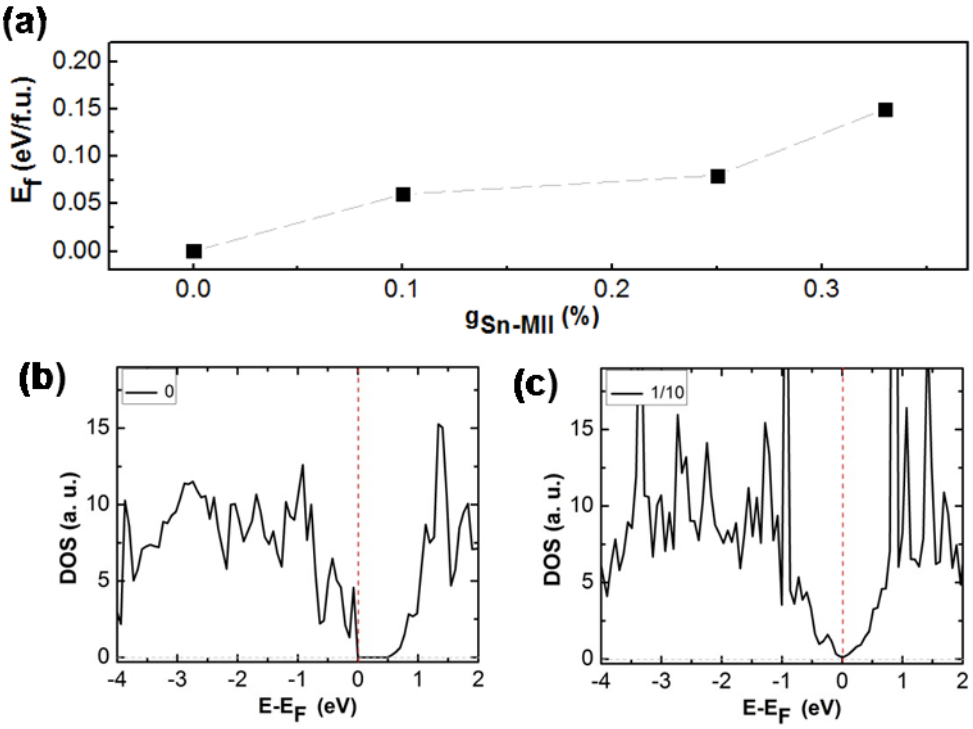


**Figure 5.** (a) Calculated formation energies of the supercells as a function of $g_{Sn\text{-}MII}$ value. (b-c) Calculated total DOS derived from the ordered (b) and 1/10 exchanged (c) supercells.

**Supporting Information**

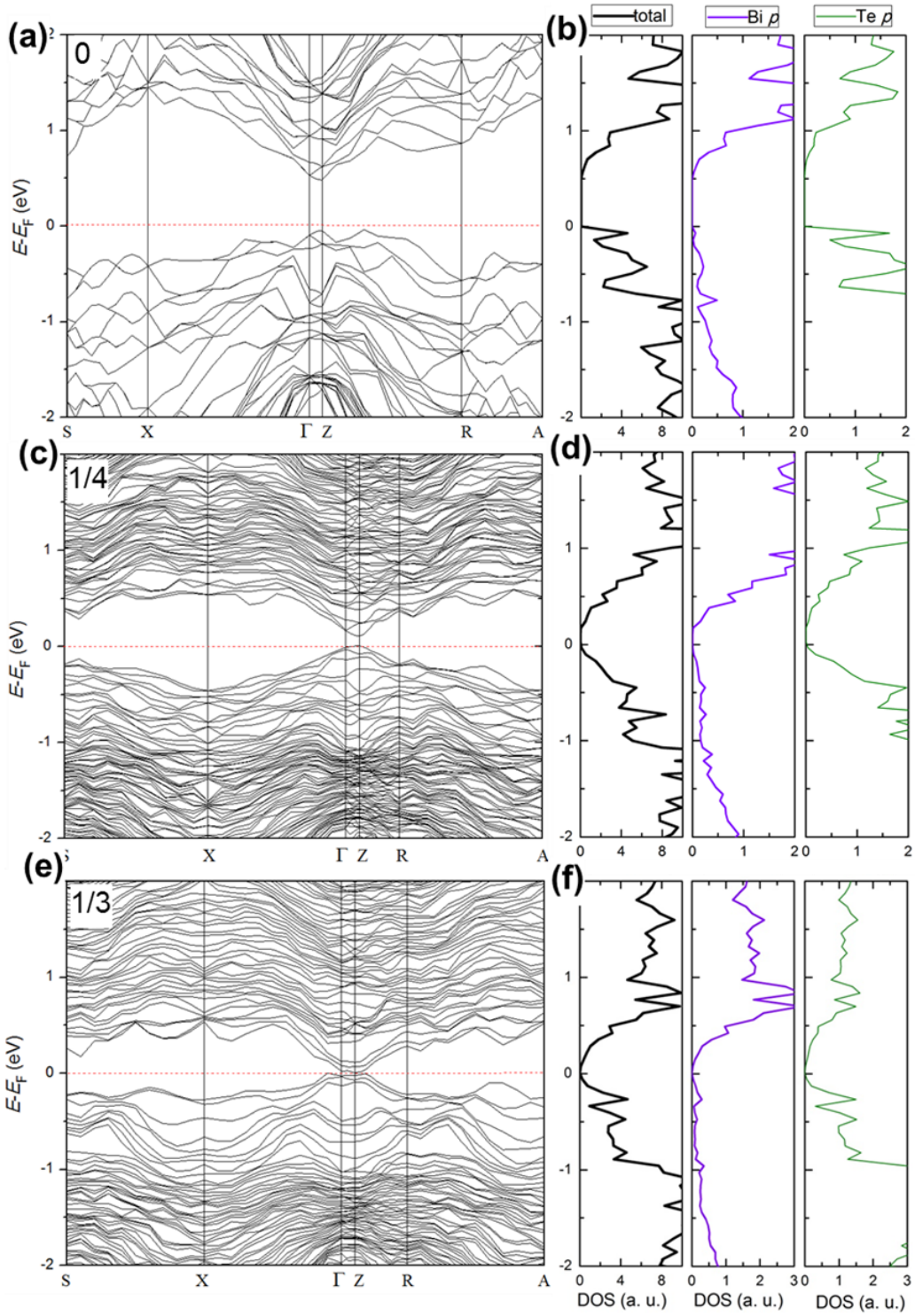


**Figure S1.** (a, c ,e) Calculated band structure from $Bi_2SnTe_4$ supercells for the ordered (a), 1/4 exchanged (b), and (c) 1/3 exchanged supercells. (b, d, f) Total DOS and corresponding partial DOS extracted for Bi and Te *p* orbitals for ordered (a), 1/4 exchanged(b), and (c) 1/3 exchanged supercells.

**References**


1. Snyder, G. J.; Toberer, E. S. Complex thermoelectric materials. *Nat. Mater.* **2008,** 7, 105-114.
2. Yang, L.; Chen, Z.-G.; Hong, M.; Han, G.; Zou, J. Enhanced thermoelectric performance of nanostructured $Bi_2Te_3$ through significant phonon scattering. *ACS Appl. Mater. Interf.* **2015,** 7, 23694-23699.
3. Hong, M.; Chen, Z. G.; Yang, L.; Zou, J. $Bi_xSb_{2-x}Te_3$ nanoplates with enhanced thermoelectric performance due to sufficiently decoupled electronic transport properties and strong wide-frequency phonon scatterings. *Nano Energy* **2016,** 20, 144-155.
4. Han, G.; Chen, Z.-G.; Yang, L.; Hong, M.; Drennan, J.; Zou, J. Rational design of $Bi_2Te_3$ polycrystalline whiskers for thermoelectric applications. *ACS Appl. Mater. Interf.* **2015,** 7, 989-995.
5. Vineis, C. J.; Shakouri, A.; Majumdar, A.; Kanatzidis, M. G. Nanostructured thermoelectrics: big efficiency gains from small features. *Adv. Mater.* **2010,** 22, 3970-3980.
6. Hsieh, D.; Xia, Y.; Qian, D.; Wray, L.; Dil, J. H.; Meier, F.; Osterwalder, J.; Patthey, L.; Checkelsky, J. G.; Ong, N. P.; Fedorov, A. V.; Lin, H.; Bansil, A.; Grauer, D.; Hor, Y. S.; Cava, R. J.; Hasan, M. Z. A tunable topological insulator in the spin helical Dirac transport regime. *Nature* **2009,** 460, 1101-1105.
7. Chen, Y. L.; Analytis, J. G.; Chu, J.-H.; Liu, Z. K.; Mo, S.-K.; Qi, X. L.; Zhang, H. J.; Lu, D. H.; Dai, X.; Fang, Z.; Zhang, S. C.; Fisher, I. R.; Hussain, Z.; Shen, Z.-X. Experimental realization of a three-dimensional topological insulator, $Bi_2Te_3$. *Science* **2009,** 325, 178-181.
8. Kong, D.; Cui, Y. Opportunities in chemistry and materials science for topological insulators and their nanostructures. *Nat. Chem.* **2011,** 3, 845-849.
9. Rosenthal, T.; Schneider, M. N.; Stiewe, C.; Döblinger, M.; Oeckler, O. Real structure and thermoelectric properties of GeTe-rich germanium antimony tellurides. *Chem. Mater.* **2011,** 23, 4349-4356.
10. Karpinsky, O. G.; Shelimova, L. E.; Kretova, M. A.; Fleurial, J. P. X-Ray study of the $nGeTe{\cdot}mBi_2Te_3$ mixed layered tetradymite-like compounds. *J. Alloy. Compd.* **1998,** 265, 170-175.

11. Kuropatwa, B. A.; Kleinke, H. Thermoelectric properties of stoichiometric compounds in the $(SnTe)_x(Bi_2Te_3)_y$ system. *Z. Anorg. Allg. Chem.* **2012,** 638, 2640-2647.
12. Shelimova, L. E.; Karpinskii, O. G.; Zemskov, V. S.; Konstantinov, P. P. Structural and electrical properties of layered tetradymite-like compounds in the GeTe-$Bi_2Te_3$ and GeTe-$Sb_2Te_3$ systems. *Inorg. Mater.* **2000,** 36, 235-242.
13. Yang, K.; Setyawan, W.; Wang, S.; Buongiorno Nardelli, M.; Curtarolo, S. A search model for topological insulators with high-throughput robustness descriptors. *Nat. Mater.* **2012,** 11, 614-619.
14. Okamoto, K.; Kuroda, K.; Miyahara, H.; Miyamoto, K.; Okuda, T.; Aliev, Z. S.; Babanly, M. B.; Amiraslanov, I. R.; Shimada, K.; Namatame, H.; Taniguchi, M.; Samorokov, D. A.; Menshchikova, T. V.; Chulkov, E. V.; Kimura, A. Observation of a highly spin-polarized topological surface state in $GeBi_2Te_4$. *Phys. Rev. B* **2012,** 86, 195304.
15. Vergniory, M. G.; Menshchikova, T. V.; Silkin, I. V.; Koroteev, Y. M.; Eremeev, S. V.; Chulkov, E. V. Electronic and spin structure of a family of Sn-based ternary topological insulators. *Phys. Rev. B* **2015,** 92, 045134.
16. Eremeev, S. V.; Landolt, G.; Menshchikova, T. V.; Slomski, B.; Koroteev, Y. M.; Aliev, Z. S.; Babanly, M. B.; Henk, J.; Ernst, A.; Patthey, L.; Eich, A.; Khajetoorians, A. A.; Hagemeister, J.; Pietzsch, O.; Wiebe, J.; Wiesendanger, R.; Echenique, P. M.; Tsirkin, S. S.; Amiraslanov, I. R.; Dil, J. H.; Chulkov, E. V. Atom-specific spin mapping and buried topological states in a homologous series of topological insulators. *Nat. Commun.* **2012,** 3, 635.
17. Ren, Z.; Taskin, A. A.; Sasaki, S.; Segawa, K.; Ando, Y. Fermi level tuning and a large activation gap achieved in the topological insulator $Bi_2Te_2Se$ by Sn doping. *Phys. Rev. B* **2012,** 85, 155301.
18. Jung, C. S.; Kim, H. S.; Im, H. S.; Park, K.; Park, J.; Ahn, J.-P.; Yoo, S. J.; Kim, J.-G.; Kim, J. N.; Shim, J. H. In situ temperature-dependent transmission electron microscopy studies of pseudobinary $mGeTe \cdot Bi_2Te_3$ (m=3-8) NWs and first-principles calculations. *Nano Lett.* **2015,** 15, 3923-3930.
19. Zhukova, T. B.; Zaslavskii, A. I. Crystal structures of $PbBi_4Te_7$, $PbBi_2Te_4$, $SnBi_4Te_7$, $SnBi_2Te_4$, $SnSb_2Te_4$, and $GeBi_4Te_7$. *Kristallografiya* **1971,** 16, 918-922.

20. Ledda, F.; Muntoni, C.; Serci, S.; Pellerito, L. Ordering of metal atoms in the SnTe-$Bi_2Te_3$ system. *Chem. Phys. Lett.* **1987,** 134, 545-548.
21. Casula, F.; Deiana, L.; Podda, A. Atomic arrangement in the mSnTe-n$Bi_2Te_3$ compounds by electronic structure calculations. *J. Phys.: Condens. Mat.* **1991,** 3, 1461.
22. McKenna, K. P.; Hofer, F.; Gilks, D.; Lazarov, V. K.; Chen, C.; Wang, Z.; Ikuhara, Y. Atomic-scale structure and properties of highly stable antiphase boundary defects in $Fe_3O_4$. *Nat. Commun.* **2014,** 5, 5740.

# 9

# Conclusions and Recommendations

## 9.1 Conclusions

This thesis investigated the growth mechanism, structural characteristics of SnTe, $Bi_2Se_3$, Bi-Sn-Te nanostructures grown by Au-catalyzed and catalyst-free CVD. Through detailed electron microscopy investigations, the morphology, crystal structure controlled growth of IV-VI and V-VI based nanostructures have been successfully achieved, and the growth mechanisms were proposed to understand their growth behaviors. Furthermore, we combined aberration-corrected STEM imaging with first-principle calculation to elucidate the complex atomic structure of ternary chalcogenides. The conclusions of this PhD thesis are summarized as follows.

- In Au catalysed growth of chalcogenide compound NWs, detailed experimental investigations have demonstrated that catalyst composition, catalyst orientation, can be used to tune the morphology and structural characteristics of the products. For $Bi_2Se_3$ nanostructure growth, the catalyst-nanostructure interface was found to have an impact on the growth directions of the products. When the catalyst/nuclei interfaces are {0001} interfaces, NWs and the NR-NW junctions can be introduced. When the catalyst/nuclei interfaces are not {0001} interfaces, NRs are likely to be formed. In SnTe nanostructures, Au-containing catalysts with different Au concentrations are used to induce specific growth behavior. Triangular SnTe nanoplates with a {100} dominated surface and {100}, {111} and {120} side facets were induced by AuSn catalysts, whereas <010> SnTe NWs with four nonpolar {100} side-facets were produced using $Au_5Sn$ catalysts. Through detailed structural and chemical characterization, coupled with surface energy calculations, it is found that NW growth is thermodynamically controlled via VSS growth mechanism, whereas nanoplate growth is kinetically controlled via VLS growth mechanism.

- In the growth of Bi doped SnTe nanostructures, we found that the surface facet and crystal structure of the SnTe nanostructures can be engineering through Bi doping. When Bi doping concentration is reaching ~8 at.%, SnTe NRs with {111} dominated surface facets can be achieved, as the incorporation of Bi significantly lowers the surface energy of $\{111\}_{Te}$ facet which reverses the relative stability between {100} and surface facet. Furthermore, Bi doping can be used to realize the vacancy engineering in highly doped SnTe NRs. An increased Bi concentration promotes the formation of compensating planar vacancies. Atomic-resolution STEM study found that the observed planar vacancies provide energetic favorable sites to accommodate Bi dopants, and exhibit local variation in structural relaxation level. When terminating at the NR surface, the planar vacancies (R-type) exhibit large structural relaxation level, and are characterized by low formation energy. Determination of the atomic structure of these planar vacancies with such atomistic detail has enabled us to predict their corresponding electronic properties. Calculations show that the Bi segregated planar vacancies introduce newly localized DOS distortion into the system, which provides new opportunities for the future applications of chalcogenide nanomaterials.
- For ternary Bi-Sn-Te nanostructures, we investigate into the atomic structure of CVD grown single-crystalline $Bi_2SnTe_4$ nanoplates by STEM imaging. We found that Bi and Sn atoms show preferences for different cation sites. However, they still coexist in each cation site, and show a small degree of metal atom disorder. DFT calculation indicates that the formation energy of such metal-atom disorder is low. Further electronic calculations suggested that the disordering of metal atoms may lead to a semiconductor-to-metallic transition in $Bi_2SnTe_4$.

## 9.2 Recommendations

The observations and conclusions that were made in the PhD thesis can be extended to explore the properties and structures of metal chalcogenide nanostructures. Suggestions are stated as follows.

- Investigate into the nano-device design of the samples and study the impact of structural, morphology and composition on the property of the nanostructure.

- Detail analysis of the magnetoresistance properties of Bi-Sn-Te compound nanostructures is desirable, since the related study on their topological surface properties is very limited from previous literature reports. Related measurements can be conducted on the grown $SnBi_2Te_4$ nanoplates. The comparison of such results with SnTe and $Bi_2Te_3$ based nanostructures may provide new opportunities for applications of Bi-Sn-Te compound nanostructures in spintronic devices.
- Further structural understanding is needed regarding the planar vacancies formation in the Bi-Sn-Te nanostructures, and their correlation with the mechanism of phase change from rock-salt to rhombohedral in ternary Bi-Sn-Te nanostructures.